INAUGURAL - DISSERTATION

zur
Erlangung der Doktorwürde
der
Gesamtfakultät für Mathematik,
Ingenieur- und Naturwissenschaften der
Ruprecht-Karls-Universität
Heidelberg

vorgelegt von
M.Tech. Praveen Narasu
aus Thrissur, India

Tag der mündlichen Prüfung: 19.12.2022

Numerical Simulation of the Heating, Evaporation, Thermal Decomposition, Puffing, and Micro-Explosion of Single Alcohol/Water and Precursor/Solvent Droplets for Nanoparticle Synthesis in Spray Flames

Gutachter: Prof. Dr. rer. nat. Eva Gutheil
Prof. Dr.-Ing. Udo Fritsching

"Dream, dream, dream. Dreams transform into thoughts
and thoughts result in action." - Dr. A. P. J. Abdul Kalam

"If you do not believe you can do it,
then you have no chance at all." - Arsene Wenger

Abstract

Nanoparticle synthesis in spray flames is a promising approach to produce nanoparticles with specific properties. A liquid precursor solution, after injection, undergoes breakup and atomization resulting in the formation of the droplets. Further, heating and evaporation of these droplets occur. The droplets may experience thermal decomposition or puffing and possible micro-explosion, depending on the choice of the precursor solution and the initial conditions. Finally, gas-phase combustion occurs followed by formation of nanoparticles. It is significant to understand the different processes experienced by the droplet under such circumstances. The precursor solution consists of more than one liquid component. However, the thermophysical properties of the different components constituting the precursor solution droplets are often unknown, thus posing a major challenge to the modeling and simulation of the various processes undergone by the droplet.

The most commonly used solvents for nanoparticle synthesis using spray flames are alcohols such as ethanol and butanol. Further, some of the precursors like iron(III) nitrate nonahydrate (INN), that are used to produce nanoparticles contain water molecules. Therefore, as the first step, a zero-dimensional multicomponent droplet evaporation model is employed in order to improve the understanding of the characteristics of heating and evaporation of single spherically symmetric ethanol/water and butanol/water droplets in convective air. The interior of the droplet is not physically resolved and the convective heating and evaporation of the multicomponent droplet is considered by extending the Abramzon and Sirignano model for single component droplets. The numerical simulation results of the ethanol/water droplet are compared with the experimental data. Further, the lifetime of single butanol/water droplets is analyzed for the initial conditions of the laminar matrix burner. The matrix burner was designed within the SPP1980 to understand the reaction kinetics of new precursor solutions associated with nanoparticle synthesis in spray flames and thus, develop reaction mechanisms. The gas phase simulations concerning the matrix burner assume that the droplets are completely evaporated at the inlet of the matrix burner. Therefore, in order to support this assumption, the droplet lifetimes are evaluated.

Next, the numerical study concerning the heating, evaporation, and possible thermal decomposition of the precursor solution droplets of iron(III) nitrate nonahydrate and ethanol are performed. The precursor/solvent system of INN and ethanol is used to synthesize iron oxide nanoparticles using spray flames. There are two pathways through which the nanoparticles may be produced from the precursor solution droplet. In one pathway, the particle is formed inside the precursor solution droplet, whereas in the second pathway, thermal decomposition occurs that transfers the droplet into the gas phase, from where the nanoparticles may be generated. The numerical model is developed to capture both these pathways. Further, the precursor solution droplet consisting of titanium(IV) isopropoxide (TTIP) and *p*-xylene is considered, which is used to produce titanium dioxide nanoparticles using spray flames. The numerical results of the INN/ethanol and TTIP/*p*-xylene droplets computed using the zero-dimensional model are parameterized using polynomial approximations for use in complex simulations concerning the production of nanoparticles using spray flames. The tabulated data is provided along with a code in the *C* programming language to read the data.

Finally, in order to understand the puffing and possible micro-explosion of TTIP/*p*-xylene precursor solution droplets, a new one-dimensional model is developed. The novelty of the model is that it can distinguish between puffing and micro-explosion. The droplet heats up causing the higher volatile *p*-xylene to evaporate preferentially which results in the accumulation of the lower volatile precursor, TTIP, at the surface of the droplet and thus a liquid shell is formed that offers resistance to the process of evaporation. Also, the higher volatile component accumulates inside the droplet and puffing occurs once the boiling temperature of that liquid is reached. As the pressure in the droplet interior reaches above the ambient pressure, micro-explosion of the droplet occurs. Detailed investigation is conducted to identify the conditions for which micro-explosion of the droplet occurs.

Zusammenfassung

Die Nanopartikelsynthese in Sprühflammen ist ein vielversprechender Ansatz zur Herstellung von Nanopartikeln mit spezifischen Eigenschaften. Eine flüssige Präkursorlösung wird nach der Injektion aufgebrochen und zerstäubt, was zur Ausbildung von Tröpfchen führt. Es folgt die Erhitzung und Verdampfung der Tröpfchen, wobei, abhängig von der eingesetzten Präkursorlösung und den entsprechenden Anfangsbedingungen, thermische Zersetzung, Verpuffung oder Mikroexplosion der Tröpfchen auftreten kann. Nach der Verbrennung in der Gasphase folgt schließlich die Nanopartikelbildung. Es ist wichtig die verschiedenen Prozesse, die das Tröpfchen unter diesen Umständen durchläuft, zu verstehen. Hierbei liegt eine große Herausforderung für die Modellierung und Simulation der Prozesse darin, dass die Präkursorlösung aus mehr als einer flüssigen Komponente besteht und die thermophysikalischen Eigenschaften der verschiedenen Komponenten meist nicht bekannt sind.

Die am häufigsten verwendeten Lösungsmittel für die Sprühflammensynthese von Nanopartikeln sind Alkohole wie Ethanol oder Butanol. Zudem enthalten einige Präkursoren die für die Nanopartikelsynthese eingesetzt werden, wie beispielsweise Eisen(III)-Nitrat-Nonahydrat (INN), auch Wassermoleküle. Daher wird als erster Schritt ein nulldimensionales Multikomponenten-Tröpfchenverdampfungsmodell verwendet um die Eigenschaften der Erhitzung und Verdampfung von einzelnen, kugelsymmetrischen Ethanol/Wasser- und Butanol/Wasser-Tröpfchen in konvektiver Luft zu beschreiben. Das Innere des Tröpfchens wird nicht physikalisch aufgelöst und die konvektive Erwärmung und Verdunstung des Mehrkomponententröpfchens wird durch Erweiterung des Modells von Abramzon and Sirignano für Einkomponententröpfchen erreicht. Die Ergebnisse der numerischen Simulation von Ethanol/Wasser-Tröpfchen werden mit experimentellen Daten verglichen. Außerdem wird die Lebensdauer einzelner Butanol/Wasser-Tröpfchen für die Anfangsbedingungen eines laminaren Matrixbrenners analysiert. Der Matrixbrenner wurde innerhalb des SPP1980 entwickelt, um die Reaktionskinetik von neuen Vorläuferlösungen im Zusammenhang mit der Nanopartikelsynthese in Sprühflammen zu verstehen und Reaktionsmechanismen zu entwickeln. Die Gasphasensimulationen für den Matrixbrenner gehen davon aus, dass die Tröpfchen am Einlass des Matrixbrenners vollständig verdampft sind. Um diese Annahme zu stützen, werden daher die Tröpfchenlebensdauern ausgewertet.

Als nächstes wird eine numerische Studie zur Erwärmung, Verdampfung und möglichen thermischen Zersetzung der Tröpfchen der Präkursorlösung aus Eisen(III)-Nitrat-Nonahydrat und Ethanol durchgeführt. Das Präkursor/Lösungsmittelsystem wird zur Synthese von Nanopartikeln in Sprühflammen eingesetzt. Dabei existieren zwei Wege, über die Tröpfchen aus der Präkursorlösung hergestellt werden können. Bei niedrigen Temperaturen werden die Partikel im Inneren des Tropfens gebildet, während bei hohen Temperaturen eine thermische Zersetzung stattfindet, bei der die Tröpfchen in die Gasphase überführt werden, in der dann die Nanopartikelsynthese stattfindet. Das numerische Modell wurde entwickelt, um diese beiden Wege zu erfassen. Weiter wurde eine Präkursorlösung aus Titan(IV)-Isopropoxid (TTIP) und *p*-Xylol betrachtet, die zur Sprühflammensynthese von Titandioxid-Nanopartikeln verwendet wird. Die numerischen Ergebnisse der INN/Ethanol- und TTIP/*p*-Xylol-Tröpfchen, die mit dem nulldimensionalen Modell berechnet wurden, werden mit polynomialen Näherungen parametrisiert, um sie in komplexen Simulationen zur Herstellung von Nanopartikeln mittels Sprühflammen zu verwenden. Die tabellierten Daten werden, zusammen mit einem Code in der Programmiersprache C, zur Verarbeitung der Daten bereitgestellt.

Schließlich wird ein neues eindimensionales Modell entwickelt, um das Verpuffen und die mögliche Mikroexplosion von TTIP/*p*-Xylol Präkursorösungen zu verstehen. Die Neuheit des Modells ist, dass zwischen Verpuffung und Mikroexplosion unterschieden werden kann. Das Tröpfchen erwärmt sich, wodurch das leichter flüchtige *p*-Xylol bevorzugt verdampft, was zu einer Anreicherung des weniger flüchtigen Präkursors, TTIP, an der Oberfläche des Tropfens führt, sodass sich eine flüssige Hülle bildet, die dem Verdampfungsprozess Widerstand bietet. Außerdem sammelt sich die stärker flüchtige Komponente im Inneren des Tröpfchens an und es kommt zur Verpuffung, sobald deren Siedetemperatur erreicht ist. Wenn der Druck im Inneren des Tröpfchens den Umgebungsdruck übersteigt, kommt es zur Mikroexplosion des Tröpfchens. Eine detaillierte Untersuchung wird durchgeführt um die Bedingungen, die zu Mikroexplosionen führen, zu identifizieren.

Publications

The following peer-reviewed journals have been published

[1] P. Narasu, S. Boschmann, P. P oschko, F. Zhao, and E. Gutheil. Modeling and simulation of single ethanol/water droplet evaporation in dry and humid air. Combustion Science and Technology, 192(7):1233–1252, 2020.

[2] P. Narasu, A. Keller, M. Kohns, H. Hasse, and E. Gutheil. Numerical study of the evaporation and thermal decomposition of a single iron (III) nitrate nonahydrate/ethanol droplet. International Journal of Thermal Sciences, 170:107133, 2021.

[3] P. Narasu, M. Nanjaiah, I. Wlokas, and E. Gutheil. Numerical simulation and parameterization of the heating and evaporation of a titanium(iv) isopropoxide/p-xylene precursor/solvent droplet in hot convective air. International Journal of Multiphase Flow, 150:104006, 2022..

[4] P. Narasu and E. Gutheil. Modeling and parameterization of the evaporation and thermal decomposition of an iron (iii) nitrate nonahydrate/ethanol droplet for flame spray pyrolysis. Fluids, 7(5):146, 2022.

[5] P. Narasu and E. Gutheil. A new model for puffing and micro-explosion of single titanium(iv) isopropoxide/p-xylene precursor solution droplets. International Journal of Heat and Mass Transfer, in press, 2022.

The following peer-reviewed conference proceedings have been published

[1] P. Narasu, A. Keller, M. Kohns, H. Hasse, and E. Gutheil. Numerical study of single iron (iii) nitrate nonahydrate/ethanol droplet evaporation in dry air. 21st Annual Conference on Liquid Atomization and Spray Systems, ILASS–Asia, 2020.

[2] P. Narasu, A. Keller, M. Kohns, H. Hasse, and E. Gutheil. Numerical study of single iron (iii) nitrate nonahydrate/ethanol droplet evaporation in humid air. Proceedings of the 5th World Congress on Momentum, Heat and Mass Transfer (MHMT'20), 2020.

[3] P. Narasu, M. Nanjaiah, I. Wlokas, and E. Gutheil. Numerical study of the interaction of a titanium (iv) isopropoxide/p-xylene precursor/solvent droplet with hot convective air. 15th Triennial International Conference on Liquid Atomization and Spray Systems (ICLASS), 2021.

[4] P. Narasu and E. Gutheil. Modeling and simulation of the evaporation and thermal decomposition of an iron(iii) nitrate nonahydrate/ethanol droplet in hot convective air. 16th International Conference on Heat Transfer, Fluid Mechanics and Thermodynamics and Editorial Board of Applied Thermal Engineering (HEFAT), 2022.

[5] P. Narasu and E. Gutheil. A new model to describe puffing and microexplosion of single titanium(iv) isopropoxide/p-xylene droplets in hot convective air. 31st Conference on Liquid Atomization and Spray Systems, ILASS–Europe, 2022.

Contents

List of Tables

List of Figures

Introduction

The particles which have size in the range of 1 – 100 nanometer (nm) are defined as nanoparticles [1]. Nanoparticles exhibit properties that are different from the larger sized particles. For instance, it is possible to shift the resonance wavelengths by tuning the geometry of the particle which has applications in the field of trace metal detection and molecular labeling [2]. Another example is that of zinc oxide nanoparticles that possess the ability to block ultra violet radiation. In fact this peculiar property of zinc oxide nanoparticles have made them a common ingredient in sunscreen lotions [3]. Nanoparticles have applications in wide variety of fields including agriculture, healthcare, textile, electronics, and so on. A brief overview of the different areas of application is displayed in Fig. 1.1. Due to its various applications there is a high demand for the production of nanoparticles with specific properties which forms a branch of nanotechnology [3].

There are two major methods to produce nanoparticles, namely, gas flame synthesis

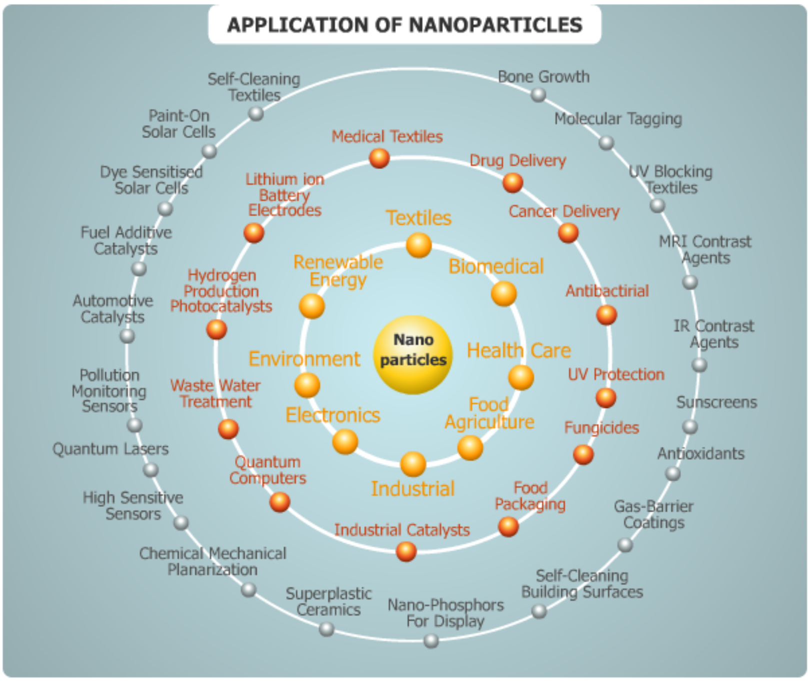

Figure 1.1: Various fields of application where nanoparticles are used [6].

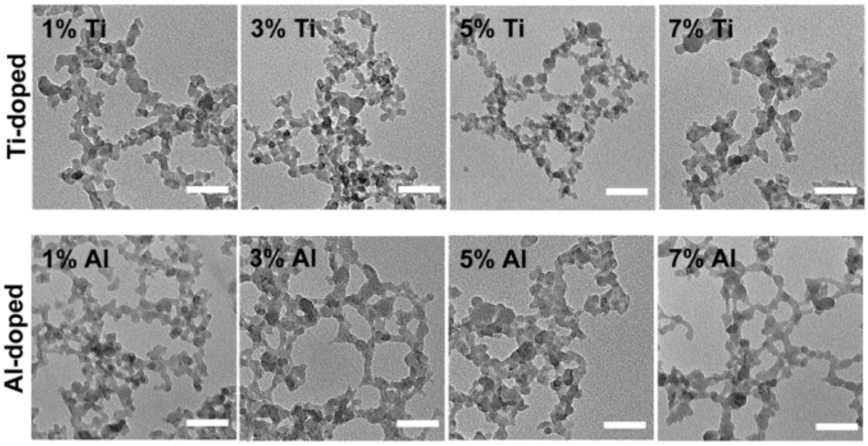

Figure 1.2: Transmission electron microscopy images of titanium (Ti) - doped and aluminium (Al) - doped fumed silica nanoparticles produced via flame spray pyrolysis [11]

and flame spray pyrolysis (FSP). Gas flame synthesis is a well established process [4, 5] to synthesize nanoparticles. The gas flame synthesis of nanoparticles involves the generation of nanoparticles via the combustion of gases using a hot wall or plasma furnace reactor. The nanoparticles produced using gas flame synthesis include carbon black [7], titanium dioxide [8], and fumed silica [9]. However, there are certain disadvantages associated with this methodology of producing nanoparticles, such as difficulties related to generating nanoparticles without agglomeration and producing materials consisting of more than one component [10]. The alternative approach is synthesizing nanoparticles via spray flames which is also known as flame spray pyrolysis.

In flame spray pyrolysis, a precursor solution is injected and sprayed which results in the formation of precursor/solvent droplets. These droplets undergo heating and evaporation and is transformed into the gas phase. There is also the possibility that, at higher ambient temperature regimes in the flame, the precursor solution droplets may thermally decompose thus, transferring themselves into gaseous species. Further, certain precursor/solvent systems, whose difference in volatility is high, experience puffing and micro-explosion before the droplet is transformed into the gas phase. In the gas phase, further reactions occur leading to the formation of the nanoparticles. Thus, knowing detailed numerical simulation results with respect to the droplet is useful for simulating more complex processes associated with flame spray synthesis of nanoparticles, since it significantly reduces the computational time. Therefore, it is very much important to understand the behavior of a single precursor solution droplet in the context of flame spray pyrolysis.

There are numerous advantages of using flame spray pyrolysis to synthesize nanoparticles as compared to that produced using gas phase synthesis. In flame spray pyrolysis, it is possible to produce a wider range of particles, such as alloys. Further, it is also possible to control the properties of the final particle that is produced. Sun et al. [11] produced titanium and aluminum doped fumed silica using flame spray pyrolysis, which are displayed in Fig. 1.2. They found that doping fumed silica with titanium or aluminium reduces the surface silanol density and thus makes it safer to use in the food and pharmaceutical industry. Different configurations of FSP were tried out by Deligiannakis et al. [12] for the controlled synthesis of nanocatalysts. Deligiannakis et al. [12] reported that flame spray pyrolysis demonstrated a huge potential for the efficient and clean production of hydrogen at conditions of ambient temperature and pressure. Gao et al. [13] synthesized catalysts with surface-supported isolated platinum atom using flame spray pyrolysis. They concluded that there was significant improvement with respect to the cost efficiency and the performance of the catalysts. The one-step synthesis of nanocatalysts was investigated by Yuan et al. [14], where the feeding rates of the precursor and the copper loadings were varied. The objective was to understand the potential of cupric oxide with respect to the catalytic combustion of methane and carbon monoxide, in order to aid in reducing the pollution emissions. Yuan et al. [15] performed experimental and theoretical investigations to understand the effect of bifunctional copper components on titanium dioxide, in order to optimize the efficiency of photothermocatalysts for use in the reduction of air pollutants. The thermally stable metal oxide-supported single-atom platinum catalysts were produced via flame spray pyrolysis by Ding et al. [16]. They found that these catalysts displayed excellent catalytic performance in methane partial oxidation reactions, methane combustion, and carbon monoxide oxidation as compared to those synthesized using the conventional methods. One of the main advantages of using flame spray pyrolysis to produce nanoparticles is that it is possible to synthesize materials with specific properties. Also, it is possible to control the purity of the final particle that is produced. Further, there exists flexibility with respect to the experimental operating conditions [17]. In addition, it is possible to produce nanoparticles with uniform size without making a compromise on the crystallinity or purity of the particles. Such particles are in high demand, especially in applications related to the medical field [18]. There are a wide variety of applications ranging from usage in batteries, fuel cells, sensors, solar cells, and functional pigments [18].

During the synthesis of nanoparticles, the quality of the final particles produced is of paramount importance. For example, the efficiency of the photocatalysts generated using flame spray pyrolysis depends highly on the final quality of the nanocrystals [19]. Teoh [19] identifies numerous challenges that have to be overcome for efficient synthesis of functional nanoparticles via flame spray pyrolysis. One of the challenges is associated with the energy transfer in phosphors as well as with regard to the transportation of charges in solar cells. Another difficulty is regarding the electrons spin related to the superconductor, magnetic, and spintronic applications. Because of the short flame residence time at extreme conditions, flame spray pyrolysis has the the ability to yield metastable photocatalysis and thus, holds the advantage over other more established processes [19].

Over the years, a lot of experimental research works have been conducted focusing on the flame spray pyrolysis. Chang et al. [20] conducted experiments to explore the synthesis of titanium dioxide nanoparticles from a precursor solution consisting of titanium(IV) isopropoxide and ethanol using flame spray pyrolysis. It was found that using a lower concentration of the precursor and a higher flame temperature enhanced the process of droplet evaporation and thus, smaller sized nanoparticles were formed from the chemical reactions. The complex processes during the generation of titanium dioxide nanoparticles using the precursor/solvent system of titanium(IV) isopropoxide/ethanol using spray flames was investigated both experimentally and numerically by Weise et al. [21]. They analyzed the effect of the composition and the mass flow rate of the precursor solution on the final size of the particle.

There exists numerical works concerning nanoparticle synthesis using flame spray pyrolysis. The synthesis of nanoparticles via flame spray pyrolysis was also numerically studied by Neto et al. [17]. In order to understand the impact of the process of combustion concerning the precursor/solvent system on the temperature of the flame and the evolution of the particle, seven different chemical reaction mechanisms were employed. Further, a Eulerian-Lagrangian approach was chosen to describe the reacting turbulent multiphase flow and the growth of the zirconium dioxide nanoparticles was evaluated by using a mono-disperse population balance model where the effects of coagulation and sintering were also included. The differences between the size and the temperature of the primary particles calculated using the model and that found from the experiment were about six and nine percent, respectively. The numerical investigation carried out by Madero et al. [22] compared the low temperature flame spray pyrolysis (LT-FSP) to a flame assisted spray pyrolysis system. They concluded that the low temperature flame spray pyrolysis process provides a more uniform temperature distribution as compared to that of the flame assisted spray pyrolysis system. Thus, more uniform final particles are formed via the LT-FSP system.

Machine learning was used by Paulson et al. [23] to optimize the process of flame spray pyrolysis and reported an improvement of around nineteen and twenty five percent after five and fifteen experimental runs, respectively. Dasgupta et al. [24] computationally investigated the generation of silica nanoparticles via flame spray pyrolysis and found that the estimated the size of the particles and their distribution were in good agreement with the experimental results. The numerical study of the formation of zirconia primary and agglomerate nanoparticles was performed by Meierhofer et al. [25] for a laboratory scaled flame spray pyrolysis reactor. The numerical model was able to predict the size of the nanoparticles with an error of twenty five per cent as compared to that of the experimental data.

Neto et al. [26] computationally studied the generation of zirconium dioxide nanoparticles using the precursor solution of zirconium n-propoxide in ethanol and propanol via flame spray pyrolysis. The error between the numerically evaluated value of the number of primary particles per agglomerate and that found from the experimental results acquired via the transmission electron microscopy (TEM) technique, was found to be approximately ten percent. The numerical simulations of the synthesis of silica nanoparticles using spray flames was performed by Dasgupta et al. [27], in a simplified annular burner. The study investigated the breakup of the liquid spray, evaporation, mixing, combustion, and formation of the particles. The calculated volume fraction and particle number density were found to be in good agreement with the numerical results reported by Rittler et al. [28].

The *SpraySyn* burner was designed by Schneider et al. [29] as a new standard research burner to synthesize nanoparticles using flame spray pyrolysis, see Fig. 1.3.

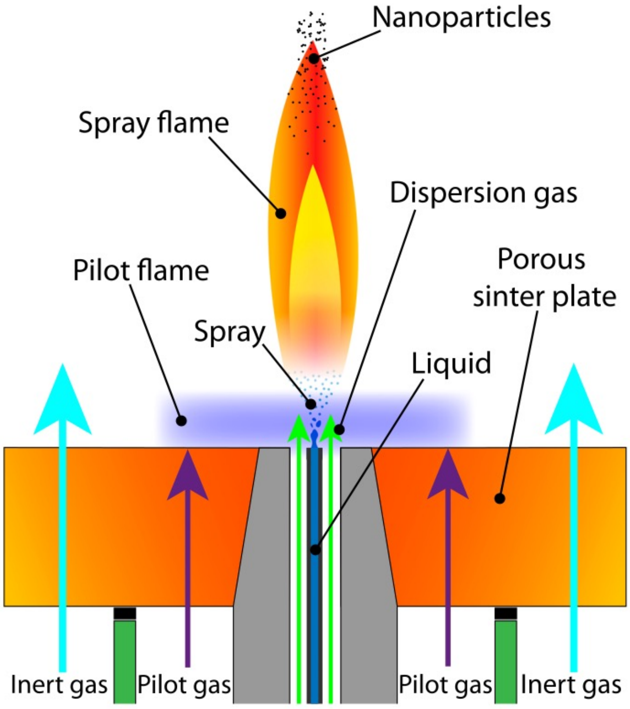

Figure 1.3: Schematic of *SpraySyn* burner designed by Schneider et al. [29].

The major advantages of the newly designed *SpraySyn* burner was that a wide variety of precursor solution combinations was possible to be used to produce nanoparticles. Further, the geometries and boundary conditions were well defined in such a way that it is possible to perform numerical simulations, which was confirmed by performing large eddy simulations, and also well accessible to conduct optical diagnostics study.

Many experimental studies have been carried out using the *SpraySyn* burner. Using the phase doppler anemometry (PDA) technique, Stodt et al. [30] conducted experiments in the *SpraySyn* burner [29], in order to understand the impact of the precursor concentration on the process of evaporation. The precursor solution system of iron(III) nitrate nonahydrate in ethanol and 2-ethylhexanoic acid (EHA) was used for the study. They found that the evaporation rates were enhanced for the spray flames consisting of the precursor solution as compared to the spray flames containing only the solvent. Suleiman et al. [31] developed a new type of particle mass spectrometery known as the atmospheric pressure particle mass spectrometery (AP-PMS) to find the distributions of the particle size in spray flames at ambient pressure using the precursor solution system of iron(III) nitrate nonahydrate in ethanol and 2-ethylhexanoic acid. Compared to the conventional measurement techniques, the newly developed atmospheric pressure particle mass spectrometery was found to be more robust to higher pressures and particle number concentrations. Thus, AP-PMS provides an appealing option to study the growth of particles in spray flames. Tischendorf et al. [32] used two precursor solution combinations, namely, iron(III) nitrate nonahydrate in ethanol and iron(III) nitrate nonahydrate in ethanol with 2-ethylhexanoic acid, to synthesize iron oxide nanoparticles in the *SpraySyn* burner designed by Schneider et al. [29], to confirm if the addition of 2-ethylhexanoic acid to the precursor solution leads to the formation of homogeneous particles via the gas-to-particle pathway [33]. The experimental study found that the droplet-to-particle and the gas-to-particle routes of particle formation may coexist. The synthesis of titanium dioxide nanoparticles using the precursor solution of titanium(IV) isopropoxide and ethanol for a configuration similar to that of the *SpraySyn* burner [29], was numerically studied by Abdelsamie et al. [34] through direct numerical simulations (DNS) . The entire process of the nanoparticle synthesis including the evaporation of the precursor/solvent system and the kinetics associated with the gas phase combustion were considered in the numerical simulations.

Droplet evaporation has a significant influence on the synthesis of nanoparticles. Kastrinaki et al. [35] conducted experimental investigation focusing on the generation of iron and iron oxide-based particles via aerosol spray pyrolysis. They found that the particles formed were more spherical when the iron nitrate precursor was used. Also, employing the the chloride precursor resulted in the generated of irregularly shaped particles. Thus, they concluded that the choice of the precursor had an impact on the morphology of the particles. The process of droplet surface evaporation was found to be the reason for such a behavior. The droplet evaporation occurring in the spray pyrolysis tube was numerically investigated by Florena et al. [36]. The study employed a droplet evaporation model with no resolution of the droplet interior. They concluded that temperature of the reactor wall had a significant influence on the size of the final particle whereas the rate of flow of the carrier gas did not affect the particle size.

Thus, the objective of the present study is the numerical simulation of the heating and evaporation of droplet for various multicomponent systems. Depending on the choice of the system and the initial conditions, other processes such as thermal decomposition, puffing or micro-explosion may occur, which are coupled with the evaporation process.

The dissertation is grouped into the following chapters. Details of the zero-dimensional and one-dimensional models are presented in chapter 2. The governing equations to describe the heating and evaporation of multicomponent droplets are discussed. Further, the coupling of the governing equations concerning thermal decomposition to the zero-dimensional model is presented. In addition, the modifications to the one-dimensional model to take into account the puffing and possible micro-explosion are discussed. Details regarding the variable thermophysical properties of various multicomponent liquid mixtures investigated in the present study are presented. Finally, the numerical procedure is discussed to solve the respective governing equations. Chapter 3 presents the results and discussions with respect to the droplet behavior for different multicomponent systems. The heating and evaporation characteristics of ethanol/water droplet at atmospheric pressure along with the experimental validation are presented. In addition, the characteristics of the evaporation of single butanol/water droplet at low ambient pressures are discussed. Further, the precursor solution droplet consisting of iron(III) nitrate nonahydrate and ethanol is considered, where the droplet-to-particle and the droplet into gas phase pathways are studied in detail, including the parameterization of the numerical results. The characteristics of the droplet constituting of the precursor/solvent system of titanium(IV) isopropoxide and *p*-xylene along with the parameterization of the numerical simulation results are discussed next. Further, the puffing and the possibility of micro-explosion of TTIP/*p*-xylene droplets are explored. Finally, chapter 4 presents the summary, the major conclusions, and the possibilities for future work.

Mathematical Model

This section focuses on the mathematical modeling of the different characteristics of a single multicomponent droplet. At first, the state of the art is presented. Further, the models to describe the droplet heating and evaporation are discussed. Depending on the liquid components constituting the droplet, the droplets may undergo thermal decomposition, puffing or micro-explosion which are presented in subsequent subsections. Finally, the details of the thermophysical properties of the different multicomponent systems are discussed along with the numerical steps involved in solving the governing equations.

2.1 State of the Art

There are various numerical studies that use different models to describe the heating and evaporation of droplet. Different assumptions are used in the formulation of various models. The distillation-limit model neglects the variation of the temperature gradient inside the droplet and thus, assumes that the temperature is uniform [37]. Similarly, the rapid-mixing model considers the temporal variation of the composition assuming that the composition within the droplet is spatially uniform [38]. Further, the conduction-limit [39, 37] and the diffusion-limit [40, 41] models take into account the temporal as well as the spatial variation of the temperature and the composition of the droplet. The comparison between the distillation-limit and the conduction limit models was performed by Kayser Jr and Bennett [42]. They found that the profiles of the droplet temperature computed using both the models agreed to within twenty percent of each other. Law and Law [43] developed the multicomponent analog of the classical d^2 law [44, 45] for the evaporation of a droplet consisting of octanol and undecane. They concluded that, even though the numerical results agreed with that found from the experiment, the model cannot be used to evaluate the profiles of the temperature and concentration during the initial period of droplet heating. During the formulation of the the classical d^2 law, Godsave [44] employed constant physical properties in the model. Over the years, numerous studies [46, 47, 48] have concluded that employing variable physical properties instead of constant properties significantly improves the computed results of the heating and evaporation of the droplet.

A numerical model was developed by Abramzon and Sirignano [49] to describe the heating and evaporation of a single component droplet. They considered non-unitary

Lewis number in the gas film as well as variable thermophysical properties. With respect to processes associated with most practical applications, the evaporation of a droplet takes place in a convective ambience. Hence, the convective effects were taken in to account by using the modified Sherwood and Nusselt numbers. Also, in order to reduce the errors of the computation, it was recommended to calculate these numbers for a non-vaporizing droplet by using the correlations provided by Clift et al. [50], instead of the well known correlations of Frössling [51]. In applications related to combustion, the droplets consist of more than one liquid components. Therefore, the single component droplet evaporation model of Abramzon and Sirignano [49] was extended to multicomponent droplets by Brenn et al. [52]. They considered different liquid mixtures consisting of more than three components of alkanes and alcohols. Some of the liquid mixtures investigated had small amounts of water in order to understand its impact on the process of evaporation. They considered the non-ideal nature of the liquid mixture by calculating the activity coefficients using the UNIFAC method. An experimental investigation was also conducted for single droplets evaporating in an acoustic levitator. The results computed using the numerical model were found to be in good agreement with that found from the experiments.

The combustion and extinction of single droplets was studied numerically by Marchese and Dryer [53]. An one-dimensional model using detailed chemical reactions was employed. The numerical results were compared with that of the experiments, where a free falling single droplet was analyzed in a microgravity drop tower. The initial radius of the droplet was varied between 125 µm and 500 µm. Also, different compositions of the water component up to fifty percent in mass was explored. Major combustion and ignition characteristics as well as the flame standoff distance computed using the numerical simulations were compared with the experimental results. They concluded that the liquid mass Peclet number had an influence on the droplet characteristics. Lupo and Duwig [54] numerically studied the evaporation of a single droplet constituting of ethanol and water, close to the azeotropic point of the mixture. The major objective of the investigation was to explore the droplet heating and evaporation characteristics at the composition of the droplet near and just below the azeotropic point of ethanol/water mixture at ambient pressure. The heat and species transport of different phases were solved. The thermophysical and transport properties used in the model vary both with respect to the temperature as well as the composition. The characteristics of the evaporation displayed were similar to that observed for a pure ethanol droplet, for a major portion of the droplet lifetime. Also, they reported that only at conditions not close to the azeotropic point of the liquid mixture, was it necessary to use the variable liquid density. However, the numerical results presented were not validated due to the lack of experimental data.

Zhang et al. [55] carried out the numerical study of the evaporation of a droplet constituting of ethanol and water components under oscillatory pressure. The two film theory using the non-ideal vapor-liquid equilibrium was employed. They found that the lifetime of the droplet was reduced because of the oscillation of the environmental pressure. The stability of the mixture consisting of alcohol and water for spray combustion in an ambience of air enriched with oxygen was investigated by Yi and

Axelbaum [56]. Both experimental as well as numerical studies were performed, which confirmed that the ethanol evaporates preferentially as compared to that of water. They recommended the use of the distillation-limit model in order to describe the process of evaporation.

An important factor in the numerical simulations of the droplet evaporation characteristics is the calculation of the vapor pressure. The numerical study performed by Filho et al. [57] investigated droplets evaporating in a combustion environment, where the major focus was on the accurate representation of the thermophysical properties of the carrier gas. The study employed various models to evaluate the vapor pressure. It was concluded that using the Antoine or Wagner [58] equations resulted in good agreement with the experimental results. The recent developments in the numerical modeling with respect to the heating and evaporation characteristics of fuel droplets was reviewed in detail by Sazhin [59]. It was found that special investigation was required to understand the evaporation of droplets consisting of complex multicomponent systems.

There are numerical studies concerning nanoparticle synthesis using flame spray pyrolysis, where the droplet evaporation have been considered. The numerical investigation of the formation of zirconium dioxide nanoparticles from flame spray pyrolysis was carried out by Heine and Pratsinis [60], where the objective was to understand the interaction between the evaporation of the droplet, the process of combustion, and the formation and growth of the particle. The droplet evaporation model proposed by the study of Abramzon and Sirignano [49] for single component droplets is extended in order to incorporate the multicomponent droplet evaporation of the precursor solvent system. The sectional population balance model is employed to account for the processes of nucleation, coagulation, and sintering. The numerical results of the distribution of the size of the particles was compared with the experimental data. With respect to synthesis of silica nanoparticles via flame spray pyrolysis using ethanol and hexamethyldisiloxane as the precursor solution and oxygen as the dispersion gas, large eddy simulations were performed by Rittler et al. [28], where the major focus was on the interaction between the process of evaporation, combustion in the gas phase, and the production of nanoparticles. Also, the distillation-limit model was used to describe the heating and evaporation of the precursor/solvent droplet. The evaporation of titanium(IV) isopropoxide/hexane and titanium(IV) isopropoxide/toluene droplets under vacuum in a pulsed-pressure chemical vapor deposition process was modeled by Boichot and Krumdieck [61]. They employed a zero-dimensional droplet evaporation model assuming constant liquid mixture properties except for the vapor pressure. It was found that the kinetic of the evaporation of the precursor solution droplets was influenced by the heat transfer and the associated thermodynamics.

There is the possibility that the precursor used for the synthesis of nanoparticles decomposes thermally during the evaporation of the precursor solvent droplet [32, 62, 63]. However, there are only a few studies that have performed numerical investigation concerning the coupling of the droplet evaporation and thermal decomposition processes. A modified spray pyrolysis system was employed by Gapale et al. [64] to perform numerical study regarding the deposition of titanium dioxide thin films on a glass substrate. The numerical model coupled the atomization of the precursor/solvent system, the transportation of the droplet in the ambience, the evaporation of the precursor solution, the decomposition, and the growth of the titanium dioxide film in order to evaluate the final size of the particle. Widiyastuti et al. [65] performed the numerical study of the formation of zirconia particles during spray pyrolysis by coupling the evaporation and thermal decomposition processes. They found that for temperatures beyond the thermal decomposition temperature, the final size of the particle was smaller as compared to that for temperatures lower than the thermal decomposition temperature. Thus, they concluded that both droplet evaporation and thermal decomposition had a significant influence in determining the final particle size.

During the generation of nanoparticles using spray flames, the precursor/solvent droplets may undergo puffing and micro-explosion in addition to the processes of heating and evaporation [30, 66, 67]. Very few numerical investigations focus on the puffing and micro-explosion of the precursor solvent droplets used for producing nanoparticles. However, there are numerical studies that explore these phenomena experienced by emulsified fuel and slurry droplets. The experimental and numerical investigation of the puffing and micro-explosion of composite droplets such as kerosene, diesel, and rapeseed oil/water was carried out by Fedorenko et al. [68]. The numerical model considered a fuel/water droplet, where a water sub-droplet is located at the droplet center. The one-dimensional heat transfer equation was solved analytically to take into account the process of heating and the well known Abramzon-Sirignano model [49] was employed to consider the evaporation of the fuel. The model predicted the time to puffing or micro-explosion and it was found to be in good agreement with the experimental data. However, the processes of puffing and micro-explosion were not well distinguished. Baek et al. [69] performed the experimental and numerical study of the micro-explosion of a slurry droplet consisting of n-heptane and aluminium. The one-dimensional heat transfer equation was employed to describe the heating of the droplet whereas the zero-dimensional model was used to consider the process of evaporation without taking into account the effects of convection. They found that the formation of the solid porous shell hindered the evaporation process and thus, the liquid gets heated beyond the boiling temperature, eventually causing micro-explosion of the slurry droplet. The time to micro-explosion computed by the numerical study for different sizes of the droplet was found to be in good agreement with the experimental results.

The micro-explosion of the precursor/solvent droplet of tin(II) 2-ethylhexanoate/m-xylene was studied computationally by Ren et al. [70] without taking into consideration the process of puffing. The heat and mass transfer were described using the one-dimensional equations and approximated thermophysical properties of the precursor were employed. It was found that as the initial concentration of the precursor was increased, the time to micro-explosion becomes shorter. High end optical techniques such as interferometric particle imaging and standard rainbow refractometry were used by Li et al. [71], to analyze the micro-explosion of single droplets during the process of combustion. The droplet consisted of the precursor solution combination of tin(II) 2-ethylhexanoate and xylene. Additionally, in order to simulate the experimental changes of rainbow pattern and droplet size, a multicomponent diffusion-limit model was employed. They found that with the increase of the initial loading of the precursor, the accumulation of the precursor at the surface of droplet is hastened and thus, quickening up the micro-explosion of the precursor/solvent droplet.

The governing equations of the numerical models associated with heating, evaporation, thermal decomposition, puffing and micro-explosion of the droplet are presented in detail next.

2.2 Zero-Dimensional Model

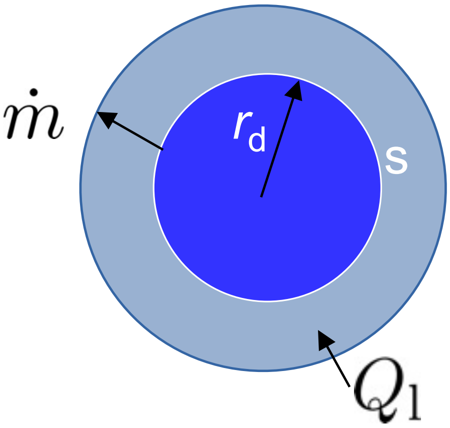

Figure 2.1: Schematic of the droplet of radius r_d, mass evaporation rate $\dot{m}$, and heat transfer rate Q_l.

The zero-dimensional model concerns the description of convective heating and evaporation of a spherically symmetric droplet in a convective gas stream at atmospheric pressure. The schematic of the droplet is displayed in Fig. 2.1. Low droplet Reynolds numbers up to about twenty are considered to ensure that there is neither inner recirculation of the droplet nor flow separation in the wake of the droplet. Further, the Weber numbers are below 0.5 to make sure that no droplet breakup would occur. The distillation-limit model is employed to account for the droplet heating and the rapid-mixing model is used to describe the droplet evaporation for low thermal and mass Peclet numbers [72], respectively. Therefore, both constant temperature and concentrations inside the droplet are assumed with no spatial resolution of the droplet interior. Thus, all characteristic variables vary only with time. The convective droplet heating and evaporation is modeled following the previous studies of Brenn et al. [52], that is an extension of the formulation of Abramzon and Sirignano [49] to account for multicomponent droplets. Also, it is assumed that the droplet is spherical all the times, the solubility of air in the liquid is negligible, mass diffusion due to temperature and pressure gradients is negligible, the gas phase is in a quasi-steady state, the droplet evaporates in a non-reacting inert environment, and heat transfer due to radiation is negligible [52]. The non-ideal behavior of the different liquid mixtures is considered through the use of appropriate activity coefficients modeled using different methods. Further, the model is extended to account for the heating and evaporation in humid air.

2.2.1 Droplet Heating

The droplet heating is described using the distillation-limit model [73], that was extended to account for convection around the droplet by Abramzon and Sirignano [49]. Thus, the temperature T_s at the droplet surface, s, varies with time, t, as

$$m c_{\mathrm{pl}} \frac{\mathrm{d}T_{\mathrm{s}}}{\mathrm{d}t} = 2\pi r_{\mathrm{d}} \lambda_{\mathrm{f}}\ \widetilde{\mathrm{Nu}}\ \ln(1+B_{\mathrm{T}}) \frac{T_{\mathrm{g}} - T_{\mathrm{s}}}{B_{\mathrm{T}}} - \sum_{i=1}^{2} \dot{m}_i L_{\mathrm{v},i}(T_{\mathrm{s}}) \equiv Q_{\mathrm{l}}, \tag{2.1}$$

where the Spalding heat transfer number, B_{T} is defined as [49, 52]

$$B_{\mathrm{T}} = (1 + \sum_{i=1}^{2} Y_{\mathrm{i}} B_{\mathrm{M},i})^{\phi} - 1.0; \quad \phi = \frac{c_{\mathrm{pl}}}{c_{\mathrm{pf}}} \frac{\widetilde{\mathrm{Sh}}}{\widetilde{\mathrm{Nu}}} \frac{1}{\mathrm{Le}}. \tag{2.2}$$

ϕ accounts for the differences in heat and mass transfer, c_{pf} and c_{pl} are the specific heat capacity in the film and of the liquid mixture, respectively, and Le denotes the Lewis number. Equation (2.1) represents the heat transfer Q_{l} between the gas and the liquid phase, m is the total mass of the droplet, λ_{f} denotes the thermal conductivity of the gas mixture in the film, T_{g} is the ambient gas temperature, and $L_{\mathrm{v},i}(T_{\mathrm{s}})$ represents the latent heat of vaporization of the component i at temperature T_{s}. The modified Sherwood, $\widetilde{\mathrm{Sh}}$, and Nusselt, $\widetilde{\mathrm{Nu}}$, numbers are employed to account for the convective effects in mass and heat transfer, respectively [49]. The Spalding mass transfer number $B_{\mathrm{M},i}$ of the component i in Eq. (2.2) is defined as [52]

$$B_{\mathrm{M},i} = \frac{Y_{\mathrm{s},i} - Y_{\infty,i}}{1 - Y_{\mathrm{s},i}} \tag{2.3}$$

In Eq. (2.3), $Y_{\mathrm{s},i}$ is the mass fraction of the component i at the surface whereas $Y_{\infty,i}$ denotes the mass fraction of the component i in the ambience.

The modified Sherwood, $\widetilde{\mathrm{Sh}}$, and Nusselt, $\widetilde{\mathrm{Nu}}$, numbers that account for the convective mass and heat transfer, respectively, are calculated as per the formulation provided by Abramzon and Sirignano [49] as

$$\widetilde{\mathrm{Sh}} = 2 + \frac{\mathrm{Sh} - 2}{F_{\mathrm{M}}}, \tag{2.4}$$

$$\widetilde{\mathrm{Nu}} = 2 + \frac{\mathrm{Nu} - 2}{F_{\mathrm{T}}}. \tag{2.5}$$

For a non-vaporizing droplet, the Sherwood, Sh, and Nusselt, Nu, numbers are calculated following the correlations of Clift et al. [50] as

$$\mathrm{Sh} = 1 + (1 + \mathrm{Re}\ \mathrm{Sc})^{1/3} f(\mathrm{Re}), \tag{2.6}$$

$$\mathrm{Nu} = 1 + (1 + \mathrm{Re}\ \mathrm{Pr})^{1/3} f(\mathrm{Re}). \tag{2.7}$$

Here, Re denotes the Reynolds number, Sc represents the Schmidt number, and Pr is the Prandtl number. $f(\mathrm{Re})$ is a function of the Reynolds number defined as [50]

$$f(\mathrm{Re}) = \begin{cases} 1 & \text{if Re} \leq 1 \\ \mathrm{Re}^{0.077} & \text{if Re} \leq 400. \end{cases} \tag{2.8}$$

In Eqs. (2.4)-(2.5), F_{M} and F_{T} are the corrections factors defined as [49]

$$F(B_{\mathrm{M}}) = (1 + B_{\mathrm{M}})^{0.7} \frac{\ln(1 + B_{\mathrm{M}})}{B_{\mathrm{M}}}, \tag{2.9}$$

$$F(B_{\mathrm{T}}) = (1 + B_{\mathrm{T}})^{0.7} \frac{\ln(1 + B_{\mathrm{T}})}{B_{\mathrm{T}}}. \tag{2.10}$$

2.2.2 Droplet Evaporation

The droplet evaporation is described by the rapid-mixing model [49], which was extended to account for the mass evaporation rate of multicomponent droplet by Brenn et al. [52] as

$$\dot{m} = \sum_{i=1}^{2} 2\pi r_{\mathrm{d},i} \rho_{\mathrm{f}} D_{\mathrm{f},i} \widetilde{\mathrm{Sh}} \, \ln(1 + B_{\mathrm{M},i}). \tag{2.11}$$

In Eq. (2.11), $r_{\mathrm{d},i}$ is the radius of component i of the droplet, ρ_{f} denotes the density of the mixture in the film, and $D_{\mathrm{f},i}$ represents the diffusivity of the component i in the film. Note that, in case of condensation, the mass evaporation rate defined in Eq. (2.11) may become negative. All properties in the film are evaluated using the one third rule [74].

In the present study, the zero-dimensional model is employed to study the heating and evaporation characteristics of ethanol/water droplets and is validated with experimental results of Ma et al. [75]. Further, the model is extended to study the evaporation of the precursor/solvent systems of iron(III) nitrate nonahydrate/ethanol and titanium(IV) isopropoxide/*p*-xylene. In the case of iron(III) nitrate nonahydrate/ethanol droplet, the zero-dimensional multicomponent evaporation model is coupled with the thermal decomposition model, which is discussed next.

2.2.3 Thermal Decomposition

For the multicomponent droplet consisting of the precursor solution of iron(III) nitrate nonahydrate (INN) and ethanol, in addition to the heating and evaporation, thermal decomposition may occur. There exists two different pathways for the evaporation of the precursor/solvent droplet which are displayed in the schematic of Fig. 2.2 [76], where $T_{\mathrm{d},0}$ is the initial droplet temperature. During the evaporation of the precursor solution droplet, the droplet heats up and the solvent evaporates. If the droplet surface temperature T_{d}, attained during the evaporation process, remains below the thermal decomposition temperature T_{th}, the solute is left behind in the particle phase as shown in the left part of Fig. 2.2. Else, if the instantaneous droplet temperature is equal or above T_{th}, thermal decomposition occurs transferring the precursor solution droplet completely into the gas phase, see right part of Fig. 2.2, which is the preferred pathway in FSP. However, there exists the possibility of particle formation via the first pathway, especially in colder regions just after liquid injection.

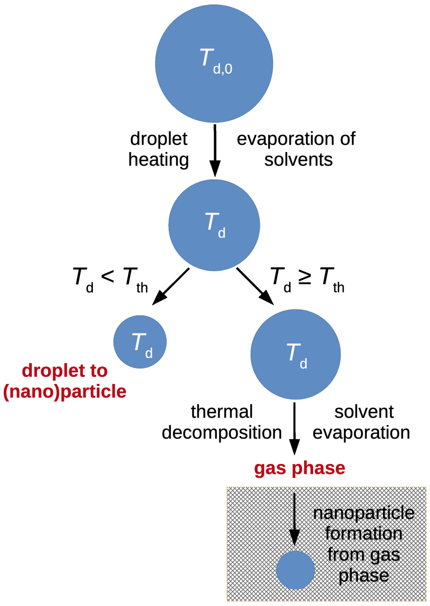

Figure 2.2: Schematic (Narasu et al. [76]) showing the two pathways for particle formation from a precursor solution droplet.

For the system of INN and ethanol, if the droplet temperature remains below the thermal decomposition temperature T_{th} of 403 K of the INN, the solvent evaporates leaving behind the iron(III) nitrate particle. Once the droplet temperature reaches or exceeds the thermal decomposition temperature, the iron(III) nitrate thermally decomposes into iron(III) oxide, Fe_2O_3, and dinitrogen pentoxide, N_2O_5, transforming the precursor solution droplet into the gas phase.

In the model, the INN is treated as two components, iron(III) nitrate and water. Hence, the precursor solution droplet constitutes of three components in total, which are iron(III) nitrate, water, and ethanol [76, 77, 78]

$$\mathrm{Fe(NO_3)_3.9\,H_2O \rightarrow Fe(NO_3)_3 + 9\,H_2O_{(l)}} \tag{2.12}$$

$$\mathrm{H_2O_{(l)} \rightleftharpoons H_2O_{(v)}} \tag{2.13}$$

$$\mathrm{C_2H_5OH_{(l)} \rightarrow C_2H_5OH_{(v)}}. \tag{2.14}$$

There is the possibility of condensation of water due to which the reverse step is included in Eq. (2.13). Further, the evaporation of the solvent ethanol is considered in Eq. (2.14). The evaporation of water and ethanol is described by the zero-dimensional model in section 2.2.

As per the studies of Gadalla and Yu [79], the reactions involving the thermal decomposition of INN in air include

$$\mathrm{Fe(NO_3)_3.9H_2O \rightarrow Fe(NO_3)_3.2H_2O + 7H_2O_{(l)}} \tag{2.15}$$

$$\mathrm{H_2O_{(l)} \rightarrow H_2O_{(v)}} \tag{2.16}$$

$$\mathrm{2[Fe(NO_3)_3.2H_2O] \rightarrow Fe_2O_3.3H_2O + 3N_2O_5 + H_2O_{(v)}} \tag{2.17}$$

$$\mathrm{Fe_2O_3.3\,H_2O \rightarrow Fe_2O_3 + 3\,H_2O_{(v)}}. \tag{2.18}$$

However, the details regarding the kinetic reaction rates for these reactions is not provided by Gadalla and Yu [79]. The reaction kinetic data for the thermal decomposition of INN in an ambience of nitrogen is given by Mu and Perlmutter [80]. Also, Mu and Perlmutter [80] observe that the decomposition of INN into $Fe(NO_3)_3$ starts at 305 K and that of $Fe(NO_3)_3$ into Fe_2O_3 starts at 403 K for which the reaction kinetic data are provided. However, there is no reaction mechanism proposed by Mu and Perlmutter [80] for the thermal decomposition of INN.

Thus, to conclude the reaction in Eq. (2.19) may be added to the reactions in Eqs. (2.12)-(2.14) to complete the global reaction of INN into the gas phase.

$$2\,\mathrm{Fe(NO_3)_3} \rightarrow \mathrm{Fe_2O_3} + 3\,\mathrm{N_2O_5} \tag{2.19}$$

Equations (2.12)-(2.14) stand for the evaporation of water and ethanol. If the thermal decomposition temperature of 403 K is breached, the iron(III) nitrate decomposes as per the reaction (2.19) for which the reaction rate is given in terms of α

$$\alpha = 1 - \frac{Y_{\mathrm{IN},t}}{Y_{\mathrm{IN},0}}, \tag{2.20}$$

where $Y_{\mathrm{IN},t}$ denotes the mass fraction of iron(III) nitrate at time t and $Y_{\mathrm{IN},0}$ represents the initial mass fraction of iron(III) nitrate. Note that, in Eq. (2.20), the final mass of iron(III) nitrate [80] is assumed to be zero.

The time derivative of α yields [80]

$$\frac{\mathrm{d}\alpha}{\mathrm{d}t} = k_{\mathrm{th}}(1-\alpha)^n \tag{2.21}$$

where k_{th} is the kinetic rate constant of the thermal decomposition given by

$$k_{\mathrm{th}} = k_0 \mathrm{e}^{-E/(\mathrm{R}T)}. \tag{2.22}$$

The pre-exponential factor k_0 in Eq. (2.22) equals 2.60 10^{44} s^{-1}, the activation energy E is 376.97 kJ/mol, R denotes the universal gas constant, and T represents the temperature. The reaction order in Eq. (2.21) is given by $n = 2/3$ [80].

2.3 One-Dimensional Model

For the multicomponent droplet consisting of the precursor/solvent system of titanium(IV) isopropoxide (TTIP) and *p*-xylene, heating and evaporation is followed by the occurrence of puffing and possible micro-explosion.

The different stages that a multicomponent droplet goes through until the occurrence of micro-explosion is depicted in Fig. 2.3a. Fig. 2.3b shows the schematic of a droplet for a multicomponent system where δ is the liquid shell thickness, T_{s} represents the droplet surface temperature, $Y_{\mathrm{s,h}}$ denotes the mass fraction of the higher volatile species, and $Y_{\mathrm{s,l}}$ is the mass fraction of lower volatile component, at the droplet surface inside the droplet. Previous studies of Grosshans et al. [82] and Nešić and Vodnik [83], related to the formation of solid layer in droplets during the processes of spray drying, provide the motivation for the present work.

Initially, the droplet heats up due to the heat transfer between the ambience and the droplet, that results in droplet expansion. This is shown by stage I in Fig. 2.3a. Next, the higher volatile component evaporates preferentially that causes the decrease in the mass fraction of the higher volatile component and also, increase in the mass fraction

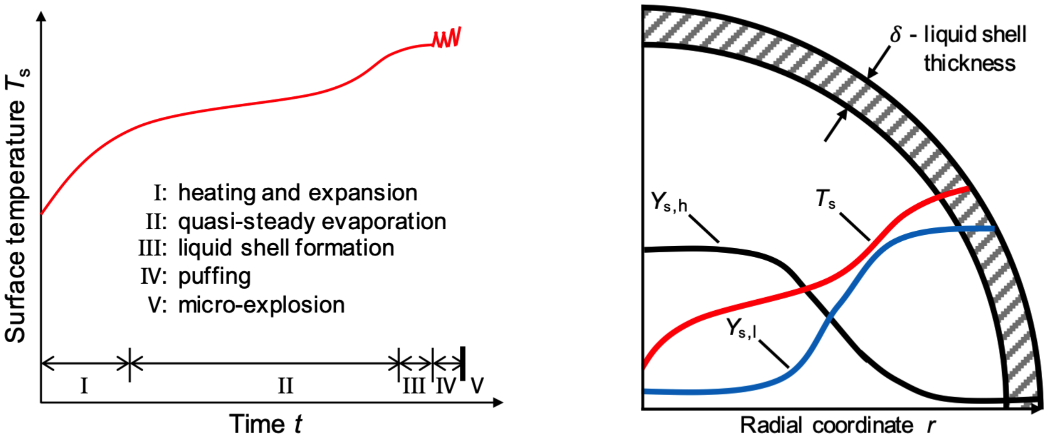

(a) Different stages related to puffing and micro-explosion, with respect to the droplet surface temperature T_{s}.

(b) Schematic showing the mass fractions of the lower, $Y_{\mathrm{s,l}}$, and higher, $Y_{\mathrm{s,h}}$, volatile components.

Figure 2.3: Schematic showing the puffing and micro-explosion model (Narasu and Gutheil [81]).

of the lower volatile species, which is called as the quasi-steady evaporation phase, depicted by stage II. Thus, the lower volatile species accumulates at the surface of the droplet that causes the liquid shell formation which hinders the process of evaporation, this is stage III. Figure 2.3b displays the third stage of the process.

The heating and evaporation at the droplet surface is hindered due to the formation of the liquid shell that results in the accumulation of the lower volatile species inside the droplet near to the liquid shell. At this position, as the boiling temperature of the higher volatile component is attained, the puffing of the droplet occurs. The liquid shell opens up during each puff, releasing mass. As the temperature reduces below the boiling temperature of the higher volatile species, the liquid shell forms again. This process continues resulting in the occurrence of several puffs, which is depicted by stage IV. Further, micro-explosion of the droplet occurs if the pressure inside the droplet increases beyond the ambient pressure, which represents stage V. It is to be noted that there is the possibility that puffing continues without the occurrence of droplet micro-explosion.

In order to describe the puffing and micro-explosion of the precursor solution droplets, the one-dimensional model is employed, which is discussed next.

The one-dimensional model focuses on the description of the convective heating and evaporation characteristics of a spherically symmetric droplet at atmospheric pressure in a hot convective ambience. To make sure that there is no inner circulation within the droplet and no flow separation occurs in the wake of the droplet, droplet Reynolds numbers up to twenty are considered. The conduction-limit and the diffusion-limit models are used to describe the droplet heating and evaporation, respectively. Thus, the droplet interior is spatially resolved providing with the details of the temporal and spatial variations of the temperature and species mass fractions inside the droplet. Taking motivation from the previous works of Grosshans et al. [82] and Nešić and

Vodnik [83], with respect to the formation of solid layer in droplets during the processes of spray drying, the one-dimensional droplet heating and evaporation model is modified to incorporate puffing and micro-explosion. The basic assumptions include that droplet remains spherical at all the times, the gas phase is in a quasi-steady state, the solubility of air in the liquid is negligible, the droplet evaporates in an ambience of non-reacting inert environment, and heat transfer caused due to the radiation is negligible [52]. Through the use of appropriate activity coefficients, which are modeled using the non-random two-liquid (NRTL) method [84], the non-ideal nature of the liquid components is taken into account.

2.3.1 Droplet Heating

The droplet heating is described using the conduction-limit model, where the equation for thermal conduction is given by

$$\frac{\partial}{\partial t}(r^2 \rho_{\mathrm{l}} c_{\mathrm{pl}} T) = \frac{\partial}{\partial r}(r^2 \lambda_{\mathrm{l}} \frac{\partial T}{\partial r}), \tag{2.23}$$

where r denotes the radial coordinate ranging from zero to the radius of the droplet r_{d}. T represents the liquid temperature, ρ_{l}, c_{pl}, and λ_{l} are the liquid density, specific heat capacity, and the thermal conductivity of the liquid mixture, respectively.

Initially, at time $t = 0$ s, the droplet is at uniform temperature

$$T|_{t=0} = T_{\mathrm{l},0}. \tag{2.24}$$

Also, at the center of the droplet, $r = 0$ m, the zero gradient condition is applied

$$\left.\frac{\partial T}{\partial r}\right|_{r=0} = 0. \tag{2.25}$$

The boundary condition representing the energy balance at the surface s of the droplet is given by

$$4\pi r^2 \left.\frac{\partial(\lambda_{\mathrm{l}} T)}{\partial r}\right|_{r=r_{\mathrm{s}}} = 4\pi r_{\mathrm{d}}^2 h(T_{\mathrm{g}} - T_{\mathrm{s}}) - L_{\mathrm{v}}(T_{\mathrm{s}})\, \dot{m}, \tag{2.26}$$

where h is the heat transfer coefficient, T_{g} represents the ambient gas temperature, T_{s} denotes the droplet surface temperature, $\dot{m}$ represents the mass evaporation rate of the multicomponent droplet, and L_{v} denotes the temperature-dependent latent heat of evaporation of the liquid mixture at the surface temperature T_{s} of the droplet. The heat transfer coefficient h is given as

$$h = \frac{\mathrm{Nu} \lambda_{\mathrm{f}}}{2 r_{\mathrm{d}}} \tag{2.27}$$

where the Nusselt number Nu is defined by the formulation provided by Abramzon and Sirignano [49] in order to incorporate the convective effects in heat transfer

$$\mathrm{Nu} = \widetilde{\mathrm{Nu}} \frac{\ln(1+B_\mathrm{T})}{B_\mathrm{T}}. \tag{2.28}$$

By taking into consideration Eqs. (2.27) and (2.28), Eq. (2.26) becomes

$$4\pi r^2 \left. \frac{\partial(\lambda_\mathrm{l} T)}{\partial r} \right|_{r=r_\mathrm{s}} = 2\pi r_\mathrm{d} \lambda_\mathrm{f} \widetilde{\mathrm{Nu}} \frac{\ln(1+B_\mathrm{T})}{B_\mathrm{T}} (T_\mathrm{g} - T_\mathrm{s}) - L_\mathrm{v}(T_\mathrm{s})\, \dot{m}$$

where the Spalding heat transfer number B_T [49] is calculated as described in section 2.2.1.

2.3.2 Droplet Evaporation

The diffusion-limit model is employed to describe the droplet evaporation, where the equation for mass diffusion is given as

$$\frac{\partial}{\partial t}(r^2 \rho_\mathrm{l} Y_i) = \frac{\partial}{\partial r}(r^2 \rho_\mathrm{l} D_\mathrm{l} \frac{\partial Y_i}{\partial r}), \tag{2.29}$$

where $i = 1, 2$ denotes the liquid component in the droplet, Y_i represents the mass fraction of component i, and D_l is the binary diffusion coefficient in the liquid.

Initially, at time $t = 0$ s, it is assumed that the droplet is a homogeneous mixture

$$Y_i|_{t=0} = Y_{i,0}. \tag{2.30}$$

Also, at the center of the droplet, $r = 0$ m, the Neumann boundary condition is employed

$$\left. \frac{\partial Y_i}{\partial r} \right|_{r=0} = 0. \tag{2.31}$$

At the surface of the droplet, the boundary condition represents the change in the size of the droplet [85]

$$-4\pi r_\mathrm{s}^2 \rho_\mathrm{l} D_\mathrm{l} \left. \frac{\partial Y_i}{\partial r} \right|_{r=r_\mathrm{s}} + Y_i \dot{m} = \dot{m}_i. \tag{2.32}$$

Here, $\dot{m}_i$ denotes the mass evaporation rate of liquid component i, that is calculated using the formulation provided by the study of Brenn et al. [52] for a droplet with multiple components, which itself is a modification to the mass evaporation rate of a single component droplet given by Abramzon and Sirignano [49]

$$\dot{m}_\mathrm{i} = 2\pi r_{\mathrm{d},i} \rho_\mathrm{f} D_{\mathrm{f},i} \widetilde{\mathrm{Sh}}\, \ln(1 + B_{\mathrm{M},i}). \tag{2.33}$$

In Eq. 2.33, $r_{\mathrm{d},i}$ denotes the radius of the droplet of component i, ρ_f represents the density of the mixture in the film, $D_{\mathrm{f},i}$ is the diffusivity of the component i in the film, $\widetilde{\mathrm{Sh}}$ denotes the modified Sherwood number [49], and $B_{\mathrm{M},i}$ represents the Spalding mass transfer number [52] of the liquid component i which is calculated as described in section 2.2.2.

2.3.3 Puffing and Micro-Explosion

The droplet heating is followed by the quasi-steady evaporation phase where the preferential evaporation of the higher volatile component results in the accumulation of the lower volatile species at the surface of the droplet, causing the formation of the liquid shell of thickness δ. The droplet temperature is resolved spatially by employing the one-dimensional model. Therefore, the spatial average droplet temperature is defined as

$$\overline{T} = \frac{\sum_{j=1}^{N} T_{\mathrm{l},j}}{N}. \tag{2.34}$$

If the spatially averaged droplet temperature $\overline{T}$, reaches the boiling point of the higher volatile species, the liquid shell is formed due to the accumulation of the lower volatile component at the droplet surface. In Eq. (2.34), j denotes the numerical grid point, N stands for the number of grid points, and $T_{\mathrm{l},j}$ represents the temperature of the droplet at the respective grid point. It is important to note that before the formation of the liquid shell, $\overline{T}$ denotes the overall spatial average temperature of the entire droplet and, after the liquid shell formation, $\overline{T}$ represents the spatial average temperature of the droplet interior excluding the liquid shell. Due to the accumulation of the lower volatile component at the surface of the droplet that causes the build up of the liquid shell, the viscosity of the liquid shell is higher compared to its interior which offers resistance to evaporation. Therefore it is to be noted that the consistency of the liquid shell is liquid and not rigid.

$\delta(t)$ is the thickness of the liquid shell which varies with time t as

$$\delta(t, \overline{T}) = \left[1 - Y_{\mathrm{TTIP,s}}(t, \overline{T})\right] r_{\mathrm{d}}(t), \tag{2.35}$$

where $Y_{\mathrm{TTIP,s}}$ denotes the mass fraction of the lower volatile TTIP at the droplet surface when the spatial average temperature, $\overline{T}$, of the droplet reaches the boiling temperature of the higher volatile component, p-xylene, and $r_{\mathrm{d}}(t)$ represents the droplet radius at time t. Therefore, after the formation of the liquid shell, its thickness varies with respect to time, which in turn depends on the processes of heating and evaporation of the droplet.

Due to the formation of the liquid shell, the mass evaporation rate is retarded similar to the crust formation that occurs during the droplet drying process [82]. Thus, in order to take into account the hindered evaporation owing to the liquid shell formation, the mass evaporation rate given by Eq. (2.33) is modified as

$$\dot{m}_i = \frac{2\pi r_{\mathrm{d},i} \rho_{\mathrm{f}} \ln(1 + B_{\mathrm{M},i})}{\frac{1}{\mathrm{D_{f,i}}\widetilde{\mathrm{Sh}}} + \frac{\delta}{2 D_{\mathrm{sh}}(r_{\mathrm{d}} - \delta)}}. \tag{2.36}$$

The first term in the denominator of Eq. (2.36) is the resistance for mass transfer due to the boundary layer and the second one represents the resistance due to the liquid shell, where D_{sh} denotes the diffusivity of the vapor in the liquid shell. It is to be noted that Eq. (2.36) becomes equal to Eq. (2.33) when the thickness of the liquid shell $\delta(t)$ is zero.

Rearranging of Eq. (2.36) results in

$$\dot{m}_i = \frac{2\pi r_{\mathrm{d},i}\rho_{\mathrm{f}} D_{\mathrm{f},i}\widetilde{\mathrm{Sh}}\,\ln(1+B_{\mathrm{M},i})}{1+\frac{\mathrm{D_{f,i}}\widetilde{\mathrm{Sh}}}{2D_{\mathrm{sh}}}\frac{\delta}{r_{\mathrm{d}}-\delta}}. \tag{2.37}$$

The energy transfer between the ambience and the surface of the droplet is also affected by the formation of the liquid shell. Hence, Eq. (2.29) is modified

$$4\pi r^2 \left.\frac{\partial(\lambda_{\mathrm{l}}T)}{\partial r}\right|_{r=r_{\mathrm{s}}} = \frac{2\pi r_{\mathrm{d}}\lambda_{\mathrm{f}}\widetilde{\mathrm{Nu}}\frac{\ln(1+B_{\mathrm{T}})}{B_{\mathrm{T}}}(T_{\mathrm{g}}-T_{\mathrm{s}})}{1+\frac{\lambda_{\mathrm{f}}\widetilde{\mathrm{Nu}}}{2\lambda_{\mathrm{sh}}}\frac{\delta}{r_{\mathrm{d}}-\delta}} - L_{\mathrm{v}}(T_{\mathrm{s}})\,\dot{m} \tag{2.38}$$

in analogy to mass transfer. The denominator of the first term of Eq. (2.38) on the right hand side of the equation describes the sum of the resistances offered for heat transfer in the boundary layer and the resistance due to the liquid shell, where, $\widetilde{\mathrm{Nu}}$ denotes the modified Nusselt number [49] included to take into consideration the convective heat transfer, λ_{f} is the thermal conductivity of the gas mixture in the film, and λ_{sh} represents the thermal conductivity in the liquid shell.

The micro-explosion of the droplet occurs if the pressure inside the droplet is higher than the ambient pressure

$$p_{\mathrm{l}}(t,r) > p_{\mathrm{amb}}. \tag{2.39}$$

The temporal and spatial variation of the pressure p_{l}, inside the droplet is calculated by combining the Raoult's law for real mixtures and Dalton's law,

$$p_{\mathrm{l}}(t,r) = \sum_{i=1}^{2} \gamma_i X_i p_{\mathrm{v},i}. \tag{2.40}$$

Here, for the component i, γ_i is the activity coefficient, X_i represents the mole fraction, and $p_{\mathrm{v},i}$ denotes the vapor pressure. The evaluation of the activity coefficient and the vapor pressure is discussed in the next subsection.

2.4 Physical Properties

There are a lot of physical properties involved in the numerical study of multicomponent droplet behavior, as can be found from the discussion of the mathematical model, see sections 2.2-2.3.3. Variable physical properties are used throughout for all the multicomponent systems considered in the study. Therefore, the thermophysical properties of the different multicomponent systems are discussed in detail next. It is to be noted that for the butanol/water system alone, the thermophysical properties are presented at low pressures of 40 mbar and 60 mbar whereas for all the other systems the variable physical properties are given at atmospheric pressure.

For the multicomponent systems of ethanol/water and TTIP/p-xylene, the non-ideal behavior of the liquid mixture is considered by taking into account the activity coefficients. At the droplet surface, the vapor mole fraction, $X_{\mathrm{s},i}$ of component i is calculated as

$$X_{\mathrm{s},i} = \gamma_i X_i \frac{p_{\mathrm{v},i}}{p_{\mathrm{atm}}}. \tag{2.41}$$

Here, γ_i denotes the activity coefficient, X_i is the mole fraction of the component i in liquid mixture, $p_{\mathrm{v},i}$ represents the vapor pressure, and p_{atm} stands for atmospheric pressure. Equation (2.41) becomes Raoult's law when $\gamma_i = 1$, as is the case for ideal mixtures.

Including the real behavior of the multicomponent liquid mixture through the use of activity coefficients forms a significant point of discussion with respect to numerical modeling of the droplet behavior. Many methods are available to calculate the activity coefficients. The vapor liquid equilibrium (VLE) was predicted for different azeotropic systems, including that of ethanol and water mixture, and was compared with the experimental data by Manojkumar and Sivaprakash [86] . They used two approaches to model the activity coefficients, namely, UNIFAC [87] and UNIQUAC [88]. It was found that both of these approaches were able to compute the vapor liquid equilibrium data with the least error for all the different systems investigated in the study. Govindaraju and Ihme [89] investigated the group contribution method for evaporation of multicomponent mixtures where the focus was on fuels employed for the purpose of transportation. The UNIFAC method was used to evaluate the activity coefficients in order to describe the non-ideal behavior of the mixtures. They presented a detailed discussion on the effect of the polar species on the process of evaporation. The numerical investigation of various multicomponent droplet evaporation models for different non-ideal mixtures was performed and validated with experimental results by Chen et al. [90]. The real behavior of the alcohol-decane mixtures was taken into account through the use of the activity coefficients modeled following the UNIFAC approach. In the present study, to consider the real behavior of the liquid mixture, the activity coefficient is incorporated using various methods for different multicomponent systems which is discussed in the next sections.

2.4.1 Ethanol/Water

Variable liquid and gas properties used in the model are taken from the study of Poling and Prausnitz [58]. Jamieson correlation is employed to calculate the thermal conductivity of the liquid mixture and Wassiljewa equation is used to evaluate the thermal conductivity of the gas mixture [58]. The viscosity of the gas mixture in the film is computed using the Wilke's rule. Diffusivity of ethanol vapor in air and that of water vapor in air is calculated using the Fuller equation and the Chapman and Enskog equation, respectively. The Antoine equation is employed to evaluate the vapor pressure of ethanol and water. Extended Watson equation [91] is used to describe the temperature dependence of the latent heat of evaporation. The non-ideal behavior of the liquid mixture is taken into account by modeling the activity coefficients using the UNIFAC approach [87], which is presented in detail in the next discussion.

The Universal Quasichemical Functional Group Activity Coefficients (UNIFAC) approach takes into account the combinatorial, $\ln\gamma_i^{\mathrm{C}}$, and the residual parts, $\ln\gamma_i^{\mathrm{R}}$, in the calculation of the activity coefficients of the components,

$$\ln\gamma_i = \ln\gamma_i^{\mathrm{C}} + \ln\gamma_i^{\mathrm{R}}. \tag{2.42}$$

The combinatorial part is evaluated using the universal quasichemical activity coefficients (UNIQUAC) method [88] as,

$$\ln\gamma_i^{\mathrm{C}} = \ln(\frac{\Psi_i}{X_i}) + 5q_{\mathrm{w},i}\ln(\frac{\vartheta_i}{\Psi_i}) + l_i - \frac{\Psi_i}{X_i}\sum_{j=1}^{H} X_j l_j \tag{2.43}$$

where

$$l_i = 5(r_{\mathrm{w},i} - q_{\mathrm{w},i}) - (r_{\mathrm{w},i} - 1), \tag{2.44}$$

and

$$\vartheta_i = \frac{q_{\mathrm{w},i}X_i}{\sum_{j=1}^{H} q_{\mathrm{w},j}X_j}, \qquad \Psi_i = \frac{r_{\mathrm{w},i}X_i}{\sum_{j=1}^{H} r_{\mathrm{w},j}X_j}. \tag{2.45}$$

Here, X_i denotes the mole fraction of component i. The relative Van-der-Waals volume, $r_{\mathrm{w},i}$, and relative Van-der-Waals surface area, $q_{\mathrm{w},i}$, are evaluated as,

$$r_{\mathrm{w},i} = \sum_{k=1}^{G} \nu_k^{(i)} R_k, \qquad q_{\mathrm{w},i} = \sum_{k=1}^{G} \nu_k^{(i)} Q_k, \tag{2.46}$$

where H represents the number of components, which is two, for the ethanol/water system and i stands for the liquid mixture component. The number of different groups in molecule i, is given by G. Ethanol consists of three groups which are $\mathrm{CH_2}, \mathrm{CH_3}$, and OH. However, water contains only one group, that is $\mathrm{H_2O}$. The number of structure groups of type k in the molecule i is given by $\nu_k^{(i)}$. Also, R_k and Q_k represent the specific constants for group k [88].

The residual part is evaluated as

$$\ln\gamma_i^{\mathrm{R}} = \sum_{k=1}^{G} \nu_k^{(i)} \left[\ln\Gamma_k - \ln\Gamma_k^{(i)}\right]. \tag{2.47}$$

Here, the group activity coefficient of group k in the mixture is represented by Γ_k and the group activity coefficient of group k in the pure liquid i is denoted by $\Gamma_k^{(i)}$, which are calculated as,

$$\ln\Gamma_k = Q_k\left[1 - \ln(\sum_{m=1}^{G}\vartheta_m\chi_{mk}) - \sum_{m=1}^{G}\frac{\vartheta_m\chi_{km}}{\sum_{n=1}^{G}\vartheta_n\chi_{nm}}\right] \tag{2.48}$$

where

$$\vartheta_m = \frac{Q_m X_m}{\sum_{n=1}^{G} Q_n X_n}, \qquad X_m = \frac{\sum_{j=1}^{H} \nu_m^j X_j}{\sum_{j=1}^{G} \sum_{n=1}^{G} \nu_n^j X_j}, \qquad \chi_{nm} = e^{-a_{nm}/T} \tag{2.49}$$

Here, the group mole fraction is represented by X_m [88] and the group interaction parameter between groups m and n is given by a_{nm} [92]. Also, T denotes the temperature under which the vapour-liquid equilibrium is considered.

2.4.2 Butanol/Water

For the liquid mixture of butanol and water, the thermophysical properties at low pressures are not available in the literature. Therefore, the liquid properties available at atmospheric pressure from the studies of Dortmund Data Bank [93], Coker [94], Majer and Svoboda [95], and Poling and Prausnitz [58] are extrapolated to lower pressures and used in the model. The variable gas properties are provided by M. Nanjaiah and I. Wlokas, Universität Duisburg-Essen, as part of the collaboration research [96]. The study of Poling and Prausnitz [58] provides with the gas phase mixture properties. The viscosity of the gas mixture in the film is calculated using Wilke's rule. The Wassiljewa equation is employed to evaluate the thermal conductivity of the gas mixture. The Antoine equation is used to compute the vapor pressure of water and butanol. The Antoine equation is valid for pressure ranges of about 0.01 to 2 bar [58]. The ideal behavior of the liquid mixture is considered and thus, the activity coefficients are neglected.

2.4.3 Iron(III) Nitrate Nonahydrate/Ethanol

The thermophysical properties of the liquid mixture of iron(III) nitrate nonahydrate (INN) and ethanol at atmospheric pressure are available from the experimental fits provided by Keller et al. [97], which are valid for INN mass fractions up to 0.34. Experimental fits are available for density, thermal conductivity, viscosity, and isobaric specific heat capacity. The experimental error ranges between less than 1 % for the density to 10 % for the isobaric specific heat capacity. The properties are valid within the temperature range of 288.15 K to 333.15 K. These properties are used in the model and are extrapolated beyond its range of validity. Variable gas properties of ethanol and water are provided by Poling and Prausnitz [58], the details of which are available from the previous section 2.4.1. The activity coefficients of the INN/ethanol mixture are neglected due its unavailability.

2.4.4 Titanium(IV) Isopropoxide/*p*-xylene

Variable liquid properties of the mixture of titanium(IV) isopropoxide (TTIP) and *p*-xylene at atmospheric pressure were measured by Keller et al. [98]. The experimental data is available for density, thermal conductivity, viscosity, isobaric specific heat capacity, and vapor-liquid equilibrium. The experimental relative standard uncertainty varies from less than 0.1 % for the density to 3 % for the viscosity. The experimental fits from the data are valid within the temperature range of 293.15 K to 373.15 K, which are used in the model and are extrapolated beyond its validity range. Antoine equation is employed to evaluate the vapor pressure of both TTIP and *p*-xylene, for which the parameters are taken from the study of Keller et al. [98]. To take care of the real behavior of the liquid mixture, the activity coefficients of TTIP and *p*-xylene are computed from the vapor-liquid equilibrium data of Keller et al. [98], and are modeled using the non-random two-liquid (NRTL) approach [84].

Variable gas properties of TTIP are calculated from the work of Shmakov et al. [99] and Buerger et al. [100]. The mixture properties in the gas phase are computed from the study of Poling and Prausnitz [58]. The Wassiljewa equation is employed to evaluate the thermal conductivity of the gas mixture and the viscosity of the gas mixture is computed using the Wilke's rule. Fuller equation is employed to calculate the diffusivity of *p*-xylene vapor and TTIP vapor in air. Majer and Svoboda [95] provides with the temperature dependence of the latent heat of evaporation of *p*-xylene whereas that of TTIP is computed using the Watson relation [58].

2.5 Numerical Solution Procedure

For the zero-dimensional model, see section 2.2, the droplet temperature is calculated by solving the energy equation (2.1), which is an ordinary differential equation, using the Runge-Kutta 4th order method. The mass evaporation rate, see Eq. (2.11), is evaluated using the step-by-step procedure of Abramzon and Sirignano [49]. The convergence criterion of the simulations is set such that the solver will stop when the droplet radius is less than or equal to 10^{-3} times the initial droplet radius, $r_\mathrm{d}/r_{\mathrm{d}_0} \leq 10^{-3}$.

In the case of INN/ethanol droplets, in addition to computing the droplet temperature and the mass evaporation rate, the amount of decomposed iron(III) nitrate is found out by solving the kinetic equation (2.21), which is also an ordinary differential equation, using the Runge-Kutta 4th order method. At high ambient temperatures above the thermal decomposition temperature of 403 K, the simulation is terminated when the iron(III) nitrate has fully decomposed into Fe_2O_3 and N_2O_5. At low ambient temperatures below the thermal decomposition temperature of 403 K, the solver will stop when the ethanol and the water have completely evaporated.

In order to solve the governing equations of the puffing and micro-explosion model, see section 2.3.3, the droplet interior is discretized using an equidistant numerical grid, and a grid independence study is performed to determine the number of grid points which is presented and discussed in chapter 3 of results. During the numerical simulation the droplet size changes, and thus, the computational domain and the grid size varies. The temperature and the mass evaporation rate are computed by solving Eqs. (2.38) and (2.37), respectively, using the second order explicit finite difference method. During the first two stages, the liquid shell thickness, $\delta(t)$, is zero. Also, the numerical time step is fixed at 10^{-5} µs such that the Courant criterion [101] is fulfilled. The Courant criterion is the limiting criteria for the numerical grid size defined as

$C = (u\Delta t)/\Delta x$, where u is the velocity of the fluid, Δt denotes the time step, Δx represents the size of the grid, and C is the Courant number whose maximum possible value is less than or equal to 0.5 [101].

Results and Discussion

This section presents the results and detailed analysis with respect to the droplet behavior for different multicomponent systems. At first, the results of the zero-dimensional droplet evaporation model for ethanol/water droplet are provided, followed by the results for the butanol/water droplet at low ambient pressures. Further, the results for the precursor solution system of iron(III) nitrate nonahydrate in ethanol are discussed, where the zero-dimensional model is coupled with the thermal decomposition model. Later, the zero-dimensional model results for the precursor/solvent system of titanium(IV) iso-propoxide/*p*-xylene are presented, after which the results of the one-dimensional model for the same multicomponent system are provided along with the results of the puffing and micro-explosion model.

3.1 Ethanol/Water Droplet

For nanoparticle synthesis using spray flames, one of the most commonly used solvents is ethanol. Ethanol poses many advantages over other conventional fuels, due to which it has various applications. As an example, one of the alternative fuels used for the purpose of transportation is ethanol. From biofuels, it is possible to produce ethanol in an efficient manner, which happens to be one of the major advantages of using ethanol as an alternative fuel [102]. Instead of pure ethanol, fueling engines with hydrous ethanol reduces the nitrogen oxide emissions from the engines. Also, it is possible to save reasonable amount of energy that is required for distillation in the production process of the ethanol [103]. In addition to the distillation process, further dewatering engineering is required in order to obtain a high purity alcohol, thus increasing the consumption of energy as well as the cost of the refining process of ethanol. Therefore, by using hydrous ethanol it is possible to reduce the consumption of energy that is needed for the process of production of the ethanol fuel. Further, it is also beneficial in reducing the emissions as well as in saving energy. In United States and Europe, bio-ethanol is used as an additive to gasoline whereas in countries such as Brazil, vehicles fueled with pure ethanol or flex fuel vehicles are being employed as an alternative to gasoline and diesel. The performance of a four-stroke engine that was fueled by gasoline-ethanol blends or hydrous ethanol was studied by Costa and Sodré [104]. The power obtained was around the same by both the fuels at low engine speeds. However, it was observed that for high engine speeds the torque, break mean effective pressure, and power attained were lower while using the gasoline-ethanol blend as compared to that obtained when using the hydrous ethanol fuel. The thermal efficiency and the specific fuel consumption were found to be lower while using the gasoline-ethanol blend in comparison with that of the hydrous ethanol, for the entire range of speed that was investigated, which provides motivation for further research focusing on combustion of hydrous ethanol fuel. The evaporation of a single ethanol droplet in an ambient environment of nitrogen was studied experimentally by Saharin [105]. They explored the dynamics of evaporation when water amounting to five percent was added to the ethanol droplet. It was reported that there exist two quasi-steady regimes for the droplet consisting of ethanol and water, as compared to one quasi-steady period for the pure ethanol droplet.

For droplets consisting of the precursor solution systems of iron(III) nitrate nonahydrate in ethanol and titianium(IV) isopropoxide in *p*-xylene, which are explored in sections 3.3 and 3.4, there are no experimental data available to validate the numerical results computed using the droplet evaporation models. Therefore, at first, the multicomponent droplet consisting of ethanol and water is considered, for which experimental data [75] is available for validation. For a single droplet consisting of the multicomponent system of ethanol and water, the numerical study is performed by using the zero-dimensional model, see section 2.2. Firstly, the results of the simulations are validated with the results available from the experimental study of Ma et al. [75]. Further, a parameter study is performed by varying the initial droplet size, the relative velocity between the droplet and the ambience, the ambient gas temperature, the initial mass fraction of the liquid components, and the amount of water content in the ambience. The real behavior of the liquid mixture is taken into account through the use of activity coefficients, and therefore, its impact on the process of droplet evaporation is also explored.

The total vapor pressure for the mixture of ethanol and water computed for various temperatures for different initial mole fractions of ethanol is displayed in Fig. 3.1. The solid lines represent the vapor pressure calculated assuming the non-ideal nature of the liquid mixture, with the activity coefficients evaluated using the UNIFAC method, whereas the dashed lines denote the values computed considering the ideal behavior of the ethanol/water mixture. The calculated data was verified using that provided by Dortmund Data Bank [93]. The ethanol/water mixture is a positive azeotrope with the boiling temperature at 351.35 K, which is lower than the boiling points of the individual components of ethanol and water of 351.55 K and 373.15 K, respectively. Therefore, the total vapor pressure is presented for the

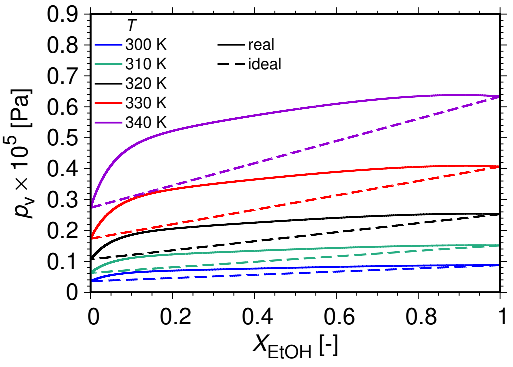

Figure 3.1: Variation of the vapor pressure, calculated assuming the real and ideal behavior of the liquid mixture, for varying initial mole fraction of ethanol at different temperatures (Narasu et al. [72]).

temperatures between 300 K to 340 K, since the corresponding range of temperature is significant for the numerical simulations performed in the present study, the details of which are discussed in section 3.1.

3.1.1 Validation with Experimental Data of Ma et al. [75]

At first, the numerical results computed using the zero-dimensional model are compared with the experimental results of Ma et al. [75]. They conducted an experimental investigation to analyze the evaporation characteristics of a droplet consisting of both ethanol and water components in an ambience of convective dry air. The experimental set up consisted of a quartz fiber that was used to attach the droplets after which these droplets were introduced into the convective ambience. The ambient conditions such as the rate of flow of the gas stream and air temperature were controlled using a flow control valve and a heater, respectively. Thus, the relative velocity between the droplet and the ambience was altered between 2 m/s and 4 m/s, which was measured using a hot wire anemometer, and the ambient gas temperature was varied between 400 K and 475 K, that was determined using a thermocouple. Larger sized droplets with initial radius of 600 µm at room temperature and atmospheric pressure were considered for the experimental study. Further, five different initial mass fractions of water of 0.0, 0.25, 0.50, 0.75, and 1.0 were taken into account, thus considering both pure ethanol and water droplets as well. The experiment utilized a high speed video camera to record and visualize the process of evaporation of the droplet.

The first experimental conditions considered consist of an ethanol/water droplet of initial droplet radius of 600 µm at relative velocity of 4 m/s and ambient gas temperature of 400 K for initial ethanol mass fractions of 0.0, 0.25, 0.50, 0.75, and 1.0. The normalized droplet surface area computed for these experimental conditions are presented in Fig. 3.2. In Fig. 3.2, the experimental results are shown by the symbols and the numerical results are represented by the lines. The dashed-dotted lines stand for the results of the simulations performed by considering the ideal nature of the liquid mixture, that is for activity coefficient $\gamma = 1$ in Eq. 2.41 whereas, the solid lines show the results taking into account the real behavior of the liquid mixture, where the activity coefficients are modeled using the UNIFAC [87] approach. The different colors represent the cases for various initial ethanol mass fractions. The temporal variation of the normalized droplet surface area calculated by the simulations are in

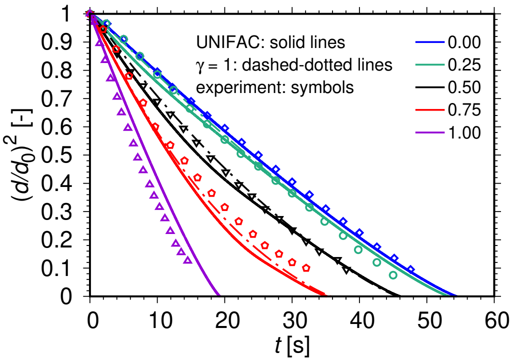

Figure 3.2: Validation of the numerical results with the experimental results displaying the temporal variation of the profiles of the normalized droplet surface area for different initial mass fractions of ethanol. Initial conditions: $r_{\mathrm{d},0} = 600$ µm, $T_{\mathrm{l},0} = 293.15$ K, $p = 1$ bar, $u_0 = 2$ m/s, $T_{\mathrm{g},0} = 400$ K, RH = 0 %. (Narasu et al. [72]).

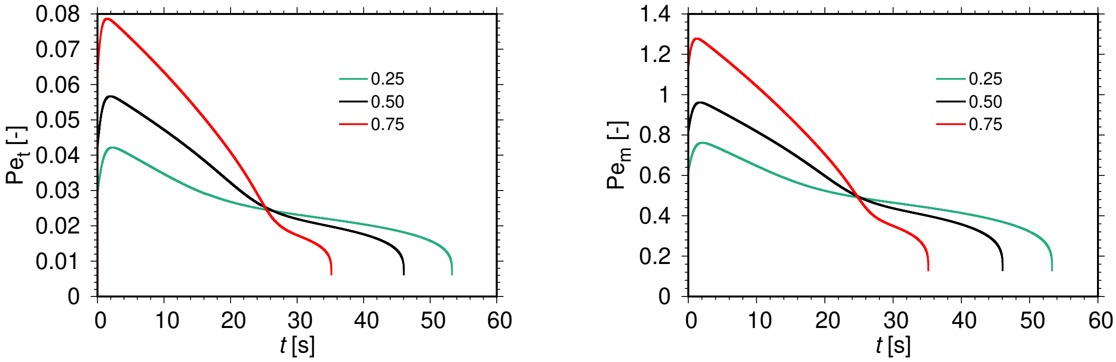

(a) Liquid thermal Peclet number. (b) Liquid mass Peclet number.

Figure 3.3: Temporal variation of the liquid thermal and mass Peclet number. Initial conditions: $r_{\mathrm{d},0}$ = 600 µm, $T_{\mathrm{l},0}$ = 293.15 K, p = 1 bar, u_0 = 2 m/s, $T_{\mathrm{g},0}$ = 400 K, RH = 0 % (Narasu et al. [72]).

good agreement with that observed from the experimental study. Ethanol is more volatile than water since the boiling point of ethanol is lower than that of water. Therefore, with the increase in the initial mass fraction of ethanol, the evaporation of the droplet becomes faster resulting in shorter lifetime of the droplet. Thus, a pure water droplet evaporates slower in comparison with that of a pure ethanol and ethanol/water droplet. The classical d^2 law is followed for none of the conditions studied here due to the variable thermophysical properties used in the model. This is evident from the difference in the slopes for normalized droplet surface area plot, which shows two regimes of evaporation. The first regime is associated with the preferential evaporation of ethanol owing to its higher volatility and is represented by a larger slope, whereas, the second regime constitutes the evaporation of the lower volatile water component. Also, with the decrease in the initial mass fraction of ethanol, the first regime becomes shorter and further, the difference in slopes between the two regimes become smaller because of the lower volatile nature of water. More details with respect to this behavior is presented in the next section.

Comparing the numerical results considering the real and ideal behavior of the liquid mixture, including the real behavior of the liquid mixture results in faster evaporation of the ethanol component but, leads to retarded regression with respect to water evaporation and thus, resulting in minor differences with regard to the droplet lifetime.

It is possible to evaluate the validity of the distillation-limit model and the rapid-mixing model by calculating the liquid thermal Peclet number and the liquid mass Peclet number [106], respectively. The liquid thermal Peclet number is given by the ratio of the gasification rate and the liquid thermal diffusivity whereas, the liquid mass Peclet number is defined as the ratio of the gasification rate and the liquid mass diffusivity. Figure 3.3 shows the liquid thermal Peclet number and the liquid mass Peclet number for the initial conditions specified in Fig. 3.2. Since the liquid thermal Peclet number remains below 0.1, see Fig. 3.3a, and the liquid mass Peclet number is below two, see Fig. 3.3b, the usage of the distillation-limit model and the rapid-mixing model is justified. Unforunately, no data is available from the present experiment to

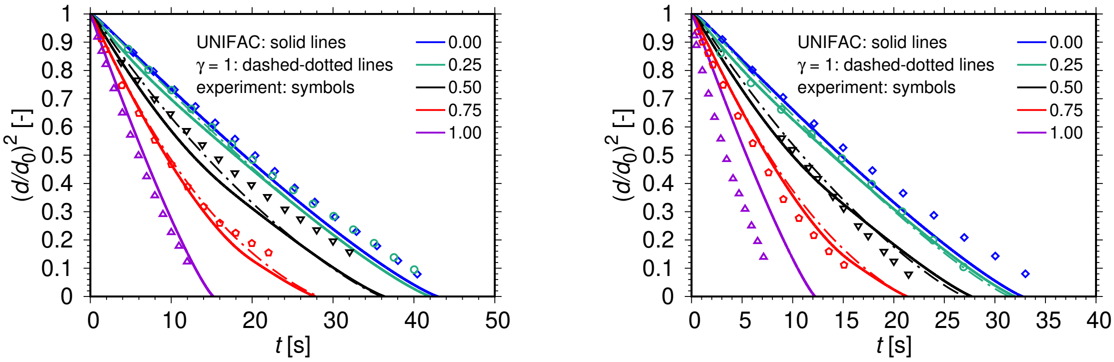

(a) $u_0 = 4$ m/s, $T_{\mathrm{g},0} = 400$ K.

(b) $u_0 = 2$ m/s, $T_{\mathrm{g},0} = 475$ K.

Figure 3.4: Validation of the numerical results with the experimental results displaying the temporal variation of the profiles of the normalized droplet surface area for different initial mass fractions of ethanol. Initial conditions: $r_{\mathrm{d},0} = 600$ μm, $T_{\mathrm{l},0} = 293.15$ K, $p = 1$ bar, RH = 0 % (Narasu et al. [72]).

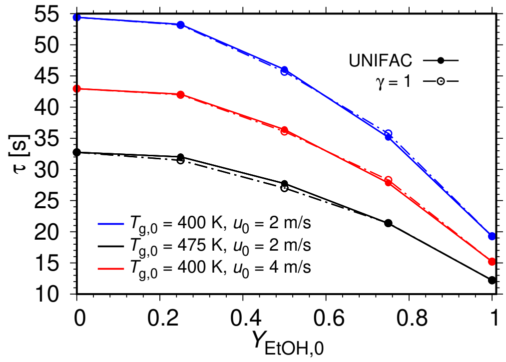

Figure 3.5: The variation of droplet lifetime with initial ethanol mass fraction. Initial conditions: $r_{\mathrm{d},0} = 600$ μm, $T_{\mathrm{l},0} = 293.15$ K, $p = 1$ bar, RH = 0 % (Narasu et al. [72]).

validate these results.

The experimental results are available for two more initial conditions and hence, the numerical study is performed for these conditions as well. The comparison between the normalized droplet surface area calculated by the numerical simulations and that available from the experiments are displayed in Fig. 3.4. Figure 3.4a shows the results for the higher relative velocity of 4 m/s at ambient temperature of 400 K whereas, Fig. 3.4b displays the results for the relative velocity of 2 m/s at higher ambient temperature of 475 K. Rest of the initial conditions remain the same as that mentioned for the previous experimental condition of Fig. 3.2. The characteristics of the droplet evaporation remain similar to that described in Fig. 3.2, except for the difference in the droplet lifetimes, which are presented in Fig. 3.5. Figure 3.5 displays the droplet lifetimes calculated by the model by considering the ideal (open symbols) and non-ideal (filled symbols) behavior of the liquid mixture for the different initial conditions studied in Figs. 3.2 and 3.4. The data with respect to the droplet lifetimes are not available from the present experiment, and therefore, are not included. The symbols represent the results computed from the simulations and the lines connecting the symbols are shown for better clarity regarding the parametric dependence. For the same ambient gas temperature of 400 K, increasing the relative velocity from 2 m/s (blue lines) to 4 m/s (red lines) results in enhanced evaporation of the droplet caused due to the stronger convection rate and thus, reduces the droplet lifetime by around 30 %. Also, for the lower relative velocity, as the ambient air temperature is increased from 400 K to 475 K (black lines), the droplet lifetime is shortened due to the increased heat transfer rate between the ambience and the droplet. Further, with an increase in the initial mass fraction of ethanol, the deviation of the droplet lifetimes becomes smaller and the droplet lifetime is reduced because of the higher volatile nature of ethanol. There is good agreement between the trends shown in Fig. 3.5 and the results available in the literature for different multicomponent systems [89]. Incorporating the real behavior of the liquid mixture does not make much difference with respect to the droplet lifetimes. Still, the non-ideal behavior of the liquid mixture is considered throughout the present study concerning the evaporation of ethanol/water droplets. Parameter study is conducted by varying the initial conditions which is discussed is detail in the next section.

3.1.2 Parameter Study

For the purpose of understanding the effect of different parameters on the process of droplet heating and evaporation, the initial conditions are varied but chosen in such a way that they are well within the regime of laminar flow. The flow around spheres was visualized by Taneda [107] and they found that vortex rings are formed in the rear of a sphere starting from Reynolds numbers of 24. Also, there are no formations of the vortex rings for Reynolds numbers below 22, which is known as the regime of attached flow. Therefore, for the present study the initial conditions are selected so that the droplet Reynolds numbers remain below twenty. Thus, the parameter study is performed for initial droplet radii of 25 μm and 50 μm at relative velocities of 4 m/s and 10 m/s for ambient air temperatures of 400 K and 1200 K in an ambience of both dry and humid air. Further, the thermal and mass Peclet numbers remain below their critical values [106] which justifies the use of the distillation-limit model and the rapid-mixing model to describe the droplet heating and evaporation, respectively, as was explained in detail in the previous section. Increasing the initial droplet size or the relative velocity results in breaching the Peclet number limits, and thus the one-dimensional model need to be employed to study the droplet behavior.

Figure 3.6 shows the profiles of the normalized droplet surface area and the mass fractions of the liquid components at the droplet surface with time for a single ethanol/water droplet of initial radius of 25 μm at relative velocity of 4 m/s for ambient gas temperature of 400 K for initial ethanol mass fractions of 0.0, 0.25, 0.50, 0.75, and 1.0. With respect to the profiles of the normalized droplet surface area, see Fig. 3.6a, the major characteristics remain similar to that displayed in Fig. 3.2 for the experimental conditions, except for the differences with respect to the droplet lifetimes which are shorter for the smaller droplets. Ethanol component evaporates faster than the water component owing to its higher volatility which can be observed from the differences in the slopes of the normalized droplet surface area plot. Larger the initial mass fraction of the higher volatile ethanol, more delayed is the deviation of the slope of the droplet regression rate. More evidence regarding the preferential evaporation of ethanol is available from the profiles of the the mass fractions of both ethanol (solid lines) and water (dashed lines) at the droplet surface, as displayed in Fig. 3.6b, where the mass fraction of the ethanol component reduces faster for the different cases presented. Once

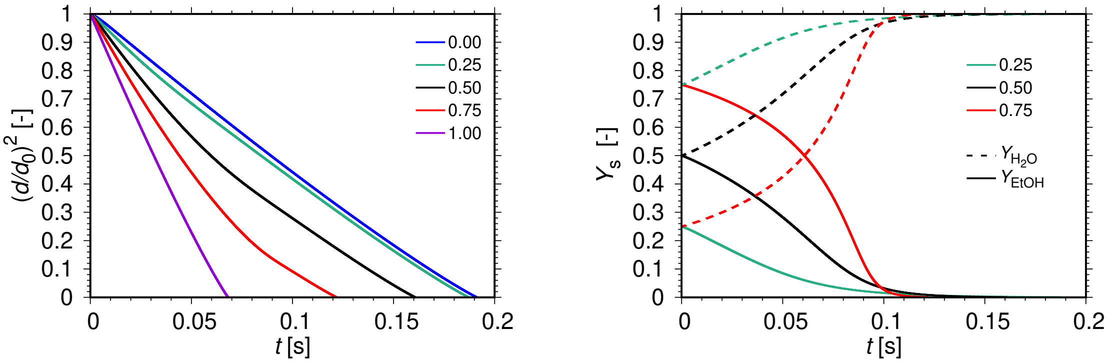

(a) Normalized droplet surface area.

(b) Surface mass fractions.

Figure 3.6: Droplet heating and evaporation characteristics. Initial conditions: $r_{d,0} = 25$ μm, $T_{l,0} = 293.15$ K, $p = 1$ bar, $u_0 = 4$ m/s, $T_{g,0} = 400$ K, RH = 0 % (Narasu et al. [72]).

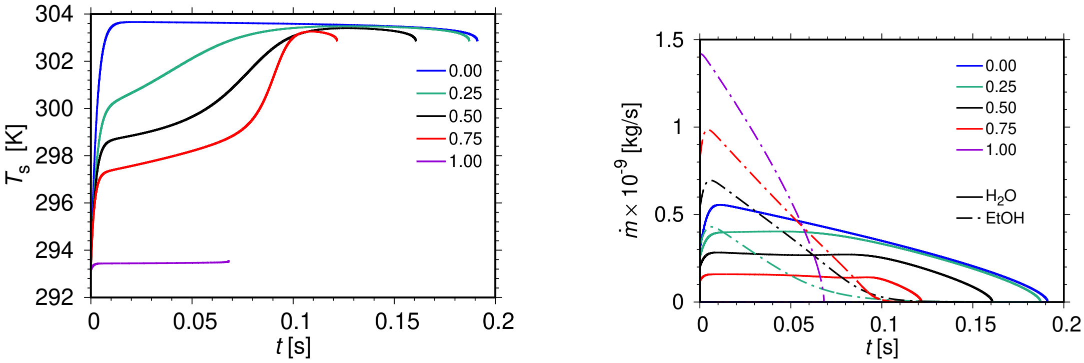

(a) Temperature at the droplet surface.

(b) Mass evaporation rates.

Figure 3.7: Droplet heating and evaporation characteristics. Initial conditions: $r_{d,0} = 25$ μm, $T_{l,0} = 293.15$ K, $p = 1$ bar, $u_0 = 4$ m/s, $T_{g,0} = 400$ K, RH = 0 % (Narasu et al. [72]).

the ethanol has almost completely evaporated, the droplet evaporation is dominated by the evaporation of the water component which coincides with the change of slope observed in the profiles of the normalized droplet surface area.

The profiles of the temperature at the surface of the droplet T_s is displayed in Fig. 3.7a, for all the five initial mass fractions of ethanol considered in the present study. Initially, the droplet heats up causing the droplet surface to increase for all the cases. Larger the initial mass fraction of the ethanol, smaller is the temperature attained by the surface of the droplet during the initial heating phase, which is due to the lower boiling point of ethanol as compared to that of water. For the ethanol/water droplet, the initial droplet heating is followed by the quasi-steady evaporation phase where the higher volatile ethanol evaporates preferentially and the temperature at the droplet surface increases slowly. Once the ethanol content becomes smaller, as shown in Fig. 3.6b, the water evaporation is the dominating factor and the droplet surface

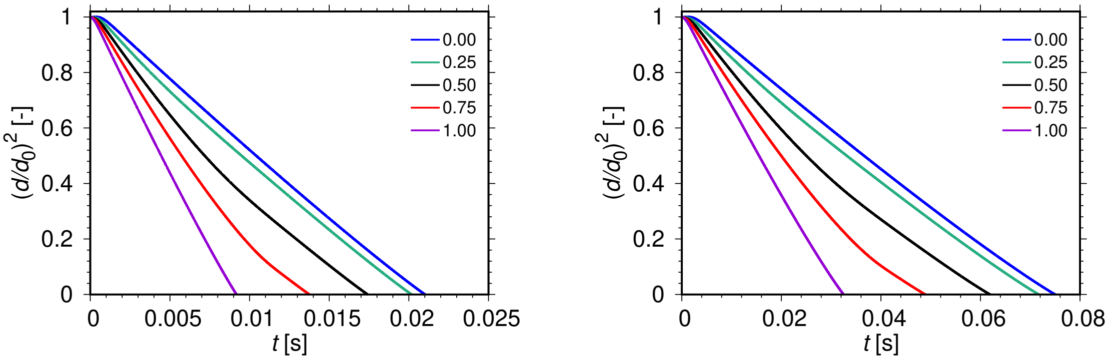

(a) $r_{\mathrm{d},0} = 25$ µm.

(b) $r_{\mathrm{d},0} = 50$ µm.

Figure 3.8: Temporal variation of the normalized droplet surface area. Initial conditions: $T_{\mathrm{l},0} = 293.15$ K, $p = 1$ bar, $u_0 = 4$ m/s, $T_{\mathrm{g},0} = 1200$ K, RH $= 0$ % (Narasu et al. [72]).

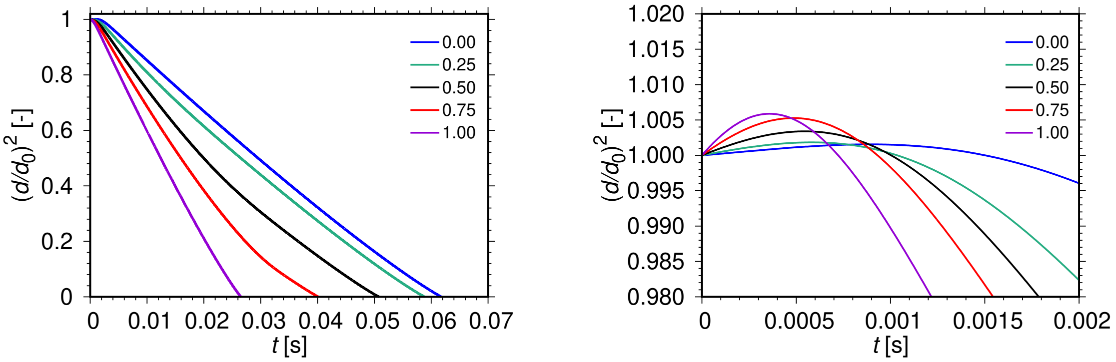

(a) Normal view.

(b) Zoomed view.

Figure 3.9: Temporal variation of the normalized droplet surface area. Initial conditions: $r_{\mathrm{d},0} = 50$ µm, $T_{\mathrm{l},0} = 293.15$ K, $p = 1$ bar, $u_0 = 10$ m/s, $T_{\mathrm{g},0} = 1200$ K, RH $= 0$ % (Narasu et al. [72]).

temperature increases drastically because of the higher boiling temperature of water. However, for the pure ethanol and water droplets, during the quasi-steady evaporation phase, the temperature remains almost constant at the maximum temperature reached by the droplet surface after the initial heating stage.

Figure 3.7b displays the mass evaporation rates of both the components of ethanol (dash dotted lines) and water (solid lines) for various initial mass fractions of ethanol investigated in the present study. Initially, the preferential evaporation of the ethanol component occurs which may be identified by the peak value attained by the mass evaporation rate of ethanol, which is higher for the larger initial mass fractions of ethanol. Also, reducing the initial mass fraction of ethanol delays the time at which the maximum value is reached. During the early stages, the mass evaporation of water remains almost constant. However, as the amount of ethanol inside the droplet reduces, see Fig. 3.6b, the evaporation is dominated by water, as is evident from the larger values of the mass evaporation rate of water.

Figure 3.8a shows the temporal variation of the normalized droplet surface for the same conditions as displayed in Fig. 3.6a, except that the ambient gas temperature

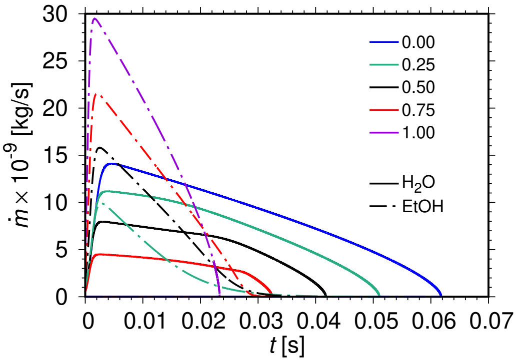

Figure 3.10: Temporal variation of the mass evaporation rates of the liquid components. Initial conditions: $r_{\mathrm{d},0} = 50$ µm, $T_{\mathrm{l},0} = 293.15$ K, $p = 1$ bar, $u_0 = 10$ m/s, $T_{\mathrm{g},0} = 1200$ K, RH = 0 % (Narasu et al. [72]).

is increased from 400 K to 1200 K, with the aim of understanding the effect of increased ambient temperature on the droplet behavior. Due to the increase of the ambient temperature, there is increased heat transfer rate between the ambience and the droplet which results in reduced droplet lifetime. For the higher ambient temperature of 1200 K, increasing the initial droplet size by a factor of two causes slower evaporation of the droplet, as displayed in Fig. 3.8b, because of the prolonged heating and evaporation time since there is a larger amount of the liquid to be evaporated. The relative velocity between the droplet and the ambience is increased from 4 m/s to 10 m/s, see Fig. 3.9a, which shortens the lifetime of the droplet because of the enhanced evaporation caused due to the stronger convection rate. Also, for the higher ambient temperature of 1200 K, during the initial droplet heating period, droplet expansion occurs which is due to the variable liquid properties used in the model. This is clearly visible in Fig. 3.9b, which presents the zoomed view of Fig. 3.9a. For the same conditions of Fig. 3.9, the mass evaporation rates of ethanol and water are shown in Fig. 3.10. The peak value attained by the mass evaporation rates of both the liquid components are higher than that computed for the conditions of Fig. 3.7b by a factor of about twenty, which further proves that increasing the ambient temperature and the relative velocity enhances the process of evaporation.

Figure 3.11 shows the summary of the lifetimes of the droplet for various initial conditions explored in the present study. Keeping all the other initial conditions same, increasing the ambient air temperature from 400 K (black line) to 1200 K (green line) shortens the droplet lifetime by a factor of ten due to the increased heat transfer rate. For the higher ambient temperature, as the initial droplet size is increased from 25 µm to 50 µm (blue line), the droplet lifetime is prolonged by a factor of three because of the prolonged droplet heating time. Doubling the relative velocity from 4 m/s to 8 m/s (red line) reduces the droplet lifetime due to the stronger convection rate. However, the influence of the relative ve-

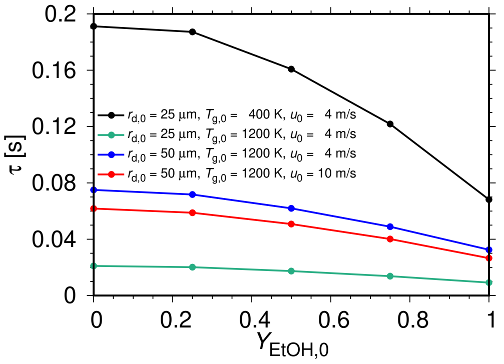

Figure 3.11: Droplet lifetime for various initial conditions. Initial conditions: $T_{\mathrm{l},0} = 293.15$ K, $p = 1$ bar, RH = 0 % (Narasu et al. [72]).

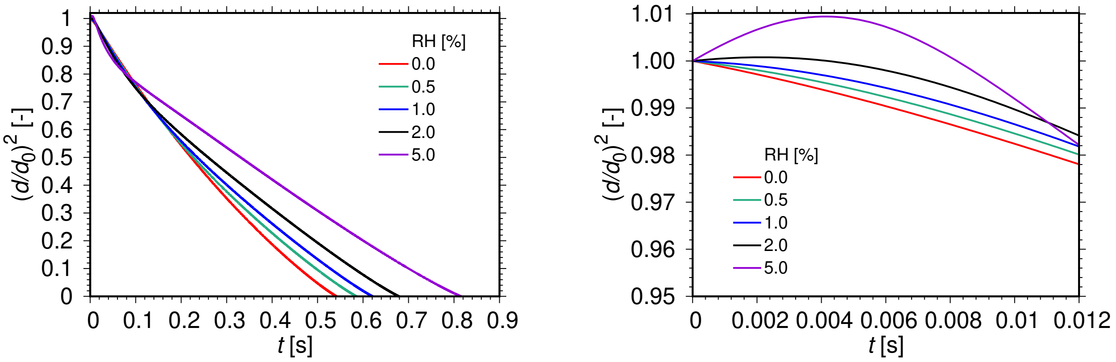

(a) Normal view. (b) Zoomed view.

Figure 3.12: Influence of the relative humidity, RH, on the normalized droplet surface area assuming ideal mixture properties. Initial conditions: $r_{\mathrm{d},0} = 50$ µm, $T_{\mathrm{l},0} = 293.15$ K, $p = 1$ bar, $u_0 = 4$ m/s, $T_{\mathrm{g},0} = 400$ K, $Y_{\mathrm{EtOH},0} = 0.50$ (Narasu et al. [72]).

locity on the droplet lifetime is small as compared to that of the ambient air temperature and the initial droplet size. For all the cases studied, larger the initial mass fraction of ethanol, the droplet lifetime is reduced since ethanol is more volatile than water.

As the droplet consisting of the components of ethanol and water evaporate, the amount of water in the ambience is enhanced. Therefore, to understand the influence of the water content in the environment on the process of droplet evaporation, a parameter study is performed for an ethanol/water droplet in humid air by considering both ideal and real behavior of the liquid mixture.

Figure 3.12 displays the impact of relative humidity on the normalized droplet surface area for an ethanol/water droplet of initial radius of 50 µm at relative velocity of 4 m/s for ambient air temperature of 400 K for initial ethanol mass fraction of 0.50. Five different relative humidity values of 0.0 %, 0.5 %, 1.0 %, 2.0 %, and 5.0 % are considered. The initial ethanol mass fraction of 0.50 is selected since the impact on the droplet heating and evaporation characteristics is the largest for this condition. For Fig. 3.12, the ideal nature of the liquid mixture is taken into account, that is the activity coefficient of the components is taken as one, $\gamma_i = 1$. Increasing the relative humidity from 0 % to 5 % enhances the evaporation of the droplet initially which is followed by retarded evaporation that eventually prolongs the droplet lifetime, see Fig. 3.12a. Figure 3.12b shows the zoomed view of Fig. 3.12a. For relative humidity of 5 %, initial droplet expansion occurs which accounts for about 1 % of the initial droplet surface area over a time period of 4 ms. To understand the reason for the initial droplet expansion for the higher relative humidity case, the profile of the temperature at the droplet surface and the mass evaporation rates of both the liquid components are displayed in Fig. 3.13. Initially, the mass evaporation rate of water becomes negative, see Fig. 3.13b, which shows evidence for the condensation of water occurring at the surface of the droplet due to which heat is released. Increasing the amount of humidity in the ambience increases the rate of condensation which further causes more heat release and eventually, results in the initial increase of the temperature at the surface of the droplet, as shown in Fig. 3.13a. Thus, the initial increase of the

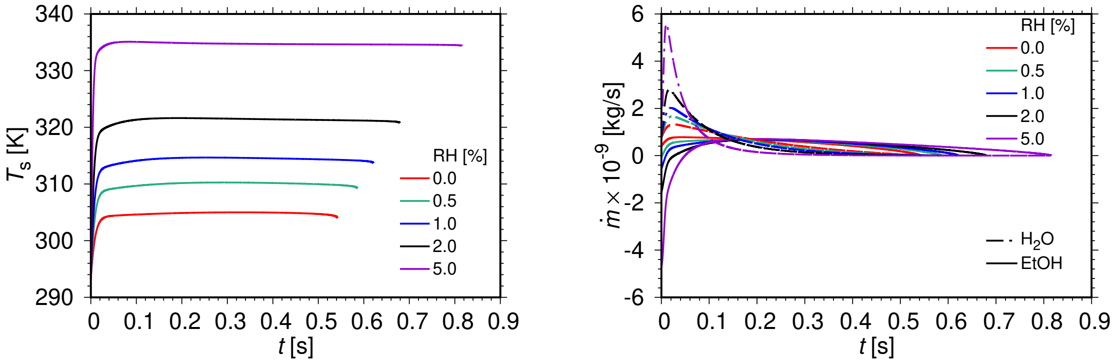

(a) Temperature at the droplet surface. (b) Mass evaporation rates.

Figure 3.13: Influence of the relative humidity, RH, on the droplet heating and evaporation characteristics assuming ideal mixture properties. Initial conditions: $r_{\mathrm{d},0}$ = 50 μm, $T_{\mathrm{l},0}$ = 293.15 K, p = 1 bar, u_0 = 4 m/s, $T_{\mathrm{g},0}$ = 400 K, $Y_{\mathrm{EtOH},0}$ = 0.50 (Narasu et al. [72]).

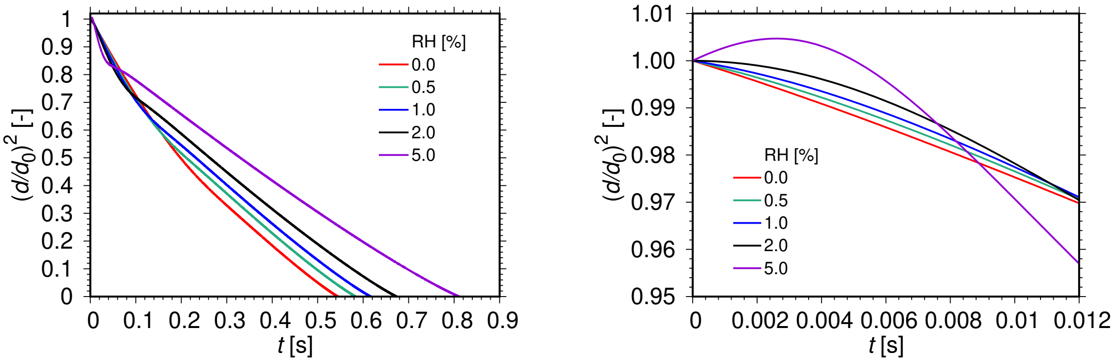

(a) Normal view. (b) Zoomed view.

Figure 3.14: Influence of the relative humidity, RH, on the normalized droplet surface area assuming real mixture properties. Initial conditions: $r_{\mathrm{d},0}$ = 50 μm, $T_{\mathrm{l},0}$ = 293.15 K, p = 1 bar, u_0 = 4 m/s, $T_{\mathrm{g},0}$ = 400 K, $Y_{\mathrm{EtOH},0}$ = 0.50 (Narasu et al. [72]).

droplet surface temperature results in enhanced evaporation of the ethanol component as can be observed from the peak values attained by the mass evaporation rates of ethanol, see Fig. 3.13b. This enhancement of the evaporation rate of the ethanol component outweighs the negative mass evaporation rate of the water component and therefore, causes the initial expansion of the droplet, as seen in Fig.3.12b. Previous study of Saharin [105] had also reported regarding water condensation on the surface of the droplet.

Figures 3.14 and 3.15 show the effect of humidity on the droplet heating and evaporation characteristics for the same conditions of Fig. 3.12, except that the real behavior of the liquid mixture is considered through the use of activity coefficients modeled following the UNIFAC method. For the non-ideal mixture, see Fig. 3.14, the initial expansion of the droplet is around 0.47 % of the initial droplet surface area

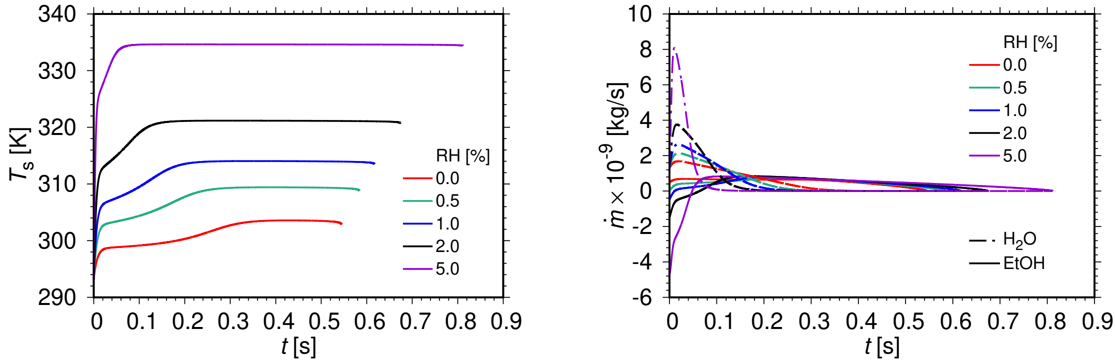

(a) Temperature at the droplet surface.

(b) Mass evaporation rates.

Figure 3.15: Influence of the relative humidity, RH, on the droplet heating and evaporation characteristics assuming real mixture properties. Initial conditions: $r_{\mathrm{d},0} = 50$ µm, $T_{\mathrm{l},0} = 293.15$ K, $p = 1$ bar, $u_0 = 4$ m/s, $T_{\mathrm{g},0} = 400$ K, $Y_{\mathrm{EtOH},0} = 0.50$ (Narasu et al. [72]).

over a time period of 2.6 ms as compared to approximately 1 % of the initial droplet surface area at 4 ms for the numerical study considering the ideal mixture behavior, see Fig. 3.12. Therefore, taking into account the real behavior of the liquid mixture causes the reduction of the initial droplet expansion by a factor of two and occurs over a shorter period of time. Comparing the mass evaporation rates of both the liquid components, see Figs. 3.13b and 3.15b, the peak value attained by the water component is almost the same whereas the maximum value of the mass evaporation rate of the ethanol component is higher by around 30 % for the real mixture which is because of the positive deviation from Raoult's law for the non-ideal mixture. For the liquid mixture considering the real behavior, the evaporation of the ethanol causes drastic reduction of the mass fraction of ethanol which results in the strong increase of the activity coefficient of ethanol that leads to higher Spalding mass transfer number and eventually, enhances the mass evaporation rate of the ethanol component. Thus, the impact of the increased droplet surface temperature is outweighed by the real behavior of the liquid mixture, see Figs. 3.13a and 3.15a, where the heating of the droplet is retarded because of the non-ideal behavior of the liquid mixture. During the initial phase of evaporation, the increase of the activity coefficient of ethanol is more drastic than the reduction of the activity coefficient of water, that leads to enhanced rate of mass evaporation while considering the real behavior of the liquid mixture. Even though incorporating the non-ideal behavior of the liquid mixture has negligible effect on the droplet lifetime, using the real mixture properties is advocated to capture the details with respect to the processes of droplet heating and evaporation.

Govindaraju and Ihme [89] studied the characteristics associated with droplet heating and evaporation of base-gasoline G1 [108] and ethanol blends in an ambience of quiescent air where the real behavior of the liquids was incorporated by modeling the activity coefficients using the UNIFAC approach and found enhanced evaporation of the higher volatile ethanol component. However, in that study, assuming ideal behavior of the liquids did not show this effect. They found that with the increase of the ethanol content, enhanced initial evaporation of the droplet takes place with prolonged droplet lifetimes as was displayed for the influence of humid air on the processes of heating and evaporation with respect to Fig. 3.14a.

In comparison with the evaporation of an ethanol/water droplet in dry air, in an ambience of humid air, the condensation of water at the droplet surface occurs which causes the strong increase of the temperature at the droplet surface and reduces the time period of the unsteady heating phase. Even though the quasi-steady evaporation starts earlier, the lifetime of the droplet in humid air is prolonged by a factor of one and a half as compared to that in dry air, since the rate of evaporation of the water component is reduced in humid air. Thus, overall, there are three stages for the evaporation of the ethanol/water droplet in air of relative humidity of 5 %. The first stage is the initial expansion of the droplet caused due to the water condensation at the surface of the droplet. The second stage is associated with the enhanced evaporation of the ethanol component and the third stage is represented by the retarded water evaporation. In dry air, there are two stages with respect to the droplet behavior. In an ambience of dry air, there is no droplet expansion due to condensation but, there is the possibility of the occurrence of initial droplet expansion due to the droplet heating associated with variable liquid properties. The first stage accounts for the preferential evaporation of the higher volatile ethanol followed by water evaporation which continues until the droplet completely evaporates.

The zero-dimensional model is applied to the multicomponent system of butanol and water at ambient pressures below atmospheric pressure and the results are presented in the next section.

3.2 Butanol/Water Droplet

The *SpraySyn* burner developed by Schneider et al. [29] is designed with the objective of producing nanoparticles on a large scale. However, the turbulence associated with the entire process makes it difficult to measure the concentration profiles of various species. Thus, in order to understand the underlying chemical kinetics of new precursor solutions and develop reaction mechanisms associated with the synthesis of nanoparticles, a laminar matrix burner was developed by Apazeller et al. [109], where the ambient pressure was set below the atmospheric pressure to measure the concentration of the species in a convenient way. For the matrix burner, knowing the droplet characteristics would help in performing more complex simulations with respect to the gas phase. Nanjaiah et al. [96] performed gas phase simulations concerning the matrix burner, where the major assumption was that at the inlet of the matrix burner, the droplets are entirely evaporated. Thus, the droplet lifetimes are evaluated in the present study to support this assumption. Therefore, in this section, a numerical investigation is performed to study the behavior of a single butanol/water droplet at low ambient pressures less than the atmospheric pressure. The characteristics of the droplet heating and evaporation are described using the zero-dimensional model, see section 2.2. There is no experimental data available to compare the numerical results of the present study. However, the zero-dimensional model was validated by Narasu et al. [72] by comparing the results of the droplet simulations performed at atmospheric pressure for the multicomponent system of ethanol and water with the experimental results provided by Ma et al. [75].

At first, the heating and evaporation characteristics of the butanol/water droplet for various initial conditions are discussed. Further, an analysis is presented with respect to the droplet lifetime. The different conditions considered in the present study include initial droplet radii of 1.25 µm and 5 µm, relative velocities of 0.01 m/s and 0.1 m/s, as well as ambient gas temperatures of 400 K and 1200 K. The various initial mass fractions of water taken into account are 0.0, 0.00810174, 0.0122411, 0.01479, 0.0218284, 0.0235751, and 0.0566031, which correspond to the composition of the precursor solution used in the matrix burner [109, 96]. Two different ambient pressures of 40 mbar and 60 mbar are considered. The ambient gas mixtures considered at 40 mbar pressure are that of methane/argon and hydrogen/argon whereas, at 60 mbar, the ambience is composed of methane and nitrogen. The initial conditions considered in this present study are based on the experimental conditions concerning the matrix burner [109, 96]. Also, for all these conditions, the Weber number remains below the critical Weber number, so that the droplet does not breakup. Further, the mass and thermal Peclet numbers are below their critical values, so that the rapid-mixing and the distillation-limit models are valid, as presented in the previous section 3.1 as well as in the numerical study of Narasu et al. [72]. The results of the numerical study are discussed next.

Figure 3.16 displays the profiles of the normalized droplet surface area for pure butanol (solid lines) and butanol/water (dashed lines) droplets of initial radius of 5 µm at relative velocity of 0.1 m/s for ambient gas temperature of 1200 K at ambient pressures of 40 mbar and 60 mbar. The ambience at 40 mbar pressure is composed of methane and argon whereas at 60 mbar, the ambient gas mixture is methane/nitrogen. At 40 mbar pressure, the liquid mass fractions of butanol and water are 0.9764249 and 0.0235751 respectively, whereas, at 60 mbar, the corresponding values are 0.9433969 and 0.0566031, respectively. The liquid mass fractions of butanol and water correspond to the composition of the precursor solution employed in the matrix burner [109, 96]. The droplet expands initially during the droplet heating due to the variable liquid properties used in the model. This is followed by the quasi-steady evaporation phase where the preferential evaporation of the higher volatile component water occurs followed by the evaporation of the butanol component. Pure butanol droplet evaporates

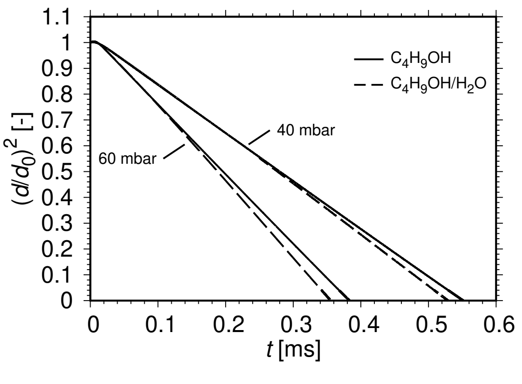

Figure 3.16: Temporal variation of the normalized droplet surface area. Initial conditions: $r_{\mathrm{d},0} = 5$ µm, $T_{\mathrm{l},0} = 293.15$ K, $u_0 = 0.1$ m/s, $T_{\mathrm{g},0} = 1200$ K. At $p = 40$ mbar: $Y_{\mathrm{C_4H_9OH},0} = 0.9764249$, $Y_{\mathrm{H_2O},0} = 0.0235751$. At $p = 60$ mbar: $Y_{\mathrm{C_4H_9OH},0} = 0.9433969$, $Y_{\mathrm{H_2O},0} = 0.0566031$ (Nanjaiah et al. [96]).

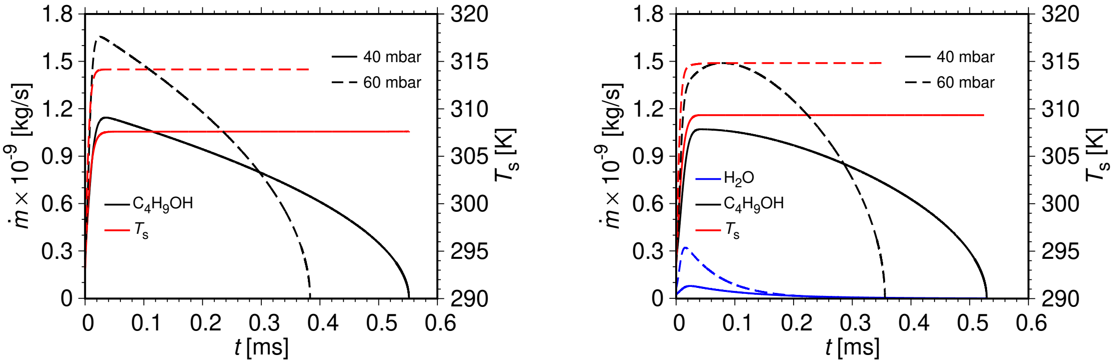

(a) Pure butanol droplet. (b) Butanol/water droplet.

Figure 3.17: Temporal variation of the mass evaporation rates and droplet surface temperature. Initial conditions: $r_{\mathrm{d},0} = 5$ μm, $T_{\mathrm{l},0} = 293.15$ K, $u_0 = 0.1$ m/s, $T_{\mathrm{g},0} = 1200$ K. (a) $Y_{\mathrm{C_4H_9OH},0} = 1.0$, $Y_{\mathrm{H_2O},0} = 0.0$. (b) At $p = 40$ mbar, $Y_{\mathrm{C_4H_9OH},0} = 0.9764249$ and $Y_{\mathrm{H_2O},0} = 0.0235751$. At $p = 60$ mbar: $Y_{\mathrm{C_4H_9OH},0} = 0.9433969$ and $Y_{\mathrm{H_2O},0} = 0.0566031$ (Nanjaiah et al. [96]).

slower than the butanol/water droplet because of the lower volatility of butanol as compared to that of water. At higher ambient pressure of 60 mbar, the droplet lifetimes are reduced by approximately 40 % as compared to that at lower pressure of 40 mbar, because of the higher mass evaporation rates of the liquid components, which is discussed next.

Figure 3.17 provides insight into the profiles of the droplet surface temperature and the mass evaporation rates for the initial conditions specified for Fig. 3.16. Figure 3.17a presents the results for the pure butanol droplet and Fig. 3.17b displays these for the butanol/water droplet. The droplet surface temperature is represented by the red color lines and the mass evaporation rates of butanol and water is showcased by the black and blue color lines, respectively. During the initial droplet heating period, the temperature at the surface of the droplet increases for both the pure butanol and the butanol/water droplets. For the butanol/water droplets, see Fig. 3.17b, after the initial heating period, the higher volatile water evaporates preferentially, as can be seen from the early peak values obtained for the mass evaporation rates of the water component. Further, the lower volatile butanol evaporates which is reflected in the mass evaporation rates of the butanol component. At higher ambient pressure of 60 mbar, the surface temperatures attained by the droplet and the mass evaporation rates of both the liquid components are higher in comparison to that at lower ambient pressure of 40 mbar, which results in faster evaporation of the droplets at 60 mbar.

The temporal evolution of the temperature (red color) at the surface of the droplet as well as the mass fractions of butanol (black color) and water (blue color) for butanol/water droplet of initial radius of 5 μm at relative velocity of 0.1 m/s for ambient gas temperature of 1200 K at ambient pressures of 40 mbar and 60 mbar are displayed in Fig. 3.18. The initial water mass fractions are 0.0235751 and 0.0566031 at ambient pressures of 40 mbar and 60 mbar, respectively. The droplet surface temperature increases initially followed by the quasi-steady evaporation phase where

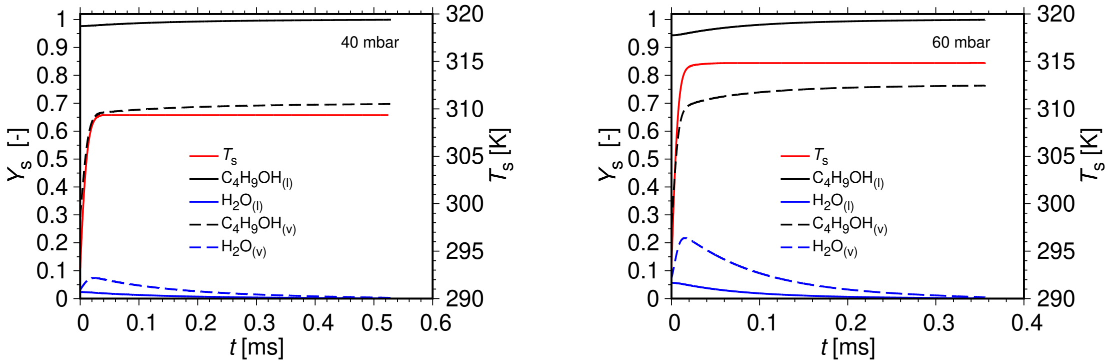

(a) $p = 40$ mbar, $Y_{C_4H_9OH,0} = 0.9764249$, $Y_{H_2O,0} = 0.0235751$.

(b) $p = 60$ mbar, $Y_{C_4H_9OH,0} = 0.9433969$, $Y_{H_2O,0} = 0.0566031$.

Figure 3.18: Temporal variation of the species mass fractions and temperature at the surface of the droplet. Initial conditions: $r_{d,0} = 5$ µm, $T_{l,0} = 293.15$ K, $u_0 = 0.1$ m/s, $T_{g,0} = 1200$ K (Nanjaiah et al. [96]).

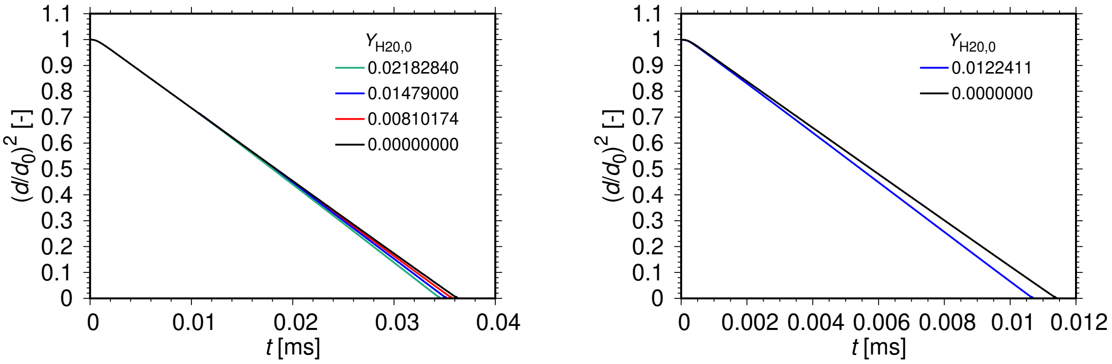

(a) methane/argon ambient gas mixture.

(b) hydrogen/argon ambient gas mixture.

Figure 3.19: Temporal variation of the normalized droplet surface area. Initial conditions: $r_{d,0} = 1.25$ µm, $T_{l,0} = 293.15$ K, $p = 40$ mbar, $u_0 = 0.01$ m/s, $T_{g,0} = 1200$ K (Nanjaiah et al. [96]).

the preferential evaporation of the higher volatile water component occurs which is reflected in the mass fraction of water, which causes the increase of the butanol content at the surface of the droplet.

Figure 3.19 shows the profiles of the normalized droplet surface area versus time for butanol/water droplets of initial radius of 1.25 µm at relative velocity of 0.01 m/s for ambient temperature of 1200 K at ambient pressure of 40 mbar for two different ambient gas mixtures of methane/argon and hydrogen/argon. Figure 3.19a displays the results for the ambient gas mixture of methane/argon and Fig. 3.19b presents these for the ambience composed of hydrogen and argon. For ambient mixture of methane/argon, four different initial mass fractions of water of 0.0, 0.00810174, 0.01479, and 0.0218284 are used, whereas, for gas mixture of hydrogen/argon, two different initial mass fractions of water of 0.0 and 0.0122411 are employed. As the droplet

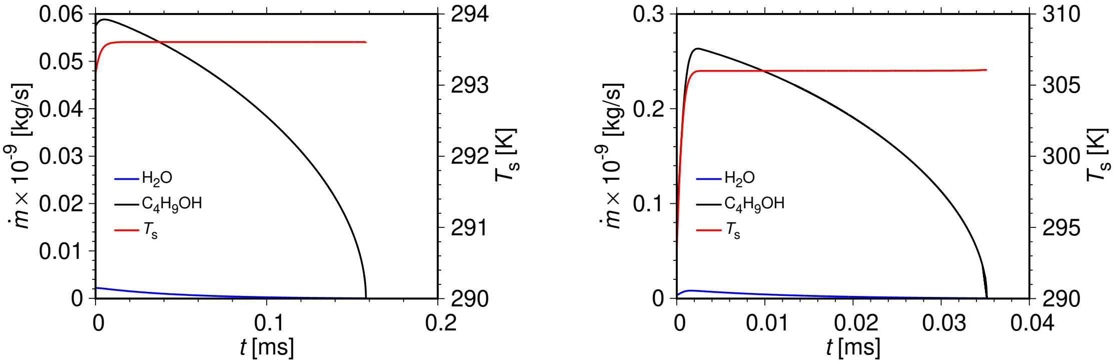

(a) $T_{g,0} = 400$ K. (b) $T_{g,0} = 1200$ K.

Figure 3.20: Temporal variation of the mass evaporation rates and droplet surface temperature. Initial conditions: $r_{d,0} = 1.25$ µm, $T_{l,0} = 293.15$ K, $p = 40$ mbar, $u_0 = 0.01$ m/s, $Y_{C_4H_9OH,0} = 0.98521$, $Y_{H_2O,0} = 0.01479$ (Nanjaiah et al. [96]).

heats up initially, droplet expansion occurs for all the cases studied here, due to the variable liquid properties employed in the model. For the butanol/water droplet, water evaporates preferentially owing to its higher volatility followed by the evaporation of butanol. Thus, increasing the initial water content results in faster evaporation of the droplet since water is more volatile than butanol. For ambient gas mixture of hydrogen/argon, the droplet lifetime is reduced by a factor of three in comparison with that of the ambient mixture of methane/argon, owing to the difference in the gas mixture properties.

The influence of the ambient gas temperature on the droplet heating and evaporation characteristics of single butanol/water droplet is presented in Fig. 3.20. Figure 3.20 shows the profiles of the mass evaporation rates of butanol (black color) and water (blue color) along with the droplet surface temperature (red color) with time for initial droplet radius of 1.25 µm with relative velocity of 0.01 m/s for initial mass fraction of water of 0.01479 at ambient pressure of 40 mbar for ambient temperatures of 400 K and 1200 K. The results for the ambient temperatures of 400 K and 1200 K are displayed in Figs. 3.20a and 3.20b, respectively. For both ambient gas temperatures, the initial droplet heating causes the increase of the temperature at the surface of the droplet. The droplet heating is followed by the preferential evaporation of the water component since water is more volatile than butanol, that is reflected in the early maxima reached for the mass evaporation rate of the water component, after which butanol evaporation dominates, as is visible from the peak values attained for the mass evaporation rate of butanol. At higher ambient temperature of 1200 K, the droplet surface temperatures and the mass evaporation rates of both the liquid components are higher than that at lower ambient gas temperature of 400 K, due to the increased heat transfer rate between the ambience and the droplet. Therefore, at higher ambient gas temperature of 1200 K, the droplet evaporates faster eventually resulting in shorter lifetime of the droplet as compared to that at 400 K. More detailed analysis with respect to the droplet lifetimes is discussed next.

Figure 3.21a shows the lifetimes of the butanol/water droplet for the initial condi-

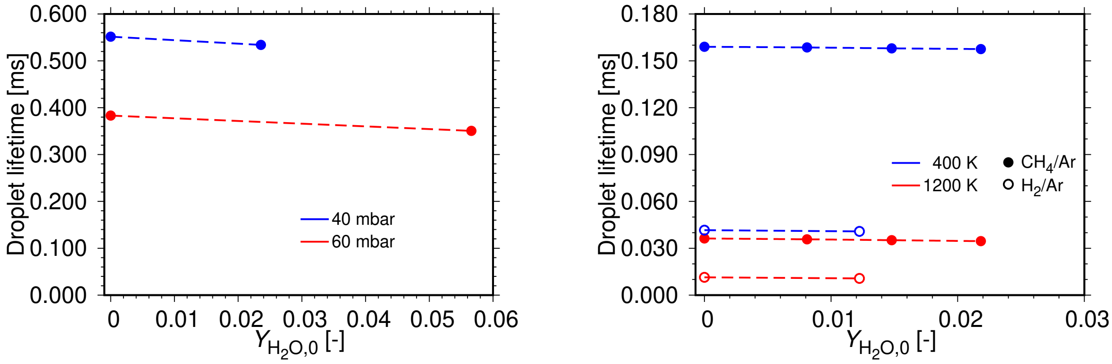

(a) $r_{d,0} = 5$ µm, $u_0 = 0.1$ m/s, $T_{g,0} = 1200$ K.

(b) $r_{d,0} = 1.25$ µm, $p = 40$ mbar, $u_0 = 0.01$ m/s.

Figure 3.21: Lifetime of the droplet for different initial conditions. Initial condition: $T_{l,0} = 293.15$ K (Nanjaiah et al. [96]).

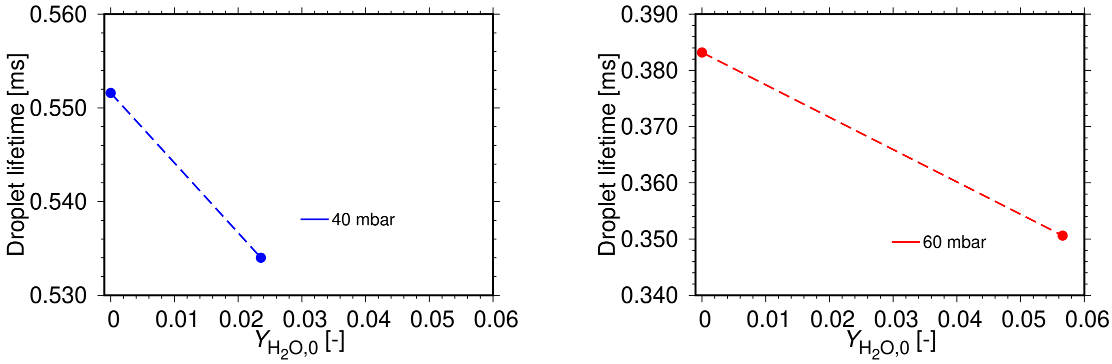

(a) At $p = 40$ mbar.

(b) At $p = 60$ mbar.

Figure 3.22: Zoomed view of Fig. 3.21a, displaying the lifetime of the droplet. Initial conditions: $r_{d,0} = 5$ µm, $T_{l,0} = 293.15$ K, $u_0 = 0.1$ m/s, $T_{g,0} = 1200$ K (Nanjaiah et al. [96]).

tions of Fig. 3.16 whereas Fig. 3.21b displays the droplet lifetimes for the conditions of Fig. 3.19 at ambient gas temperatures of 400 K and 1200 K. At higher ambient pressure of 60 mbar (red color), see Fig. 3.21a, the droplets evaporate faster and thus, the lifetimes of the droplet are shorter than at an ambience of lower pressure of 40 mbar (blue color), because of the higher droplet surface temperatures and mass evaporation rates of the liquid components at 60 mbar, see Fig. 3.17. For lower ambient temperature of 400 K (blue color), see Fig. 3.21b, the droplet evaporation is slowed down and therefore, the droplet lifetimes are prolonged as compared to that at higher ambient temperature of 1200 K (red color), due to the reduced heat transfer rate between the ambience and the droplet. For ambient gas mixture of methane/argon (filled symbols), see Fig. 3.21b, the droplet lifetime is increased by a factor of three in comparison with that of the ambient mixture of hydrogen and argon (open symbols), because of the difference in the gas mixture properties. As the

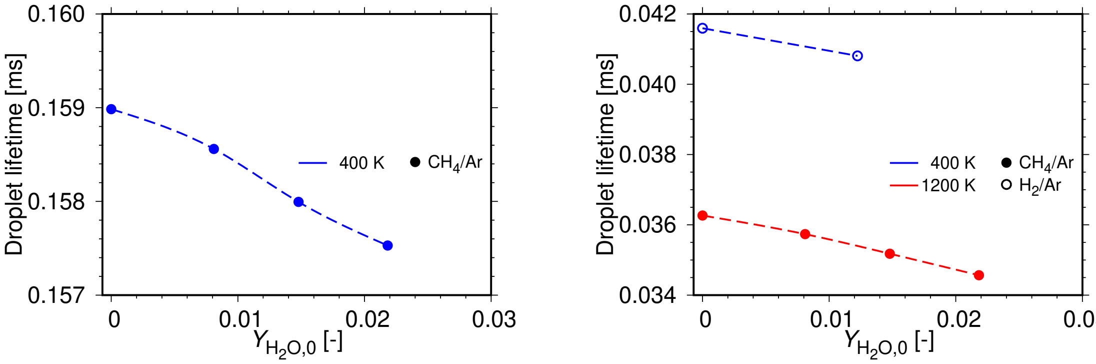

(a) At $T_{g,0} = 400$ K.

(b) At $T_{g,0} = 400$ K and 1200 K.

Figure 3.23: Zoomed view of Fig. 3.21b, displaying the lifetime of the droplet. Initial conditions: $r_{d,0} = 1.25$ µm, $T_{l,0} = 293.15$ K, $p = 40$ mbar, $u_0 = 0.01$ m/s (Nanjaiah et al. [96]).

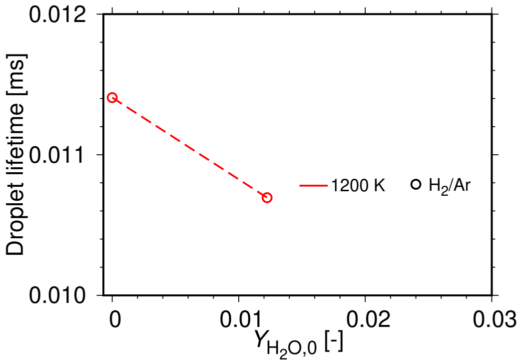

Figure 3.24: Zoomed view of Fig. 3.21b, displaying the lifetime of the droplet. Initial conditions: $r_{d,0} = 1.25$ µm, $T_{l,0} = 293.15$ K, $p = 40$ mbar, $u_0 = 0.01$ m/s (Nanjaiah et al. [96]).

initial mass fraction of water is increased, the droplet evaporates faster for all the cases investigated in this present study, since the volatility of water is higher than that of butanol. This is visible clearly in Figs. 3.22 - 3.24, which present the zoomed views of Fig. 3.21. Figure 3.22 displays the zoomed view of Fig. 3.21a whereas Figs 3.23 and 3.24 show better resolved images of Fig. 3.21b. Thus, the lifetime of the butanol/water droplet is less than 1 ms for various conditions considered in the present study.

For the precursor solution system of iron(III) nitrate nonahydrate and ethanol, the zero-dimensional model is coupled with the thermal decomposition model and the results are discussed in the next section.

3.3 Iron(III) Nitrate Nonahydrate/Ethanol Droplet

During the generation of nanoparticles via spray flames, previous studies confirm that particles are formed via two routes [32, 33]. Either the particles are formed directly from the droplet or the droplets evaporate into the gas phase from where the particles are generated. Wang and Huang [112] conducted experimental study of flame aerosol synthesis of cerium(IV) oxide and tungsten trioxide. It was concluded that there are two pathways through which particles are generated, droplet-particle and droplet-vapor-particle. They found that the pathway chosen for the generation of particles depends on the vapor pressure and the flame temperature. Experimental and numerical investigation of the production of luminescent europium doped yttrium oxide nanophosphors using flame synthesis was carried out by Abram et al. [113]. The study found that the particles were formed via two different mechanisms, namely, droplet-to-particle and gas-to-particle, which depended on the synthesis temperature. In the experimental study conducted by Majerič et al. [114], regarding the synthesis of gold nanoparticles via redesigned ultrasonic spray pyrolysis, the droplet-to-particle and gas-to-particle routes of particle formation were discussed. Stodt et al. [62] employed the phase selective laser induced breakdown spectroscopy (PS-LIBS) method to investigate the formation of iron oxide in an external mixing spray flame reactor, in order to differentiate between the droplet-to-particle and the gas-to-particle pathways of particle formation. They concluded that the transition of the unreacted precursor from the droplet-to-particle phase was not possible to detect using the phase selective laser induced breakdown spectroscopy technique in the underlying dense spray flame. Majerič and Rudolf [63] discusses the droplet-to-particle and the gas-to-particle mechanisms through which the particles are formed in the review paper on the synthesis and processing of noble metal nanoparticles using ultrasonic spray pyrolysis.

For the present study, in order to explore both the droplet-to-particle and the droplet into gas phase pathways, the precursor solution of iron(III) nitrate nonahydrate and ethanol is considered. In flame spray pyrolysis, iron(III) oxide nanoparticles are produced using the precursor/solvent system of iron(III) nitrate nonahydrate and ethanol. Iron(III) nitrate nonahydrate consists of nine crystal water molecules, as shown in Fig. 3.25a, and is commonly used as the precursor for synthesis of iron(III) oxide nanoparticles, see Fig. 3.25b, using spray flames. The iron oxide nanoparticles have wide range of applications in various fields such as biomedical field [115], healthcare

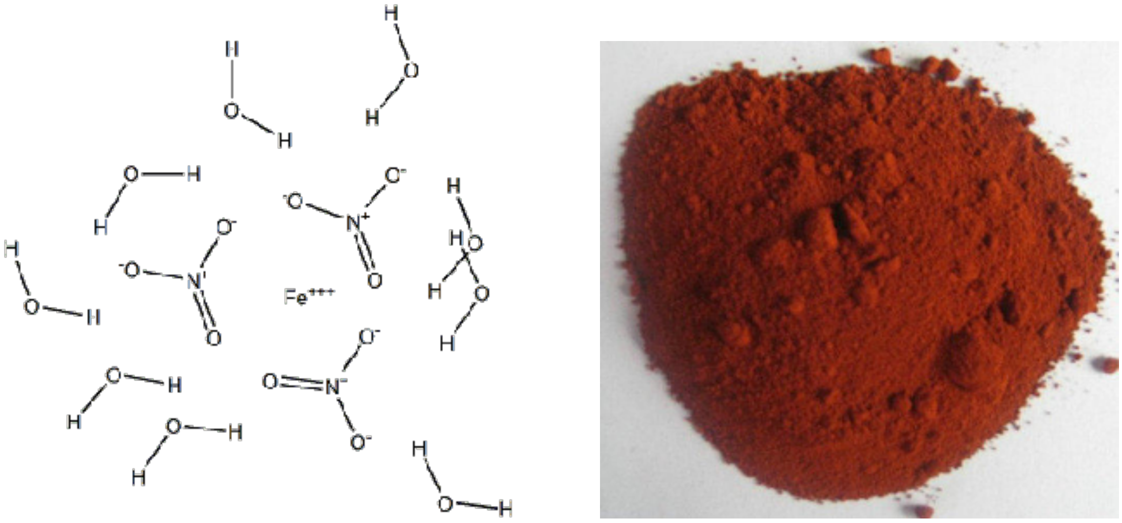

(a) Chemical structure of INN.

(b) Iron(III) oxide nanoparticles.

Figure 3.25: The chemical structure of iron(III) nitrate nonahydrate (INN) [110] and iron(III) oxide nanoparticles [111]

industry [116], agriculture and food industry [117], aerospace industry [118] etc. For example, in the field of medicine, the iron oxide nanoparticles are used in treating cancer via the methodology of magnetic hyperthermia [119, 120, 121]. In this approach, a fluid consisting of iron oxide, known as the ferrofluid, is injected to the location of the tumor. Further, by employing a magnetic field, it gets heated up and thus, causes the destruction of the cancerous cells. Another application is that, in the aerospace industry, the iron oxide nanoparticles are added as a catalyst to increase the burning rate of the solid propellants [122].

In this section, the results of the numerical study of the behavior of a single iron(III) nitrate nonahydrate/ethanol droplet at atmospheric pressure is presented where the droplet heating and evaporation is described by employing the zero-dimensional model, see section 2.2, and possible thermal decomposition is taken into account using the thermal decomposition model, see section 2.2.3. Unfortunately, there is no experimental results available for validation of the present numerical study. However, the zero-dimensional model was validated by Narasu et al. [72] for the evaporation of a single ethanol/water droplet with the experimental results of Ma et al. [75], as was discussed in the previous section 3.1.

A parameter study is performed by varying the initial droplet radius, the initial precursor mass fraction, the relative velocity between the droplet and the ambience, the ambient gas temperature, and the relative humidity in air. For the parameter study, the initial droplet radii considered vary from 1 μm to 25 μm. Further, two relative velocities of 4 m/s and 8 m/s and relative humidities from 0 % to 10 % are taken into account. The initial precursor mass fractions considered are 0.0125, 0.025, and 0.20. Also, in order to explore both the pathways, the droplet-to-particle and droplet into gas phase, see sec 2.2.3, ambient air temperatures of 400 K, 800 K, and 1200 K are taken into account for the parameter study. The initial conditions are chosen based on the experimental conditions of a burner developed for the purpose of FSP [29], where the droplet breakup is not considered since the Weber numbers stay below the critical Weber number. Also, the thermal and mass Peclet numbers are below their critical values so that the distillation-limit and the rapid-mixing models are valid, as was explained in detail in the study of Narasu et al. [72] as well as in the previous section 3.1.

Firstly, the results for the droplet-to-particle pathway, that is where only droplet evaporation occurs without thermal decomposition, are discussed. Further, the results of the droplet into gas phase pathway are presented. Finally, the numerical results are parameterized using polynomial fits for use in more complex simulations of FSP.

3.3.1 Droplet-to-Particle Pathway

Figure 3.26 shows the profiles of the normalized droplet surface with time for a precursor solution droplet of INN and ethanol of initial droplet radius of 5 μm at relative velocities of 4 m/s (solid lines) and 8 m/s (dashed lines) for initial INN mass fractions of 0.0125 and 0.250 in an ambience of dry (relative humidity of 0 %) as well as humid air. The relative humidity in air of 0 % (black and green lines), 5 % (red lines), and 10 % (blue lines) are considered. The ambient air temperature of 400 K, which is below the

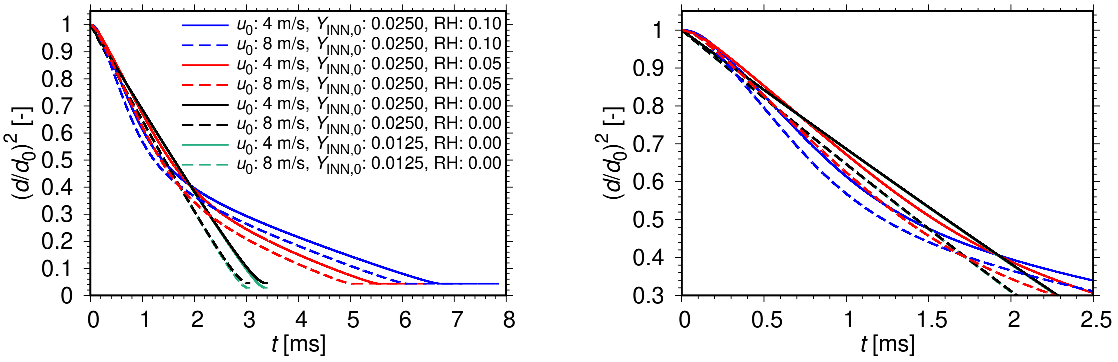

(a) Normal view. (b) Zoomed view.

Figure 3.26: Temporal variation of the normalized droplet surface area. Initial conditions: $r_{\mathrm{d},0} = 5$ µm, $T_{\mathrm{l},0} = 293.15$ K, $p = 1$ bar, $T_{\mathrm{g},0} = 400$ K (Narasu et al. [76]).

thermal decomposition temperature of 403 K, is taken into account with the objective of understanding the characteristics associated with the droplet-to-particle pathway, see Fig 2.2. In this pathway, the liquids ethanol and water evaporate leaving behind a solid particle. Figure 3.26b displays the zoomed view of Fig. 3.26a. In dry air, at lower relative velocity of 4 m/s for initial INN mass fraction of 0.0250 (solid black line), the INN/ethanol droplet evaporates at around 3.5 ms. As the initial INN mass fraction is reduced to 0.0125 (solid green line), the size of the final particle formed is smaller. For higher relative velocity of 8 m/s (dashed black and green lines), the evaporation is faster due to the stronger convection rate. Increasing the relative humidity to 5 % and 10 % results in initial increase of the profile of the normalized droplet surface area due to condensation of water at the surface of the droplet, after which enhanced evaporation of the droplet occurs followed by retarded evaporation, see Fig. 3.26b. In Fig. 3.26b, the black lines are only visible, since the black and green curves almost coincide with each other. The profile of the normalized droplet surface area, see Fig. 3.26b, at relative velocity of 8 m/s intersects at approximately 1.7 ms, as shown in the zoomed view of Fig. 3.26b. For relative velocity of 4 m/s, the intersection occurs at around 2 ms because of the slower droplet evaporation caused due to the reduced convection rate. Also, the deviation of the normalized droplet surface area profile from the classical d^2 law, due to the variable liquid properties, is visible from the differences in the slopes before and after around 2 ms in humid air.

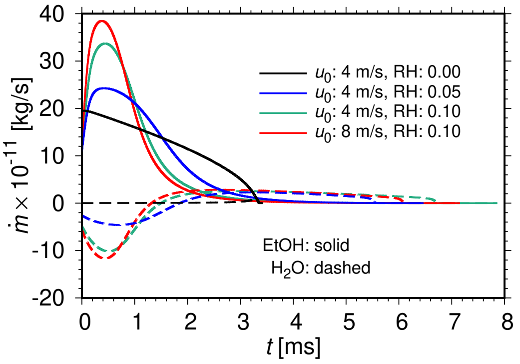

Figure 3.27: Temporal variation of the mass evaporation rates of ethanol and water. Initial conditions: $r_{\mathrm{d},0} = 5$ µm, $T_{\mathrm{l},0} = 293.15$ K, $p = 1$ bar, $u_0 = 4$ m/s, $T_{\mathrm{g},0} = 400$ K, $Y_{\mathrm{IN},0} = 0.014$, $Y_{\mathrm{H_2O},0} = 0.011$, $Y_{\mathrm{EtOH},0} = 0.975$ (Narasu et al. [76]).

The mass evaporation rates of both

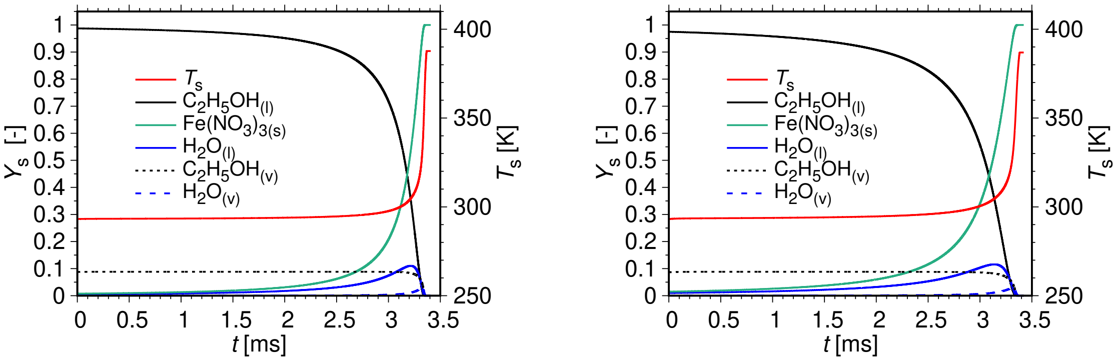

(a) $Y_{\mathrm{IN},0} = 0.0075$, $Y_{\mathrm{H_2O},0} = 0.005$, $Y_{\mathrm{EtOH},0} = 0.9875$.

(b) $Y_{\mathrm{IN},0} = 0.014$, $Y_{\mathrm{H_2O},0} = 0.011$, $Y_{\mathrm{EtOH},0} = 0.975$.

Figure 3.28: Temporal variation of the species mass fractions and temperature at the surface of the droplet. Initial conditions: $r_{\mathrm{d},0} = 5$ µm, $T_{\mathrm{l},0} = 293.15$ K, $p = 1$ bar, $u_0 = 4$ m/s, $T_{\mathrm{g},0} = 400$ K, RH = 0 % (Narasu et al. [76]).

ethanol (solid lines) and water (dashed lines) are presented in Fig. 3.27, for the same initial conditions of Fig. 3.26 for initial mass fraction of INN of 0.025. In dry air (black lines), the rates of evaporation of the ethanol component is higher than that of the water component due to the higher volatility of ethanol. This shows evidence of preferential evaporation of ethanol followed by water evaporation, that leads to decrease of the normalized droplet surface area, see Fig. 3.26b. In humid air, condensation of water occurs at the droplet surface, as seen from the negative mass evaporation rates of the water component, that leads to enhanced ethanol evaporation, which is stronger at higher relative velocity of 8 m/s and higher relative humidity of 10 %, and thus, causes more pronounced reduction of the normalized droplet surface area profile, see Fig. 3.26b. The water condensation is terminated at around 2 ms, after which the evaporation process is dominated by that of the water component. The condensation of water at the droplet surface results in increase of the droplet temperature and enhanced evaporation of the ethanol component, which is more pronounced at the higher relative velocity of 8 m/s when compared to that of 4 m/s, and thus leads to reduced droplet lifetime.

Figure 3.28 shows the profiles of the temperature and species mass fractions at the surface of the droplet for the initial conditions of Fig. 3.26 at relative velocity of 4 m/s and initial INN mass fractions of 0.0125 and 0.0250 in an ambience of dry air. Initially, the droplet heats up and the temperature (red line) at the surface of the droplet increases and the preferential evaporation of ethanol (black line) occurs owing to its higher volatility, which results in the increase of water content (blue line). Further, a second increase of the droplet surface temperature occurs during which the ethanol and the water are almost completely evaporated, and the iron(III) nitrate particle is formed. For initial INN mass fractions of 0.0125, see Fig. 3.28a, and 0.025, see Fig. 3.28b, total process times are independent of the initial INN mass fraction, since the evaporation of ethanol and water dominates the overall process. However, the radius of the final particle left behind for initial mass fraction of INN of 0.0125

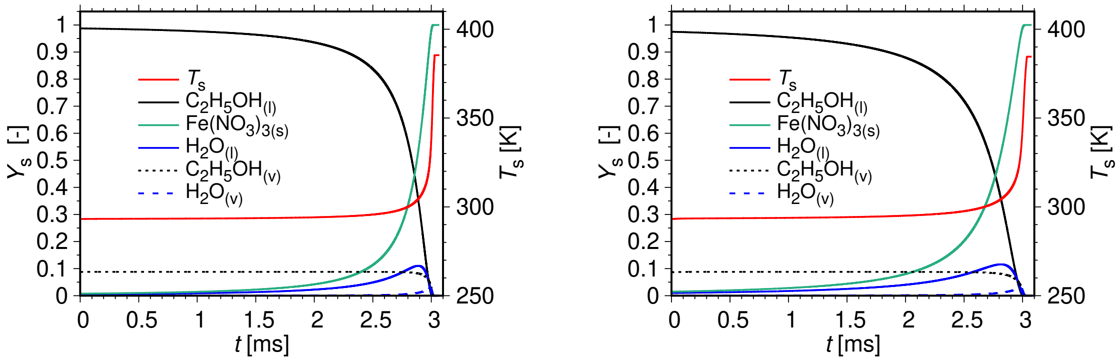

(a) $Y_{\mathrm{IN},0} = 0.0075$, $Y_{\mathrm{H_2O},0} = 0.005$, $Y_{\mathrm{EtOH},0} = 0.9875$.

(b) $Y_{\mathrm{IN},0} = 0.014$, $Y_{\mathrm{H_2O},0} = 0.011$, $Y_{\mathrm{EtOH},0} = 0.975$.

Figure 3.29: Temporal variation of the species mass fractions and temperature at the surface of the droplet. Initial conditions: $r_{\mathrm{d},0} = 5$ µm, $T_{\mathrm{l},0} = 293.15$ K, $p = 1$ bar, $u_0 = 8$ m/s, $T_{\mathrm{g},0} = 400$ K, RH = 0 % (Narasu et al. [76]).

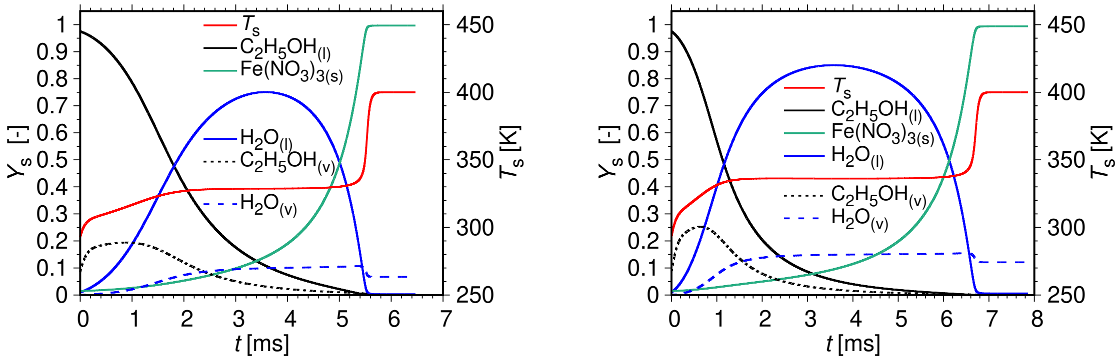

(a) RH = 5 %.

(b) RH = 10 %.

Figure 3.30: Temporal variation of the species mass fractions and temperature at the surface of the droplet. Initial conditions: $r_{\mathrm{d},0} = 5$ µm, $T_{\mathrm{l},0} = 293.15$ K, $p = 1$ bar, $u_0 = 4$ m/s, $T_{\mathrm{g},0} = 400$ K, $Y_{\mathrm{IN},0} = 0.014$, $Y_{\mathrm{H_2O},0} = 0.011$, $Y_{\mathrm{EtOH},0} = 0.975$ (Narasu et al. [76]).

is 847 nm which is smaller than that of 1067 nm for the initial INN mass fraction of 0.250. At relative velocity of 8 m/s, see Figure 3.29, the process times reduce in comparison with those at 4 m/s, because of the enhanced evaporation due to the stronger convection rate, whereas the final particle sizes are not affected.

Figure 3.30 displays the temporal evolution of the species mass fractions and the droplet surface temperature for the conditions of Fig. 3.28b at relative humidities of 5 % and 10 %. In comparison with the heating and evaporation characteristics in dry air, the initial increase of the droplet surface temperature is higher in an ambience of humid air. Also, the final temperature reached by the droplet surface is higher than that attained in dry air and also higher than the boiling points of both the liquid components. The reason for these differences in the droplet temperature is the

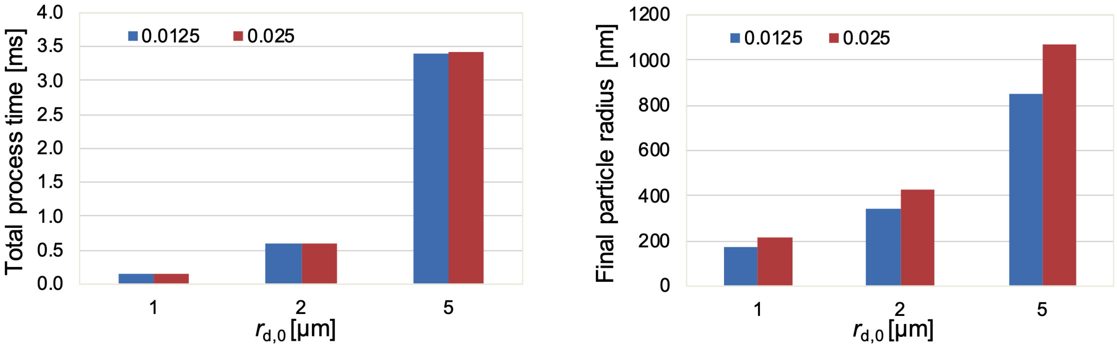

(a) Total process time. (b) Final particle radius.

Figure 3.31: Histograms showing the total process time and the final particle radius for different initial droplet radii and INN mass fractions of 0.0125 and 0.025. Initial conditions: $T_{\mathrm{l},0} = 293.15$ K, $p = 1$ bar, $u_0 = 4$ m/s, $T_{\mathrm{g},0} = 400$ K, RH = 0 % (Narasu et al. [76]).

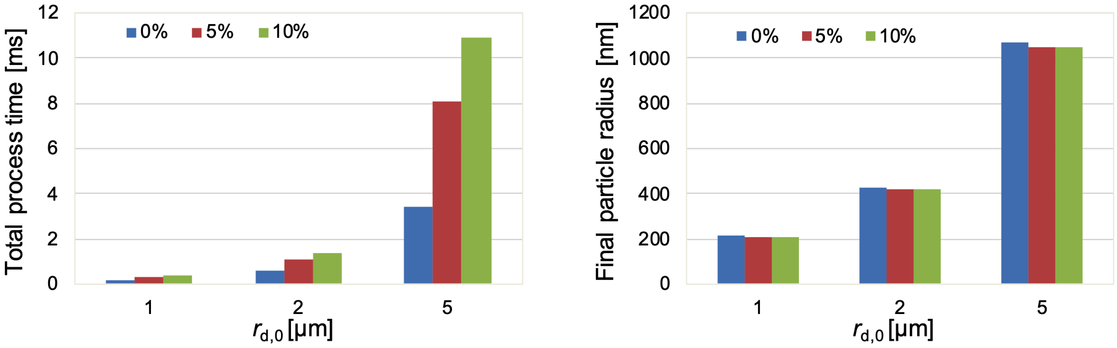

(a) Total process time. (b) Final particle radius.

Figure 3.32: Histograms showing the total process time and the final particle radius for different initial droplet radii and relative humidities of 0 %, 5 %, and 10 % in air. Initial conditions: $T_{\mathrm{l},0} = 293.15$ K, $p = 1$ bar, $u_0 = 4$ m/s, $T_{\mathrm{g},0} = 400$ K, $Y_{\mathrm{IN},0} = 0.014$, $Y_{\mathrm{H_2O},0} = 0.011$, $Y_{\mathrm{EtOH},0} = 0.975$ (Narasu et al. [76]).

condensation of water at the surface of the droplet, as seen with the negative water evaporation rates in Fig. 3.27, as was discussed before. Further, the overall process time is strongly prolonged in humid air, but the size of the final particle is hardly affected. The final temperature attained by the surface of the droplet is closer to the ambient air temperature that results in reduced heat transfer rate between the ambience and the droplet, and thus retards the process of evaporation, as seen from the almost constant normalized droplet surface area at the end of the process time in Fig. 3.26.

Figure 3.31 shows the total process times and the final particle radii for different initial droplet radii of 1 µm, 2 µm, and 5 µm for initial mass fractions of INN of 0.0125 (blue) and 0.0250 (red) at relative velocity of 4 m/s in dry air. With the increase in the initial droplet size, the overall process time is prolonged for both the initial INN mass fractions because of the prolonged droplet heating and evaporation time due to the larger mass of the liquid to be evaporated, see Fig.3.31a. However, the total process time does not vary with respect to the initial amount of INN in the precursor solution since the overall process is dominated by the evaporation of the liquid components. The size of the final particle increases with the increase in the initial droplet size and is larger for the higher initial INN mass fraction, see Fig.3.31b. The influence of humidity on the total process times and the final particle radii are presented in Fig. 3.32 for different initial droplet radii of 1 µm, 2 µm, and 5 µm at relative humidities of 0 % (blue), 5 % (red), and 10 % (green) for relative velocity of 4 m/s. With larger amount of water in the ambience, the process times are increased strongly for all the different droplet sizes, see Fig. 3.32a. In dry air, the final temperature reached by the droplet surface is lower than that attained in humid air, as was discussed before. Therefore, the final particle formed in an ambience of dry air is at a lower temperature as compared to that in humid air. As temperature decreases, the density of iron(III) nitrate also decreases [97]. Hence, the size of the final particle left behind in dry air is around 1.7 % larger than that in humid air, see Fig. 3.32b. Thus, the overall process time depends on both the initial droplet size and the relative humidity whereas the size of the final particle formed is governed by both the initial droplet radius and the initial composition of the precursor in the solution.

The particles formed via the droplet-to-particle pathway have radii roughly between 150 nm and 1,000 nm for the conditions investigated in this study. Since the target of FSP is to produce particles of much more smaller sizes from the gas phase, the droplet into gas phase approach is discussed next, where the process of droplet evaporation is coupled with thermal decomposition.

3.3.2 Droplet into Gas Phase Pathway

In this section, in order to understand the process of thermal decomposition in addition to the heating and evaporation of the precursor solution droplet, ambient air temperatures above the thermal decomposition temperature T_{th} of 403 K are chosen. Therefore, the ambient gas temperatures of 800 K and 1200 K are considered in the present study.

Figure 3.33 shows the profiles of the temporal variation of the normalized droplet surface area and the mass evaporation rate of a pure ethanol droplet, ethanol/water droplet, and INN/ethanol droplet of initial radius of 5 µm at relative velocity of 4 m/s for ambient gas temperature of 1200 K in dry air. Both the ethanol/water droplet and the INN/ethanol droplet are composed of initial ethanol mass fraction of 0.975, which corresponds to initial mass fractions of water and INN of 0.025 for ethanol/water droplet and INN/ethanol droplet, respectively. During the initial heating period, droplet expansion occurs, see Fig. 3.33a, followed by quasi-steady evaporation where the ethanol component evaporates preferentially, owing to its higher volatility as compared to that of water, after which the evaporation of the water component occurs. For pure ethanol droplet and ethanol/water droplets, complete evaporation of the droplet occurs whereas for INN/ethanol droplet, thermal decomposition occurs. Initially, the evaporation is enhanced for the pure ethanol droplet, as can be seen from the maximum peak value attained for the mass evaporation rate, see Fig. 3.33b. Due to higher volatile nature of ethanol, the peak is attained earliest for the pure ethanol

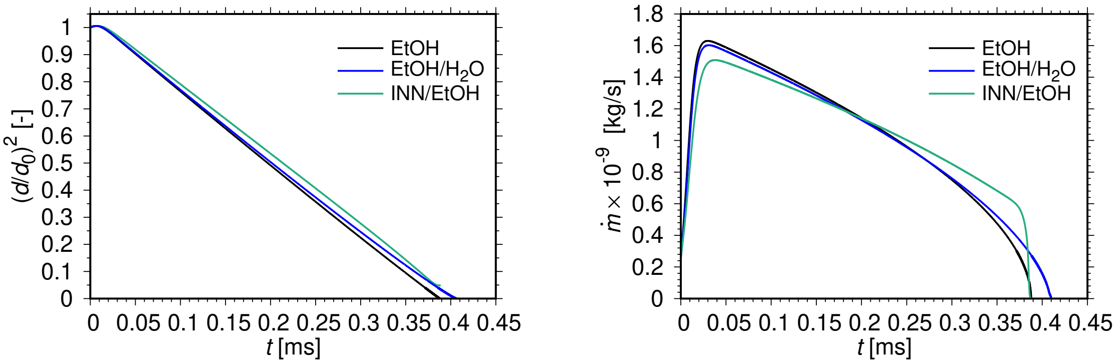

(a) Normalized droplet surface area.

(b) Mass evaporation rate.

Figure 3.33: Temporal variation of the normalized droplet surface area and mass evaporation rate. Initial conditions: $r_{\mathrm{d},0} = 5$ µm, $T_{\mathrm{l},0} = 293.15$ K, $p = 1$ bar, $u_0 = 4$ m/s, $T_{\mathrm{g},0} = 1200$ K. EtOH: $Y_{\mathrm{EtOH},0} = 1.0$. EtOH/H$_2$O: $Y_{\mathrm{EtOH},0} = 0.975$, $Y_{\mathrm{H_2O},0} = 0.025$. INN/EtOH: $Y_{\mathrm{IN},0} = 0.014$, $Y_{\mathrm{H_2O},0} = 0.011$, $Y_{\mathrm{EtOH},0} = 0.975$, RH $= 0$ % (Narasu et al. [76]).

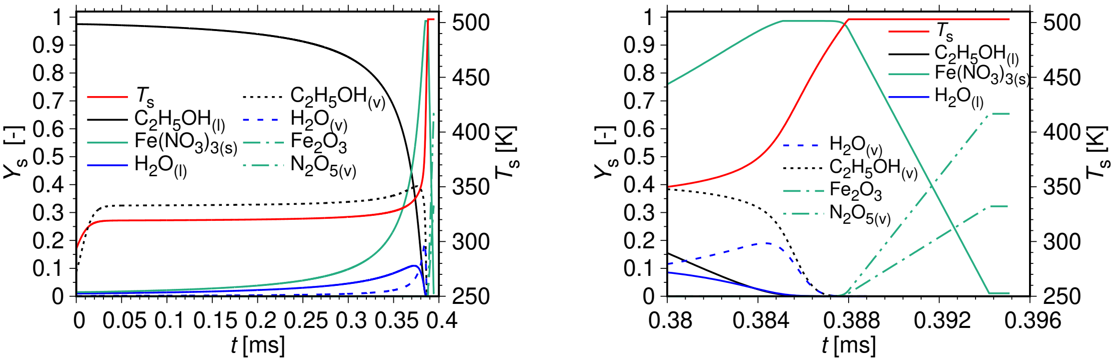

(a) Normal view.

(b) Zoomed view.

Figure 3.34: Temporal variation of the species mass fractions and temperature at the surface of the droplet. Initial conditions: $r_{\mathrm{d},0} = 5$ µm, $T_{\mathrm{l},0} = 293.15$ K, $p = 1$ bar, $u_0 = 4$ m/s, $T_{\mathrm{g},0} = 1200$ K, $Y_{\mathrm{IN},0} = 0.014$, $Y_{\mathrm{H_2O},0} = 0.011$, $Y_{\mathrm{EtOH},0} = 0.975$, RH $= 0$ % (Narasu et al. [76]).

droplet as compared to that of ethanol/water droplet and INN/ethanol droplet. In the case of INN/ethanol droplets, the overall process is faster as compared to the other two droplets due to the occurrence of thermal decomposition, which is more enhanced for the present conditions studied. Details regarding the process of thermal decomposition are discussed later.

Figure 3.34 displays the temporal evolution of the temperature and the species mass fractions at the surface of the droplet for a single INN/ethanol droplet of initial droplet radius of 5 µm at relative velocity of 4 m/s for ambient gas temperature of 1200 K and initial mass fraction of INN of 0.025 in an ambience of dry air. Initially, the droplet heats up which causes the initial increase of the droplet surface temperature (red line)

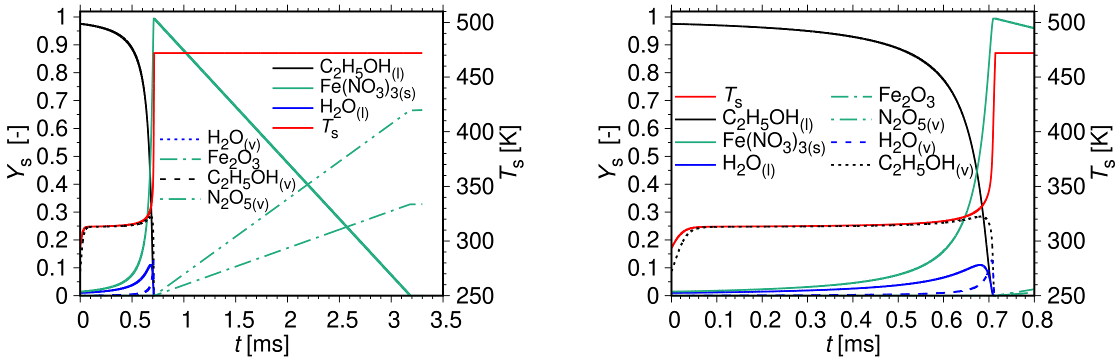

(a) Normal view.

(b) Zoomed view.

Figure 3.35: Temporal variation of the species mass fractions and temperature at the surface of the droplet. Initial conditions: $r_{\mathrm{d},0} = 5$ µm, $T_{\mathrm{l},0} = 293.15$ K, $p = 1$ bar, $u_0 = 4$ m/s, $T_{\mathrm{g},0} = 800$ K, $Y_{\mathrm{IN},0} = 0.014$, $Y_{\mathrm{H_2O},0} = 0.011$, $Y_{\mathrm{EtOH},0} = 0.975$, RH = 0 % (Narasu et al. [76]).

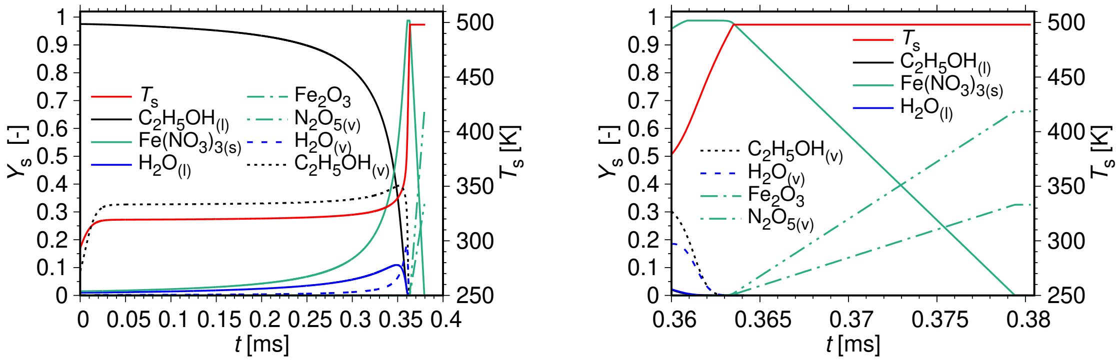

(a) Normal view.

(b) Zoomed view.

Figure 3.36: Temporal variation of the species mass fractions and temperature at the surface of the droplet. Initial conditions: $r_{\mathrm{d},0} = 5$ µm, $T_{\mathrm{l},0} = 293.15$ K, $p = 1$ bar, $u_0 = 8$ m/s, $T_{\mathrm{g},0} = 1200$ K, $Y_{\mathrm{IN},0} = 0.014$, $Y_{\mathrm{H_2O},0} = 0.011$, $Y_{\mathrm{EtOH},0} = 0.975$, RH = 0 % (Narasu et al. [76]).

and further, the higher volatile ethanol (black line) evaporates followed by evaporation of the water (blue line) component. The second increase of the droplet temperature occurs and as it reaches the thermal decomposition temperature of 403 K, the iron(III) nitrate (solid green line) starts to decompose into the gas phase. Once the ethanol and water are completely evaporated at around 0.388 ms, thermal decomposition is the only process occurring in the system, during which the temperature is constant since the final temperature attained by the droplet surface is determined by the process of droplet evaporation, see Fig. 3.34b which provides zoomed view of Fig. 3.34a. Decreasing the ambient gas temperature to 800 K, see Fig. 3.35, lowers the final droplet temperature reached by the surface of the droplet by about 30 K and the overall process is strongly prolonged due to the reduced heat transfer between the gas and the liquid phases.

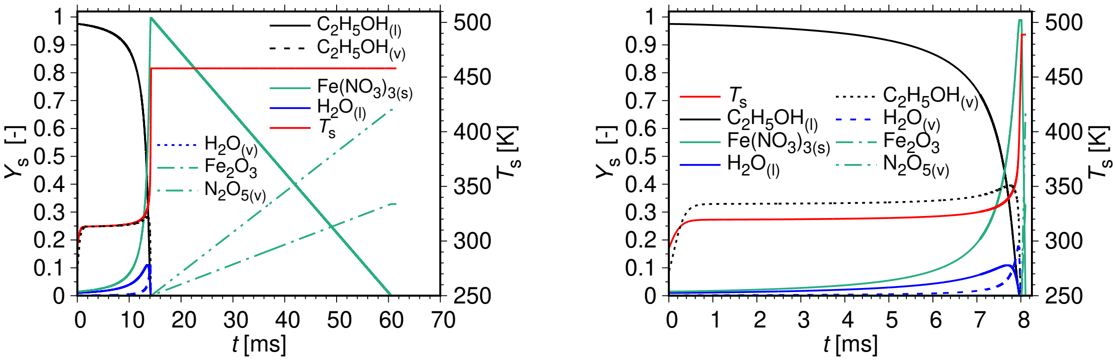

(a) $T_{g,0}$ = 800 K.

(b) $T_{g,0}$ = 1200 K.

Figure 3.37: Temporal variation of the species mass fractions and temperature at the surface of the droplet. Initial conditions: $r_{d,0} = 25$ µm, $T_{l,0} = 293.15$ K, $p = 1$ bar, $u_0 = 4$ m/s, $Y_{IN,0} = 0.014$, $Y_{H_2O,0} = 0.011$, $Y_{EtOH,0} = 0.975$, RH = 0 % (Narasu et al. [76]).

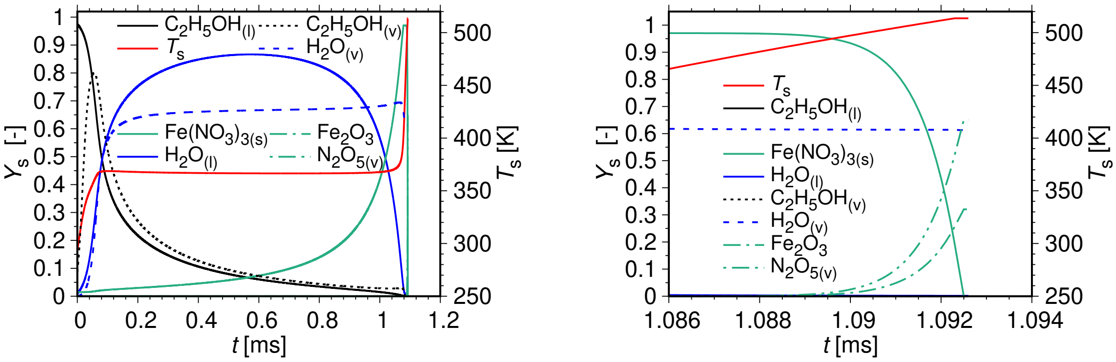

(a) Normal view.

(b) Zoomed view.

Figure 3.38: Temporal variation of the species mass fractions and temperature at the surface of the droplet. Initial conditions: $r_{d,0} = 5$ µm, $T_{l,0} = 293.15$ K, $p = 1$ bar, $u_0 = 4$ m/s, $T_{g,0} = 800$ K, $Y_{IN,0} = 0.014$, $Y_{H_2O,0} = 0.011$, $Y_{EtOH,0} = 0.975$, RH = 10 % (Narasu et al. [76]).

For ambient temperature of 1200 K, as the relative velocity is increased to 8 m/s, see Fig. 3.36, the process of evaporation is enhanced due to the stronger convection rate and the final temperature attained by the droplet surface is reduced by approximately 5 K. For larger droplet radius of 25 µm at relative velocity of 4 m/s, see Fig. 3.37, the total process times are prolonged for both ambient temperatures of 800 K and 1200 K, since the heating and evaporation times are prolonged due to the larger amount of liquid to be evaporated. Further, the final droplet surface temperatures reached during the process of evaporation is lowered considerably for both the ambient gas temperatures. For lower ambient air temperature of 800 K, see Fig. 3.37a, the overall process is dominated by the thermal decomposition with respect to the total process time whereas droplet evaporation is the dominating factor at higher ambient temperature of 1200 K,

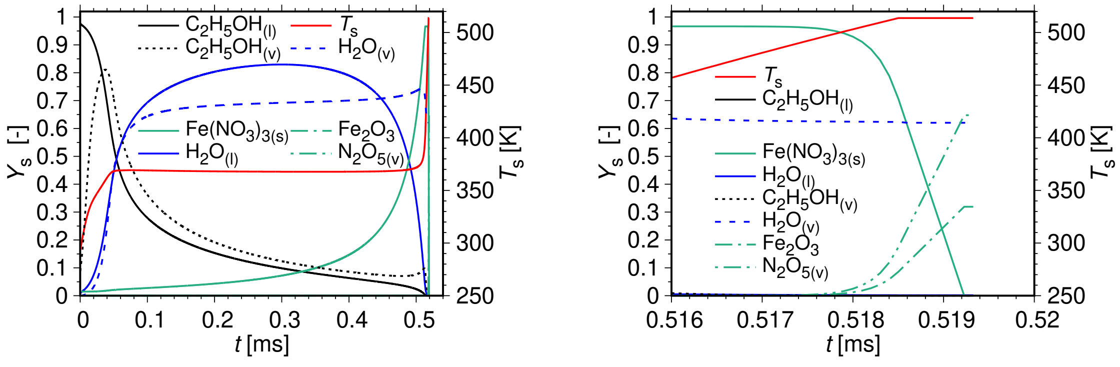

(a) Normal view. (b) Zoomed view.

Figure 3.39: Temporal variation of the species mass fractions and temperature at the surface of the droplet. Initial conditions: $r_{\mathrm{d},0} = 5$ µm, $T_{\mathrm{l},0} = 293.15$ K, $p = 1$ bar, $u_0 = 4$ m/s, $T_{\mathrm{g},0} = 1200$ K, $Y_{\mathrm{IN},0} = 0.014$, $Y_{\mathrm{H_2O},0} = 0.011$, $Y_{\mathrm{EtOH},0} = 0.975$, RH = 10 % (Narasu et al. [76]).

see Fig. 3.37b. In depth analysis regarding the interaction between the processes of droplet evaporation and thermal decomposition is provided in the upcoming sections.

Figure 3.38 presents the profiles of the species mass fractions and temperature at the droplet surface for INN/ethanol droplet of initial radius of 5 µm at relative velocity of 4 m/s at ambient gas temperature of 800 K for initial mass fraction of INN of 0.025 in an ambience with relative humidity of 10 %. In humid air, condensation of water occurs at the surface of the droplet, as was discussed in the previous section 3.3.1. Initially, the water condensation at the droplet surface leads to enhanced evaporation of the ethanol component due to the increased droplet surface temperature. This results in decrease of the ethanol mass fraction inside the droplet and also increase of the mass fraction of water. After the quasi-steady evaporation phase, the second increase of the droplet temperature occurs where the thermal decomposition temperature of 403 K is breached and eventually, causes the thermal decomposition of iron(III) nitrate transferring the precursor droplet entirely into the gas phase. In humid air, the process of evaporation is prolonged as compared to that in dry air. But, the final droplet temperature attained in an ambience of humid air is higher than that reached in dry air, which leads to faster thermal decomposition. At higher ambient temperature of 1200 K, see Fig. 3.39, the time taken for the liquid components to evaporate completely is reduced by a factor of two because of the increased heat transfer rate. Also, faster thermal decomposition takes place due to the higher final droplet surface temperature attained in humid air.

The rate of thermal decomposition, see Eq. 2.21, depends on the final temperature attained by the droplet surface as well as on the INN concentration through the term α, which is defined through Eq. 2.20. The kinetic rate coefficient varies exponentially with respect to the temperature, see Eq. 2.22. Therefore, the dependence of the rate coefficient on temperature is stronger than than that on mixing. Figure 3.40 displays the kinetic rate constant of the thermal decomposition, where the solid line represents the chemical kinetic rate coefficient versus the temperature. The symbols refer to the

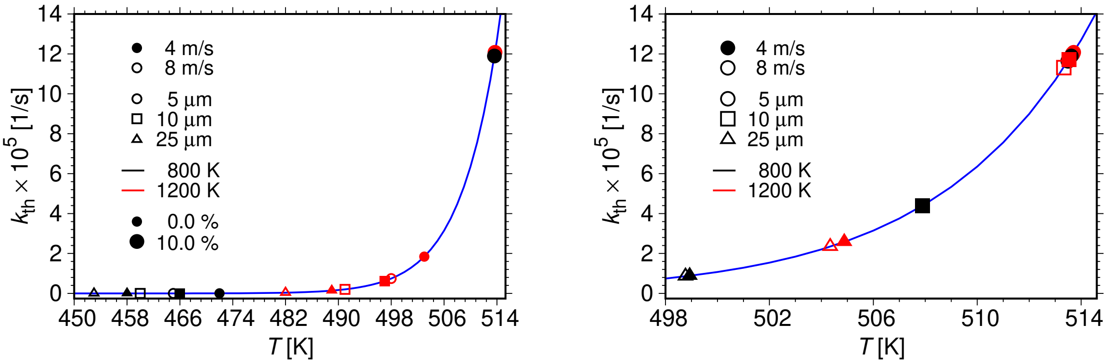

(a) Normal view.

(b) Zoomed view, RH = 10 %.

Figure 3.40: Thermal decomposition rate coefficient k_{th} with temperature and the final temperature attained by the surface of the droplet for various initial conditions (Narasu et al. [76]).

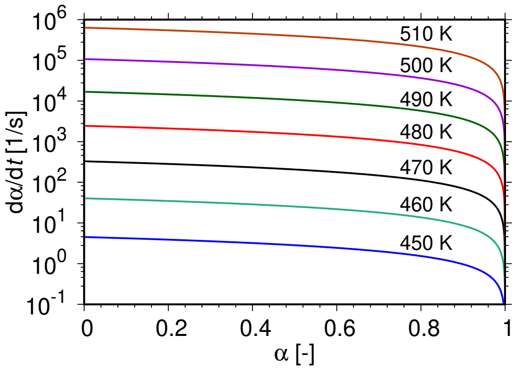

Figure 3.41: Rate of thermal decomposition versus α for various temperatures (Narasu et al. [76]).

final temperature reached at surface of the droplet for the different initial conditions investigated in this study. Figure 3.40a shows the results in dry air and Fig. 3.40b displays the results in an ambience of humid air with relative humidity of 10 %. For INN/ethanol droplets of initial radius of 5 µm at relative velocity of 4 m/s for initial mass fraction of INN of 0.025 at ambient temperatures of 800 K and 1200 K in humid air with relative humidity of 10 %, the final droplet surface temperature attained is shown in Fig. 3.40a also, for the purpose of reference. Please note that the final droplet temperatures reached in humid air are shown using larger symbols and that attained in dry air are marked using smaller symbols.

In an ambience of dry air, see Fig. 3.40a, at higher relative velocity of 8 m/s (open symbols), the droplet evaporation is enhanced because of the stronger convection rate which results in lower final droplet surface temperature and thus, the corresponding reaction rate coefficient is smaller as compared to that at 4 m/s (filled symbols). For larger initial droplet sizes, the droplet heating and evaporation is prolonged which results in lower final droplet temperature and therefore, smaller reaction rate coefficient. At lower ambient gas temperature of 800 K (black color), the heat transfer rate is reduced which results in the droplet reaching lower final temperature and hence, the corresponding rate coefficient values are also smaller as compared to ambient temperature of 1200 K (red color). In humid air with relative humidity of 10 %, seeFig. 3.40b, the final droplet temperatures and the reaction rate coefficients are larger, especially for the smaller droplets. For the same initial droplet radii, variation of the other parameters has very small effect on the final droplet surface temperature

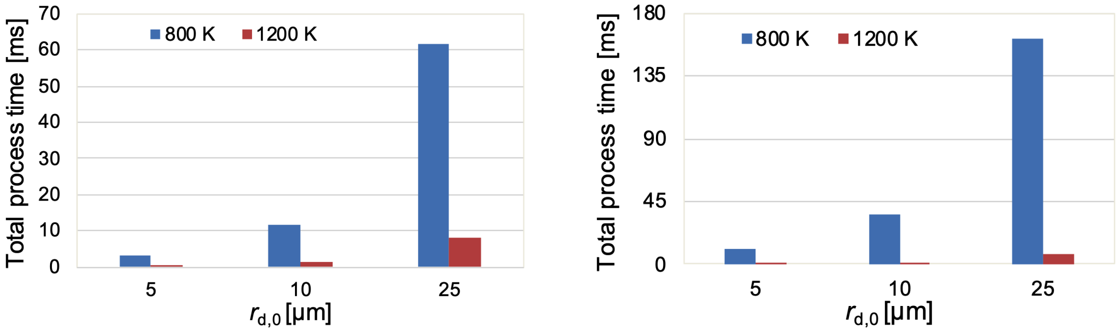

(a) $u_0 = 4$ m/s.

(b) $u_0 = 8$ m/s.

Figure 3.42: Histograms showing the total process time for different initial droplet radii and ambient air temperatures of 800 K and 1200 K in dry air. Initial conditions: $T_{l,0} = 293.15$ K, $p = 1$ bar, $Y_{IN,0} = 0.014$, $Y_{H_2O,0} = 0.011$, $Y_{EtOH,0} = 0.975$, RH = 0 % (Narasu et al. [76]).

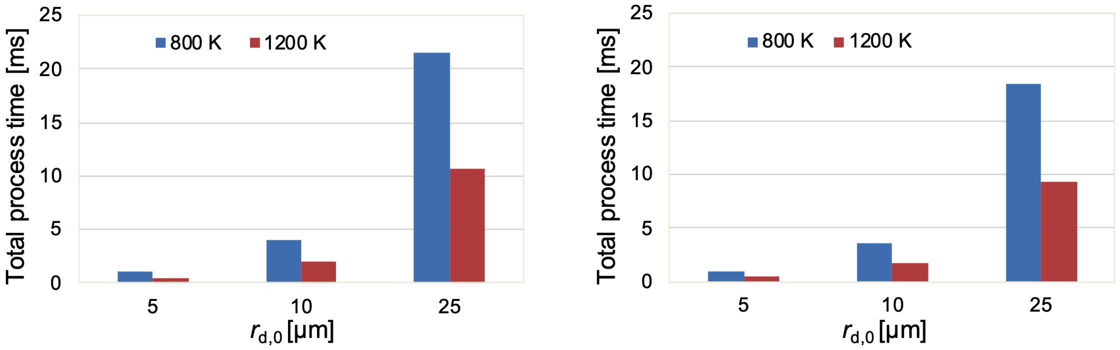

(a) $u_0 = 4$ m/s.

(b) $u_0 = 8$ m/s.

Figure 3.43: Histograms showing the total process time for different initial droplet radii and and ambient air temperatures of 800 K and 1200 K in humid air. Initial conditions: $T_{l,0} = 293.15$ K, $p = 1$ bar, $Y_{IN,0} = 0.014$, $Y_{H_2O,0} = 0.011$, $Y_{EtOH,0} = 0.975$, RH = 10 % (Narasu et al. [76]).

and the corresponding rate coefficient, as can be seen from the overlap between the symbols.

Figure 3.41 presents the variation of the rate of thermal decomposition with α, which ranges from zero to unity over the course of thermal decomposition during which the droplet surface temperature increases so that the dependence of the thermal decomposition rate on the mixing is the strongest during the initial period of the thermal decomposition. The dependence of the rate of thermal decomposition on the final droplet surface temperature and mixing strongly influence the process times, which is analyzed next.

Figure 3.42a displays the variation of the total process time for different initial droplet radii of 5 μm, 10 μm, and 25 μm for ambient gas temperatures of 800 K (blue) and 1200 K (red) at relative velocity of 4 m/s in dry air. As the initial droplet radius is increased, the total process time is prolonged for both ambient temperatures due

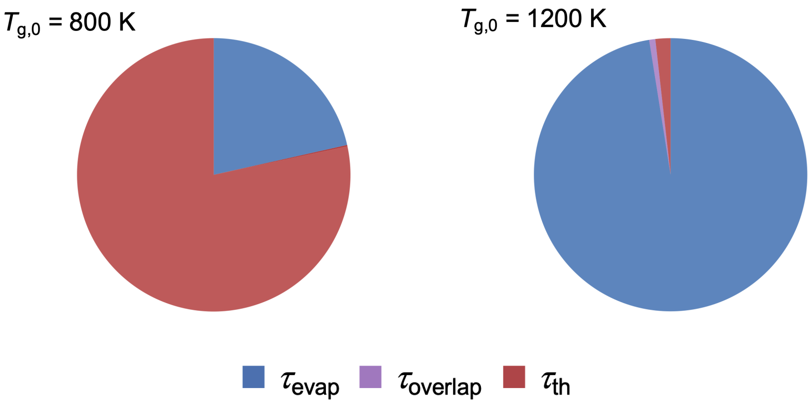

Figure 3.44: Pie charts showing the contributions to the total process time in dry air. Initial conditions: $r_{d,0} = 5$ µm, $T_{l,0} = 293.15$ K, $p = 1$ bar, $u_0 = 4$ m/s, $Y_{IN,0} = 0.014$, $Y_{H_2O,0} = 0.011$, $Y_{EtOH,0} = 0.975$, RH = 0 % (Narasu et al. [76]).

to the prolonged droplet heating and evaporation time for larger droplets and also because of the lower final droplet surface temperatures attained, see Fig. 3.40a, which slows down the process of thermal decomposition. At lower ambient air temperature of 800 K, the overall process is prolonged for all the different droplet sizes because of the reduced heat transfer rate and the lower final droplet temperatures. Doubling the relative velocity to 8 m/s, see Fig. 3.42b, enhances the droplet evaporation [73, 49, 72] but strongly increases the total process time owing to the slower thermal decomposition rate because of the lower temperatures reached by the droplet surface. Figure 3.43 shows the total process times for the conditions of Fig. 3.42 in humid air with relative humidity of 10 %. In an ambience of humid air, the process of evaporation is slowed down due to the condensation of water at the surface of the droplet, which also results in higher final droplet surface temperatures, see Fig. 3.40b, that fastens the thermal decomposition process and thus, reduces the overall process time in comparison with that of dry air.

Figure 3.44 presents the pie chart showing the contribution of the evaporation time, τ_{evap} (blue), the thermal decomposition time, τ_{th} (red), and the overlap time, $\tau_{overlap}$ (purple). The evaporation time denotes the time taken for the complete evaporation of the liquid components, the thermal decomposition time represents the time period during which the iron(III) nitrate decomposes into the gas phase, and the overlap time is the time during which both the processes of evaporation and thermal decomposition occur simultaneously. The results are shown for INN/ethanol droplet of initial radius of 5 µm at relative velocity of 4 m/s for initial mass fraction of INN of 0.025 for both ambient gas temperatures of 800 K and 1200 K in dry air. At ambient temperature of 800 K, the thermal decomposition dominates the overall process due to the lower final droplet temperatures reached by the surface of the droplet, see Fig. 3.40a, which prolongs the process of thermal decomposition. For higher ambient temperature of 1200 K, the droplet evaporation is the dominating factor because of the higher final droplet surface temperatures. Increasing the relative velocity to 8 m/s, see Fig. 3.45, the thermal decomposition becomes much more influential as compared to at

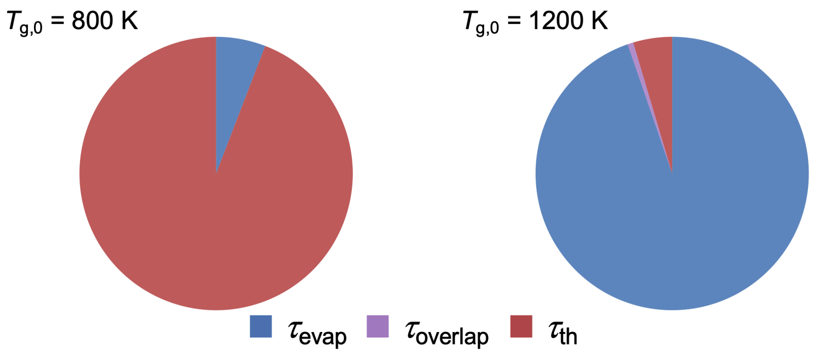

Figure 3.45: Pie charts showing the contributions to the total process time in dry air. Initial conditions: $r_{d,0} = 5$ µm, $T_{l,0} = 293.15$ K, $p = 1$ bar, $u_0 = 8$ m/s, $Y_{IN,0} = 0.014$, $Y_{H_2O,0} = 0.011$, $Y_{EtOH,0} = 0.975$, RH = 0 % (Narasu et al. [76]).

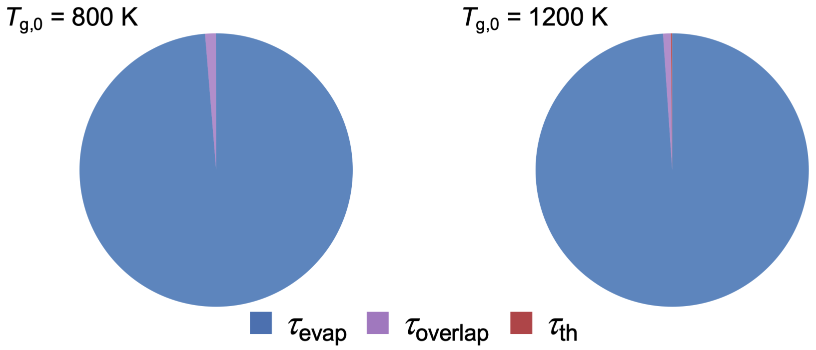

Figure 3.46: Pie charts showing the contributions to the total process time in humid air. Initial conditions: $r_{d,0} = 5$ µm, $T_{l,0} = 293.15$ K, $p = 1$ bar, $u_0 = 4$ m/s, $Y_{IN,0} = 0.014$, $Y_{H_2O,0} = 0.011$, $Y_{EtOH,0} = 0.975$, RH = 10 % (Narasu et al. [76]).

4 m/s, since much more lower final temperatures are attained by the droplet surface, which slows down the thermal decomposition process further. Therefore, at ambient air temperature of 800 K, the thermal decomposition becomes more dominant and at 1200 K, droplet evaporation still remains as the domination factor albeit with lesser influence. In an ambience of humid air with relative humidity of 10 % at relative velocity of 4 m/s, see Fig. 3.46, droplet evaporation dominates the total process at both ambient temperatures of 800 K and 1200 K, due to the water condensation at the droplet surface which retards the evaporation process, and also because of the higher final droplet surface temperatures, see Fig. 3.40b, which fastens the process of thermal decomposition. Also, the droplet evaporation and thermal decomposition overlap with each other and the thermal decomposition time is very short as compared to that in dry air. Please note that although the results shown in Figs. 3.44 - 3.46, are for INN/ethanol droplet of initial radius of 5 µm, these are also valid for the other droplet sizes considered in this study even though there are differences with respect to the absolute values, as displayed in Figs. 3.42 - 3.43.

The processes of heating, evaporation, and thermal decomposition that a precursor solution droplet of INN/ethanol undergo are strongly connected with each other and depend on the final temperature reached by the surface of the droplet. The relative humidity in the ambience has a strong impact on all these processes. Condensation of water at the surface of the droplet enhances the evaporation of ethanol, but retards the overall evaporation process, and high droplet surface temperatures are attained which fastens the thermal decomposition process owing to the exponential dependence of thermal decomposition rate coefficient with respect to temperature.

The influence of different parameters on the characteristics of heating, evaporation, and thermal decomposition were presented in this section, except for the impact of varying the initial loading of the precursor, which is focused upon in the next section.

Influence of initial precursor loading

In this section, for a precursor solution droplet, the impact of varying the initial precursor loading on the characteristics of the droplet into gas phase pathway is explored. For that purpose, in addition to the mass fraction of INN of 0.025 studied before, the initial INN mass fractions of 0.0125 and 0.20 are also taken into consideration in the present study, following the experimental study of Schneider et al. [29].

Figure 3.47 presents the evolution of the profiles of the normalized droplet surface area, the mass evaporation rates of both the liquid components, and the temperature at the surface of the droplet with time for a single INN/ethanol droplet of initial radius of 5 µm of initial INN mass fraction of 0.200 at relative velocities of 4 m/s (dark color) and 8 m/s (light color) for ambient gas temperatures of 800 K (solid lines) and 1200 K (dashed lines) in dry air. During the initial heating period, the precursor solution droplet expands initially, as seen in the normalized droplet surface area profile of Fig. 3.47a, due to the variable physical properties employed in the model. During this time period, the droplet surface temperature (red line) increases, see Fig. 3.47b, after which the quasi-steady evaporation occurs during which the temperature remains more or less constant. Also, the higher volatile ethanol evaporates preferentially which is

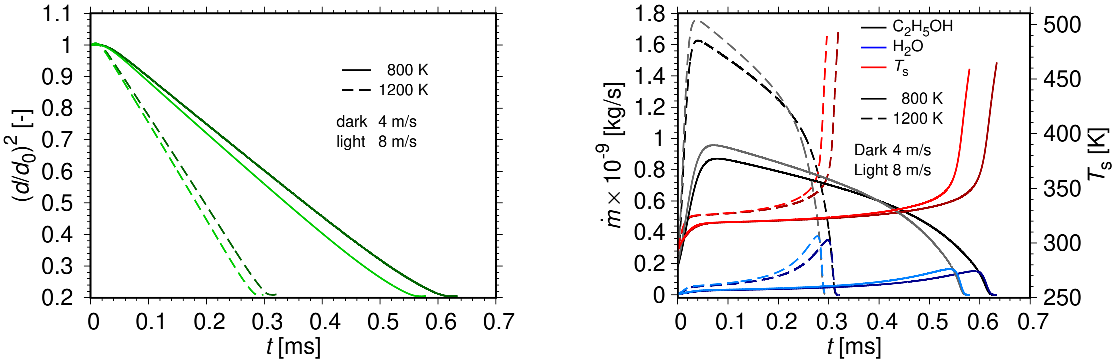

(a) Normalized droplet surface area.

(b) Mass evaporation rates and T_s.

Figure 3.47: Temporal variation of the normalized droplet surface area, mass evaporation rates, and droplet surface temperature, T_s. Initial conditions: $r_{d,0} = 5$ µm, $T_{l,0} = 293.15$ K, $p = 1$ bar, $u_0 = 4$ m/s and 8 m/s, $T_{g,0} = 800$ K and 1200 K, $Y_{IN,0} = 0.12$, $Y_{H_2O,0} = 0.08$, $Y_{EtOH,0} = 0.80$, RH = 0 % (Narasu and Gutheil [123]).

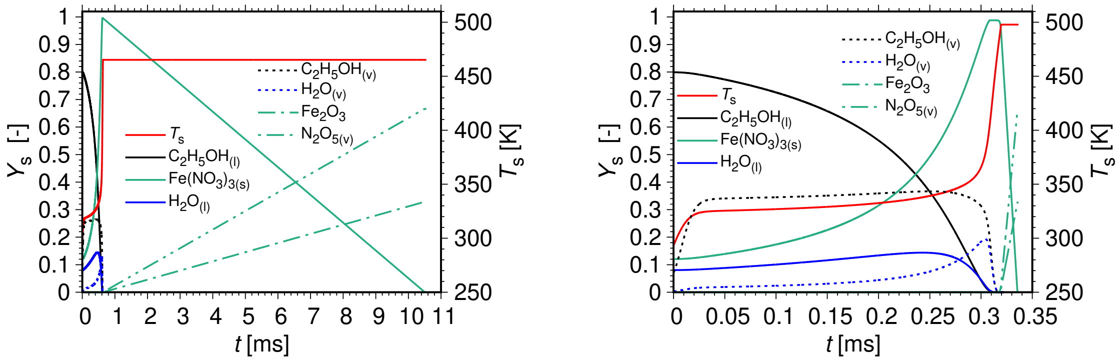

(a) $T_{g,0} = 800$ K.

(b) $T_{g,0} = 1200$ K.

Figure 3.48: Temporal variation of the species mass fractions and temperature at the surface of the droplet. Initial conditions: $r_{d,0} = 5$ µm, $T_{l,0} = 293.15$ K, $p = 1$ bar, $u_0 = 4$ m/s, $T_{g,0} = 800$ K and 1200 K, $Y_{IN,0} = 0.12$, $Y_{H_2O,0} = 0.08$, $Y_{EtOH,0} = 0.80$, RH = 0 % (Narasu and Gutheil [123]).

evident from the peak attained by the mass evaporation rate of the ethanol component followed by water evaporation. Further, a second increase of the droplet temperature occurs which enhances the evaporation of the water component, and as the temperature reaches the thermal decomposition temperature of 403 K, the decomposition of iron(III) nitrate is initiated. For higher relative velocity of 8 m/s, the process of evaporation is enhanced because of the stronger convection rate, and the final temperature reached by the surface of the droplet is lower by around 10 K as compared to at lower relative velocity of 4 m/s. Also, for higher ambient temperature of 1200 K, the evaporation of the liquid components are faster and the final droplet surface temperatures attained are increased by about 30 K when compared with that of the lower ambient temperature of 800 K. These differences in the final droplet temperatures strongly influence the thermal decomposition process, which is discussed later.

The temporal variation of the species mass fractions and the droplet surface temperature are displayed in Fig. 3.48, for a droplet consisting of the precursor/solvent system of INN/ethanol of initial droplet radius of 5 µm at relative velocity of 4 m/s for higher initial mass fraction of INN of 0.200 at ambient gas temperatures of 800 K and 1200 K. During the initial unsteady heating period, the droplet surface temperature increases, followed by the quasi-steady evaporation phase where the ethanol content decreases, due to the preferential evaporation of the ethanol component owing to its higher volatility, that contributes to the increase of the mass fraction of water. The ethanol and water are completely evaporated after the second major increase of the droplet temperature. Also, the iron(III) nitrate starts to decompose into the gas phase as soon as the droplet temperature reaches the thermal decomposition temperature. As the liquid components are completely evaporated, thermal decomposition is the only process that occurs and continues until the complete transfer of the precursor droplet into the gas phase. For lower ambient air temperature of 800 K, see Fig. 3.48a, the overall process is prolonged since the heat transfer rate between the ambience and the droplet is reduced as compared to that for ambient temperature of 1200 K, see

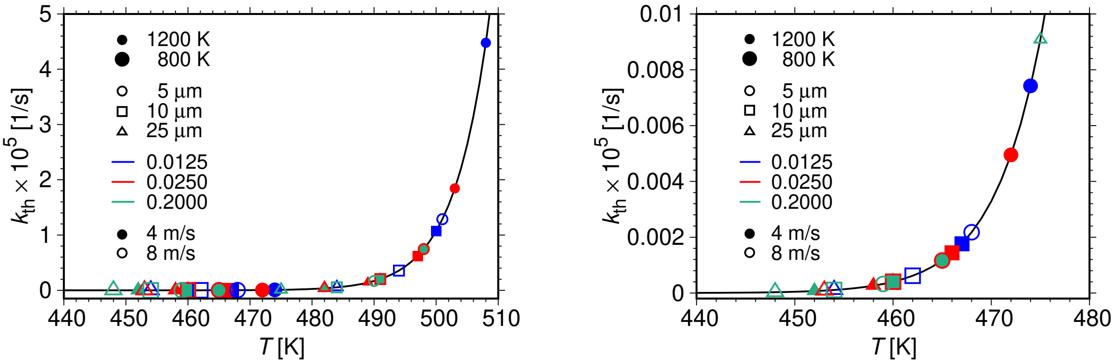

(a) Normal view.

(b) Zoomed view.

Figure 3.49: Thermal decomposition rate coefficient k_{th} with temperature and the final temperature attained by the surface of the droplet for various initial conditions (Narasu and Gutheil [123]).

Fig. 3.48b. Further, the thermal decomposition is the dominating factor with respect to the total process time at ambient temperature of 800 K whereas the process of droplet evaporation is more influential at high-temperature ambience of 1200 K, which is the reason for the difference in the overall process time of approximately 10.5 ms.

The dependence of the kinetic rate coefficient on the temperature is presented in Fig. 3.49 along with the final temperature attained by the surface of the droplet for various initial conditions explored in the present study. The solid line represents the kinetic rate coefficient whereas the symbols denote the final droplet temperature. For higher ambient temperature of 1200 K, large symbols are used and the condition of the low-temperature ambience of 800 K is represented by small symbols. Also, for better resolution of the lower temperature condition, Fig. 3.49b provides with a zoomed view of Fig. 3.49a. At higher ambient temperature of 1200 K, the final droplet surface temperature reached is higher owing to the increased heat transfer rate, and thus the corresponding rate coefficients are also higher which leads to faster thermal decomposition as compared to that at lower ambient temperature of 800 K. For larger sized droplets, the prolonged droplet heating and evaporation time leads to lower final droplet temperatures that slows down the thermal decomposition process. Increasing the relative velocity from 4 m/s (filled symbols) to 8 m/s (open symbols) results in faster evaporation of the droplet due to enhanced convection rate, which reduces the droplet temperature and therefore, prolongs thermal decomposition. With the increase of the initial mass fraction of INN to 0.200 (green color), the precursor solution droplet evaporates faster and thus, results in the droplet surface attaining temperatures smaller than those for the smaller initial INN mass fractions of 0.0125 (blue) and 0.025 (red), eventually causing prolonged thermal decomposition. Hence, the final temperature reached by the surface of the droplet during the process of evaporation and the corresponding kinetic rate coefficient influences the total time taken for the completion of the entire process, which is analyzed in detail next.

Figure 3.50 displays the total process times for different initial droplet radii of 5 µm, 10 µm, and 25 µm for the initial INN mass fractions of 0.0125, 0.025, and

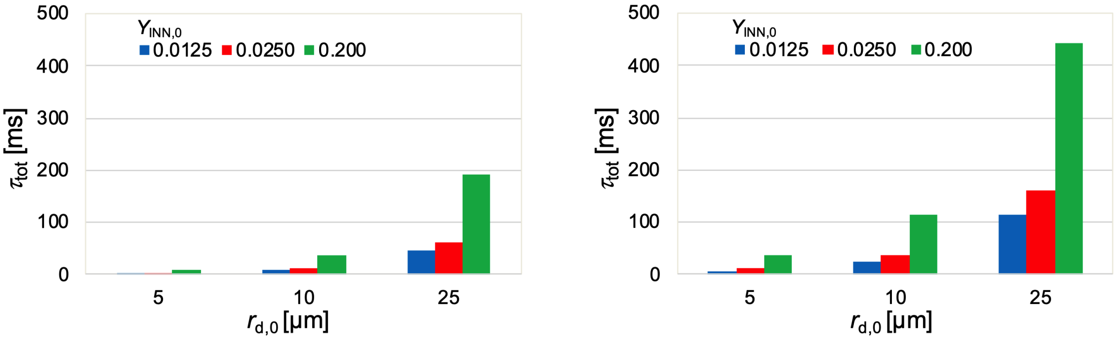

(a) $u_0 = 4$ m/s. (b) $u_0 = 8$ m/s.

Figure 3.50: Histograms showing the total process time for different initial droplet radii and initial INN mass fractions of 0.0125, 0.025, and 0.200. Initial conditions: $T_{l,0} = 293.15$ K, $p = 1$ bar, $T_{g,0} = 800$ K, RH = 0 % (Narasu and Gutheil [123]).

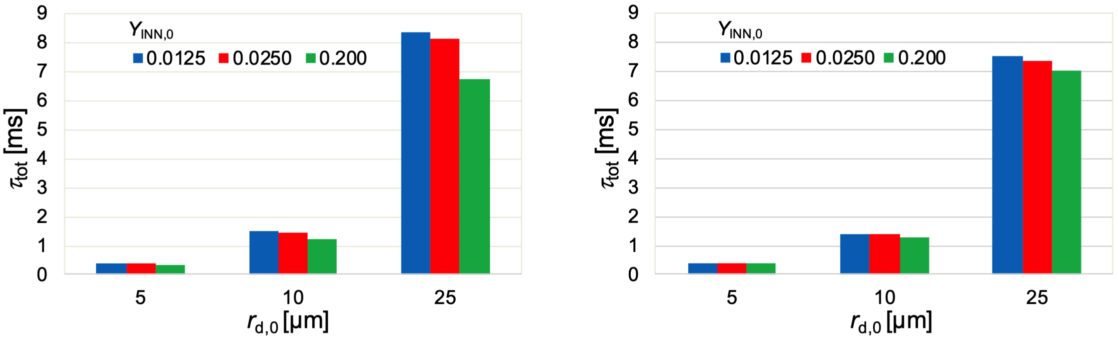

(a) $u_0 = 4$ m/s. (b) $u_0 = 8$ m/s.

Figure 3.51: Histograms showing the total process time for different initial droplet radii and initial INN mass fractions of 0.0125, 0.025, and 0.200. Initial conditions: $T_{l,0} = 293.15$ K, $p = 1$ bar, $T_{g,0} = 1200$ K, RH = 0 % (Narasu and Gutheil [123]).

0.200 at relative velocities of 4 m/s and 8 m/s for ambient temperature of 800 K. The overall process times are prolonged with the increase in the initial droplet size, due to the prolonged droplet heating and evaporation time and the lower final temperatures reached by the surface of the droplet, see Fig. 3.49, that prolongs the process of thermal decomposition. For higher ambient gas temperature of 1200 K, see Fig. 3.51, the overall process times are much shorter than at lower ambient air temperature of 800 K, due to the enhanced evaporation and the higher final temperatures that fastens the thermal decomposition process. At lower ambient temperature of 800 K, for the higher relative velocity of 8 m/s, see Fig. 3.50b, the droplets evaporate faster but the total process times are longer compared to lower velocity of 4 m/s, see Fig. 3.50a, because of the prolonged thermal decomposition owing to the lower final droplet surface temperatures. But, for higher ambient air temperature of 1200 K, the total process times become shorter at higher relative velocity for initial INN mas fractions of 0.0125 (blue color) and 0.025 (red color), see Fig. 3.51b. The reason for this behavior is that at higher ambient gas temperature of 1200 K, droplet evaporation is the dominating factor whereas

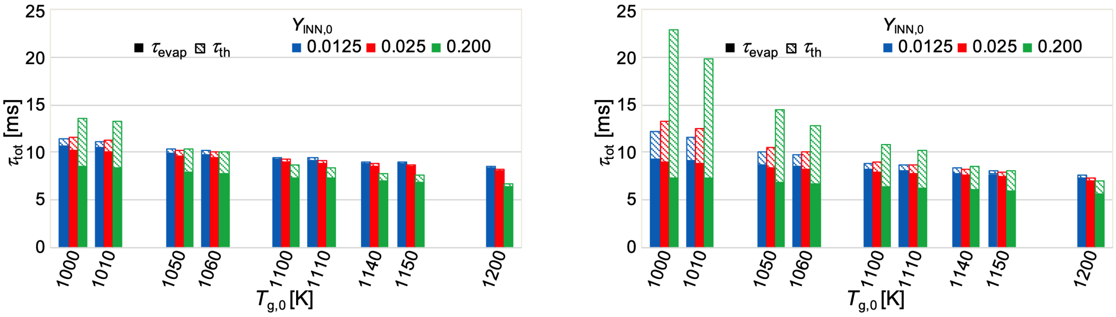

(a) $u_0 = 4$ m/s. (b) $u_0 = 8$ m/s.

Figure 3.52: Histograms showing contributions to the total process times for different initial INN mass fractions of 0.0125, 0.025, and 0.200 at various ambient gas temperatures. Initial conditions: $r_{\mathrm{d},0} = 25$ µm, $T_{\mathrm{l},0} = 293.15$ K, $p = 1$ bar, RH $= 0$ % (Narasu and Gutheil [123]).

thermal decomposition dominates the overall process at low-temperature ambience of 800 K, as was discussed before. For the highest initial INN mass fraction of 0.200 (green color), since lower final temperatures are reached by the surface of the droplet, the process of thermal decomposition is prolonged, that results in small increase of the total process time. At lower ambient temperature of 800 K, as the initial precursor mass fraction is increased from 0.0125 to 0.025 and 0.200, the process times are prolonged due to the faster evaporation that results in reduced final temperatures and thus, prolonged thermal decomposition. However, at higher ambient temperature of 1200 K, increasing the initial precursor loading results in shorter total process time. This shows that there must exist an intermediate temperature, T^+, at which this effect is reversed. The total process time with respect to the heating, evaporation, and thermal decomposition of the precursor solution droplet contributes to the overall process time of the synthesis of nanoparticles via flame spray pyrolysis. Therefore, evaluating T^+ would be beneficial in choosing the conditions for flame spray pyrolysis, which is discussed next.

Figure 3.52 displays the evaporation times, τ_{evap} (filled region), thermal decomposition times, τ_{th} (shaded region), and the total process times, τ_{tot}, for different ambient gas temperatures ranging from 1000 K to 1200 K, for INN/ethanol droplet of initial radius of 25 µm at relative velocities of 4 m/s and 8 m/s for initial mass fractions of INN of 0.0125 (blue color), 0.025(red color), and 0.200 (green color). At lower relative velocity of 4 m/s, see Fig. 3.52a, the overall process time for initial mass fraction of INN of 0.200 is longer than that for initial INN mass fraction of 0.025 at ambient temperature of 1000 K. As the ambient air temperature is increased, this difference in the total process time between the initial mass fractions of 0.200 and 0.025 decreases due to the disparities in the evaporation and thermal decomposition times, as discussed before. This behavior is reversed at around T^+ of 1060 K as the total process time of the larger initial INN mass fraction becomes shorter than that of the smaller initial mass fraction of INN. For initial mass fractions of INN of 0.0125 and 0.200, the value of T^+ is approximately 1050 K and for INN mass fractions of 0.0125 and 0.025, T^+ is about 1010 K. The final temperature reached by the surface of the droplet during

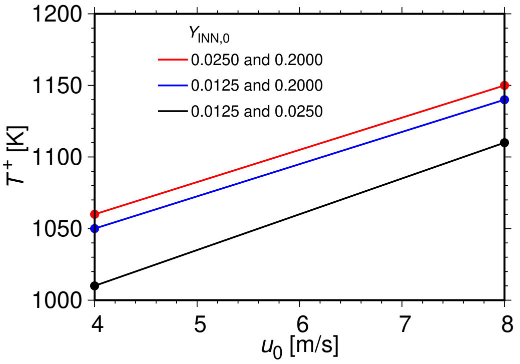

Figure 3.53: T^+ plotted against relative velocity for different initial INN mass fractions. Initial conditions: $T_{l,0} = 293.15$ K, $p = 1$ bar, RH = 0 % (Narasu and Gutheil [124]).

the process of evaporation and the corresponding kinetic rate coefficient, see Fig. 3.49, are the reasons responsible for such a behavior. At higher ambient gas temperature of 1200 K, the droplet evaporation is shortened due to the increased heat transfer between the ambience and the droplet, that leads to higher droplet surface temperatures and therefore, reduces the thermal decomposition time. Also, as the initial precursor loading is increased, the droplet evaporates faster resulting in lower droplet temperatures and thus, causes prolonged thermal decomposition. Further, at higher relative velocity of 8 m/s, see Fig. 3.52b, the stronger convection results in shorter droplet evaporation times, and the lower final droplet surface temperatures lead to more prolonged thermal decomposition. Hence, T^+ at relative velocity of 8 m/s is higher than that at 4 m/s, for the various precursor mass fractions investigated in this study.

Figure 3.53 presents the T^+ values for the various initial precursor mass fractions considered in this study at relative velocities of 4 m/s and 8 m/s. Increasing the initial precursor loading leads to higher values of T^+ for both relative velocities, because of the faster evaporation process that results in the droplet surface attaining lower final temperatures as well as smaller rate coefficient values, thus slowing down the process of thermal decomposition more than that for the smaller mass fraction of the precursor. Also, at relative velocity of 8 m/s, the T^+ values are higher by about 100 K as compared to that at lower relative velocity of 4 m/s. It is to be noted that the even though T^+ changes with respect to the variation of the initial precursor loading as well as the relative velocity between the droplet and the ambience, it is independent of the choice of the initial droplet size considered in this study. Further, an ambient temperature higher than T^+ is recommended to be selected so as to keep the overall process times short.

The droplet heating, evaporation, and thermal decomposition characteristics of the precursor/solvent droplet are parameterized using polynomial fits for use in more complex simulations of flame spray pyrolysis, which is presented in the next section.

3.3.3 Parameterization of the Numerical Results

There exists some similarity regarding the numerical results of the heating, evaporation, and thermal decomposition of a precursor solution droplet, presented in the previous sections, which could be utilized for the purpose of parameterization, with the objective of including these results in simulations related to sprays. The details of the procedure are presented and discussed next.

The results discussed in the previous sections show that the profiles of the mass evaporation rates for ethanol and water, the droplet surface temperature, the normalized droplet surface area, and the mass fraction of iron(III) nitrate show some similarity, which motivates a parameterization of these variables for use in more complex simulations of sprays. Therefore, the time is normalized by the droplet evaporation time, t_{evap}, and the thermal decomposition time, t_{th}, the surface temperature T_{s} of the droplet is normalized by the boiling temperature of the lower volatile component water, $T_{\text{H}_2\text{O,b}}$, and the mass evaporation rates $\dot{m}_i$ of the two components i are normalized by the initial droplet mass, m_0 divided by the droplet evaporation time. Thus, for the purpose of parameterization, the non-dimensionalized quantities read as

$$\tau_{\text{evap}} = \frac{t}{t_{\text{evap}}} \tag{3.1}$$

$$\mathcal{T}_{\text{s}} = \frac{T_{\text{s}}}{T_{\text{H}_2\text{O,b}}} \tag{3.2}$$

$$\dot{\mathcal{M}}_i = \frac{\dot{m}_i}{m_0/t_{\text{evap}}}, \quad i = 1, 2 \tag{3.3}$$

$$\tau_{\text{th}} = \frac{t}{t_{\text{th}}} \tag{3.4}$$

where t_{evap} is the droplet evaporation time, t_{th} stands for the thermal decomposition time, $T_{\text{H}_2\text{O,b}}$, represents the boiling temperature of the lower volatile component water, and m_0 denotes the initial droplet mass calculated as $m_0 = 4/3\pi r_{\text{d},0}^3\,\rho_0$, where the density of the droplet is evaluated as $\rho_0 = Y_{\text{INN},0}\,\rho_{0,\text{INN}} + (1 - Y_{\text{INN},0})\,\rho_{0,\text{C}_2\text{H}_5\text{OH}}$. Please note that the initial densities $\rho_{0,i}$ are computed at the initial droplet temperature [97]. Also, τ_{evap} represents the dimensionless evaporation time, τ_{th} denotes the non-dimensionalized thermal decomposition time, $\mathcal{T}_{\text{s}}$ stands for the dimensionless droplet surface temperature, and $\dot{\mathcal{M}}_i, i = 1, 2$ represents the normalized mass evaporation rates of the ethanol and the water components. Further, parameterization of the normalized droplet surface area and the iron(III) nitrate mass fraction, which are non-dimensional as per definition, are also performed.

For Eqs. (3.1)-(3.4), the reference values are known a priori, except for the droplet evaporation time and the thermal decomposition time. Relative velocity is the only parameter that is related to time and known a priori. But, there exists no distinct relation between the relative velocity and the characteristics of evaporation and thermal decomposition that were discussed in the previous section. Another option is employing the ratio of the square of the initial droplet radius and the mass diffusion coefficient, which also does not show any evident dependence of the characteristics. Therefore, the droplet evaporation time and thermal decomposition time are selected and are also tabulated for the respective conditions considered in the study, which will be discussed later in this section.

Analyzing the normalized results with respect to the evaporation characteristics, the significant impact is exercised through the initial mass fraction of the precursor and the ambient air temperature. The similarity is shown with regard to the different initial droplet sizes and the relative velocities which are represented via the non-dimensional

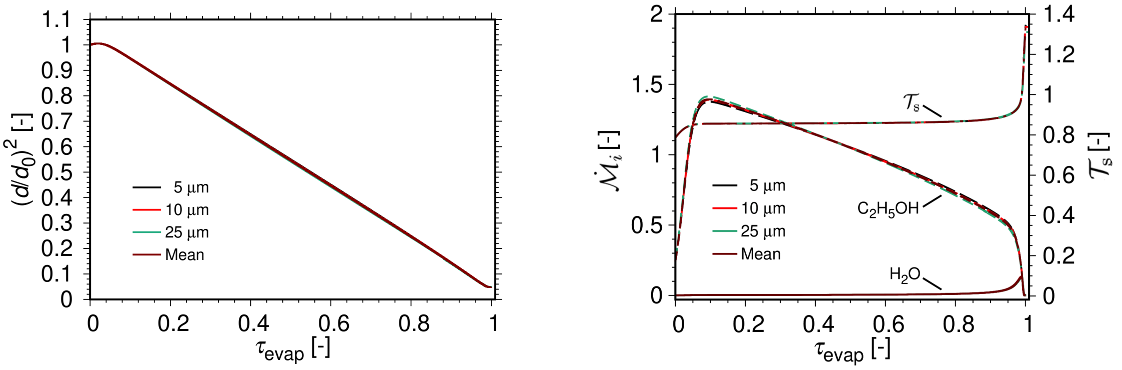

(a) Normalized droplet surface area. (b) Mass evaporation rates and $\mathcal{T}_s$.

Figure 3.54: Normalized profiles of the droplet surface area, mass evaporation rates, and droplet surface temperature with normalized droplet evaporation time τ_{evap} for different initial droplet sizes. Initial conditions: $T_{l,0} = 293.15$ K, $p = 1$ bar, $u_0 = 4$ m/s and 8 m/s, $T_{g,0} = 1200$ K, $Y_{IN,0} = 0.014$, $Y_{H_2O,0} = 0.011$, $Y_{EtOH,0} = 0.975$, RH = 0 % (Narasu and Gutheil [123]).

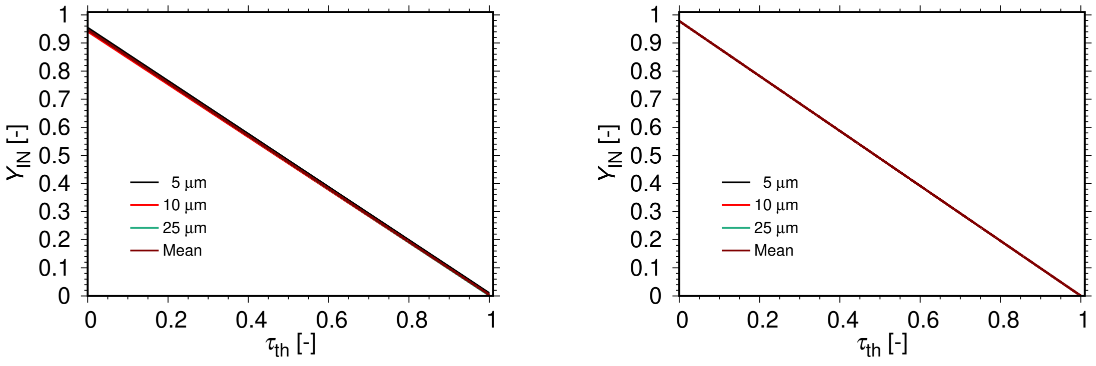

(a) $u_0 = 4$ m/s. (b) $u_0 = 8$ m/s.

Figure 3.55: Profiles of the mass fraction of iron(III) nitrate with normalized thermal decomposition time τ_{th} for different initial droplet sizes. Initial conditions: $T_{l,0} = 293.15$ K, $p = 1$ bar, $T_{g,0} = 1200$ K, $Y_{IN,0} = 0.014$, $Y_{H_2O,0} = 0.011$, $Y_{EtOH,0} = 0.975$, RH = 0 % (Narasu and Gutheil [123]).

parameters, that include the initial droplet mass and the droplet evaporation times. Figure 3.54a shows the profiles of the normalized droplet surface for initial droplet radii from 5 µm to 25 µm and relative velocities of 4 m/s and 8 m/s, at ambient gas temperature of 1200 K, for the initial mass fraction of INN of 0.025. For the same conditions, Fig. 3.54b displays normalized profiles of the droplet surface temperatures and the mass evaporation rates of ethanol and water. For the various initial droplet radii considered in this study, the arithmetic mean of the normalized profiles is calculated and presented in Fig. 3.54. For every numerical simulation, the total number of times steps vary. Hence, for the purpose of evaluating the mean profile, the total number of time steps was adjusted to ten thousand. For the droplet into gas phase pathway, the thermal decomposition of iron(III) nitrate occurs. With respect to the thermal decomposition characteristics, the normalized results exhibited significant influence via the the initial precursor mass fraction, the relative velocity, and the ambient temperature. The similarity is demonstrated only for the various initial droplet radii investigated in this study through the non-dimensionalized thermal decomposition times, see Fig. 3.55. Figure 3.55a presents the mass fraction of iron(III) nitrate for initial droplet radii from 5 µm to 25 µm for the initial mass fraction of INN of 0.025 at relative velocity of 4 m/s for the ambient air temperature of 1200 K. For the same conditions, Fig. 3.55b displays profiles of the iron(III) nitrate mass fractions at relative velocity of 8 m/s. In order to parametrize the numerical results, a polynomial fit is employed for the averaged values, which is discussed next.

The mean evaporation characteristics are parametrized using polynomial fits, since this approach works remarkably well to represent the numerical results [123]. A polynomial degree of ten is chosen so that the approximation reads as

$$\Gamma_{ik} = \sum_{j=0}^{10} a_{ikj} {\tau_{\mathrm{evap}}}_{ik}^{j} \begin{cases} k = 1 & \text{for } \Gamma_i = (d/d_0)^2 \\ k = 1, 2 & \text{for } \Gamma_i = \mathcal{T}_\mathrm{s} \\ k = 1, 2, 3 & \text{for } \Gamma_i = \dot{\mathcal{M}}_{\mathrm{C_2H_5OH}} \\ k = 1, 2, 3 & \text{for } \Gamma_i = \dot{\mathcal{M}}_{\mathrm{H_2O}}. \end{cases} \tag{3.5}$$

Here, i denotes the parameter that is being approximated, j represents the polynomial degree, and k stands for the number of polynomial fits that are necessary to describe the parameter. Two polynomial fits are employed to describe the normalized droplet surface temperature whereas three polynomial approximations are required to describe the normalized profiles of the mass evaporation rates of ethanol and water. Also, the normalized droplet surface area is described using only one polynomial approximation. Further, although three polynomial approximations are required to describe the normalized profiles of the mass evaporation rates of both the liquid components, the retrieval may be carried out using only two of those fits, because the third approximation is valid for only the last part of the normalized droplet evaporation time, which constitutes to only about one percent of the total normalized droplet evaporation time. An exception to this is the condition of the highest initial mass fraction of INN of 0.200, for which all the three approximations are required.

Figure 3.56a shows the profile of the normalized droplet surface area with normalized evaporation time fitted using the polynomial approximation, provided in Eq. 3.5, for the mean curves shown in Fig. 3.54a, for initial mass fraction of INN of 0.025 at relative velocities of 4 m/s and 8 m/s for ambient gas temperature of 1200 K. For the same conditions, Fig. 3.56b displays the fitted normalized profiles of the droplet surface temperature and the mass evaporation rates of ethanol and water. The colors red, blue, and green represent the different polynomial fits used for the particular range, *k*, of the normalized droplet evaporation time. For all the three initial precursor mass fractions considered in the study, two polynomial fits are used to describe the profile of the non-dimensionalized droplet surface temperature and three polynomial approximations are required to capture the normalized profile of the dimensionless mass evaporation

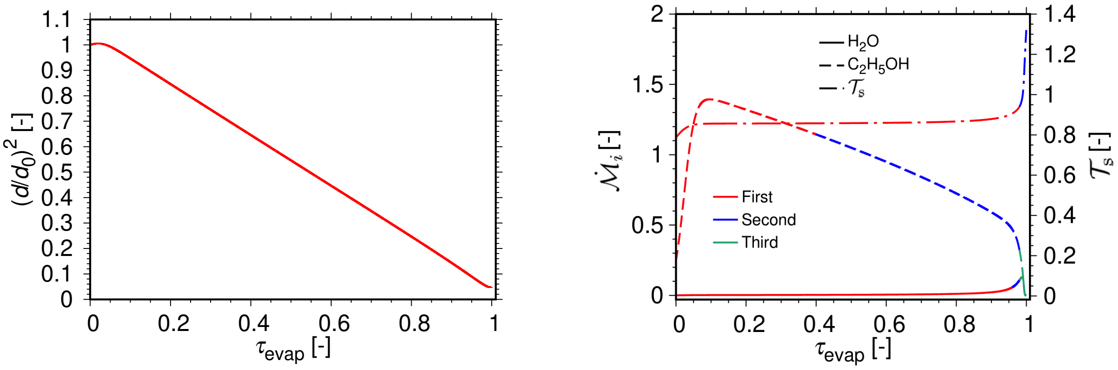

(a) Normalized droplet surface area.

(b) Mass evaporation rates and $\mathcal{T}_s$.

Figure 3.56: Fitted normalized profiles of the droplet surface area, mass evaporation rates, and droplet surface temperature with normalized droplet evaporation time τ_{evap} for different initial droplet sizes. Initial conditions: $T_{l,0} = 293.15$ K, $p = 1$ bar, $u_0 = 4$ m/s and 8 m/s, $T_{g,0} = 1200$ K, $Y_{IN,0} = 0.014$, $Y_{H_2O,0} = 0.011$, $Y_{EtOH,0} = 0.975$, RH $= 0$ % (Narasu and Gutheil [123]).

rates of both the liquid components. Also, only one polynomial fit is employed to describe the normalized droplet surface area profile. From Fig. 3.55, it is noticeable that profile of the mean of the mass fraction of iron(III) nitrate is linear with the normalized thermal decomposition time. Therefore, it is sufficient to provide with the mean of the initial value of the mass fraction of iron(III) nitrate to describe the average profile of the iron(III) nitrate mass fraction with the normalized thermal decomposition time.

Knowing the boiling point of water, along with the droplet evaporation times and the thermal decomposition times for each specific condition, as well as the normalization parameters defined in Eqs. (3.1)–(3.4), it is possible to retrieve the profiles of the normalized droplet surface area, the droplet surface temperature, the mass evaporation rates of the ethanol and the water components as well as the mass fraction of iron(III) nitrate. The particulars related to the retrieval of the simulation results is discussed next.

The tabulation to retrieve the numerical simulation results for a single INN/ethanol droplet of initial mass fraction of INN of 0.025 at an ambient gas temperature of 1200 K is presented in Tab. 3.1. The first four rows of the first line of the data consists of the names of the variables for which parameterization is performed, T_s, mdot_ethanol, mdot_water, and $(d/d\_0)^2$. The last two rows of the first line mentions the initial INN mass fraction and the ambient air temperature for which the following data is valid. Two polynomial fits are required to describe the droplet surface temperature T_s, which are given in lines 2 to 5 in red color. The eleven polynomial coefficients of Eq. (3.5) followed by their upper normalized droplet evaporation time limit of validity is displayed in lines 2 and 3 as well as lines 4 and 5. The subsequent four lines in blue color provide with the coefficients for the two polynomial fits required to describe the the mass evaporation rate of ethanol along with their range of validity and the next four black lines give the two polynomial sets for the mass evaporation rate of water. The

Table 3.1: The polynomial coefficients for normalized droplet surface area, mass evaporation rates, and droplet surface temperature along with the droplet evaporation and thermal decomposition times for various initial conditions at $T_{g,0} = 1200$ K and $Y_{INN,0} = 0.025$ (Narasu and Gutheil [123]).

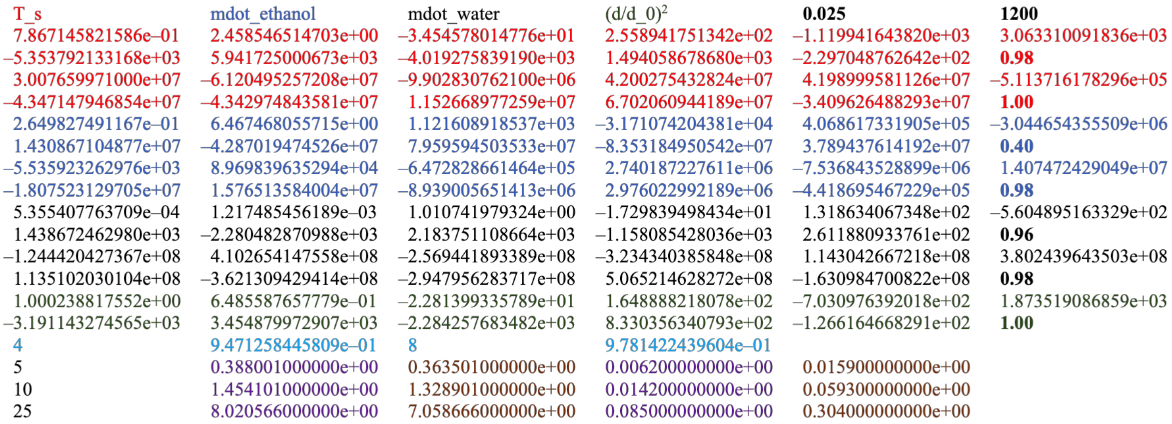

T_s	mdot_ethanol	mdot_water	(d/d_0)^2	**0.025**	**1200**
7.867145821586e–01	2.458546514703e+00	–3.454578014776e+01	2.558941751342e+02	–1.119941643820e+03	3.063310091836e+03
–5.353792133168e+03	5.941725000673e+03	–4.019275839190e+03	1.494058678680e+03	–2.297048762642e+02	**0.98**
3.007659971000e+07	–6.120495257208e+07	–9.902830762100e+06	4.200275432824e+07	4.198999581126e+07	–5.113716178296e+05
–4.347147946854e+07	–4.342974843581e+07	1.152668977259e+07	6.702060944189e+07	–3.409626488293e+07	**1.00**
2.649827491167e–01	6.467468055715e+00	1.121608918537e+03	–3.171074204381e+04	4.068617331905e+05	–3.044654355509e+06
1.430867104877e+07	–4.287019474526e+07	7.959594503533e+07	–8.353184950542e+07	3.789437614192e+07	**0.40**
–5.535923262976e+03	8.969839635294e+04	–6.472828661464e+05	2.740187227611e+06	–7.536843528899e+06	1.407472429049e+07
–1.807523129705e+07	1.576513584004e+07	–8.939005651413e+06	2.976022992189e+06	–4.418695467229e+05	**0.98**
5.355407763709e–04	1.217485456189e–03	1.010741979324e+00	–1.729839498434e+01	1.318634067348e+02	–5.604895163329e+02
1.438672462980e+03	–2.280482870988e+03	2.183751108664e+03	–1.158085428036e+03	2.611880933761e+02	**0.96**
–1.244420427367e+08	4.102654147558e+08	–2.569441893389e+08	–3.234340385848e+08	1.143042667218e+08	3.802439643503e+08
1.135102030104e+08	–3.621309429414e+08	–2.947956283717e+08	5.065214628272e+08	–1.630984700822e+08	**0.98**
1.000238817552e+00	6.485587657779e–01	–2.281399335789e+01	1.648888218078e+02	–7.030976392018e+02	1.873519086859e+03
–3.191143274565e+03	3.454879972907e+03	–2.284257683482e+03	8.330356340793e+02	–1.266164668291e+02	**1.00**
4	9.471258445809e–01	8	9.781422439604e–01		
5	0.388001000000e+00	0.363501000000e+00	0.006200000000e+00	0.015900000000e+00	
10	1.454101000000e+00	1.328901000000e+00	0.014200000000e+00	0.059300000000e+00	
25	8.020566000000e+00	7.058666000000e+00	0.085000000000e+00	0.304000000000e+00	

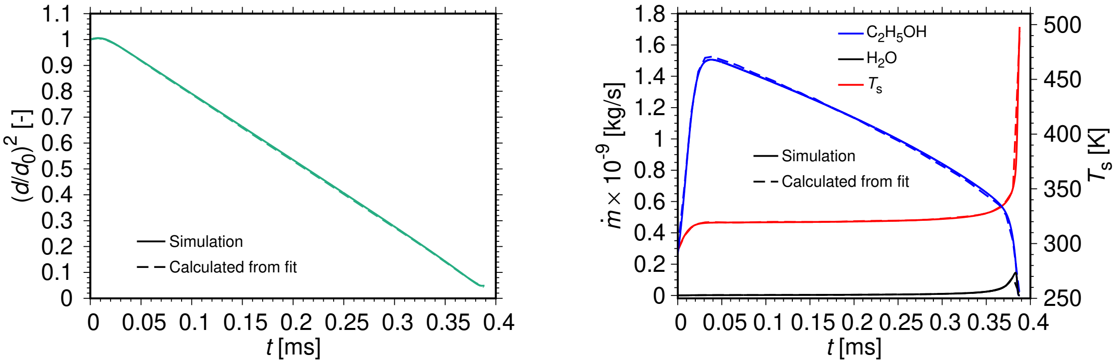

(a) Normalized droplet surface area.

(b) Mass evaporation rates and T_s.

Figure 3.57: Temporal variation of the droplet surface area, mass evaporation rates, and droplet surface temperature. Initial conditions: $r_{d,0} = 5$ µm, $T_{l,0} = 293.15$ K, $p = 1$ bar, $u_0 = 4$ m/s, $T_{g,0} = 1200$ K, $Y_{IN,0} = 0.014$, $Y_{H_2O,0} = 0.011$, $Y_{EtOH,0} = 0.975$, RH = 0 % (Narasu and Gutheil [123]).

following two lines in green color give the same information for the normalized droplet surface area. The next line in light blue color provides with two pairs of the relative velocity in m/s and the corresponding initial value of the mass fraction of iron(III) nitrate. Finally, the initial droplet radius and two pairs of the droplet evaporation time and the thermal decomposition time for the relative velocities of 4 m/s and 8 m/s are given in each of the last three lines, where the units of the droplet radii are in µm and that of the droplet evaporation and thermal decomposition times are in ms.

The procedure for the retrieval of the original numerical simulation results is explained for a single INN/ethanol droplet of initial radius of 5 µm at relative velocity of 4 m/s for initial mass fraction of INN of 0.025 at ambient air temperature of 1200 K. Firstly, the polynomial approximations given by Eq. (3.5) are employed to evaluate the

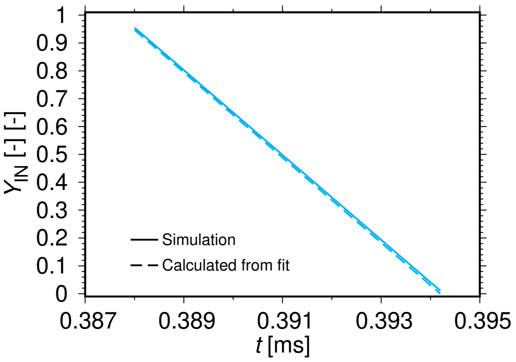

Figure 3.58: Temporal variation of the mass fraction of iron(III) nitrate. Initial conditions: $r_{\mathrm{d},0} = 5$ µm, $T_{\mathrm{l},0} = 293.15$ K, $p = 1$ bar, $u_0 = 4$ m/s, $T_{\mathrm{g},0} = 1200$ K, $Y_{\mathrm{IN},0} = 0.014$, $Y_{\mathrm{H_2O},0} = 0.011$, $Y_{\mathrm{EtOH},0} = 0.975$, RH = 0 % (Narasu and Gutheil [123]).

mean values of the normalized parameter using a normalized time step of 0.02. For the mass evaporation rates of ethanol and water, the third range of the polynomial fit has the range of validity between 0.99 and 1.0 of the normalized evaporation time, during which both the ethanol and the water components are almost completely evaporated. Therefore, the third polynomial approximation corresponding to the normalized mass evaporation rates of ethanol and water was neglected and at the final time step, their value was considered to be zero. Thus, Figs. 3.57 and 3.58 show the profiles of the normalized droplet surface area, the droplet surface temperature, the mass evaporation rates of ethanol and water, and the mass fraction of iron(III) nitrate with time for an INN/ethanol droplet of initial radius of 5 µm at relative velocity of 4 m/s for initial INN mass fraction of 0.025 at ambient gas temperature of 1200 K, where the solid lines show the original numerical simulation results and the dashed lines represent the curves that were evaluated using the polynomial fits by taking into consideration the value of the boiling point of water, the droplet evaporation time and the thermal decomposition time for the particular condition studied, and the equations for the normalized parameters.

There are certain recommendations that are to be taken into consideration for using the dataset provided in this study, in order to make sure that there is no loss of precision with respect to the evaluated profiles of the parameters. The given values of the droplet evaporation time and the thermal decomposition time are to be used with a minimum of four decimal places. Also, the coefficients of the polynomial approximations are to be employed with at least twelve decimal places. The total error between the profiles calculated using the polynomial approximations and the original numerical simulation results is below 1.5 %, for each of the parameters investigated in this study. The total error comprises of the contributions from different types of errors. Depending on the initial droplet size considered for the numerical study, the total number of time steps in each simulation is different. Therefore, to evaluate the mean profile, the number of time steps are adjusted to the same value of ten thousand, which contributes a maximum error of 0.75 %. Employing the mean profiles of the three different droplet sizes to replicate the original numerical simulation results for a specific droplet size results in an error of less than 0.40 %. Both, reduction of the number of time steps to fifty and adaptation of the different profile ranges using polynomial approximations causes an error of about 0.1 %. Due to the limitations of the available computational resources, it is not possible to perform complex simulations by including the intricate details of multicomponent droplet heating, evaporation, and thermal decomposition characteristics. In such situations, the parameterization provided in the present study is very much beneficial.

Table 3.2 gives the entire dataset for the initial mass fractions of INN of 0.0125 and 0.025 at ambient gas temperature of 400 K which represents the conditions for the droplet-to-particle pathway, as well as for initial INN mass fractions of 0.0125, 0.025, and 0.200 at ambient air temperatures of 800 K and 1200 K, that is representative of the conditions for the droplet into gas phase pathway. The data presented in Tab. 3.1 is the same as the one given by the second set of Tab. 3.2. Additionally, Tab. 3.3 provides with a code in *C* programming language to read the datasets given in Tab. 3.2.

The behavior of the droplet consisting of the precursor solution system of titanium(IV) isopropoxide and *p*-xylene is presented in the next section.

Table 3.2: The polynomial coefficients for normalized droplet surface area, mass evaporation rates, and droplet surface temperature along with the droplet evaporation and thermal decomposition times for various initial conditions (Narasu and Gutheil [123]).

T_s	mdot_ethanol	mdot_water	(d/d_0)^2	**0.025**	**800**
7.867359690591e–01	1.747616394195e+00	–2.312503267622e+01	1.615854300254e+02	–6.634820152282e+02	1.681763960325e+03
–2.664277105596e+03	2.576599396956e+03	–1.405152642616e+03	3.470305154648e+02	–1.251614391388e+01	**0.98**
1.321788785208e+07	–2.698997242649e+07	–4.289653155658e+06	1.860013374498e+07	1.851624158345e+07	–3.214339097653e+05
–1.929862335301e+07	–1.919975663692e+07	5.198552438105e+06	2.975354052134e+07	–1.518691541518e+07	**1.00**
4.049928500265e–01	1.402068766769e+01	5.590321897474e+02	–1.837923088876e+04	2.417769740843e+05	–1.817936365063e+06
8.540484953760e+06	–2.554575902726e+07	4.734574245018e+07	–4.961016526826e+07	2.247808444881e+07	**0.40**
–2.042865679835e+03	3.324992865363e+04	–2.409797491151e+05	1.024856616974e+06	–2.832688925475e+06	5.317552375646e+06
–6.866898241760e+06	6.024603170622e+06	–3.437402257253e+06	1.151999845723e+06	–1.722499714524e+05	**0.98**
7.004499984111e–04	7.320841215824e–03	6.985636575392e–01	–1.264700266326e+01	9.813146413021e+01	–4.211053619002e+02
1.088454183635e+03	–1.735749149109e+03	1.671629805079e+03	–8.915648471500e+02	2.022706210720e+02	**0.96**
–9.382191114812e+07	3.094568746672e+08	–1.939972472475e+08	–2.439799160664e+08	8.645600620347e+07	2.870304398015e+08
8.550078823384e+07	–2.735465696351e+08	–2.224800808429e+08	3.826532228996e+08	–1.232716072344e+08	**0.98**
1.000289904692e+00	2.936087644462e–01	–1.773320982005e+01	1.252323804627e+02	–5.234968870397e+02	1.369006095653e+03
–2.284585819393e+03	2.411780969212e+03	–1.540582055775e+03	5.335670240812e+02	–7.443802056633e+01	**1.00**
4	9.953996022681e–01	8	9.959139590121e–01		
5	0.714201000000e+00	0.659601000000e+00	2.470800000000e+00	10.27039900000e+00	
10	2.638701000000e+00	2.371301000000e+00	8.705399000000e+00	31.68709900000e+00	
25	14.23037000000e+00	12.30450000000e+00	46.28680000000e+00	145.3087000000e+00	
T_s	mdot_ethanol	mdot_water	(d/d_0)^2	**0.025**	**1200**
7.867145821586e–01	2.458546514703e+00	–3.454578014776e+01	2.558941751342e+02	–1.119941643820e+03	3.063310091836e+03
–5.353792133168e+03	5.941725000673e+03	–4.019275839190e+03	1.494058678680e+03	–2.297048762642e+02	**0.98**
3.007659971000e+07	–6.120495257208e+07	–9.902830762100e+06	4.200275432824e+07	4.198999581126e+07	–5.113716178296e+05
–4.347147946854e+07	–4.342974843581e+07	1.152668977259e+07	6.702060944189e+07	–3.409626488293e+07	**1.00**
2.649827491167e–01	6.467468055715e+00	1.121608918537e+03	–3.171074204381e+04	4.068617331905e+05	–3.044654355509e+06
1.430867104877e+07	–4.287019474526e+07	7.959594503533e+07	–8.353184950542e+07	3.789437614192e+07	**0.40**
–5.535923262976e+03	8.969839635294e+04	–6.472828661464e+05	2.740187227611e+06	–7.536843528899e+06	1.407472429049e+07
–1.807523129705e+07	1.576513584004e+07	–8.939005651413e+06	2.976022992189e+06	–4.418695467229e+05	**0.98**
5.355407763709e–04	1.217485456189e–03	1.010741979324e+00	–1.729839498434e+01	1.318634067348e+02	–5.604895163329e+02
1.438672462980e+03	–2.280482870988e+03	2.183751108664e+03	–1.158085428036e+03	2.611880933761e+02	**0.96**
–1.244420427367e+08	4.102654147558e+08	–2.569441893389e+08	–3.234340385848e+08	1.143042667218e+08	3.802439643503e+08
1.135102030104e+08	–3.621309429414e+08	–2.947956283717e+08	5.065214628272e+08	–1.630984700822e+08	**0.98**
1.000238817552e+00	6.485587657779e–01	–2.281399335789e+01	1.648888218078e+02	–7.030976392018e+02	1.873519086859e+03
–3.191143274565e+03	3.454879972907e+03	–2.284257683482e+03	8.330356340793e+02	–1.266164668291e+02	**1.00**
4	9.471258445809e–01	8	9.781422439604e–01		
5	0.388001000000e+00	0.363501000000e+00	0.006200000000e+00	0.015900000000e+00	
10	1.454101000000e+00	1.328901000000e+00	0.014200000000e+00	0.059300000000e+00	
25	8.020566000000e+00	7.058666000000e+00	0.085000000000e+00	0.304000000000e+00	
T_s	mdot_ethanol	mdot_water	(d/d_0)^2	**0.025**	**400**
7.863412201930e–01	–5.596710255187e–03	7.798673182253e–01	–1.297379984485e+01	9.975999440013e+01	–4.294562346831e+02
1.115593134769e+03	–1.786913375918e+03	1.726649103043e+03	–9.229611868066e+02	2.096557240873e+02	**0.96**
4.327485463200e+07	–1.420829733550e+08	8.878482597668e+07	1.107328831258e+08	–3.931565613548e+07	–1.289473838013e+08
–3.788109751754e+07	1.216241556876e+08	9.787607058016e+07	–1.678799308370e+08	5.381425268914e+07	**1.00**
1.531480084513e+00	4.785051289419e–01	–2.248358016042e+01	1.895204961594e+02	–9.673053825490e+02	3.126326310656e+03
–6.552662882402e+03	8.876379844265e+03	–7.497755187025e+03	3.590661591465e+03	–7.448170524673e+02	**0.96**
–1.627867255534e+06	5.723643530561e+06	–4.077842548455e+06	–4.510212130202e+06	2.209964176216e+06	5.765295109952e+06
1.219165401094e+06	–5.923272862578e+06	–4.250988691443e+06	8.268980803539e+06	–2.796865533756e+06	**0.98**
2.007980299564e–03	–2.849737850328e–03	2.110074500648e–01	–3.058608732265e+00	2.311805681849e+01	–1.011391492653e+02
2.711026039274e+02	–4.516878664993e+02	4.563090602700e+02	–2.559639457377e+02	6.122727040275e+01	**0.96**
–3.434773944602e+07	1.128861736657e+08	–7.069061556954e+07	–8.799281912150e+07	3.142472975938e+07	1.026209107149e+08
3.000416840101e+07	–9.693919852327e+07	–7.785546174139e+07	1.338354041063e+08	–4.294555224574e+07	**0.98**
1.000021336987e+00	–1.050836018406e+00	6.470737723956e–02	–2.486456955154e+00	2.384077785236e+01	–1.104888213757e+02
2.952114185993e+02	–4.770194050724e+02	4.608457970917e+02	–2.453507475778e+02	5.547886968102e+01	**1.00**
1	0.157760100000e+00	0.149597000000e+00			
2	0.598526300000e+00	0.556698900000e+00			
5	3.421601000000e+00	3.077001000000e+00			
T_s	mdot_ethanol	mdot_water	(d/d_0)^2	**0.0125**	**800**
7.868617734492e–01	1.758780317274e+00	–2.393496998021e+01	1.723320694844e+02	–7.331690010150e+02	1.943564131765e+03
–3.271580345032e+03	3.459558997750e+03	–2.188901128876e+03	7.353653211725e+02	–9.485217956632e+01	**0.98**
7.047907477452e+07	–1.426166002927e+08	–2.375181013842e+07	9.719035423592e+07	9.784591995507e+07	–3.517901502225e+05
–1.001680200667e+08	–1.007750366360e+08	2.584768640802e+07	1.544258868402e+08	–7.812566367591e+07	**1.00**
4.216990862295e–01	1.587859279807e+01	5.433748013738e+02	–1.895347351970e+04	2.557331123657e+05	–1.957513503559e+06
9.326856980810e+06	–2.822461589634e+07	5.282737130968e+07	–5.582212640641e+07	2.547792913217e+07	**0.40**
–3.140067363750e+03	5.086094640437e+04	–3.668092331303e+05	1.551877336283e+06	–4.265667520147e+06	7.960630714181e+06
–1.021626005120e+07	8.904253978322e+06	–5.045138362832e+06	1.678408981624e+06	–2.490167132284e+05	**0.98**
3.488613880948e–04	–4.106384001527e–03	5.049113808918e–01	–8.083100839664e+00	6.051457177350e+01	–2.555678218551e+02
6.544282754021e+02	–1.036614480031e+03	9.927020829343e+02	–5.266801462965e+02	1.188617578409e+02	**0.96**
–1.817677000307e+07	5.992416850793e+07	–3.752691593343e+07	–4.724149621272e+07	1.669139818970e+07	5.553594621465e+07
1.658230407641e+07	–5.288642034695e+07	–4.305706005033e+07	7.397204317396e+07	–2.381719756600e+07	**0.98**
1.000397035942e+00	2.816568944608e–01	–1.822081457925e+01	1.314280025592e+02	–5.616104055967e+02	1.505933670780e+03
–2.590696388545e+03	2.843975334046e+03	–1.915774359678e+03	7.165594632266e+02	–1.128504033771e+02	**1.00**
4	9.950563337973e–01	8	9.960927572051e–01		
5	0.730385500000e+00	0.675492900000e+00	1.470090500000e+00	5.706780100000e+00	
10	2.702001000000e+00	2.433001000000e+00	5.802500000000e+00	20.75199900000e+00	
25	14.60533000000e+00	12.65355000000e+00	31.25400000000e+00	102.2839500000e+00	

T_s	mdot_ethanol	mdot_water	$(d/d\_0)^2$	**0.0125**	**1200**
7.871035810002e–01	2.479094384565e+00	–3.576394894957e+01	2.715466214038e+02	–1.219165305031e+03	3.429086238996e+03
–6.188502974257e+03	7.138163354789e+03	–5.068241127543e+03	2.008263136505e+03	–3.377133696950e+02	**0.98**
1.012954373676e+08	–2.048628275244e+08	–3.421278542091e+07	1.395148551837e+08	1.405520582274e+08	–3.882704757331e+05
–1.437301465432e+08	–1.447002895719e+08	3.698812745779e+07	2.215835426858e+08	–1.120397000414e+08	**1.00**
2.752934134304e–01	8.707277836448e+00	1.144218965316e+03	–3.388048706465e+04	4.468226790854e+05	–3.415698564249e+06
1.633777778876e+07	–4.968757607717e+07	9.345149910740e+07	–9.918132590929e+07	4.544055887417e+07	**0.40**
–4.586897364055e+03	7.410091534510e+04	–5.330157992488e+05	2.248815850944e+06	–6.163267447106e+06	1.146642122359e+07
–1.466748471041e+07	1.273999892127e+07	–7.192432053384e+06	2.383700014722e+06	–3.522499073032e+05	**0.98**
2.404315546780e–04	–8.923341400677e–04	4.612883566157e–01	–7.767130012944e+00	5.906199992866e+01	–2.510067357691e+02
6.444422065762e+02	–1.021694965030e+03	9.783366505097e+02	–5.187127455111e+02	1.169382345802e+02	**0.96**
–1.773905585902e+07	5.843584501314e+07	–3.653333345290e+07	–4.606281056233e+07	1.619802607015e+07	5.408538264495e+07
1.621101469014e+07	–5.144098071221e+07	–4.194918461684e+07	7.193648320012e+07	–2.314138629057e+07	**0.98**
1.000559287474e+00	6.448389870227e–01	–2.393847518557e+01	1.795996121322e+02	–7.983513079578e+02	2.231880452443e+03
–4.022602048469e+03	4.661556690390e+03	–3.351063881763e+03	1.358337273817e+03	–2.370385908777e+02	**1.00**
4	9.419233225215e–01	8	9.773408658583e–01		
5	0.400735600000e+00	0.375837300000e+00	0.002330000000e+00	0.009580000000e+00	
10	1.503314000000e+00	1.376226000000e+00	0.010300000000e+00	0.036300000000e+00	
25	8.311198000000e+00	7.329095000000e+00	0.053700000000e+00	0.205800000000e+00	
T_s	mdot_ethanol	mdot_water	$(d/d\_0)^2$	**0.0125**	**400**
7.862289962779e–01	–1.905590358774e–02	8.246785670685e–01	–1.189278170599e+01	8.651374286353e+01	–3.621138473748e+02
9.252367142150e+02	–1.466295075690e+03	1.406483886905e+03	–7.478317983028e+02	1.691849238766e+02	**0.96**
–2.632780788706e+06	8.756215047302e+06	–5.635015992938e+06	–6.830810004370e+06	2.639894271472e+06	8.131213030150e+06
2.210078937118e+06	–7.857067320592e+06	–6.121967511837e+06	1.089707035414e+07	–3.556828976121e+06	**1.00**
1.560434982301e+00	–3.584909539160e–01	–1.002599438306e+01	9.143432826663e+01	–5.079572110053e+02	1.772075950528e+03
–3.976159979558e+03	5.720137301422e+03	–5.093793946382e+03	2.554642949221e+03	–5.516078934044e+02	**0.96**
–1.019233689173e+08	3.355736007823e+08	–2.095540536280e+08	–2.644960160142e+08	9.271265825957e+07	3.103094381255e+08
9.324450303629e+07	–2.948950637107e+08	–2.407416453108e+08	4.123432219334e+08	–1.325732748154e+08	**0.98**
9.402921380123e–04	–1.994466791369e–02	6.611844369495e–01	–8.797787970135e+00	6.182363992352e+01	–2.542505313592e+02
6.434200264873e+02	–1.014333780203e+03	9.704339743269e+02	–5.155566044707e+02	1.166918331272e+02	**0.96**
–2.924799743519e+07	9.692792270974e+07	–6.137504854373e+07	–7.647925312632e+07	2.785359590473e+07	9.061249660100e+07
2.639540122732e+07	–8.697030805188e+07	–7.007536730384e+07	1.217798940888e+08	–3.942133636662e+07	**0.98**
1.000050076479e+00	–1.062935295689e+00	7.245769617629e–01	–9.798521692955e+00	6.905498511958e+01	–2.797130992485e+02
6.916110567934e+02	–1.060807127053e+03	9.850863108643e+02	–5.072496164753e+02	1.111820518397e+02	**1.00**
1	0.156710100000e+00	0.148750100000e+00			
2	0.595168700000e+00	0.554198100000e+00			
5	3.407837000000e+00	3.068738000000e+00			
T_s	mdot_ethanol	mdot_water	$(d/d\_0)^2$	**0.200**	**800**
7.855192690555e–01	1.838584458814e+00	–1.939381754150e+01	1.014231619311e+02	–2.525476466730e+02	9.952791292086e+01
1.075057907659e+03	–2.962036192513e+03	3.611865130408e+03	–2.194732350432e+03	5.393937884827e+02	**0.96**
–6.185737573626e+06	2.017953708989e+07	–1.243901167741e+07	–1.570941653181e+07	5.371475191215e+06	1.811928759723e+07
5.482737922654e+06	–1.692716034608e+07	–1.379509011181e+07	2.333497911437e+07	–7.431599444048e+06	**1.00**
2.437551893200e–01	9.383573504797e+00	1.543877298855e+02	9.118228320071e+02	–1.145967871160e+05	1.863926378632e+06
–1.499536169791e+07	6.988466249010e+07	–1.921440765174e+08	2.901435383933e+08	–1.859631243589e+08	**0.30**
–7.124197329133e+01	1.379566883424e+03	–1.162476576074e+04	5.705410528614e+04	–1.807399559133e+05	3.862591840428e+05
–5.641731760705e+05	5.563408619606e+05	–3.546411464371e+05	1.320237741952e+05	–2.180745838176e+04	**0.96**
8.150182735870e+06	–2.695515127347e+07	1.709579083723e+07	2.103683809293e+07	–7.767692059457e+06	–2.475081198232e+07
–7.043391174153e+06	2.357583125696e+07	1.872797798648e+07	–3.257933248603e+07	1.050975806630e+07	**1.00**
5.158183206384e–03	5.052144773312e–01	–7.155630553926e–01	–3.095923339265e+01	2.860284934387e+02	–1.210039772187e+03
2.959010285807e+03	–4.416309705418e+03	3.973192996209e+03	–1.980895625701e+03	4.204763162322e+02	**0.90**
–1.536378626823e+07	7.710523562694e+07	–1.219828904231e+08	1.327579682698e+07	1.171145827961e+08	–7.124952058481e+06
–1.339786977567e+08	–2.064156773762e+06	1.769124067650e+08	–1.361571147800e+08	3.226357686589e+07	**0.98**
–1.931978544127e+05	3.970437400385e+05	6.114688294366e+04	–2.756380153123e+05	–2.725084802087e+05	6.974234266885e+03
2.870410001606e+05	2.837685708678e+05	–7.902788571659e+04	–4.423583453077e+05	2.267561527146e+05	**1.00**
9.976420896304e–01	4.692846983512e–01	–1.648966737344e+01	1.033136121470e+02	–3.871833168029e+02	9.074919704247e+02
–1.339729551873e+03	1.209796161179e+03	–6.107918394416e+02	1.330733405877e+02	–7.419910249997e–01	**1.00**
4	9.964083311610e–01	8	9.972790618083e–01		
5	0.633801000000e+00	0.580001000000e+00	9.866199000000e+00	34.95999900000e+00	
10	2.320001000000e+00	2.059901000000e+00	34.58999900000e+00	111.4400990000e+00	
25	12.31005000000e+00	10.52005000000e+00	177.6900500000e+00	429.4799500000e+00	
T_s	mdot_ethanol	mdot_water	$(d/d\_0)^2$	**0.200**	**1200**
7.845309427488e–01	2.370679345354e+00	–2.490086336832e+01	1.270988572169e+02	–2.935275698215e+02	–1.004054362685e+01
1.728219025810e+03	–4.327089095261e+03	5.104106989917e+03	–3.044262366896e+03	7.384879679082e+02	**0.96**
–5.854194548888e+06	1.914222913185e+07	–1.185631674012e+07	–1.490884575436e+07	5.164373888153e+06	1.725266648586e+07
5.169625765463e+06	–1.616890662531e+07	–1.312223578000e+07	2.229745750862e+07	–7.115852017365e+06	**1.00**
1.382051357139e–01	7.934434006405e+00	–4.741032640278e+01	1.241709408340e+04	–3.543175089794e+05	4.553170480702e+06
–3.317560691007e+07	1.463740008506e+08	–3.885849698733e+08	5.724934174109e+08	–3.602142480115e+08	**0.30**
–1.251805075437e+02	2.394939408786e+03	–2.008584833515e+04	9.810361490887e+04	–3.091412549280e+05	6.568937027490e+05
–9.535534375929e+05	9.340961704319e+05	–5.912397148592e+05	2.184592841669e+05	–3.580263826150e+04	**0.96**
–2.411516746177e+06	7.373941988366e+06	–3.902809970567e+06	–5.668520727874e+06	1.171614126754e+06	5.888020968782e+06
2.375092084350e+06	–4.897996663699e+06	–4.636914987621e+06	6.649476059941e+06	–1.940386131946e+06	**1.00**
2.126415958657e–03	4.044694312886e–01	2.284158088441e+00	–6.496759255324e+01	4.880846933457e+02	–1.922030625384e+03
4.524275323404e+03	–6.584380673730e+03	5.811071243140e+03	–2.851128901724e+03	5.967707432399e+02	**0.90**
5.981939302691e+06	–2.713378373838e+07	3.707289849013e+07	1.841040994755e+06	–3.365493863366e+07	–5.020883370496e+06
3.408100863614e+07	7.757722844659e+06	–4.179462252090e+07	2.594014909607e+07	–5.070530089315e+06	**0.98**
–3.928338353321e+04	8.602717920480e+04	8.969023467818e+03	–6.406657986003e+04	–5.911574909882e+04	6.692931872158e+03
6.923801207092e+04	6.422948794436e+04	–2.325586848341e+04	–1.065958672595e+05	5.716081369710e+04	**1.00**
9.964473759538e–01	7.960782429415e–01	–1.970806765188e+01	1.247298968972e+02	–4.760331344206e+02	1.147698790469e+03
–1.771068750443e+03	1.718389922394e+03	–9.873926269677e+02	2.907544429969e+02	–2.895263373342e+01	**1.00**
4	9.455739490290e–01	8	9.807882531989e–01		
5	0.319601000000e+00	0.296401000000e+00	0.015900000000e+00	0.071200000000e+00	
10	1.186001000000e+00	1.071401000000e+00	0.060400000000e+00	0.223200000000e+00	
25	6.440050000000e+00	5.590050000000e+00	0.315000000000e+00	1.410000000000e+00	

Table 3.3: Code in programming language *C* to read the data set provided in Tab. 3.2 (Narasu and Gutheil [123]).

```c
/*A C Program to read the polynomial coefficients, the droplet evaporation and thermal decomposition times*/
#include<stdio.h>

void main()
{
        FILE *fptrnew;
        fptrnew = fopen("coeffs.dat","r");

        double Yinn_0[9], Tg_0[9], a_temp1[2][6][9], a_temp2[2][6][9], a_eth1[2][6][9], a_eth2[2][6][9], a_eth3[2][6][9], a_wat1[20][6][9], a_wat2[2][6][9];
        double a_wat3[2][6][9], a_d1[2][6][9], a_u4_in[9][3], a_u8_in[9][3], coeffs[159][7], k_d1[9];
        int i, j, k, r, N, L1, L2, L3, L4, L5, L6, r_0[9][4], u_0[9][3];
        char a[159][7];
        double k_temp1[9], k_temp2[9], k_eth1[9], k_eth2[9], k_eth3[9], k_wat1[9], k_wat2[9], k_wat3[9], tth_u8[9][3], tth_u4[9][3], t_u8[9][3], t_u4[9][3];

        for(k=1; k<=8; k++)
        {
        if(k==3||k==6) N = 18; // number of lines corresponding to ambient temperature of 400 K
        else if(k>=7)   N = 23; // number of lines corresponding to ambient temperature of 800 K and 1200 K, Y_INN = 0.2000
        else            N = 19; // number of lines corresponding to ambient temperature of 800 K and 1200 K, Y_INN = 0.0250 and 0.0125
        for(i=1; i<=N; i++) // Starts reading the lines
        {
        for(j=1; j<=6; j++)
        {
        if(i==1&&j==1)          fscanf(fptrnew,"%s",&a[i][j]);
        else if(i==1&&j==2)     fscanf(fptrnew,"%s",&a[i][j]);
        else if(i==1&&j==3)     fscanf(fptrnew,"%s",&a[i][j]);
        else if(i==1&&j==4)     fscanf(fptrnew,"%s",&a[i][j]);
        else
        {
        fscanf(fptrnew,"%lf",&coeffs[i][j]);
        if(i==1&&j==5)          Yinn_0[k] = coeffs[i][j]; // reads the initial INN mass fraction
        if(i==1&&j==6)          Tg_0[k] = coeffs[i][j]; // reads the initial ambient temperature

        L1 = 2; L2 = 3; L3 = 4; L4 = 5;
        if(i==L2&&j==6)         k_temp1[k] = coeffs[i][j]; // reads the range up to which the coefficients for the temperature is valid
        else if(i==L4&&j==6)    k_temp2[k] = coeffs[i][j]; // reads the second range up to which the coefficients for the temperature is valid
        else if(i==L1||i==L2)   a_temp1[i][j][k] = coeffs[i][j]; // reads the coefficients for the temperature
        else if(i==L3||i==L4)   a_temp2[i][j][k] = coeffs[i][j]; // reads the coefficients for the second range of temperature

        L1 = 6; L2 = 7; L3 = 8; L4 = 9;
        if(i==L2&&j==6)         k_eth1[k] = coeffs[i][j]; // reads the first range up to which the coefficients for the mass evaporation rate of ethanol is valid
        else if(i==L4&&j==6)    k_eth2[k] = coeffs[i][j]; // reads the second range up to which the coefficients for the mass evaporation rate of ethanol is valid
        else if(i==L1||i==L2)   a_eth1[i][j][k] = coeffs[i][j]; // reads the coefficients for the first range of ethanol
        else if(i==L3||i==L4)   a_eth2[i][j][k] = coeffs[i][j];  // reads the coefficients for the second range of ethanol

        if(k>=7)
        {L5 = 10; L6 = 11;
        if(i==L6&&j==6)         k_eth3[k] = coeffs[i][j]; // reads the third range up to which the coefficients for the mass evaporation rate of ethanol is valid
        else if(i==L5||i==L6)   a_eth3[i][j][k] = coeffs[i][j];  // reads the coefficients for the third range of ethanol
        }

        if(k<=6)        {L1 = 10; L2 = 11; L3 = 12; L4 = 13;}
        else            {L1 = 12; L2 = 13; L3 = 14; L4 = 15;}

        if(i==L2&&j==6)         k_wat1[k] = coeffs[i][j]; // reads the first range up to which the coefficients for the mass evaporation rate of water is valid
        else if(i==L4&&j==6)    k_wat2[k] = coeffs[i][j];  // reads the second range up to which the coefficients for the mass evaporation rate of water is valid
        else if(i==L1||i==L2)   a_wat1[i][j][k] = coeffs[i][j]; // reads the coefficients for the first range of water
        else if(i==L3||i==L4)   a_wat2[i][j][k] = coeffs[i][j]; // reads the coefficients for the second range of water

        if(k>=7)
        {L5 = 16; L6 = 17;
        if(i==L6&&j==6)         k_wat3[k] = coeffs[i][j]; // reads the third range up to which the coefficients for the mass evaporation rate of water is valid
        else if(i==L5||i==L6)   a_wat3[i][j][k] = coeffs[i][j];  // reads the coefficients for the third range of water
        }

        if(k<=6)        {L1 = 14; L2 = 15;}
        else            {L1 = 18; L2 = 19;}

        if(i==L2&&j==6)         k_d1[k] = coeffs[i][j]; // reads the range up to which the coefficients for the normalized droplet surface area is valid
        else if(i==L1||i==L2)   a_d1[i][j][k] = coeffs[i][j]; // reads the coefficients for the normalized droplet surface area
```

```
            if(k<=2||k==4||k==5) {L1 = 16;}
            else if(k>=7)            {L1 = 20;}

            if(k<=2||k==4||k==5||k>=7)
            {
            if(i==L1)
            {
            if(j==1)       u_0[k][1] = coeffs[i][j]; // reads the relative velocity of 4 m/s
            else if(j==2)  a_u4_in[k][1] = coeffs[i][j]; // reads the initial value and the slope for the iron nitrate mass fraction for 4 m/s
            else if(j==3)  u_0[k][2] = coeffs[i][j]; // reads the relative velocity of 8 m/s
            else if(j==4) {a_u8_in[k][2] = coeffs[i][j]; // reads the initial value and the slope for the iron nitrate mass fraction for 8 m/s
            break;} // the last two columns of the line are not used
            }
            }

            if(k<=2||k==4||k==5) {L1 = 17; L2 = 18; L3 = 19;}
            else if(k>=7)            {L1 = 21; L2 = 22; L3 = 23;}
            else                     {L1 = 16; L2 = 17; L3 = 18;}

            if(i==L1)       r=1;
            else if(i==L2) r=2;
            else if(i==L3) r=3;

            if(k<=2||k==4||k==5||k>=7)
            {
            if(i==L1||i==L2||i==L3)
            {
            if(j==1)        r_0[k][r] = coeffs[i][j]; // reads the droplet radius
            if(j==2)        t_u4[k][r] = coeffs[i][j]; // reads the droplet lifetime for corresponding radius and relative velocity of 4 m/s
            if(j==3)        t_u8[k][r] = coeffs[i][j]; // reads the droplet lifetime for corresponding radius and relative velocity of 8 m/s
            if(j==4)        tth_u4[k][r] = coeffs[i][j]; // reads the thermal decomposition for corresponding radius and relative velocity of 4 m/s
            if(j==5)       {tth_u8[k][r] = coeffs[i][j]; // reads the thermal decomposition for corresponding radius and relative velocity of 8 m/s
            break;} // the last column of the line is not used
            }
            }
            if(k==3||k==6)
            {
            if(i==L1||i==L2||i==L3)
            {
            if(j==1)        r_0[k][r] = coeffs[i][j]; // reads the droplet radius
            if(j==2)        t_u4[k][r] = coeffs[i][j]; // reads the droplet lifetime for corresponding radius and relative velocity of 4 m/s
            if(j==3)       {t_u8[k][r] = coeffs[i][j]; // reads the droplet lifetime for corresponding radius and relative velocity of 8 m/s
            break;} // the last three columns of the line are not used
            }
            }

            }
            }
            }

            }

} // end of program
```

3.4 Titanium(IV) Isopropoxide/*p*-Xylene Droplet

In flame spray pyrolysis, titanium dioxide nanoparticles [21, 127, 128] may be produced using the precursor solution of titanium(IV) isopropoxide and *p*-xylene. The chemical structure of titanium(IV) isopropoxide is complex and is shown in Fig.3.59a. Titanium dioxide nanoparticles, see Fig.3.60, are used for gas sensors and also as photocatalyst [20]. These nanoparticles are employed in controlled drug delivery applications and are also used as a coating material [129] because of its non-toxic nature [128]. Further, the solvent chosen is *p*-xylene, whose chemical structure is shown in Fig. 3.59b,

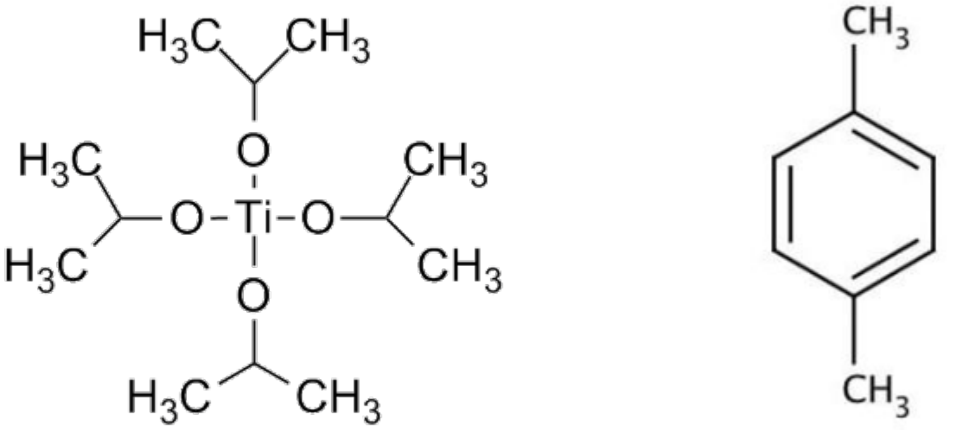

(a) Chemical structure of TTIP. (b) Chemical structure of *p*-xylene.

Figure 3.59: The chemical structure of titanium(IV) isopropoxide (TTIP) [125] and *p*-xylene [126].

Figure 3.60: The titanium dioxide nanoparticles in the form of powder as provided by All India Metal Corporation [132].

since it does not react with titanium(IV) isopropoxide as was confirmed by the study of [130]. Thermal decomposition of sprays constituting of different precursor solution combinations of ferrocene, titanium(IV) isopropoxide, and iron pentacarbonyl in solutions of xylene or ethanol was experimentally investigated by Gonchikzhapov and Kasper [130]. For the precursor/solvent system of titanium(IV) isopropoxide and xylene, it was concluded that the chemical interaction between the precursor and the solvent does not occur in the liquid phase. Also, the combustion of single titanium(IV) isopropoxide in xylene droplets was experimentally studied by Li et al. [131]. They reported that titanium(IV) isopropoxide does not react with the water vapor produced during the process of combustion.

For the numerical study presented in this section, the precursor solution system of titanium(IV) isopropoxide (TTIP) in *p*-xylene is considered. The droplet heating and evaporation characteristics of a single TTIP/*p*-xylene droplet is investigated. At first, the zero-dimensional model, see section 2.2, is used to perform the numerical study of the droplet behavior in an atmosphere of hot convective air. Further, in order to explore the occurrence of puffing and possible micro-explosion, the one-dimensional model, see section 2.3, is employed with appropriate modifications, see section 2.3.3. Unfortunately, there exists no experimental data to which the numerical results may be compared with. But, the validation for the zero-dimensional model was performed by Narasu et al. [72] for the heating and evaporation of ethanol/water droplets with the results available from the experiments conducted by Ma et al. [75]. Please refer to the previous section 3.1 for further details. The results of the one-dimensional model are compared with that computed using the zero-dimensional model, before exploring the processes of puffing and micro-explosion for the present precursor solution system.

In this section, firstly, the numerical simulation results of the zero-dimensional model are discussed, where a parameter study is performed and an analysis is presented with respect to the lifetimes of the droplet for different initial conditions. Also, a detailed analysis and discussion on the parameterization of these numerical results for use in more complex spray flames, is demonstrated. Finally, the results of the one-dimensional model are presented that includes the droplet behavior during puffing and micro-explosion.

For the parameter study, the initial droplet radii of 5 µm, 10 µm, 25 µm, and 50 µm are taken into consideration at relative velocities of 4 m/s and 8 m/s for ambient gas temperatures of 800 K and 1200 K along with the initial mass fractions of TTIP of 0.025, 0.155, and 0.25. The initial conditions are determined following the previous experimental investigations [29, 130, 131] with respect to flame spray pyrolysis. For these conditions, the distillation-limit and the rapid-mixing models are valid because of the thermal and mass Peclet numbers being below their critical values, as was discussed extensively in the numerical investigation of Narasu et al. [72] as well as in the previous section 3.1. Further, the droplet does not breakup since the Weber number remains below the critical Weber number.

The detailed results of the parameter study are presented next.

3.4.1 Parameter Study

First, the heating and evaporation characteristics of the TTIP/*p*-xylene droplet computed by employing the real behavior of the TTIP/*p*-xylene mixture is compared with that calculated using the ideal mixture properties. The non-ideal behavior of the mixture is taken into consideration through the use of activity coefficients evaluated using the NRTL method [84] and for the ideal case, the activity coefficients are taken as equal to one, $\gamma = 1$. The impact of considering the real and ideal behavior of the mixture of TTIP and *p*-xylene is shown in Fig. 3.61.

Figure 3.61 shows the temporal evolution of the profiles of the normalized droplet surface area, the temperature (red color) at the surface of the droplet as well as the mass evaporation rates of TTIP (black color) and *p*-xylene (blue color) for a TTIP/*p*-xylene

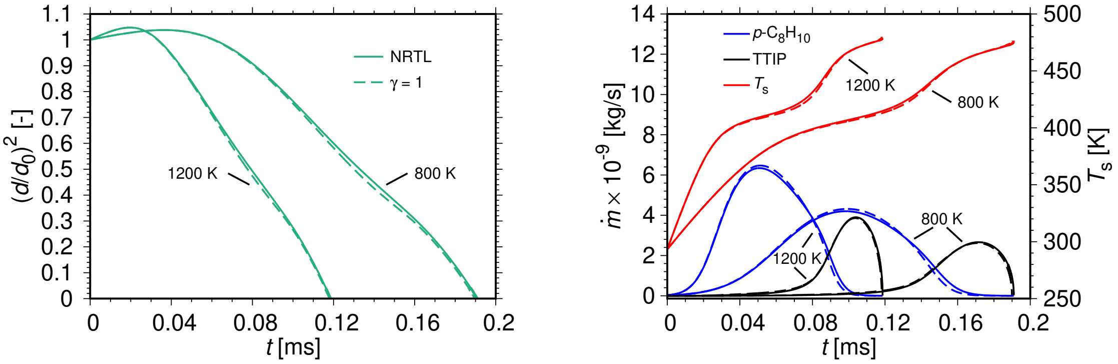

(a) Normalized droplet surface area.

(b) Mass evaporation rates and T_s.

Figure 3.61: Temporal variation of the droplet surface area, mass evaporation rates, and droplet surface temperature. Initial conditions: $r_{\mathrm{d},0} = 5$ µm, $T_{\mathrm{l},0} = 293.15$ K, $p = 1$ bar, $u_0 = 4$ m/s, $T_{\mathrm{g},0} = 800$ K and 1200 K, $Y_{\mathrm{TTIP},0} = 0.25$, $Y_{p\text{-}\mathrm{C_8H_{10}},0} = 0.75$ (Narasu et al. [133]).

droplet of initial radius of 5 µm at relative velocity of 4 m/s for initial mass fraction of TTIP of 0.25 at ambient gas temperatures of 800 K and 1200 K. The numerical results taking into account the real behavior of the mixture are displayed by the solid lines and that considering the ideal behavior are represented using the dashed lines. During the initial droplet heating, the droplet expands as can be seen from the normalized droplet surface area profile presented in Fig. 3.61a. This is followed by the quasi steady evaporation phase where the preferential evaporation of the higher volatile *p*-xylene occurs followed by evaporation of the TTIP component, which is evident from the profiles of the mass evaporation rates of both the liquid components, see Fig. 3.61b. The model predicts smaller deviation of the profile of the normalized droplet surface area while taking into account the real behavior of the TTIP/*p*-xylene mixture, as compared to that computed using the ideal mixture properties. The reason for such a behavior is the smaller mass evaporation rate of *p*-xylene which also fastens the rate of increase of the droplet surface temperature. Further, the lifetime of the droplet is increased by about 0.54 % and 0.41% for the lower and higher ambient temperatures, respectively, when the non-ideal nature of the TTIP/*p*-xylene mixture is considered. Thus, taking into consideration the real behavior of the TTIP/*p*-xylene mixture causes only very small differences when compared to the assumption of ideal behavior. Still, real mixture properties are used throughout the remaining study.

Parameter study is performed by varying the initial droplet radius, the initial precursor mass fraction, the ambient gas temperature, and the relative velocity between the droplet and the ambience.

Figure 3.62 displays the profiles of the normalized droplet surface area with time for TTIP/*p*-xylene droplets of initial radii of 5 µm and 25 µm at relative velocity of 4 m/s for initial mass fractions of TTIP of 0.0 (black color), 0.025 (red color), 0.0155 (blue color), and 0.25 (green color) at ambient gas temperatures of 800 K (dashed lines) and 1200 K (solid lines). At first, the droplet expands during the initial droplet heating period, because of the variable physical properties employed in the model, especially

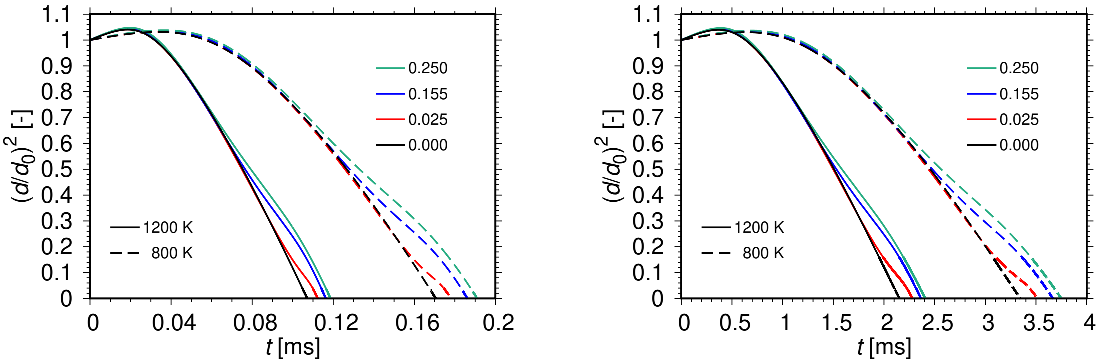

(a) $r_{\mathrm{d},0} = 5$ µm.

(b) $r_{\mathrm{d},0} = 25$ µm.

Figure 3.62: Temporal variation of the droplet surface area. Initial conditions: $T_{\mathrm{l},0} = 293.15$ K, $p = 1$ bar, $u_0 = 4$ m/s, $T_{\mathrm{g},0} = 800$ K and 1200 K (Narasu et al. [133]).

that of the liquid density. At lower ambient temperature of 800 K, the droplet expansion is about 3.5 % of the initial droplet surface area which is around one percent lower than that at higher ambient air temperature of 1200 K, thus evidently showing the liquid density variation with temperature. The initial droplet heating is followed by the quasi-steady evaporation phase where the preferential evaporation of the *p*-xylene component takes place since *p*-xylene is more volatile than TTIP due to the lower boiling temperature of *p*-xylene of 412 K [95], followed by evaporation of the TTIP component. This is evident from the difference in the slopes for the normalized droplet surface area. Also, as the initial precursor loading is increased, the deviation of the slope of the droplet regression rate occurs earlier. Further, with an increase in the initial TTIP mass fraction, the droplet evaporation is slowed down due to the lower volatile nature of TTIP owing to its higher boiling point of 505 K [134] and therefore, the lifetime of the droplet is prolonged. Thus, the pure *p*-xylene droplet evaporates the fastest. At lower ambient temperature of 800 K, the droplets evaporate slower and thus, the droplet lifetime is prolonged by approximately 30 % as compared to that at higher ambient air temperature of 1200 K, owing to the reduced heat transfer rate between the ambience and the droplet at the lower ambient gas temperature. Further, for a droplet with larger initial radius of 25 µm, see Fig. 3.62b, the droplet lifetime is increased by a factor of about twenty as compared to that for the smaller initial droplet radius of 5 µm, see Fig. 3.62a, due to the prolong droplet heating and evaporation time since there is larger mass of the droplet to be evaporated.

Figure 3.63 presents the temporal evolution of the droplet surface temperature (red color) and the mass evaporation rates of both TTIP (black color) and *p*-xylene (blue color), for the precursor/solvent droplet of TTIP/*p*-xylene of initial radii of 5 µm and 25 µm for initial mass fraction of TTIP of 0.025 at relative velocity of 4 m/s for ambient gas temperatures of 800 K (dashed lines) and 1200 K (solid lines). The temperature at the surface of the droplet increases during the initial droplet heating period for all the cases shown in Fig. 3.63. The quasi-steady evaporation phase follows the initial droplet heating period, where the higher volatile *p*-xylene evaporates preferentially which is

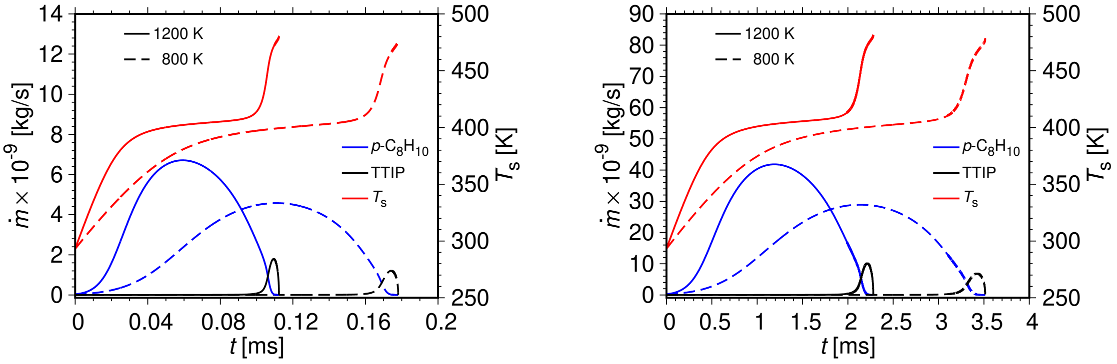

(a) $r_{\mathrm{d},0} = 5$ µm.

(b) $r_{\mathrm{d},0} = 25$ µm.

Figure 3.63: Temporal variation of the mass evaporation rates and droplet surface temperature. Initial conditions: $T_{\mathrm{l},0} = 293.15$ K, $p = 1$ bar, $u_0 = 4$ m/s, $T_{\mathrm{g},0} = 800$ K and 1200 K, $Y_{\mathrm{TTIP},0} = 0.025$, $Y_{p\text{-}\mathrm{C_8H_{10}},0} = 0.975$ (Narasu et al. [133]).

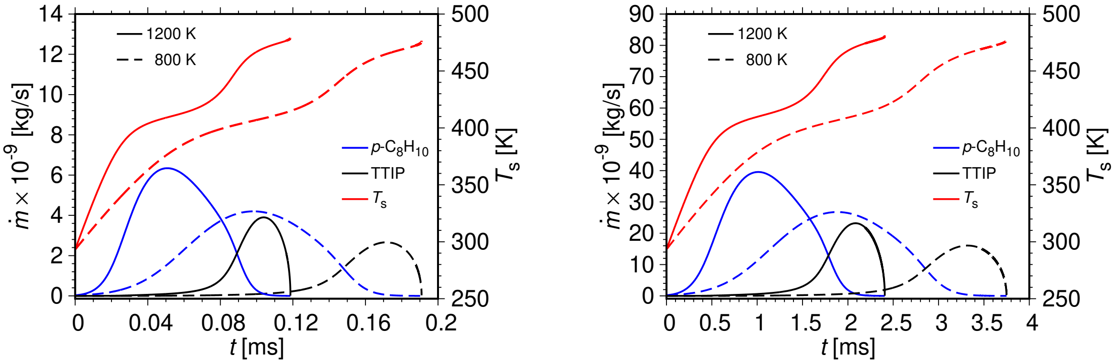

(a) $r_{\mathrm{d},0} = 5$ µm.

(b) $r_{\mathrm{d},0} = 25$ µm.

Figure 3.64: Temporal variation of the mass evaporation rates and droplet surface temperature. Initial conditions: $T_{\mathrm{l},0} = 293.15$ K, $p = 1$ bar, $u_0 = 4$ m/s, $T_{\mathrm{g},0} = 800$ K and 1200 K, $Y_{\mathrm{TTIP},0} = 0.25$, $Y_{p\text{-}\mathrm{C_8H_{10}},0} = 0.75$ (Narasu et al. [133]).

evident from the peak value obtained by the mass evaporation rate of *p*-xylene. Further, the second increase of the surface temperature occurs during which the evaporation of the lower volatile TTIP dominates as is visible from the peak attained by the TTIP mass evaporation rate. For the smaller initial droplet radius of 5 µm, see Fig. 3.63a, the mass evaporation rates are lower as compared to that at larger initial droplet radius of 25 µm, see Fig. 3.63b, due to the smaller mass of the droplet that is to be evaporated. As the initial mass fraction of TTIP is increased to 0.25, see Fig. 3.64, the mass evaporation rates of TTIP are higher as compared to that at initial TTIP mass fraction of 0.025, for both the initial droplet sizes at both ambient gas temperatures. Please note that while comparing the numerical results of both the droplet sizes, the characteristics of the normalized profiles are qualitatively the same, which provides motivation to perform parameterization of the results, as was carried out for the INN/ethanol droplets, see section 3.3.3, which is discussed in detail later.

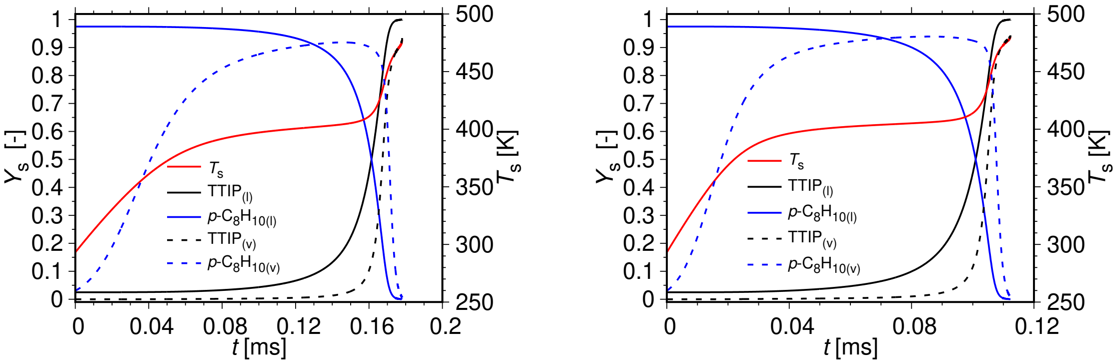

(a) $T_{g,0}$ = 800 K.

(b) $T_{g,0}$ = 1200 K.

Figure 3.65: Temporal variation of the species mass fractions and temperature at the surface of the droplet. Initial conditions: $r_{d,0} = 5$ µm, $T_{l,0} = 293.15$ K, $p = 1$ bar, $u_0 = 4$ m/s, $Y_{\mathrm{TTIP},0} = 0.025$, $Y_{p\text{-}\mathrm{C_8H_{10}},0} = 0.975$ (Narasu et al. [133]).

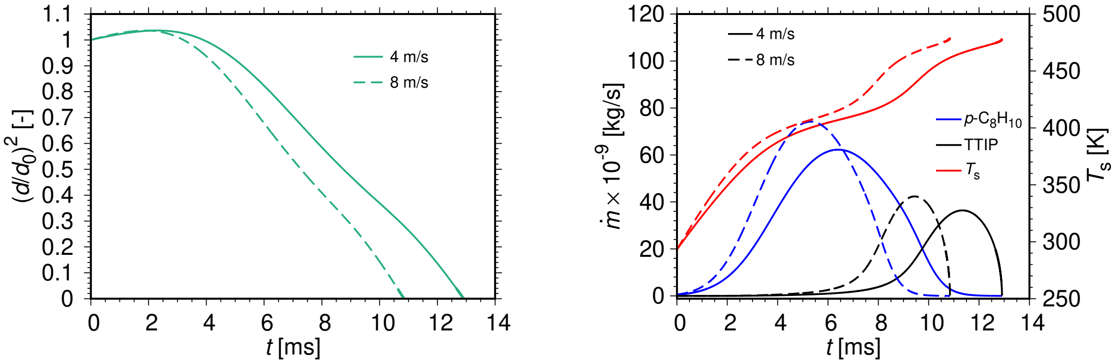

(a) Normalized droplet surface area.

(b) Mass evaporation rates and T_s.

Figure 3.66: Temporal variation of the droplet surface area, mass evaporation rates, and droplet surface temperature. Initial conditions: $r_{d,0} = 50$ µm, $T_{l,0} = 293.15$ K, $p = 1$ bar, $u_0 = 4$ m/s and 8 m/s, $T_{g,0} = 800$ K, $Y_{\mathrm{TTIP},0} = 0.25$, $Y_{p\text{-}\mathrm{C_8H_{10}},0} = 0.75$ (Narasu et al. [133]).

The temporal variation of the species mass fractions and the droplet surface temperature is displayed in Fig. 3.65 for TTIP/*p*-xylene precursor solution droplet of initial radius of 5 µm at relative velocity of 4 m/s for initial TTIP mass fraction of 0.025 for ambient air temperatures of 800 K and 1200 K. Initially, the droplet heats up so that the droplet surface temperature (red color) increases. During the quasi-steady evaporation regime, the preferential evaporation of *p*-xylene occurs, which results in the decrease of the mass fraction of *p*-xylene (blue solid lines) and the increase of the amount of TTIP inside the droplet as well as further increase of the droplet surface temperature. The processes associated with respect to the droplet surface temperature and the mass evaporation rates of the both the components, see Fig. 3.63, are reflected in the mass fraction profiles. At higher ambient temperature of 1200 K, see Fig. 3.65b, the droplet lifetime is shortened as compared to that at 800 K, see Fig. 3.65a, due to

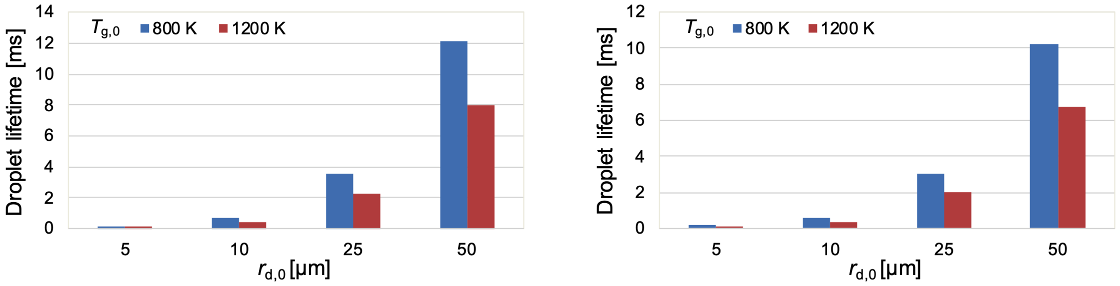

(a) $u_0 = 4$ m/s. (b) $u_0 = 8$ m/s.

Figure 3.67: Histograms showing the lifetime of the droplet for different initial droplet radii and ambient air temperatures of 800 K and 1200 K. Initial conditions: $T_{l,0} = 293.15$ K, $p = 1$ bar, $Y_{\mathrm{TTIP},0} = 0.025$, $Y_{p\text{-}\mathrm{C_8H_{10}},0} = 0.975$ (Narasu et al. [135]).

the enhanced heat transfer rate.

The influence of the relative velocity on the droplet heating and evaporation characteristics of a droplet consisting of the precursor solution system of TTIP and *p*-xylene is presented in Fig. 3.66. For a TTIP/*p*-xylene droplet of larger initial radius of 50 μm at ambient temperature of 800 K for the initial mass fraction of TTIP of 0.25, Fig. 3.66 shows the profiles of the normalized droplet surface area, the droplet surface temperature, and the mass evaporation rates of both the components versus time at relative velocities of 4 m/s (solid lines) and 8 m/s (dashed lines). For the higher relative velocity of 8 m/s, the convection rate is enhanced, as confirmed by the previous studies [73, 49], which results in more pronounced evaporation as compared to that at lower relative velocity of 4 m/s. This is visible from the higher mass evaporation rates of TTIP and *p*-xylene, see Fig. 3.66b, at relative velocity of 8 m/s, which eventually shortens the lifetime of the droplet.

The conditions of the flame spray pyrolysis are selected based on the desired properties that the final nanoparticles produced should possess and also depend on the global process requirements. The parameters such as the initial droplet size, the initial precursor loading, the relative velocity, and the ambient gas temperature affect the lifetimes of the droplet, which in turn affect the global process time of flame spray pyrolysis. Hence, a detailed analysis of the droplet lifetimes is presented next.

Figure 3.67 displays the histograms showing the droplet lifetimes for initial droplet radii of 5 μm, 10 μm, 25 μm, and 50 μm at relative velocities of 4 m/s and 8 m/s for ambient gas temperatures of 800 K (blue color) and 1200 K (red color) for initial mass fraction of TTIP of 0.025. For larger initial droplet size, the droplet lifetime is increased due to the prolonged droplet heating and evaporation time because of the larger mass of the liquid to be evaporated. Further, at higher ambient temperature of 1200 K, the droplet evaporation is enhanced resulting in shorter droplet lifetimes as compared to that at 800 K, since the heat transfer between the ambience and the droplet is more pronounced at higher ambient temperature. Increasing the relative velocity from 4 m/s, see Fig. 3.67a, to 8 m/s, see Fig. 3.67b, causes the droplets to evaporate faster due to the stronger convection rate and thus, reduces the droplet lifetime, which is found in the literature related to droplet evaporation studies [72].

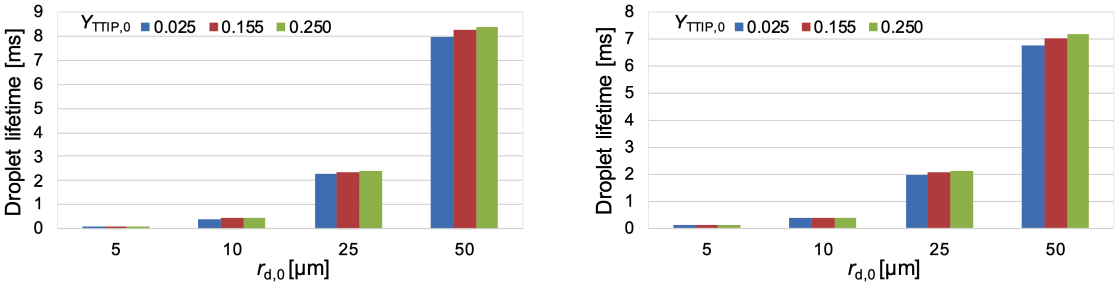

(a) $u_0 = 4$ m/s.

(b) $u_0 = 8$ m/s.

Figure 3.68: Histograms showing the lifetime of the droplet for different initial droplet radii and TTIP mass fractions of 0.025, 0.155, and 0.250. Initial conditions: $T_{l,0} = 293.15$ K, $p = 1$ bar, $T_{g,0} = 1200$ K (Narasu et al. [133]).

Figure 3.68 shows the effect of varying the initial precursor loading on the droplet lifetimes for initial droplet radii of 5 µm, 10 µm, 25 µm, and 50 µm for ambient air temperature of 1200 K at relative velocities of 4 m/s and 8 m/s . Three different initial TTIP mass fractions of 0.025, 0.155, and 0.25 are considered. With the increase of the initial mass fraction of TTIP, the droplet evaporation is slowed down and thus, the droplet lifetimes are prolonged owing to the lower volatility of TTIP as compared to that of *p*-xylene. Therefore, the typical characteristics of the bi-component droplet behavior [55, 90] is reflected in the droplet heating and evaporation characteristics of the precursor/solvent droplets.

With the aim of using the heating and evaporation characteristics of TTIP/*p*-xylene precursor/solvent droplets in spray simulations, the present numerical results are parametrized using polynomial approximations so that these can be retrieved in more complex simulations related to flame spray pyrolysis.

3.4.2 Parameterization of the Numerical Results

The heating and evaporation characteristics of the TTIP/*p*-xylene precursor solution droplet, discussed in the previous section, are non-dimensionalized for the purpose of paramterization, which is discussed in detail in this section.

Analyzing the numerical results, it is evident that the normalized droplet surface area, the temperature at the surface of the droplet, and the mass evaporation rates of TTIP and *p*-xylene show some similarity, which may be utilized and parametrized so that these variables may be employed in more complex spray simulations. To achieve this motivation, the parameters investigated as part of the parameter study in the previous section are non-dimensionalized. Thus, the droplet lifetime is used to normalize the time, the boiling temperature of the lower volatile TTIP, $T_{\mathrm{TTIP,b}}$, is employed to normalize the droplet surface temperature, and the ratio of the initial droplet mass, m_0 and the droplet lifetime is used for the normalization of the mass evaporation rates $\dot{m}_i$ of both the components i. Thus, the dimensionless quantities are

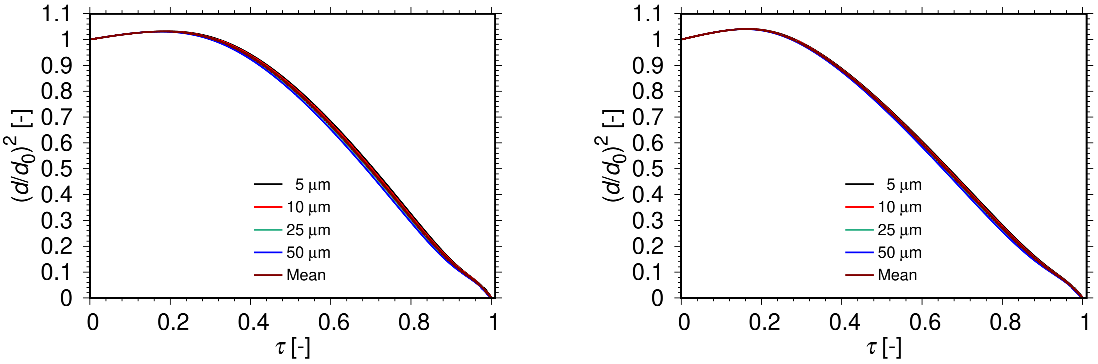

(a) $T_{\mathrm{g},0} = 800$ K.

(b) $T_{\mathrm{g},0} = 1200$ K.

Figure 3.69: Normalized profiles of the droplet surface area with normalized droplet lifetime τ for different initial droplet sizes. Initial conditions: $T_{\mathrm{l},0} = 293.15$ K, $p = 1$ bar, $u_0 = 4$ m/s and 8 m/s, $Y_{\mathrm{TTIP},0} = 0.025$, $Y_{p\text{-}\mathrm{C_8H_{10}},0} = 0.975$ (Narasu et al. [133]).

$$\tau = \frac{t}{t_{\mathrm{max}}} \tag{3.6}$$

$$\mathcal{T}_{\mathrm{s}} = \frac{T_{\mathrm{s}}}{T_{\mathrm{TTIP,b}}} \tag{3.7}$$

$$\dot{\mathcal{M}}_i = \frac{\dot{m}_i}{m_0/t_{\mathrm{max}}}, \quad i = 1, 2. \tag{3.8}$$

Here, m_0 is the initial mass evaluated as, $m_0 = 4/3\pi r_{\mathrm{d},0}^3 \rho_0$. Also, ρ_0 denotes the density of the droplet given by, $\rho_0 = Y_{\mathrm{TTIP},0}\, \rho_{0,\mathrm{TTIP}} + (1 - Y_{\mathrm{TTIP},0})\, \rho_{0,p-\mathrm{C_8H_{10}}}$, where $\rho_{0,i}$ represents the initial density of the components calculated at the initial temperature of the droplet [98]. Further, τ stands for the non-dimensionalized time, $\mathcal{T}_{\mathrm{s}}$ denotes the normalized droplet surface temperature, and $\dot{\mathcal{M}}_i$ represents the dimensionless mass evaporation rates of TTIP and p-xylene. Also, the normalized droplet surface area, that is also parameterized, is non-dimensional as per the definition.

For Eqs. 3.6-3.8, the reference values are known a priori, with the exception of the droplet lifetime. With respect to time, even though relative velocity between the droplet and the ambience is the only parameter that is known a priori, there exists no clear-cut relation between the relative velocity and the characteristics of heating and evaporation discussed in the previous section. Another alternative is using the ratio of the square of the initial droplet radius and the mass diffusion coefficient, which also does not show any distinct dependence of the characteristics of heating and evaporation. Hence, the lifetime of the droplet is chosen, the values of which are tabulated for different initial conditions investigated in this study, which will be presented later.

The normalized results of the precursor/solvent droplet of TTIP/p-xylene demonstrate significant influence via the ambient temperature and the initial precursor mass fraction. Also, the different initial droplet radii and the relative velocities considered in the present study show similarity and are represented via the non-dimensional

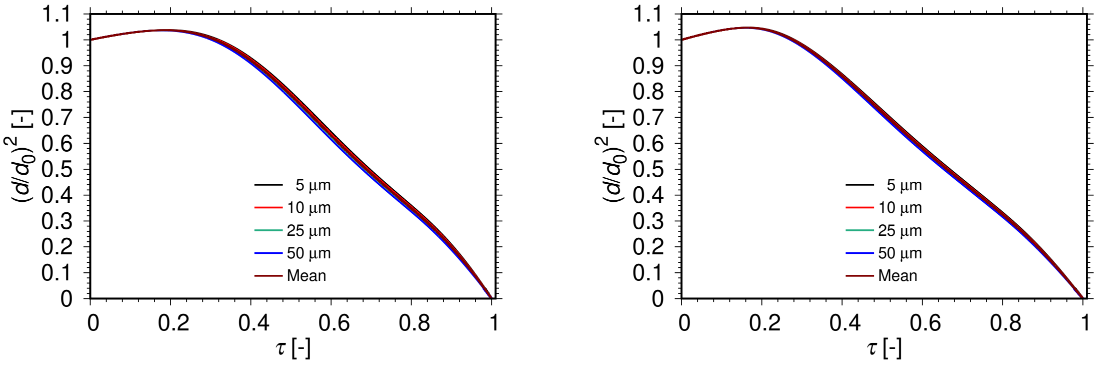

(a) $T_{\mathrm{g},0}$ = 800 K. (b) $T_{\mathrm{g},0}$ = 1200 K.

Figure 3.70: Normalized profiles of the droplet surface area with normalized droplet lifetime τ for different initial droplet sizes. Initial conditions: $T_{\mathrm{l},0} = 293.15$ K, $p = 1$ bar, $u_0 = 4$ m/s and 8 m/s, $Y_{\mathrm{TTIP},0} = 0.25$, $Y_{p\text{-}\mathrm{C_8H_{10}},0} = 0.75$ (Narasu et al. [133]).

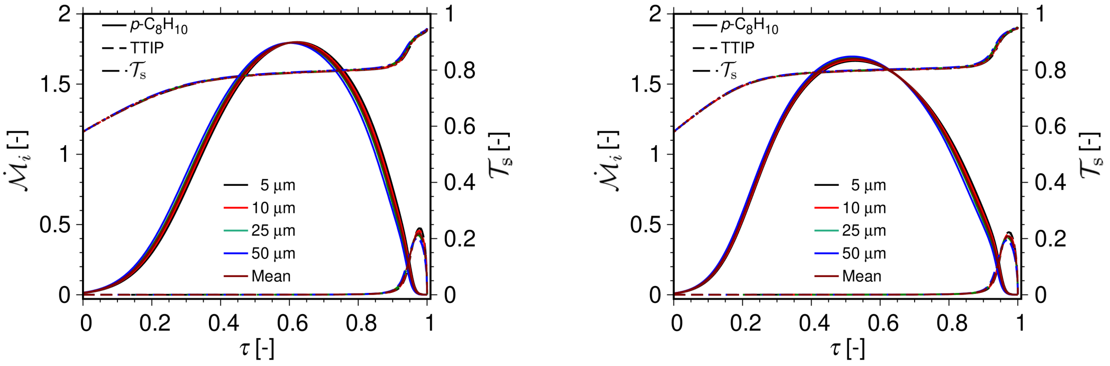

(a) $T_{\mathrm{g},0}$ = 800 K. (b) $T_{\mathrm{g},0}$ = 1200 K.

Figure 3.71: Normalized profiles of the mass evaporation rates and droplet surface temperature with normalized droplet lifetime τ for different initial droplet sizes. Initial conditions: $T_{\mathrm{l},0} = 293.15$ K, $p = 1$ bar, $u_0 = 4$ m/s and 8 m/s, $Y_{\mathrm{TTIP},0} = 0.025$, $Y_{p\text{-}\mathrm{C_8H_{10}},0} = 0.975$ (Narasu et al. [133]).

parameters, that include the initial droplet mass and the lifetime of the droplet.

Figure 3.69 display the profiles of the normalized droplet surface area versus the normalized droplet lifetime for the four different initial droplet radii of 5 µm (black color), 10 µm (red color), 25 µm (green color), and 50 µm (blue color) at relative velocities of 4 m/s and 8 m/s for the initial mass fraction of TTIP of 0.025 at ambient gas temperatures of 800 K and 1200 K. The arithmetic mean (brown color) is computed for the normalized profiles and is also displayed in the figure. For every simulation of the TTIP/p-xylene droplet, the total number of times are different. Thus, the mean profile is evaluated by adjusting the overall number of times steps to ten thousand for every simulation.

Similarly, Fig. 3.70 presents the normalized droplet surface area profile for the same conditions of Fig. 3.69, but for the larger initial mass fraction of TTIP of 0.25. Further,

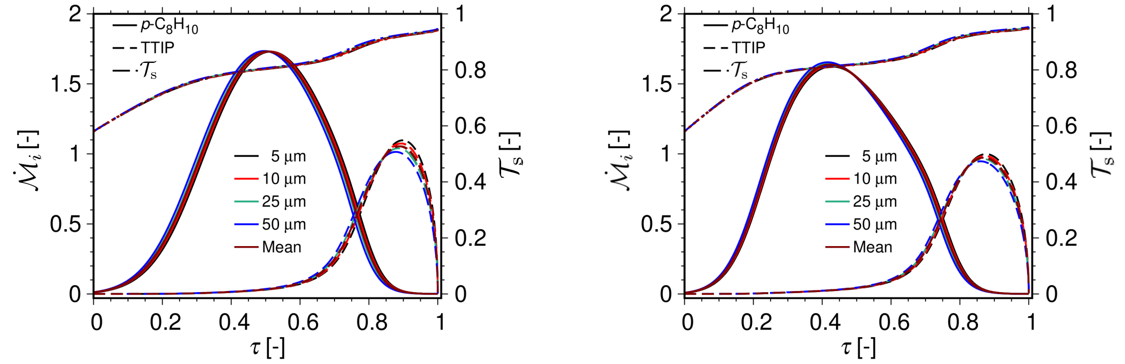

(a) $T_{g,0} = 800$ K.

(b) $T_{g,0} = 1200$ K.

Figure 3.72: Normalized profiles of the mass evaporation rates and droplet surface temperature with normalized droplet lifetime τ for different initial droplet sizes. Initial conditions: $T_{l,0} = 293.15$ K, $p = 1$ bar, $u_0 = 4$ m/s and 8 m/s, $Y_{\mathrm{TTIP},0} = 0.25$, $Y_{p\text{-}\mathrm{C_8H_{10}},0} = 0.75$ (Narasu et al. [133]).

Figs. 3.71 and 3.72 present the normalized profiles of the temperature (dashed dotted lines) at the surface of the droplet and the mass evaporation rates of TTIP (dashed lines) and p-xylene (solid lines) for the conditions represented in Figs. 3.69 and 3.70, respectively. A polynomial fit is performed for the mean of the normalized profiles in order to achieve the goal of parameterization, which is presented next.

The mean of the normalized heating and evaporation characteristics are parameterized using polynomial approximations, similar to those presented for INN/ethanol droplets in section 3.3.3. A tenth degree polynomial is applied to describe the various parameters so that the approximation reads as

$$\Gamma_{i,k} = \sum_{j=0}^{10} a_{ikj} \tau_{i,k}^{j} \begin{cases} k = 1 & \text{for } \Gamma_i = (d/d_0)^2 \\ k = 1,2 & \text{for } \Gamma_i = \mathcal{T}_\mathrm{s}, Y_{\mathrm{TTIP},0} = 0.025 \\ k = 1 & \text{for } \Gamma_i = \mathcal{T}_\mathrm{s}, Y_{\mathrm{TTIP},0} = 0.25 \\ k = 1,2 & \text{for } \Gamma_i = \dot{\mathcal{M}}_{p\text{-}\mathrm{C_8H_{10}}} \\ k = 1,2,3 & \text{for } \Gamma_i = \dot{\mathcal{M}}_{\mathrm{TTIP}} \end{cases} \tag{3.9}$$

where, i stands for the parameter that is approximated, j denotes the polynomial degree, and k represents the number of polynomial approximations that are needed to describe the parameter.

A single polynomial approximation is sufficient to describe the normalized droplet surface area profile. For the smaller initial mass fraction of TTIP of 0.025, two polynomial fits are used to describe the normalized droplet surface temperature, whereas for the higher initial TTIP mass fraction of 0.25, only one polynomial approximation is required. Two polynomial fits are employed to describe the normalized mass evaporation rate of p-xylene and three are required to describe that of TTIP. Although three polynomial approximations are required to describe the normalized profiles of the mass evaporation rate of the TTIP component, the retrieval may be pursued using

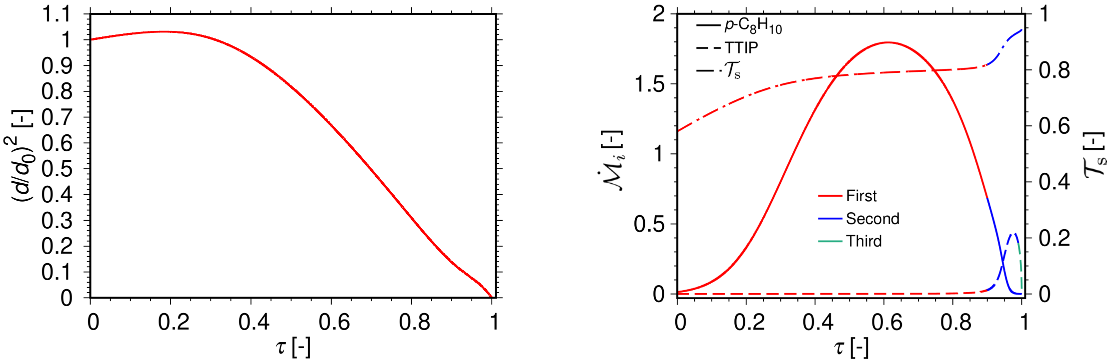

(a) Normalized droplet surface area.

(b) Mass evaporation rates and $\mathcal{T}_\mathrm{s}$.

Figure 3.73: Fitted normalized profiles of the droplet surface area, mass evaporation rates, and droplet surface temperature with normalized droplet lifetime τ for different initial droplet sizes. Initial conditions: $T_{\mathrm{l},0} = 293.15$ K, $p = 1$ bar, $u_0 = 4$ m/s and 8 m/s, $T_{\mathrm{g},0} = 800$ K, $Y_{\mathrm{TTIP},0} = 0.025$, $Y_{p\text{-}\mathrm{C_8H_{10}},0} = 0.975$ (Narasu et al. [133]).

only two of those approximations, because the third fit covers only the final part of the normalized lifetime of the droplet, which ranges for only around one percent of the entire normalized droplet lifetime.

Using polynomials of degrees six, eight, and ten showed errors of 0.6 %, 0.2 %, and 0.1 %, respectively, as compared to that of the original numerical simulation results. Thus, using polynomial of degree ten for the purpose of parameterization caused the least error. Further, the transition of the profiles from one approximation to another is the smoothest when polynomials of degree ten are employed, which is one of the significant reasons for the selection of the tenth degree polynomials for parameterization of the numerical results. The overall error caused due to the use of these polynomial fits are discussed in detail later.

Figure 3.73 displays the plots of the normalized profiles of the droplet surface area, the temperature (dashed dotted lines) at the surface of the droplet as well as the mass evaporation rates of TTIP (dashed lines) and p-xylene (solid lines) with normalized time fitted using the polynomial equations, see Eq. 3.9, for the mean curves shown in Figs. 3.69a and 3.71a, for the initial mass fraction of the precursor of 0.025 at ambient air temperature of 800 K at relative velocities of 4 m/s and 8 m/s. Figure 3.74 shows the normalized profiles of the droplet surface area, the droplet surface temperature, and the mass evaporation rates of both the components versus normalized time fitted using the polynomial approximations for the mean curves shown in Figs. 3.70a and 3.72a, for the higher initial TTIP mass fraction of 0.25 at relative velocities of 4 m/s and 8 m/s for ambient temperature of 800 K. The different polynomial approximations employed for the particular range, k, of the normalized time are denoted by the various colors red, blue, and green. A single polynomial fit is used to describe the normalized droplet surface area profile, see Figs. 3.73a and 3.74a. Two polynomial fits are needed to describe the normalized profile of the droplet surface temperature for the smaller initial mass fraction of TTIP, see Fig. 3.73b, whereas for the larger initial TTIP mass fraction, only one polynomial approximation is enough, see Fig. 3.74b. The normalized

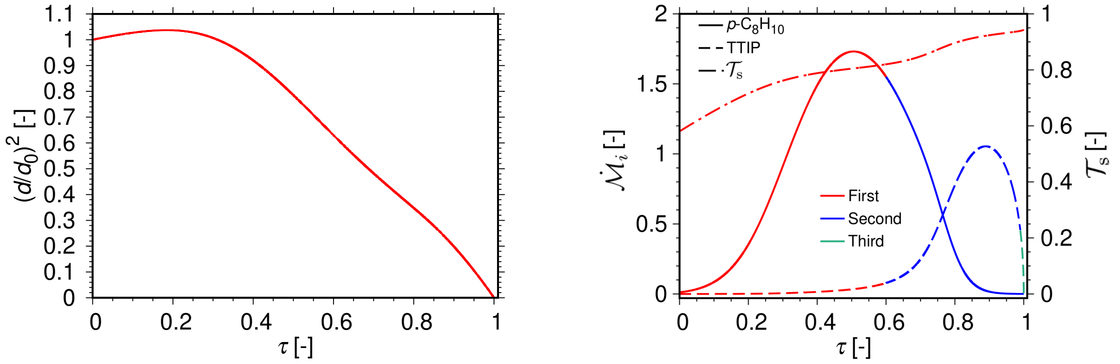

(a) Normalized droplet surface area. (b) Mass evaporation rates and $\mathcal{T}_s$.

Figure 3.74: Fitted normalized profiles of the droplet surface area, mass evaporation rates, and droplet surface temperature with normalized droplet lifetime τ for different initial droplet sizes. Initial conditions: $T_{l,0} = 293.15$ K, $p = 1$ bar, $u_0 = 4$ m/s and 8 m/s, $T_{g,0} = 800$ K, $Y_{\mathrm{TTIP},0} = 0.25$, $Y_{p\text{-}\mathrm{C_8H_{10}},0} = 0.75$ (Narasu et al. [133]).

Table 3.4: The polynomial coefficients for normalized droplet surface area, mass evaporation rates, and droplet surface temperature along with the lifetimes of the droplet for various initial conditions at $T_{g,0} = 800$ K and $Y_{\mathrm{TTIP},0} = 0.25$ (Narasu et al. [133]).

T_s	mdot_p-xylene	mdot_TTIP	(d/d_0)^2	**0.25**	**800**
5.786411863335e–01	9.921384844510e–01	–7.146219245076e+00	8.441316825843e+01	–5.457919897736e+02	2.017766081568e+03
–4.560015249911e+03	6.397435616191e+03	–5.416114191724e+03	2.526581761710e+03	–4.977569969594e+02	**1.00**
1.050799670253e–02	4.954782105080e–01	–8.313008192118e+00	2.476511371876e+02	–2.497098011637e+03	1.553272682435e+04
–5.480070371541e+04	1.104360500583e+05	–1.263947428216e+05	7.595563248731e+04	–1.830608969640e+04	**0.60**
2.553365705688e+03	–6.932396358383e+04	5.078482452392e+05	–1.735739827051e+06	3.056016255592e+06	–2.155494966950e+06
–1.679215289182e+06	4.981428002998e+06	–4.542822312106e+06	1.985375523754e+06	–3.506250344144e+05	**1.00**
1.718710000000e–06	1.345007970993e–03	–5.410849240512e–02	9.992277039120e–01	–7.434697282191e+00	2.286317344798e+01
4.841146337495e+01	–4.613989536747e+02	1.131769788048e+03	–1.235729439426e+03	5.239730506376e+02	**0.60**
3.219322387983e+04	–3.235445625627e+05	1.377863737425e+06	–3.147644279626e+06	3.827882460161e+06	–1.357252787276e+06
–2.915180529334e+06	4.998800497823e+06	–3.631887609653e+06	1.347660166346e+06	–2.088900607777e+05	**1.00**
9.995521864682e–01	3.676412959894e–01	–1.653073008970e+00	1.231773986581e+01	–6.219632600118e+01	1.103540776847e+02
–6.284972096235e+01	–5.362890113381e+01	1.170268418134e+02	–8.453883709362e+01	2.380211754709e+01	**1.00**
5	0.190952100000e+00	0.175232100000e+00	10	0.700926900000e+00	0.625860000000e+00
25	3.749095000000e+00	3.228029000000e+00	50	12.91216000000e+00	10.84631000000e+00

profile of the mass evaporation rate of p-xylene is captured by using two polynomial approximations, and that of TTIP is described by employing three polynomial fits, see Figs. 3.73b and 3.74b.

The profiles of the normalized droplet surface area, the surface temperature of the droplet as well as the mass evaporation rates of both the liquid components may be retrieved using the polynomial equations, provided the boiling temperature of TTIP, the lifetime of the droplet for the different initial conditions, and the normalization parameters defined in Eqs. (3.6)–(3.8) are known. The details with respect to recovering the original numerical simulation results by using the polynomial approximations is presented next.

The data to retrieve the original numerical simulation results of a TTIP/p-xylene droplet of initial mass fraction of TTIP of 0.25 at ambient gas temperature of 800 K is presented in Tab. 3.4. The names of the variables, T_s, mdot_p-xylene, mdot_TTIP,

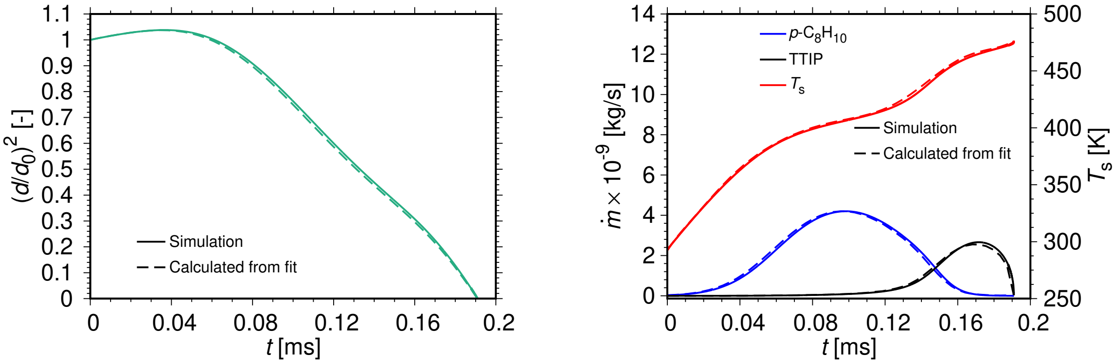

(a) Normalized droplet surface area. (b) Mass evaporation rates and T_s.

Figure 3.75: Temporal variation of the droplet surface area, mass evaporation rates, and droplet surface temperature. Initial conditions: $r_{\mathrm{d},0} = 5$ µm, $T_{\mathrm{l},0} = 293.15$ K, $p = 1$ bar, $u_0 = 4$ m/s, $T_{\mathrm{g},0} = 800$ K, $Y_{\mathrm{TTIP},0} = 0.25$, $Y_{p\text{-}\mathrm{C_8H_{10}},0} = 0.75$ (Narasu et al. [133]).

and (d/d_0)^2, for which the parameterization is performed, are given in the first line of the table. The last two columns of the first line provide with the initial TTIP mass fraction and the ambient air temperature. The eleven polynomial coefficients of Eq. (3.9), required to describe the surface temperature of the droplet, T_s, along with the upper normalized time limit up to which these coefficients are valid are displayed in the second and third lines in red color. Only a single polynomial fit is needed to capture the temperature profile for this specific initial condition. Therefore, the entire dimensionless droplet lifetime of unity is taken into account. The two sets of polynomials required for the recovery of the mass evaporation rate of p-xylene along with their validity range is given in the subsequent four lines in blue color. The next four black lines present the two polynomial sets for the mass evaporation rate of TTIP. The following two lines in green color provide with the same information for the normalized droplet surface area. Finally, four triplets of the initial droplet radius and its droplet lifetimes at relative velocities of 4 m/s and 8 m/s are presented in the last two lines. It is to be noted that the droplet radii are given in µm and the lifetimes of the droplet are provided in ms.

For a TTIP/p-xylene droplet of initial radius of 5 µm at relative velocity of 4 m/s for initial mass fraction of TTIP of 0.25 at ambient gas temperature of 800 K, the procedure for the recovery of the original numerical simulation results using the data provided in Tab. 3.5, is presented next. With respect to the conditions of initial TTIP mass fraction of 0.25 and ambient temperature of 800 K, the polynomial approximations given by Eq. (3.9) are employed to calculate the mean profiles of the normalized parameters using a normalized time step of 0.02. For the mass evaporation rate of the TTIP component, the third polynomial approximation is valid within the range of 0.99 to 1.0 of the normalized time, during which the precursor solution droplet is almost completely evaporated and the size of the droplet becomes very small, about less than one percent of the initial droplet size, which is tantamount to 10^{-9} times the initial droplet mass. Therefore, for the normalized mass evaporation rate of TTIP, the third polynomial approximation is neglected and thus, for the final normalized time step, the second polynomial fit is employed. Figure 3.75 displays the profiles of the temporal evolution of the normalized droplet surface area, the droplet surface temperature, and the mass evaporation rates of the both the liquid components for a TTIP/*p*-xylene droplet of initial radius of 5 µm at ambient gas temperature of 800 K for initial mass fraction of TTIP of 0.25 at relative velocity of 4 m/s. The solid lines represent the original numerical simulation results and the dashed lines display the curves computed using the polynomial approximations by taking into account the equations for the normalized parameters, the value of the boiling temperature of TTIP, and the lifetime of the droplet for the corresponding initial condition that is investigated.

There are a few recommendations that needs to be taken into account regarding the use of the data provided in Tab. 3.5, to ensure that there is no compromise on precision while calculating the profiles of various parameters. While using the values of the lifetime of the droplet, that is provided for different initial conditions investigated in the present study, it needs to be taken care to use these values at least up to four decimal places. Further, a minimum of twelve decimal places is required to be used while employing the coefficients of the polynomial fits. The total error between the profiles of the parameters computed using the polynomial fits and the original numerical simulation results is less than two percent. The total error comprises of the accumulation of different types of errors, which is discussed next. As the initial size of the droplet is varied, so does the total number of times steps in each numerical simulation. Thus, the number of time steps are adapted to the same value of ten thousand in order to compute the mean profile of various parameters, which results in a maximum error of approximately 0.75%. The mean profiles of the four different droplet sizes are used to recreate the original simulation results for a specific droplet size that contributes an error of about 0.67 %. The number of time steps are reduced to fifty and the different profile ranges are adapted using polynomial approximations, both of which cause an error of around 0.1 %. The simulations concerning flame spray pyrolysis are very complex and computationally expensive. Therefore, it is not possible to incorporate detailed simulations of sprays considering the precursor/solvent droplet heating and evaporation characteristics. In such scenarios, the parameterization given in the present study is very much helpful.

For the ambient gas temperatures of 800 K and 1200 K as well as for the initial mass fractions of TTIP of 0.025 and 0.25, the tabulated data for the various parameters are provided in Tab. 3.5. Table 3.4 represents the data given by the third set of Tab. 3.5. Further, a code in the *C* programming language is presented in Tab. 3.6, to read the data provided in Tab. 3.5.

The precursor/solvent droplet of titanium(IV) isopropoxide and *p*-xylene undergoes puffing and micro-explosion [131]. In order to study these processes a new one dimensional model is developed which is discussed in the next section.

Table 3.5: The polynomial coefficients for normalized droplet surface area, mass evaporation rates, and droplet surface temperature along with the lifetimes of the droplet for various initial conditions (Narasu et al. [133]).

T_s	mdot_p-xylene	mdot_TTIP	(d/d_0)^{2}	**0.025**	**800**
5.805844037628e–01	7.040066636610e–01	5.866081246482e–02	–6.981662175211e+00	5.934528001454e+01	–3.170143491127e+02
9.670886032134e+02	–1.724189377894e+03	1.795372067264e+03	–1.016017139636e+03	2.420701058308e+02	**0.90**
1.927876380754e+05	–1.100331356676e+06	2.000846046819e+06	–4.889931315665e+05	–1.956782387552e+06	4.334052914010e+05
2.359368071398e+06	–2.742365283220e+05	–3.134123940129e+06	2.618450808441e+06	–6.503895684627e+05	**1.00**
1.825322842717e–02	–3.930216029149e–01	2.618381493363e+01	–3.129292754331e+02	2.313442354332e+03	–8.684693388918e+03
1.858078858578e+04	–2.412193173236e+04	1.899686040652e+04	–8.419662079912e+03	1.622080954600e+03	**0.90**
–4.202830226579e+07	2.058004955686e+08	–3.166999488744e+08	2.992429795503e+07	2.938548610572e+08	–1.342719453565e+07
–3.226035416508e+08	–8.456717501336e+06	4.090852506281e+08	–3.061713124361e+08	7.072211206123e+07	**1.00**
3.368230115332e–04	–3.285294007150e–02	1.092192613978e+00	–1.544351439900e+01	1.152063462980e+02	–5.030781516811e+02
1.352094213959e+03	–2.264137769521e+03	2.300912307306e+03	–1.298258871385e+03	3.119820328577e+02	**0.90**
4.087415775633e+07	–1.994997694353e+08	3.049555224263e+08	–2.461593337570e+07	–2.858078416259e+08	7.624842722785e+06
3.157101298405e+08	1.425561164292e+07	–4.053255052881e+08	3.011902317031e+08	–6.936144622301e+07	**1.00**
9.986855105016e–01	4.250231149167e–01	–4.985053465586e+00	5.817961637435e+01	–3.858930344366e+02	1.441056785376e+03
–3.374707883693e+03	5.029652641506e+03	–4.608006955973e+03	2.356925287354e+03	–5.136443120000e+02	**1.00**
5	0.178042100000e+00	0.163734400000e+00	10	0.654936500000e+00	0.586204800000e+00
25	3.514266000000e+00	3.032695000000e+00	50	12.13086000000e+00	10.20970000000e+00
T_s	mdot_p-xylene	mdot_TTIP	(d/d_0)^{2}	**0.025**	**1200**
5.803167941360e–01	1.027753707434e+00	–2.121754395414e+00	2.800713692321e+01	–2.360840587066e+02	9.316140120707e+02
–2.049535117154e+03	2.672638350758e+03	–2.042405064833e+03	8.351397521497e+02	–1.378312447888e+02	**0.90**
–1.603384685247e+06	7.566442156338e+06	–1.107815969115e+07	4.896809733252e+05	1.009507313790e+07	1.827635536493e+05
–1.068761579231e+07	–9.145676706101e+05	1.328125832062e+07	–9.419219989796e+06	2.087730638262e+06	**1.00**
3.361992011817e–03	8.566253839477e–01	–3.677614646636e+00	–7.147155859479e+01	2.448222300102e+03	–1.555194499205e+04
4.677137113278e+04	–7.903330225980e+04	7.725229028134e+04	–4.093790995331e+04	9.127672572053e+03	**0.90**
–3.810783050544e+07	1.871241124150e+08	–2.890001035275e+08	2.833912663858e+07	2.684908116529e+08	–1.346846589530e+07
–2.954938119280e+08	–6.556411693407e+06	3.752210034426e+08	–2.818118348368e+08	6.526340424508e+07	**1.00**
3.823302500081e–04	–3.699058747171e–02	1.232649795596e+00	–1.747393471576e+01	1.306492839306e+02	–5.710023699305e+02
1.534286827451e+03	–2.566977650973e+03	2.605514886438e+03	–1.468106715527e+03	3.522856306382e+02	**0.90**
5.543997249976e+07	–2.714144773912e+08	4.165511141075e+08	–3.530745938736e+07	–3.909560824701e+08	1.242245630899e+07
4.330944164488e+08	1.753390812866e+07	–5.569062278079e+08	4.155312009026e+08	–9.598882128843e+07	**1.00**
9.999505632669e–01	5.077603555637e–01	–4.872695271502e+00	6.331433446027e+01	–4.647759127010e+02	1.747336270991e+03
–3.896197368050e+03	5.404614821289e+03	–4.595398843135e+03	2.197011966843e+03	–4.525401853463e+02	**1.00**
5	0.112315500000e+00	0.104445900000e+00	10	0.417782400000e+00	0.378763200000e+00
25	2.280303000000e+00	1.993087000000e+00	50	7.972444000000e+00	6.787167000000e+00
T_s	mdot_p-xylene	mdot_TTIP	(d/d_0)^{2}	**0.25**	**800**
5.786411863335e–01	9.921384844510e–01	–7.146219245076e+00	8.441316825843e+01	–5.457919897736e+02	2.017766081568e+03
–4.560015249911e+03	6.397435616191e+03	–5.416114191724e+03	2.526581761710e+03	–4.977569969594e+02	**1.00**
1.050799670253e–02	4.954782105080e–01	–8.313008192118e+00	2.476511371876e+02	–2.497098011637e+03	1.553272682435e+04
–5.480070371541e+04	1.104360500583e+05	–1.263947428216e+05	7.595563248731e+04	–1.830608969640e+04	**0.60**
2.553365705688e+03	–6.932396358383e+04	5.078482452392e+05	–1.735739827051e+06	3.056016255592e+06	–2.155494966950e+06
–1.679215289182e+06	4.981428002998e+06	–4.542822312106e+06	1.985375523754e+06	–3.506250344144e+05	**1.00**
1.718710000000e–06	1.345007970993e–03	–5.410849240512e–02	9.992277039120e–01	–7.434697282191e+00	2.286317344798e+01
4.841146337495e+01	–4.613989536747e+02	1.131769788048e+03	–1.235729439426e+03	5.239730506376e+02	**0.60**
3.219322387983e+04	–3.235445625627e+05	1.377863737425e+06	–3.147644279626e+06	3.827882460161e+06	–1.357252787276e+06
–2.915180529334e+06	4.998800497823e+06	–3.631887609653e+06	1.347660166346e+06	–2.088900607777e+05	**1.00**
9.995521864682e–01	3.676412959894e–01	–1.653073008970e+00	1.231773986581e+01	–6.219632600118e+01	1.103540776847e+02
–6.284972096235e+01	–5.362890113381e+01	1.170268418134e+02	–8.453883709362e+01	2.380211754709e+01	**1.00**
5	0.190952100000e+00	0.175232100000e+00	10	0.700926900000e+00	0.625860000000e+00
25	3.749095000000e+00	3.228029000000e+00	50	12.91216000000e+00	10.84631000000e+00
T_s	mdot_p-xylene	mdot_TTIP	(d/d_0)^{2}	**0.25**	**1200**
5.786147633266e–01	1.306583335756e+00	–9.305303342509e+00	1.250129813165e+02	–9.014406937495e+02	3.547540792700e+03
–8.313689685649e+03	1.195465835107e+04	–1.033845575147e+04	4.930010678498e+03	–9.952688923941e+02	**1.00**
1.244734080980e–02	–5.998474717454e–01	4.103763525584e+01	–5.988933425090e+02	4.639914922008e+03	–1.065173773268e+04
–2.773101377632e+04	1.954895804179e+05	–4.176556173995e+05	4.095125762153e+05	–1.566902064524e+05	**0.60**
–1.142857599276e+05	1.167687963520e+06	–5.053741243812e+06	1.173210239465e+07	–1.453548834389e+07	5.488957072068e+06
1.059909680186e+07	–1.856166467948e+07	1.346985120375e+07	–4.944071342096e+06	7.515559333452e+05	**1.00**
5.159454443846e–05	–4.568716037421e–03	1.414304924222e–01	–5.137181141616e–01	–2.286066635094e+01	3.406931692011e+02
–1.883816939625e+03	5.376859574590e+03	–8.471179474114e+03	7.015943989250e+03	–2.384363903510e+03	**0.60**
9.768876650431e+04	–1.017350146553e+06	4.496051270305e+06	–1.068389979979e+07	1.361294747951e+07	–5.452249893305e+06
–1.006409920190e+07	1.841455972743e+07	–1.382985875545e+07	5.254174819648e+06	–8.279640737214e+05	**1.00**
9.991672481841e–01	5.593239241382e–01	–4.683715183220e+00	5.870627591036e+01	–4.191664010908e+02	1.460709689353e+03
–2.936521154310e+03	3.620014826509e+03	–2.710620548822e+03	1.132145181426e+03	–2.021423533500e+02	**1.00**
5	0.118647200000e+00	0.110309000000e+00	10	0.441219100000e+00	0.399872800000e+00
25	2.407211000000e+00	2.103634000000e+00	50	8.414424000000e+00	7.164424000000e+00

Table 3.6: Code in programming language *C* to read the data set provided in Tab. 3.2 (Narasu et al. [133]).

```c
/*A C Program to read the polynomial coefficients and the droplet lifetimes*/
#include<stdio.h>

void main()
{
        FILE *fptrnew;
        fptrnew = fopen("coeffs.dat","r");

        double Yttip_0[4], Tg_0[4], a_temp1[2][6][4], a_temp2[2][6][4], a_xyl1[2][6][4], a_xyl2[2][6][4], a_ttip1[2][6][4], a_ttip2[2][6][4], a_d1[2][6][4];
        double t_r10_u8[4], t_r10_u4[4], t_r5_u8[4], t_r5_u4[4], coeffs[65][6];
        int i, j, k, N, L1, L2, L3, L4, r_0[4];
        char a[65][6];
        double k_d1[4], k_temp1[4], k_temp2[4], k_xyl1[4], k_xyl2[4], k_ttip1[4], k_ttip2[4], t_r50_u8[4], t_r50_u4[4], t_r25_u8[4], t_r25_u4[4],

        for(k=1; k<=4; k++)
        {
        if(k<=2)      N = 17; // number of lines corresponding to initial TTIP mass fraction of 0.25
        else          N = 15; // number of lines corresponding to initial TTIP mass fraction of 0.025
        for(i=1; i<=N; i++) // Starts reading the lines
        {
        for(j=1; j<=6; j++)
        {
        if(i==1&&j==1)             fscanf(fptrnew,"%s",&a[i][j]);
        else if(i==1&&j==2)        fscanf(fptrnew,"%s",&a[i][j]);
        else if(i==1&&j==3)        fscanf(fptrnew,"%s",&a[i][j]);
        else if(i==1&&j==4)        fscanf(fptrnew,"%s",&a[i][j]);
        else
        {
        fscanf(fptrnew,"%lf",&coeffs[i][j]);
        if(i==1&&j==5) Yttip_0[k] = coeffs[i][j]; // reads the initial TTIP mass fraction
        if(i==1&&j==6) Tg_0[k] = coeffs[i][j]; // reads the initial ambient temperature

        if(k>2)       {L1 = 2; L2 = 3;}
        else          {L1 = 2; L2 = 3; L3 = 4; L4 = 5;}
        if(i==L2&&j==6)            k_temp1[k] = coeffs[i][j]; // reads the range up to which the coefficients for the temperature is valid
        else if(i==L1||i==L2)      a_temp1[i][j][k] = coeffs[i][j]; // reads the coefficients for the temperature
        if(k<=2)
        {if(i==L4&&j==6)           k_temp2[k] = coeffs[i][j]; // reads the second range up to which the coefficients for the temperature is valid
        else if(i==L3||i==L4)      a_temp2[i][j][k] = coeffs[i][j];} // reads the coefficients for the second range of temperature (Y_TTIP = 0.025)

        if(k>2)       {L1 = 4; L2 = 5; L3 = 6; L4 = 7;}
        else          {L1 = 6; L2 = 7; L3 = 8; L4 = 9;}
        if(i==L2&&j==6)            k_xyl1[k] = coeffs[i][j]; // reads the first range up to which the coefficients for the mass evaporation rate of p-xylene is valid
        else if(i==L4&&j==6)       k_xyl2[k] = coeffs[i][j]; // reads the second range up to which the coefficients for the mass evaporation rate of p-xylene is valid
        else if(i==L1||i==L2)      a_xyl1[i][j][k] = coeffs[i][j]; // reads the coefficients for the first range of p-xylene
        else if(i==L3||i==L4)      a_xyl2[i][j][k] = coeffs[i][j];  // reads the coefficients for the second range of p-xylene

        if(k>2)       {L1 = 8; L2 = 9; L3 = 10; L4 = 11;}
        else          {L1 = 10; L2 = 11; L3 = 12; L4 = 13;}
        if(i==L2&&j==6)            k_ttip1[k] = coeffs[i][j]; // reads the first range up to which the coefficients for the mass evaporation rate of ttip is valid
        else if(i==L4&&j==6)       k_ttip2[k] = coeffs[i][j];  // reads the second range up to which the coefficients for the mass evaporation rate of ttip is valid
        else if(i==L1||i==L2)      a_ttip1[i][j][k] = coeffs[i][j]; // reads the coefficients for the first range of ttip
        else if(i==L3||i==L4)      a_ttip2[i][j][k] = coeffs[i][j]; // reads the coefficients for the second range of ttip

        if(k>2)       {L1 = 12; L2 = 13;}
        else          {L1 = 14; L2 = 15;}
        if(i==L2&&j==6)            k_d1[k] = coeffs[i][j]; // reads the range up to which the coefficients for the normalized droplet surface area is valid
        else if(i==L1||i==L2)      a_d1[i][j][k] = coeffs[i][j]; // reads the coefficients for the normalized droplet surface area

        if(k>2)       {L1 = 14; L2 = 15;}
        else          {L1 = 16; L2 = 17;}
        if(i==L1)
        {
        if(j==1) r_0[1] = coeffs[i][j]; // reads the droplet radius of 5 µm
        if(j==2) t_r5_u4[k] = coeffs[i][j]; // reads the droplet lifetime for radius of 5 µm and relative velocity of 4 m/s
        if(j==3) t_r5_u8[k] = coeffs[i][j]; // reads the droplet lifetime for radius of 5 µm and relative velocity of 8 m/s
        if(j==4) r_0[2] = coeffs[i][j];  // reads the droplet radius of 10 µm
        if(j==5) t_r10_u4[k] = coeffs[i][j]; // reads the droplet lifetime for radius of 10 µm and relative velocity of 4 m/s
        if(j==6) t_r10_u8[k] = coeffs[i][j]; // reads the droplet lifetime for radius of 10 µm and relative velocity of 8 m/s
        }
        else if(i==L2)
        {
        if(j==1) r_0[3] = coeffs[i][j];  // reads the droplet radius of 25 µm
        if(j==2) t_r25_u4[k] = coeffs[i][j]; // reads the droplet lifetime for radius of 25 µm and relative velocity of 4 m/s
        if(j==3) t_r25_u8[k] = coeffs[i][j]; // reads the droplet lifetime for radius of 25 µm and relative velocity of 8 m/s
        if(j==4) r_0[4] = coeffs[i][j];  // reads the droplet radius of 50 µm
        if(j==5) t_r50_u4[k] = coeffs[i][j]; // reads the droplet lifetime for radius of 50 µm and relative velocity of 4 m/s
        if(j==6) t_r50_u8[k] = coeffs[i][j]; // reads the droplet lifetime for radius of 50 µm and relative velocity of 8 m/s
        }
        }
        }
        }
        }

} // end of program
```

3.4.3 Analysis of the One-Dimensional Model Results

In this section, the processes of puffing and possible micro-explosion are investigated in addition to the heating and evaporation for the precursor solution system of TTIP and *p*-xylene. For this purpose, the one-dimensional model, see section 2.3, is employed to describe the droplet heating and evaporation and is modified appropriately to incorporate the effects of puffing and micro-explosion, see section 2.3.3. Following the previous experimental studies concerning FSP [29, 130, 131], the initial conditions for the numerical simulations are selected. At first, the results calculated using the one-dimensional model are compared with that computed employing the zero-dimensional model, see Narasu et al. [133] as well as previous section, due to the unavailability of the experimental data to validate the results of the present numerical study. Further, the numerical investigation of the characteristics of puffing and micro-explosion of the precursor/solvent droplet of TTIP/*p*-xylene are carried out and additionally, a parameter study is also performed.

Firstly, the results of the one-dimensional and the zero-dimensional models are compared with each other without taking into consideration the puffing and micro-explosion. Since the one-dimensional model requires the discretization of the interior of the droplet, a grid independence study is performed with the objective of evaluating the resolution of the numerical grid. For that purpose, Fig. 3.76 displays the temporal variation of the mass fractions of TTIP (blue color) and *p*-xylene (black color) along with the temperature (red color) of the droplet at the surface and center for a TTIP/*p*-xylene droplet of initial radius of 50 μm for initial mass fraction of TTIP of 0.25 at a relative velocity of 4 m/s for ambient gas temperature of 1200 K. Figure 3.76a shows the profiles of the mass fractions of both the components whereas Fig. 3.76b presents the plot of the surface temperature of the droplet. The initial conditions for the grid independence study are chosen based on the expectation that the maximum

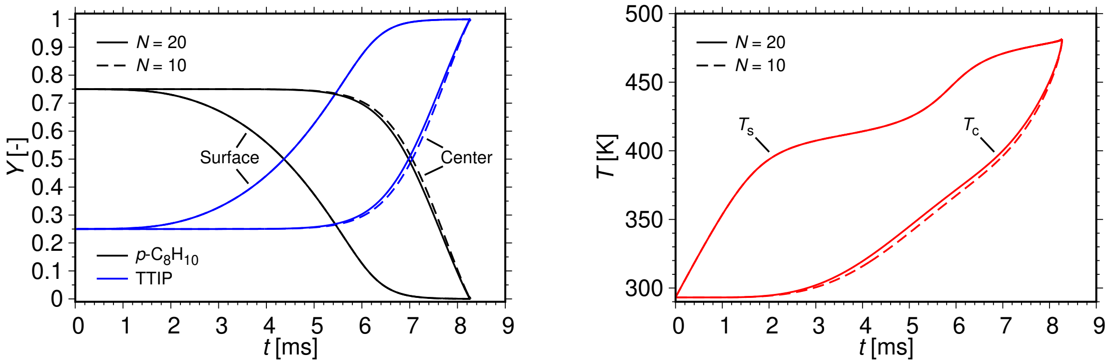

(a) Species mass fractions at the surface and center of the droplet with time.

(b) Temperature at the surface and center of the droplet with time.

Figure 3.76: Temporal variation of the species mass fractions and temperature at the surface and center of the droplet for different grid sizes, N, for the purpose of grid independence study. Initial conditions: $r_{\mathrm{d},0} = 50$ μm, $T_{\mathrm{l},0} = 293.15$ K, $p = 1$ bar, $u_0 = 4$ m/s, $T_{\mathrm{g},0} = 1200$ K, $Y_{\mathrm{TTIP},0} = 0.25$, $Y_{p\text{-}\mathrm{C_8H_{10}},0} = 0.75$ (Narasu and Gutheil [81]).

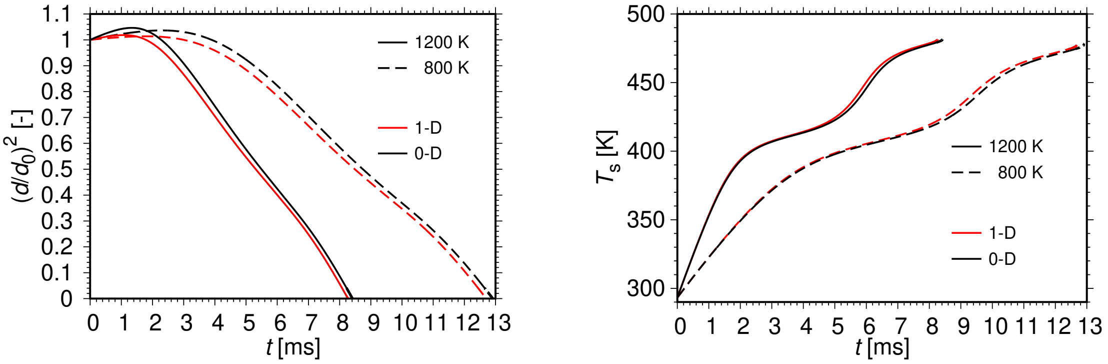

(a) Normalized droplet surface area.

(b) Droplet surface temperature.

Figure 3.77: Temporal variation of the normalized droplet surface area and droplet surface temperature. Initial conditions: $r_{\mathrm{d},0} = 50$ μm, $T_{\mathrm{l},0} = 293.15$ K, $p = 1$ bar, $u_0 = 4$ m/s, $T_{\mathrm{g},0} = 800$ K and 1200 K, $Y_{\mathrm{TTIP},0} = 0.25$, $Y_{p\text{-}\mathrm{C_8H_{10}},0} = 0.75$ (Narasu and Gutheil [81]).

differences are observed for the highest initial precursor mass fraction for the larger sized droplets. The different grid resolutions of ten (dashed lines) and twenty (solid lines) are considered. As the number of grid points used to resolve the droplet interior is increased from ten to twenty, the lifetime of the droplet is reduced by 0.01 %. Further, increasing the resolution of the grid by a factor of two has a minor effect on the evolution of the profiles of the temperature and the mass fraction of the liquid components. Hence, ten grid points are used for the discretization of the droplet throughout the present study.

Figure 3.77 presents the profiles of the normalized droplet surface area and the temperature at the surface of the droplet versus time for a TTIP/*p*-xylene droplet of initial radius of 50 μm at relative velocity of 4 m/s for initial TTIP mass fraction of 0.25 at ambient temperatures of 800 K (dashed lines) and 1200 K (solid lines). The red color curves represent the results calculated using the one-dimensional model and the black, that by employing the zero-dimensional model. Initially, the droplet heats up and expands due to the variable liquid properties used in the model. At the higher ambient temperature of 1200 K, the variation of the liquid density is much stronger than at lower ambient temperature of 800 K, which results in larger initial droplet expansion at 1200 K. The initial heating period is followed by the quasi-steady evaporation phase where the preferential evaporation of *p*-xylene occurs since *p*-xylene is more volatile than TTIP. The temperature of the droplet increases further and the evaporation of the TTIP component becomes dominant. Also, for the lower ambient air temperature, the heat transfer between the ambience and the droplet is reduced as compared to that at higher ambient temperature, which results in slower evaporation of the precursor solution droplet and thus, prolongs the droplet lifetime. At both ambient gas temperatures, the difference in the lifetimes of the droplet calculated by the one-dimensional and the zero-dimensional models is less than two percent.

For a droplet consisting of the precursor solution of TTIP and *p*-xylene, Fig. 3.78 shows the temporal variation of the droplet temperature (red color) as well as the mass fractions of TTIP (blue color) and *p*-xylene (black color) at the surface (solid lines)

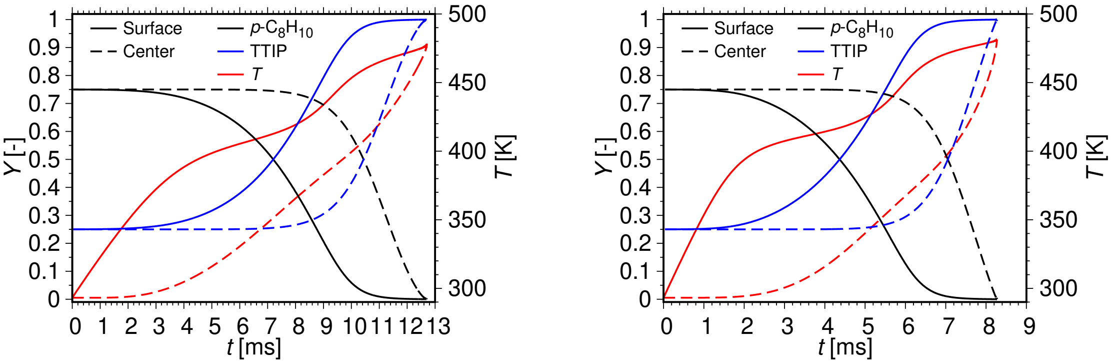

(a) $T_{\mathrm{g},0} = 800$ K.

(b) $T_{\mathrm{g},0} = 1200$ K.

Figure 3.78: Temporal variation of the species mass fractions and temperature at the surface and center of the droplet. Initial conditions: $r_{\mathrm{d},0} = 50$ µm, $T_{\mathrm{l},0} = 293.15$ K, $p = 1$ bar, $u_0 = 4$ m/s, $Y_{\mathrm{TTIP},0} = 0.25$, $Y_{p\text{-}\mathrm{C_8H_{10}},0} = 0.75$ (Narasu and Gutheil [81]).

and center (dashed lines) of the droplet for initial droplet radius of 50 µm at relative velocity of 4 m/s for initial mass fraction of TTIP of 0.25 at ambient gas temperatures of 800 K and 1200 K. During the initial heating period of the droplet, the temperature at the surface of the droplet increases. Further, quasi-steady evaporation occurs where the higher volatile *p*-xylene evaporates preferentially causing the decrease of the mass fraction of *p*-xylene at the droplet surface and thus, resulting in the increase of the TTIP mass fraction. Because of the diffusive nature of the whole process, the values of the temperature of the droplet and the mass fractions of TTIP and *p*-xylene at the center of the droplet lag behind their corresponding values at the droplet surface. But, the change in the mass fractions of the liquid components at the droplet interior is slower as compared to the rise of the temperature, since mass diffusion is slower than thermal conduction [83]. This creates a situation where there is a significant amount of the higher volatile component of *p*-xylene at its boiling point, that may lead to the occurrence of puffing and possible micro-explosion, which is discussed in detail in the next section.

Puffing and Micro-Explosion

During the synthesis of nanoparticles using flame spray pyrolysis, some of the experimental studies found that the precursor solution droplets undergo puffing and micro-explosion in addition to the processes of heating and evaporation [30, 66, 67]. There exists numerous experimental investigations focusing on the phenomena of puffing and micro-explosion of droplets. These phenomena are not restricted to precursor solution droplets in flame spray pyrolysis alone. Slurry [136] and emulsified fuels [137] droplets also depict such behavior. Puffing and micro-explosions of composite rapeseed oil/water and diesel/water droplets were studied experimentally by Antonov et al. [138]. It was concluded that for larger sized droplets, the time to micro-explosion was prolonged. Also, with the increase in the temperature, the time to micro-explosion decreased. An experimental study was conducted by Zhang et al. [139] on droplets consisting of n-pentanol and diesel using the droplet suspension methodology. They reported the occurrence of puffing for different concentrations of n-pentanol and diesel at an ambient temperature of 973 K.

Recent experimental investigations have reported that during the generation of nanoparticles via flame spray pyrolysis, puffing as well as micro-explosion of the precursor solution droplets occur. Stodt et al. [66] used high speed shadowgraphy technique in order to analyze the generation of iron oxide nanoparticles via flame spray pyrolysis, using iron(III) nitrate nonahydrate as the precursor in a solution consisting of ethanol and 2-ethylhexanoic acid. They confirmed the occurrence of micro-explosion for the concerned precursor/solvent droplets. High spatiotemporal resolution shadowgraphy imaging methodology was employed by Jüngst et al. [67] to understand the nanoparticle synthesis using spray flames, where the precursor solution system of iron(III) nitrate nonahydrate in ethanol and 2-ethylhexanoic acid was used. The experimental study visualized and confirmed micro-explosions of the precursor/solvent droplets. Also, it was found that the size of the disrupting droplets were about sixty eight percent of that of the regular droplets. During the nanoparticle generation using spray flames, micro-explosion of the precursor/solvent droplets consisting of iron(III) nitrate nonahydrate, ethanol, and 2-ethylhexanoic acid was found by Stodt et al. [30]. They used high-speed camera imaging methodology to confirm the occurrence of micro-explosion.

The micro-explosion of single burning precursor solution droplets constituting of titanium(IV) isopropoxide and xylene was experimentally studied by Li et al. [131]. They reported that the lower volatile precursor, that is titanium(IV) isopropoxide, gets accumulated at the surface of the droplet, which was the reason for the occurrence of micro-explosion of the precursor/solvent droplet. Further, the higher volatile solvent, which is xylene, inside the droplet gets heated up which causes the increase of the pressure, thus leading to micro-explosion. Therefore, the puffing and micro-explosion of a precursor solution droplet consisting of TTIP and p-xylene is investigated in detail in this section.

Before discussing the characteristics of puffing and micro-explosion, a grid independence study is performed to evaluate the numerical resolution of the grid. For that purpose, Fig. 3.79 presents the profiles of the temperature (red color) and the mass fractions of TTIP (blue color) and p-xylene (black color) at the surface and center of a single TTIP/p-xylene droplet of initial radius of 50 μm for initial TTIP mass fraction of 0.25 at relative velocity of 4 m/s for ambient temperature of 1200 K. The profiles of the mass fractions of TTIP and p-xylene are displayed in Fig. 3.79a and that of the droplet surface temperature is shown in Fig. 3.79b. Ten (dashed lines) and twenty (solid lines) grids are considered for the grid independence study. Comparing the temporal profiles of the temperature and the mass fractions of the liquid components computed by both the grid resolutions, there is no significant difference initially. However, at the later stages, there exist differences amounting to less than one percent with respect to the lifetime of the droplet. Also, as the number of grid points is increased from ten to twenty, the time to micro-explosion decreases by less than one percent. Most importantly, there is negligible effect on the puffing and micro-explosion of the precursor/solvent

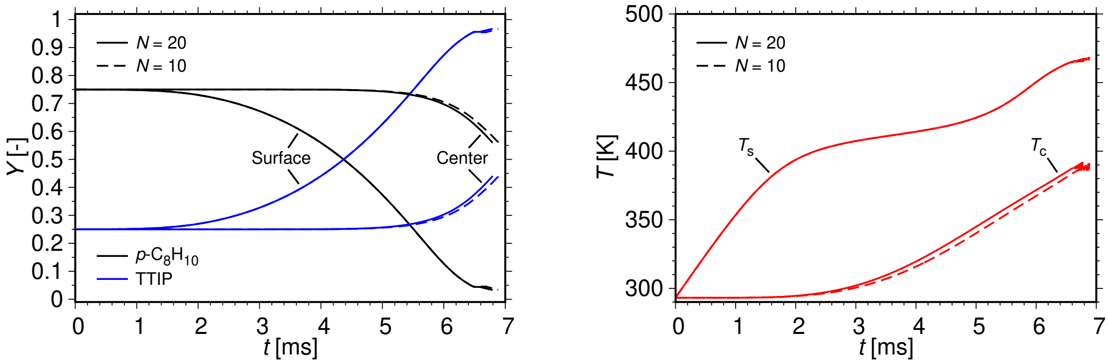

(a) Species mass fractions at the surface and center of the droplet with time.

(b) Temperature at the surface and center of the droplet with time.

Figure 3.79: Temporal variation of the species mass fractions and temperature at the surface and center of the droplet for different grid sizes, N, for the purpose of grid independence study. Initial conditions: $r_{\mathrm{d},0} = 50$ µm, $T_{\mathrm{l},0} = 293.15$ K, $p = 1$ bar, $u_0 = 4$ m/s, $T_{\mathrm{g},0} = 1200$ K, $Y_{\mathrm{TTIP},0} = 0.25$, $Y_{p\text{-}\mathrm{C_8H_{10}},0} = 0.75$ (Narasu and Gutheil [81]).

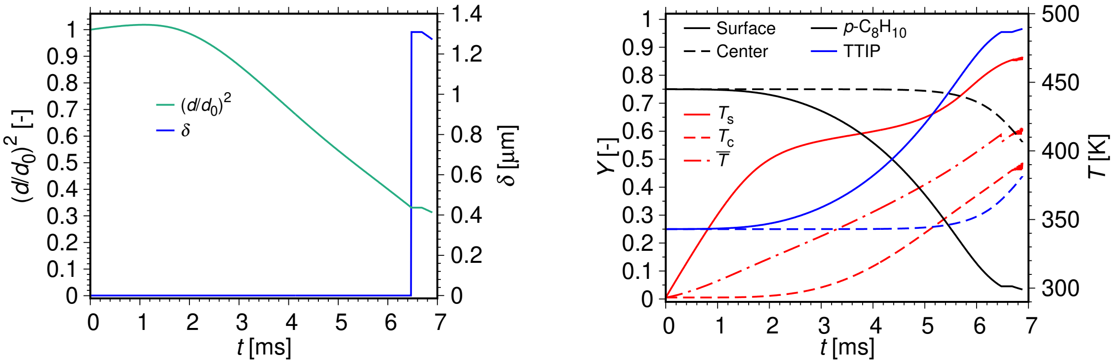

(a) Normalized droplet surface area and liquid shell thickness.

(b) Species mass fractions, temperature at droplet surface and center, $\overline{T}$.

Figure 3.80: Temporal variation of the normalized droplet surface area, liquid shell thickness, species mass fractions and temperature at the surface and center of the droplet, and spatially averaged droplet temperature, $\overline{T}$. Initial conditions: $r_{\mathrm{d},0} = 50$ µm, $T_{\mathrm{l},0} = 293.15$ K, $p = 1$ bar, $u_0 = 4$ m/s, $T_{\mathrm{g},0} = 1200$ K, $Y_{\mathrm{TTIP},0} = 0.25$, $Y_{p\text{-}\mathrm{C_8H_{10}},0} = 0.75$ (Narasu and Gutheil [81]).

droplet because of employing of a larger grid resolution. Further, for both resolutions of the numerical grid, the number of puffs remains the same. Hence, for the rest of the numerical study, in order to discretize the interior of the droplet, ten grid points are used.

The puffing and micro-explosion is visible, see the oscillations of the temperature profile in Fig. 3.79, at the final stages of the lifetime of the droplet. Figure 3.80 displays the characteristics of heating, evaporation, puffing, and micro-explosion for a TTIP/p-xylene droplet of initial radius of 50 µm with relative velocity of 4 m/s for

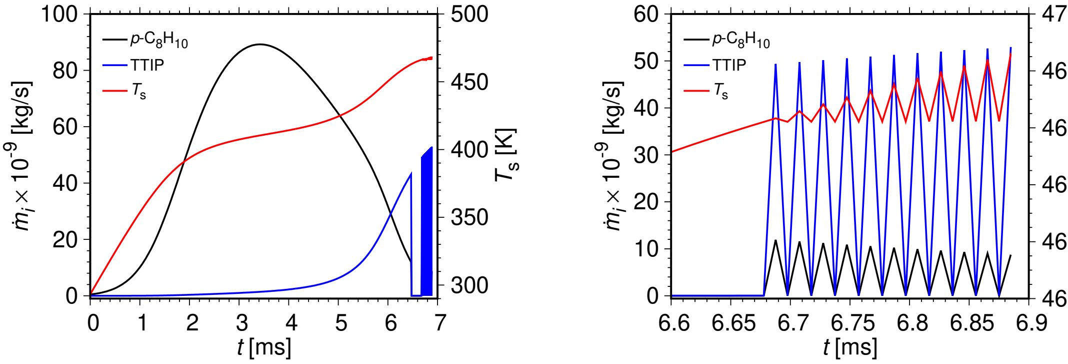

(a) Normal view.

(b) Zoomed view.

Figure 3.81: Temporal variation of the mass evaporation rates and droplet surface temperature. Initial conditions: $r_{\mathrm{d},0} = 50$ µm, $T_{\mathrm{l},0} = 293.15$ K, $p = 1$ bar, $u_0 = 4$ m/s, $T_{\mathrm{g},0} = 1200$ K, $Y_{\mathrm{TTIP},0} = 0.25$, $Y_{p\text{-C}_8\text{H}_{10},0} = 0.75$ (Narasu and Gutheil [81]).

initial TTIP mass fraction of 0.25 at ambient air temperature of 1200 K. Figure 3.80a shows the temporal evolution of the normalized droplet surface area (green color) and the liquid shell thickness (blue color) whereas Fig. 3.80b presents the temporal variation of the temperature (red color) and the mass fractions of TTIP (blue color) and p-xylene (black color) at the surface (solid lines) and center (dashed lines) of the droplet along with the spatial average temperature, $\overline{T}$ (dash dotted line) inside the droplet.

The initial droplet expansion occurs due to the heating, see Fig 3.80a, which is attributed to the variable liquid properties employed in the model. At the surface of the droplet, the initial droplet heating causes the increase of the temperature. Further, the preferential evaporation of the higher volatile p-xylene occurs which causes the increase of the mass fraction of the lower volatile TTIP at the droplet surface. Because of the diffusive nature of the entire process, the temperature and the TTIP mass fraction remain lower than their corresponding values at the droplet surface whereas the mass fraction of p-xylene is higher than that at the surface of the droplet, see Fig 3.80b. The spatial average temperature, $\overline{T}$, reaches the boiling temperature of p-xylene of 412 K, at a time of 6.48 ms, as shown in Fig 3.80b. Because of the formation of the liquid shell, $\overline{T}$ reduces slightly after which it increases further. The lower volatile precursor accumulates at the surface of the droplet, thus resulting in the liquid shell formation. The formation of the liquid shell offers resistance to the process of evaporation which results in a very slight increase of the thickness of the liquid shell and the normalized droplet surface area. Previous experimental investigations focusing on the micro-explosion of of water/fuel [68] and TTIP/xylene [131] droplets had reported such instances with respect to the increase of the size of the droplet.

The spatial average temperature, $\overline{T}$, increases further and reaches the boiling temperature of the higher volatile p-xylene once again at 6.69 ms, which initiates the puffing and thus, the hindrance to evaporation is lifted. This is reflected in the profiles of the droplet temperature at the surface and center along with the $\overline{T}$, see Fig 3.80b, as well as the profiles of the mass evaporation rates of both the liquid components shown

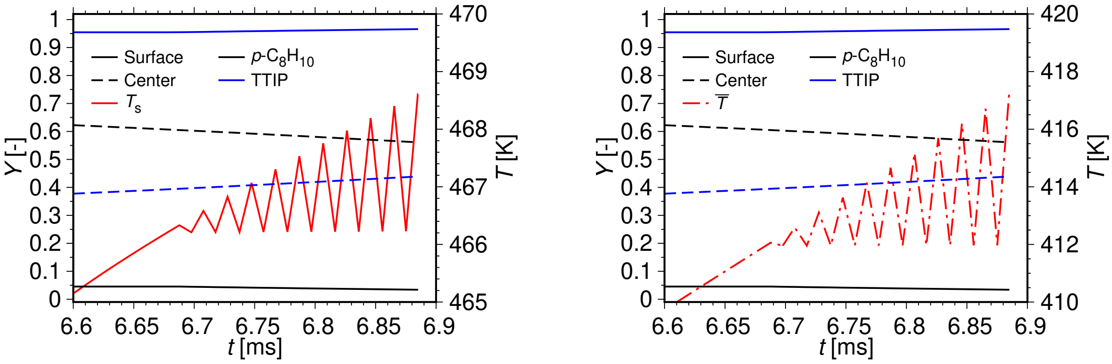

(a) Zoomed view of T_{s}. (b) Zoomed view of $\overline{T}$.

Figure 3.82: Temporal variation of the species mass fractions and temperature at the surface and center of the droplet and spatially averaged droplet temperature, $\overline{T}$. Initial conditions: $r_{\mathrm{d},0} = 50$ µm, $T_{\mathrm{l},0} = 293.15$ K, $p = 1$ bar, $u_0 = 4$ m/s, $T_{\mathrm{g},0} = 1200$ K, $Y_{\mathrm{TTIP},0} = 0.25$, $Y_{p\text{-}\mathrm{C_8H_{10}},0} = 0.75$ (Narasu and Gutheil [81]).

in Fig. 3.81. The mass evaporation rates of TTIP (blue color) and p-xylene (black) along with the surface temperature (red color) of the droplet are displayed in Fig. 3.81 for the same conditions of Fig 3.80. Figure 3.81b shows the zoomed view of Fig. 3.81a for the purpose of better resolution. Once the puffing is initiated, the thickness of the liquid shell reduces because of the the decrease of the size of the droplet, as displayed in Fig 3.80a. These processes repeat resulting in a sequence of ten puffs. At about 6.89 ms, as the pressure inside the droplet exceeds the ambient pressure, see Eq. 2.39, the micro-explosion of the droplet occurs resulting in the complete evaporation of the droplet. The trigger for the puffing of the precursor solution droplet is the variation of the temperature. However, the puffing is also reflected in the mass evaporation rates of both the components, as displayed in Fig. 3.81b. Hence, the evaluation of the number of puffs may be performed by analyzing the variation of the mass evaporation rates of both the components as well as the droplet temperature.

In order to view better the oscillations of the profiles of the temperature, a zoomed view of these are provided in Fig. 3.82. Figure 3.82a displays the zoomed view of the temperature at the surface of the droplet and Fig. 3.82b provides with the zoomed view of the spatial average temperature, $\overline{T}$. The hindrance to heating and evaporation is released during each puff, thus causing the spatial average temperature to breach the boiling point of p-xylene temporarily, as shown in Fig. 3.82b. The building up of the liquid shell occurs and the whole process is repeated. Thus, the lower value of the temperature remains the same as the boiling temperature of the higher volatile species. But, during puffing, the maximum value of the temperature increases since the liquid shell becomes thinner with each puff, see Fig. 3.80a. It is noticeable that the increase of the temperature at the surface of the droplet, during the process of puffing, is smaller than that of the spatial average temperature, $\overline{T}$, since the thermal conductivity of the liquid shell is lower than the thermal conductivity at the interior of the droplet.

The spatial variation of the profiles of the temperature (red color) and the mass fractions of TTIP (blue color) and p-xylene (black) is presented in Fig. 3.83. Figure 3.83a

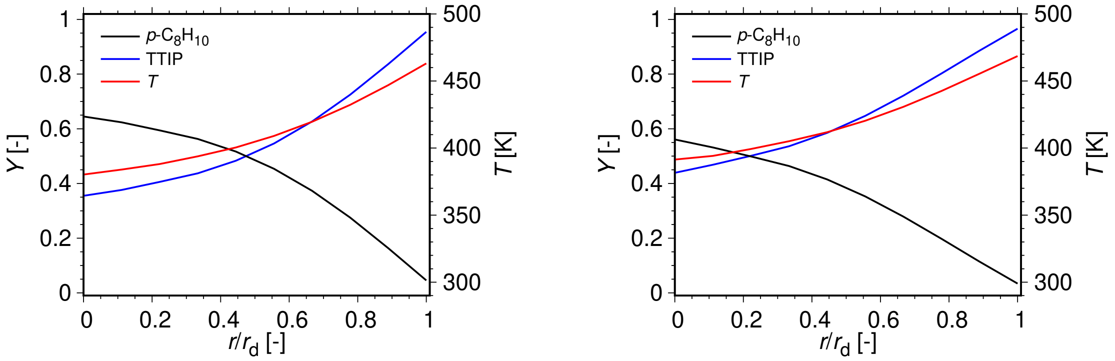

(a) At the time of liquid shell formation at $t = 6.48$ ms.

(b) At the time of micro-explosion at $t = 6.89$ ms.

Figure 3.83: Spatial variation of the species mass fractions and temperature inside the droplet. Initial conditions: $r_{d,0} = 50$ µm, $T_{l,0} = 293.15$ K, $p = 1$ bar, $u_0 = 4$ m/s, $T_{g,0} = 1200$ K, $Y_{TTIP,0} = 0.25$, $Y_{p\text{-}C_8H_{10},0} = 0.75$ (Narasu and Gutheil [81]).

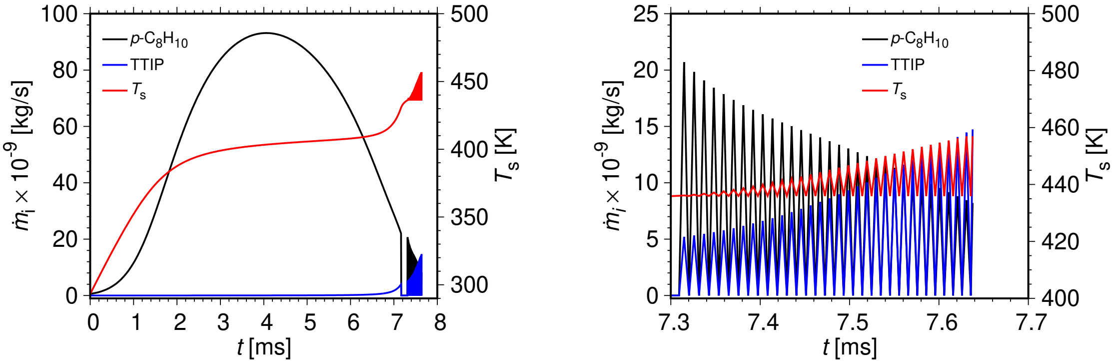

(a) Normal view.

(b) Zoomed view.

Figure 3.84: Temporal variation of the mass evaporation rates and droplet surface temperature. Initial conditions: $r_{d,0} = 50$ µm, $T_{l,0} = 293.15$ K, $p = 1$ bar, $u_0 = 4$ m/s, $T_{g,0} = 1200$ K, $Y_{TTIP,0} = 0.025$, $Y_{p\text{-}C_8H_{10},0} = 0.975$ (Narasu and Gutheil [81]).

presents these profiles at the time of formation of the liquid shell, at $t = 6.48$ ms, whereas Fig. 3.83b shows these curves at the time of micro-explosion of the precursor solution droplet, at $t = 6.89$ ms. The diffusion of the liquid components from the surface to the center of the droplet is slower than the conduction of heat because of the differences in the mass and thermal diffusivity. Therefore, an ideal situation is created which is suitable for the occurrence of puffing and micro-explosion, where there is a large amount of the higher volatile component of p-xylene at its boiling temperature inside the droplet. It is to be noted that this is only a necessary condition for the puffing and micro-explosion of the precursor/solvent droplet and not a sufficient condition.

To understand the influence of the initial precursor loading on the characteristics of puffing and micro-explosion, for a reduced initial mass fraction of TTIP of 0.025,

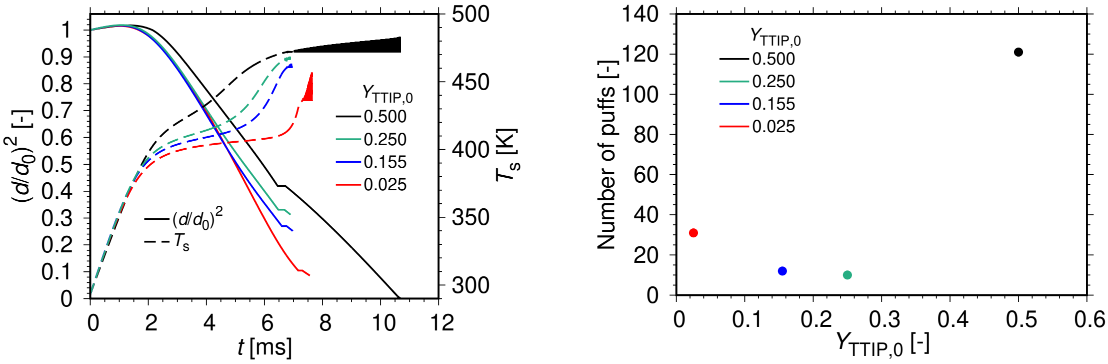

(a) Normalized droplet surface area and droplet surface temperature.

(b) Number of puffs for different initial TTIP mass fractions.

Figure 3.85: Temporal variation of the normalized droplet surface area and droplet surface temperature along with the number of puffs for different initial mass fractions of TTIP. Initial conditions: $r_{d,0} = 50$ µm, $T_{l,0} = 293.15$ K, $p = 1$ bar, $u_0 = 4$ m/s, $T_{g,0} = 1200$ K (Narasu and Gutheil [140]).

Fig. 3.84 displays the temporal evolution of the droplet surface temperature (red color) along with the the mass evaporation rates of TTIP (blue color) and p-xylene (black color) for a TTIP/p-xylene droplet of initial radius of 50 µm at relative velocity of 4 m/s for ambient temperature of 1200 K, where the zoomed view of Fig. 3.84a is shown in Fig. 3.84b. Comparing Figs. 3.81 and 3.84, with the decrease of the initial precursor mass fraction, more p-xylene is available to evaporate that delays the initiation of puffing since the spatial average droplet temperature $\overline{T}$ takes more time in attaining the boiling temperature of the higher volatile p-xylene, and thus, prolongs the lifetime of the droplet. Therefore, the process of puffing starts at 7.31 ms and the micro-explosion of the precursor/solvent droplet occurs at 7.63 ms. Further, reducing the initial mass fraction of TTIP from 0.25 to 0.025, doubles the frequency at which the puffs occur and thus, increases the number of puffs from 10 to 31, see Figs. 3.81b and 3.84b. Further, for the higher initial mass fraction of the precursor of 0.25, the peak values of the mass evaporation rates of both the liquid components remain almost constant, Fig. 3.81b. However, for the lower initial TTIP mass fraction of 0.025, it is striking to note that the maxima values of the mass evaporation rate of the TTIP component strongly increase and that for p-xylene staunchly decrease, Fig. 3.84b. During puffing, the range of variation of the temperature at the surface of the droplet is around 2 K for the higher initial TTIP mas fraction of 0.25, whereas for the lower initial mass fraction of precursor of 0.025, it is about 22 K. Thus, it is found that varying the initial precursor loading strongly influences the number of puffs as well as the lifetime of the droplet. Hence, a more detailed study is presented next.

Figure 3.85a displays the temporal evolution of the normalized droplet area (solid lines) and the temperature (dashed lines) at the surface of the droplet for a TTIP/p-xylene droplet of initial radius of 50 µm at relative velocity of 4 m/s for ambient gas temperature of 1200 K. Figure 3.85b shows the number of puffs for the different initial mass fractions investigated in this present study. In total, four different initial TTIP

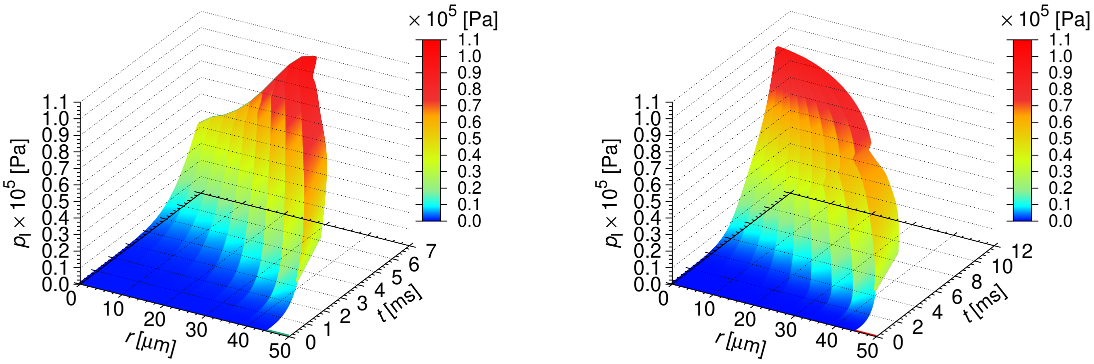

(a) $Y_{\mathrm{TTIP},0} = 0.25$.

(b) $Y_{\mathrm{TTIP},0} = 0.50$.

Figure 3.86: Temporal and spatial variation of the pressure in the interior of the droplet for initial mass fractions of TTIP of 0.25 and 0.50. Initial conditions: $r_{\mathrm{d},0} = 50$ μm, $T_{\mathrm{l},0} = 293.15$ K, $p = 1$ bar, $u_0 = 4$ m/s, $T_{\mathrm{g},0} = 1200$ K (Narasu and Gutheil [81]).

mass fractions of 0.025 (red color), 0.155 (blue color), 0.25 (green color), and 0.50 (black color) are considered. With the increase of the initial mass fraction of the precursor, the lower volatile TTIP accumulates faster at the surface of the droplet and therefore, speeds up the formation of the liquid shell, eventually causing earlier puffing of the precursor solvent droplet. Further, increasing the initial precursor loading reduces the number of puffs, see Fig. 3.85b, because of the reduced lifetime of the droplet and the less steep increase in the temperature at the surface of the droplet. Also, as the initial precursor mass fraction is increased, the time between the puffing and micro-explosion is reduced, thus resulting in earlier micro-explosion of the droplet as confirmed by the previous investigations concerning various precursor solvent systems [71, 70]. But, for the highest initial precursor mass fraction of 0.50, the TTIP/*p*-xylene droplet experiences continuous puffing until the complete evaporation of the droplet without the occurrence of micro-explosion, since the pressure at the interior of the droplet never increases beyond the ambient pressure. Hence, for the TTIP mass fraction of 0.50, the number of puffs is very high, see Fig. 3.85b, as compared to the other initial precursor compositions considered in this present study.

Figure 3.86 displays the temporal and spatial variation of the pressure, as defined in Eq. 2.40, in the interior of a TTIP/*p*-xylene droplet of initial radius of 50 μm with relative velocity of 4 m/s at ambient gas temperature of 1200 K. Figure 3.86a shows the variation of the pressure for initial TTIP mass fraction of 0.25 whereas Fig. 3.86b presents the pressure variation for initial mass fraction of TTIP of 0.50. It is found that for both the cases, the pressure is highest at the surface of the droplet and lowest at the center of the droplet. As the process of evaporation of the droplet progresses, the size of the droplet becomes smaller, as seen in Fig. 3.86, which causes the pressure in the droplet interior to increase. For the lower initial mass fraction of TTIP of 0.25, see Fig. 3.86a, the pressure at the surface of the droplet reaches the ambient pressure at 6.89 ms, thus resulting in the micro-explosion of the droplet. However, for the higher initial TTIP mass fraction of 0.50, the pressure inside the droplet does not reach the ambient pressure and therefore, the puffing continues until the droplet completely

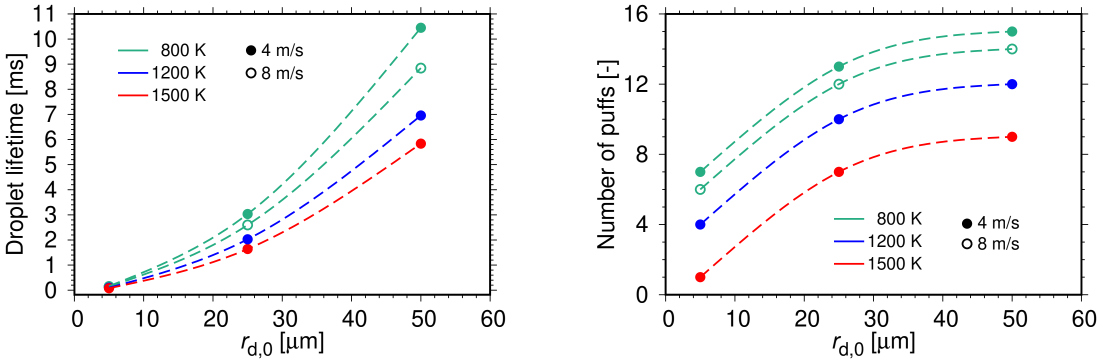

(a) Droplet lifetime.

(b) Number of puffs.

Figure 3.87: Lifetime of the droplet and number of puffs for different initial droplet radii, ambient gas temperatures, and relative velocities. Initial conditions: $T_{\mathrm{l},0} = 293.15$ K, $p = 1$ bar, $Y_{\mathrm{TTIP},0} = 0.155$, $Y_{p\text{-}\mathrm{C_8H_{10}},0} = 0.845$ (Narasu and Gutheil [81]).

evaporates without causing micro-explosion, see Fig. 3.86b.

A parameter study is performed to explore the impact of varying the initial size of the droplet, the ambient air temperature, and the relative velocity on the lifetime of the droplet and number of puffs, which is presented in Fig. 3.87, for a TTIP/*p*-xylene droplet of initial mass fraction of TTIP of 0.155. Initial droplet radii of 5 μm, 25 μm, and 50 μm are considered at relative velocities of 4 m/s (filled symbols) and 8 m/s (open symbols) for ambient gas temperatures of 800 K (green color), 1200 K (blue color), and 1500 K (red color). Figure 3.87a displays the lifetime of the droplet and Fig. 3.87b presents the number of puffs for various initial conditions investigated in the present study. For droplets with initial radius of 50 μm at relative velocity of 4 m/s, as the ambient gas temperature is increased from 800 K to 1500 K, the droplets evaporate faster, see Fig. 3.87a, due to the increased heat transfer rate between the ambience and the droplet which results in fewer number of puffs before the occurrence of micro-explosion, see Fig. 3.87b. Increasing the relative velocity by a factor of two leads to enhanced evaporation of the droplet, see Fig. 3.87a, because of the stronger convection rate and thus, decreases the number of puffs, see Fig. 3.87b. Further, as the initial size of the droplet is decreased from 50 μm to 5μm, the evaporation of the droplet is faster, see Fig. 3.87a, because of the reduced heating and evaporation time owing to the smaller mass of the droplet to be evaporated, and thus, decreases the number of puffs that occur before micro-explosion, see Fig. 3.87b. It is to be noted that for the precursor/solvent droplet of TTIP/*p*-xylene of initial radius of 5 μm at ambient temperature of 1500 K with relative velocity of 4 m/s, the droplet undergoes only one puff before the onset of micro-explosion.

Thus, puffing is initiated as the boiling point of the higher volatile component is reached at the interior of the droplet, and micro-explosion of the droplet occurs once the pressure inside the droplet breaches the ambient pressure. The various factors that influence the characteristics of the puffing and micro-explosion of a precursor solution droplet during the synthesis of nanoparticles via flame sprays is understood through the detailed parameter study performed for the TTIP/*p*-xylene droplet.

Summary and Outlook

In order to generate nanoparticles via spray flames, a precursor solution is injected and sprayed which results in the formation of droplets. These droplets may experience various processes such as heating, evaporation, thermal decomposition, puffing, and micro-explosion Further, gas phase combustion occurs followed by formation of nanoparticles. For the purpose of understanding the various processes experienced by the droplet, the numerical study of the multicomponent droplet behavior in an ambience of hot convective air is performed. The different multicomponent systems explored are ethanol/water, butanol/water, iron(III) nitrate nonahydrate/ethanol, and titanium(IV) isopropoxide/*p*-xylene. The multicomponent droplet heating and evaporation is described using the zero-dimensional and one-dimensional models. The zero-dimensional model, is an extension of the model formulated by Brenn et al. [52] for multicomponent droplets, which itself is an extension of the convective droplet heating and evaporation model of Abramzon and Sirignano [49] for single component droplets. The zero-dimensional model is coupled with the thermal decomposition model for the precursor solution system of INN and ethanol whereas for the precursor/solvent droplet of TTIP/*p*-xylene, the one-dimensional model is modified to accommodate the effects of puffing and possible micro-explosion.

For ethanol/water droplets, the zero-dimensional model is employed to describe the heating and evaporation characteristics in both dry and humid air. The results of the numerical investigation of ethanol/water droplet is validated against the experimental data of Ma et al. [141] and Ma et al. [75] at atmospheric pressure in an ambience of dry air. The non-ideal behavior of the liquid mixture is considered through the use of activity coefficients modeled using the UNIFAC approach [87]. Considering the real behavior of the liquids does not have an impact on the lifetime of the droplet, but, it does influence the characteristics of the heating and evaporation of the multicomponent droplet, particularly in an ambience of humid air. For ethanol/water droplets, increasing the initial composition of ethanol results in faster evaporation of the droplet due to the higher volatility of ethanol as compared to that of water. In an ambience of humid air, there occurs condensation of water at the surface of the droplet that causes enhanced evaporation of the ethanol component and retarded evaporation of the water component, thus prolonging the lifetime of the droplet. The water condensation is found to be stronger while employing the ideal mixture assumption as compared to when considering the real behavior of the liquid mixture.

A numerical study of the heating and evaporation of single butanol/water droplets in convective ambience at low ambient pressures is performed by employing the zero-dimensional model. During the droplet heating period, the droplet expands initially because of the variable liquid properties used in the model. The temperature at the surface of the droplet increases due to the initial droplet heating which is followed by the quasi-steady evaporation phase where the preferential evaporation of the water component occurs since water is more volatile than butanol after which, the evaporation of the butanol component dominates. Also, at higher ambient pressure of 60 mbar, the droplet surface temperature as well as the mass evaporation rates of butanol and water are higher than that at lower ambient pressure of 40 mbar, which results in reduced droplet lifetime of around forty percent. Further, at pressure of 40 mbar, changing the ambient gas mixture from methane/argon to hydrogen/argon, reduces the droplet lifetime by a factor of three because of the difference in the gas mixture properties. At lower ambient gas temperature of 400 K, the droplet evaporation is slowed down because of the reduced heat transfer rate between the ambience and the droplet, thus prolonging the lifetime of the droplet. With the increase of the initial mass fraction of water, the droplet evaporates faster owing to the higher volatility of water for both the ambient pressures of 40 mbar and 60 mbar.

In the case of INN/ethanol droplets, in addition to heating and evaporation, the thermal decomposition is also investigated. The numerical investigation of the droplet behavior is carried out in an ambience of both dry and humid air. If the temperature reached by the surface of the droplet during the process of evaporation is less than the thermal decomposition temperature of 403 K, the particle is formed inside the droplet, which is known as the droplet-to-particle pathway. Otherwise, thermal decomposition occurs transforming the precursor solution droplet entirely into the gas phase, known as the droplet into gas phase pathway. In the case of the droplet-to-particle pathway, the heating and evaporation of the liquid components of ethanol and water influence the overall process time. Increasing the initial mass fraction of INN results in the formation of larger sized particles, but does not affect the total process time. As the relative velocity is increased, the droplets evaporate faster resulting in slightly reduced process times, but does not affect the size of the final particle formed. Increasing the initial droplet radius from 1 μm to 5 μm prolongs the total process times and increases the final particle size in both dry and humid air. In an ambience of humid air, the condensation of water at the surface of the droplet increases the droplet surface temperature which results in enhanced evaporation of the ethanol component and retarded water evaporation, thus leading to increased process times. However, humidity has negligible effect on the final particle size.

In flame spray pyrolysis, there is the possibility that particles are formed following the droplet-to-particle pathway in colder regimes, such as close to the injector. This needs to be avoided since the particles formed via the droplet-to-particle pathway are larger in size as one of the major goal of flame spray pyrolysis is to produce smaller sized particles.

The thermal decomposition rate varies exponentially with respect to the temperature reached by the surface of the droplet during the process of heating and evaporation. In an ambience of dry air, at higher ambient air temperature of 1200 K, the temperature attained by the droplet surface is higher than that reached at lower ambient temperature of 800 K, which leads to faster thermal decomposition at 1200 K as compared to that at 800 K. Hence, the droplet heating and evaporation is the dominating factor with respect to the overall process time at higher ambient gas temperature of 1200 K whereas thermal decomposition dominates at lower ambient temperature of 800 K. In humid air, for both the ambient gas temperatures, due to condensation of water at the surface of the droplet, higher droplet surface temperatures are attained which promotes the process of thermal decomposition. Thus, the heating and evaporation dominates the process time for both the ambient gas temperatures in humid air. Even though the process of evaporation is slowed down due to the retarded evaporation of the water component, the enhanced thermal decomposition compensates for it. Therefore, the overall process times are shorter in humid air as compared to that in an ambience of dry air. In dry air, doubling the relative velocity from 4 m/s to 8 m/s, fastens the evaporation of the droplet, but the final temperatures reached by the droplet surface are lower at 8 m/s as compared to that attained at 4 m/s, which slows down the thermal decomposition process, thus prolonging the overall process time. However, in humid air, as the relative velocity is increased from 4 m/s to 8 m/s, the differences in the temperatures attained by the droplet surface at both the relative velocities is very small, and thus the disparity regarding the total process time is negligible. Increasing the initial size of the droplet prolongs the total process time for all the cases studied in dry and humid air because of the prolonged droplet heating and evaporation time as well as the lower final droplet surface temperatures attained for the larger droplets.

As the initial precursor loading is increased, the evaporation of the droplet becomes faster, but lower final droplet surface temperatures are reached that prolongs the thermal decomposition process. At lower ambient air temperature of 800 K, increasing the initial mass fraction of the precursor from 0.0125 to 0.025 and further to 0.200, increases the overall process time whereas at higher ambient temperature of 1200 K, the total process time is reduced. This confirms the existence of an intermediate transitional temperature, T^+, at which this reversal effect occurs for two particular initial precursor mass fractions considered in the present study, which was found to independent of the choice of the initial size of the droplet investigated in this study. However, with the increase of the relative velocity from 4 m/s to 8 m/s, T^+ increases by about 100 K. The total process time contributes to the global process time of flame spray pyrolysis. Therefore, it is recommended to choose an ambient gas temperature above T^+ in order to keep the overall process time short.

Polynomial approximations were used to parameterize the profiles of the normalized droplet surface area, the droplet surface temperature, the mass evaporation rates of ethanol and water, and the mass fraction of iron(III) nitrate. These results may be used in more complex simulations where iron(III) nitrate nonahydrate in ethanol is used as the precursor solution system to produce nanoparticles via flame spray pyrolysis .

For the precursor/solvent droplet of TTIP/p-xylene, at first, the characteristics of the heating and evaporation are investigated using the zero-dimensional model. The new variable physical properties of TTIP and p-xylene available from the study of Keller et al. [98] is employed. During the initial droplet heating, the droplet expands due to the use of the variable physical properties in the model. Further, the preferential evaporation of *p*-xylene occurs owing to its higher volatility as compared to that of TTIP, after which the evaporation of the TTIP component dominates. At higher ambient gas temperature of 1200 K, the droplets evaporate faster resulting in reduced droplet lifetimes as compared to that at lower ambient temperature of 800 K. As the relative velocity is doubled from 4 m/s to 8 m/s, the evaporation of the droplet is enhanced leading to reduced lifetimes of the droplet. Increasing the initial size of the droplet results in increased droplet lifetimes because of the prolonged droplet heating and evaporation time. With the increase of the initial mass fraction of TTIP, the droplet evaporation is slowed down due to the higher boiling point of TTIP as compared to that of *p*-xylene, thus prolonging the lifetimes of the droplet. The similarity of the profiles of the normalized droplet surface area, the droplet surface temperature as well as the mass evaporation rates of *p*-xylene and TTIP with respect to different initial droplet radii and relative velocity considered in the study, is utilized and these results are parameterized using polynomial fits. The parametrized results may be used in more complex simulations concerning flame spray pyrolysis where the precursor solution of titanium(IV) isopropoxide and *p*-xylene is used to synthesize TiO_2 nanoparticles.

The one-dimensional model is employed to describe the heating, evaporation, puffing, and possible micro-explosion of TTIP/*p*-xylene precursor solution droplets. There are five stages that a precursor solution droplet goes through, namely, heating, evaporation, liquid shell formation, puffing, and micro-explosion. Initial expansion of the droplet occurs during the droplet heating period. The droplet surface temperature increases causing the evaporation of the higher volatile *p*-xylene and eventually, resulting in the increase of the mass fraction of the lower volatile TTIP at the surface of the droplet. Thus, the liquid shell is formed at the droplet surface which offers resistance to evaporation. Once the boiling point of the higher volatile component of *p*-xylene is reached, puffing is initiated releasing the hinderance to evaporation. If the pressure at the droplet interior is higher than the ambient pressure, micro-explosion of the precursor/solvent droplet occurs. Increasing the initial mass fraction of TTIP shortens the time span between puffing and micro-explosion and causes earlier droplet micro-explosion. Further, with the increase of the initial precursor loading, the number of puffs and its frequency decreases. As the ambient gas temperature is increased, the droplets evaporate faster and thus, reduces the number of puffs before droplet micro-explosion occurs. With the increase of the relative velocity from 4 m/s to 8 m/s, the droplet evaporation is enhanced leading to fewer number of puffs before the occurrence of droplet micro-explosion. Increasing the initial size of the droplet prolongs the droplet heating and evaporation time and therefore, increases the number of puffs that occur before micro-explosion. For TTIP/*p*-xylene droplet of initial radius of 50 μm at relative velocity of 4 m/s for ambient air temperature of 1200 K, as the initial mass fraction of TTIP is increased to 0.50, the precursor solution droplet undergoes continuous puffing until the complete evaporation of the droplet without the occurrence of micro-explosion.

The present study is useful to understand the behavior of the droplet during the synthesis of nanoparticles via spray flames. Moreover, the simulations associated with flame spray pyrolysis are computationally very expensive and also complex in nature.

Hence, including elaborate spray simulations by taking into account the details of every process experienced by the droplet is not possible. In such circumstances the parameterized results are very useful, since it helps in reducing the computational time significantly.

The zero-dimensional and one-dimensional multicomponent droplet evaporation models may be extended to many more precursor solutions, to study their respective heating and evaporation characteristics and their influence on the generation of nanoparticles using spray flames. Future work should focus on including the parametrized results of the precursor solution droplets of iron(III) nitrate nonahydrate/ethanol and titanium(IV) isopropoxide/p-xylene in more complex spray simulations where these precursor/solvent systems are employed to produce nanoparticles. Further, another interesting challenge that is required to be looked into is regarding the inclusion of the gas phase reactions to study the generation of nanoparticles from the gas phase. In flame spray pyrolysis, the evaporation of the precursor solution is enhanced due to the occurrence of puffing and micro-explosion. Therefore, the influence of these phenomena on the properties of the nanoparticles that are synthesized using flame spray pyrolysis needs to be analyzed in the future.

Bibliography

[1] M. Vert, Y. Doi, K.-H. Hellwich, M. Hess, P. Hodge, P. Kubisa, M. Rinaudo, and F. Schué. Terminology for biorelated polymers and applications (iupac recommendations 2012). *Pure and Applied Chemistry*, 84(2):377–410, 2012.

[2] A. Knauer and J. M. Koehler. Explanation of the size dependent in-plane optical resonance of triangular silver nanoprisms. *Physical Chemistry Chemical Physics*, 18(23):15943–15949, 2016.

[3] Wikipedia contributors. Nanoparticle - Wikipedia, the free encyclopedia. https://en.wikipedia.org/wiki/NanoparticleProperties, 2022.

[4] T. Johannessen, R. Jensen, M. Mosleh, J. Johansen, U. Quaade, and H. Livbjerg. Flame synthesis of nanoparticles: applications in catalysis and product/process engineering. *Chemical Engineering Research and Design*, 82:1444–1452, 2004.

[5] W. Merchan-Merchan, W. C. Jimenez, O. R. Coria, and C. Wallis. Flame synthesis of nanostructured transition metal oxides: Trends, developments, and recent advances. In J. Pottathara, N. Kalarikkal, V. Kokol, S. Thomas, and Y. Grohens, editors, *Nanomaterials Synthesis*, pages 201–263. Elsevier, 2019.

[6] ProChimia Surfaces. Nanoparticles. https://prochimia.com/nanoparticles, 2022.

[7] R. Koirala, S. Pratsinis, and A. Baiker. Synthesis of catalytic materials in flames: opportunities and challenges. *Chemical Society Reviews*, 45:3053–3068, 2016.

[8] C. S. Lindberg, M. Y. Manuputty, J. Akroyd, and M. Kraft. A two-step simulation methodology for modelling stagnation flame synthesised aggregate nanoparticles. *Combustion and Flame*, 202:143–153, 2019. ISSN 0010-2180. doi: https://doi.org/10.1016/j.combustflame.2019.01.010. URL `http://www.sciencedirect.com/science/article/pii/S0010218019300215`.

[9] S. E. Pratsinis. Flame aerosol synthesis of ceramic powders. *Progress in Energy and Combustion Science*, 24(3):197–219, 1998.

[10] H. K. Kammler, L. Mädler, and S. E. Pratsinis. Flame synthesis of nanoparticles. *Chemical Engineering & Technology: Industrial Chemistry-Plant Equipment-Process Engineering-Biotechnology*, 24(6):583–596, 2001.

[11] B. Sun, S. Pokhrel, D. R. Dunphy, H. Zhang, Z. Ji, X. Wang, M. Wang, Y.-P. Liao, C. H. Chang, J. Dong, et al. Reduction of acute inflammatory effects of fumed silica nanoparticles in the lung by adjusting silanol display through calcination and metal doping. *ACS nano*, 9(9):9357–9372, 2015.

[12] Y. Deligiannakis, V. Tsikourkitoudi, P. Stathi, K. Wegner, J. Papavasiliou, and M. Louloudi. Pdo/pd^0/TiO$_2$ nanocatalysts engineered by flame spray pyrolysis: Study of the synergy of pdo/pd^0 on h2 production by hcooh dehydrogenation and the deactivation mechanism. *Energy & Fuels*, 34(11):15026–15038, 2020.

[13] F. Gao, Z. Xu, and H. Zhao. Flame spray pyrolysis made pt/TiO$_2$ photocatalysts with ultralow platinum loading and high hydrogen production activity. *Proceedings of the Combustion Institute*, 38(4):6503–6511, 2021.

[14] X. Yuan, L. Meng, Z. Xu, C. Zheng, and H. Zhao. Cuo quantum dots supported by SrTiO$_3$ perovskite using the flame spray pyrolysis method: Enhanced activity and excellent thermal resistance for catalytic combustion of co and CH$_4$. *Environmental Science & Technology*, 55(20):14080–14086, 2021.

[15] X. Yuan, C. Zheng, and H. Zhao. Photothermocatalytic removal of co and formaldehyde with excellent water vapor stability over dual-functional copper loading on TiO$_2$ synthesized via flame spray pyrolysis. *Solar RRL*, 5(9):2100490, 2021.

[16] S. Ding, H.-A. Chen, O. Mekasuwandumrong, M. J. Hülsey, X. Fu, Q. He, J. Panpranot, C.-M. Yang, and N. Yan. High-temperature flame spray pyrolysis induced stabilization of pt single-atom catalysts. *Applied Catalysis, B*, 281:119471, 2021.

[17] P. B. Neto, L. Buss, F. Meierhofer, H. F. Meier, U. Fritsching, and D. Noriler. Combustion kinetic analysis of flame spray pyrolysis process. *Chemical Engineering and Processing-Process Intensification*, 129:17–27, 2018.

[18] W. Y. Teoh, R. Amal, and L. Mädler. Flame spray pyrolysis: An enabling technology for nanoparticles design and fabrication. *Nanoscale*, 2(8):1324–1347, 2010.

[19] W. Y. Teoh. A perspective on the flame spray synthesis of photocatalyst nanoparticles. *Materials*, 6(8):3194–3212, 2013.

[20] H. Chang, S. J. Kim, H. D. Jang, and J. W. Choi. Synthetic routes for titania nanoparticles in the flame spray pyrolysis. *Colloids and Surfaces A: Physicochemical and Engineering Aspects*, 313:282–287, 2008.

[21] C. Weise, J. Menser, S. Kaiser, A. Kempf, and I. Wlokas. Numerical investigation of the process steps in a spray flame reactor for nanoparticle synthesis. *Proceedings of the Combustion Institute*, 35(2):2259–2266, 2015.

[22] J. E. Madero, J. Li, K.-Y. Shen, J. Wojtak, and R. L. Axelbaum. An approach to low-temperature flame spray pyrolysis for the synthesis of temperature-sensitive materials: Application to $Li_{1.2}Mn_{0.54}Ni_{0.13}Co_{0.13}O_2$. *Applications in Energy and Combustion Science*, 5:100020, 2021.

[23] N. H. Paulson, J. A. Libera, and M. Stan. Flame spray pyrolysis optimization via statistics and machine learning. *Materials & Design*, 196:108972, 2020.

[24] D. Dasgupta, P. Pal, R. Torelli, S. Som, N. Paulson, J. Libera, and M. Stan. Computational fluid dynamics modeling and analysis of silica nanoparticle synthesis in a flame spray pyrolysis reactor. *Combustion and Flame*, 236:111789, 2022.

[25] F. Meierhofer, L. Mädler, and U. Fritsching. Nanoparticle evolution in flame spray pyrolysis—process design via experimental and computational analysis. *AIChE Journal*, 66(2):e16885, 2020.

[26] P. B. Neto, F. Meierhofer, H. F. Meier, U. Fritsching, and D. Noriler. Modelling polydisperse nanoparticle size distributions as produced via flame spray pyrolysis. *Powder Technology*, 370:116–128, 2020.

[27] D. Dasgupta, P. Pal, R. Torelli, and S. Som. Computational fluid dynamics modeling of flame spray pyrolysis for nanoparticle synthesis. *2020 Spring Technical Meeting of the Central States Section of The Comb. Inst.*, 2020.

[28] A. Rittler, L. Deng, I. Wlokas, and A. Kempf. Large eddy simulations of nanoparticle synthesis from flame spray pyrolysis. *Proceedings of the Combustion Institute*, 36(1):1077 – 1087, 2017. ISSN 1540-7489. URL `http://www.sciencedirect.com/science/article/pii/S1540748916303947`.

[29] F. Schneider, S. Suleiman, J. Menser, E. Borukhovich, I. Wlokas, A. Kempf, H. Wiggers, and C. Schulz. Spraysyn–a standardized burner configuration for nanoparticle synthesis in spray flames. *Review of Scientific Instruments*, 90(8): 085108, 2019.

[30] M. F. Stodt, J. Kiefer, and U. Fritsching. Drop dynamics in heterogeneous spray flames for nanoparticle synthesis. *Atomization and Sprays*, 30(11), 2020.

[31] S. Suleiman, M. Nanjaiah, I. Skenderovic, T. Rosenberger, F. Kunze, I. Wlokas, E. Kruis, H. Wiggers, and C. Schulz. Atmospheric-pressure particle mass spectrometer for investigating particle growth in spray flames. *Journal of Aerosol Science*, page 105827, 2021.

[32] R. Tischendorf, M. Simmler, C. Weinberger, M. Bieber, M. Reddemann, F. Fröde, J. Lindner, H. Pitsch, R. Kneer, M. Tiemann, H. Nirschl, and H.-J. Schmid. Examination of the evolution of iron oxide nanoparticles in flame spray pyrolysis by tailored in situ particle sampling techniques. *Journal of Aerosol Science*, 154: 105722, 2021.

[33] R. Strobel and S. E. Pratsinis. Effect of solvent composition on oxide morphology during flame spray pyrolysis of metal nitrates. *Physical Chemistry Chemical Physics*, 13(20):9246–9252, 2011.

[34] A. Abdelsamie, F. E. Kruis, H. Wiggers, and D. Thévenin. Nanoparticle formation and behavior in turbulent spray flames investigated by DNS. *Flow, Turbulence and Combustion*, 105:497–516, 2020.

[35] G. Kastrinaki, S. Lorentzou, G. Karagiannakis, M. Rattenbury, J. Woodhead, and A. Konstandopoulos. Parametric synthesis study of iron based nanoparticles via aerosol spray pyrolysis route. *Journal of Aerosol Science*, 115:96 – 107, 2018. ISSN 0021-8502. doi: https://doi.org/10.1016/j.jaerosci.2017.10.005. URL `http://www.sciencedirect.com/science/article/pii/S0021850217300836`.

[36] F. F. Florena, F. Faizal, D. W. Maulana, S. T. Satrio, C. Panatarani, I. M. Joni, and S. Viridi. Numerical investigation of droplet evaporation phenomena in the spray methods. *IOP Conference Series: Materials Science and Engineering*, 550:012031, aug 2019. doi: 10.1088/1757-899x/550/1/012031. URL `https://doi.org/10.1088%2F1757-899x%2F550%2F1%2F012031`.

[37] W. A. Sirignano. *Fluid Dynamics and Transport of Droplets and Sprays*, volume 2. Cambridge University Press, Cambridge, 2010.

[38] C. K. Law. Multicomponent droplet combustion with rapid internal mixing. *Combustion and Flame*, 26:219–233, 1976.

[39] S. S. Sazhin. Advanced models of fuel droplet heating and evaporation. *Progress in energy and combustion science*, 32(2):162–214, 2006.

[40] R. Landis and A. F. Mills. Effect of internal diffusional resistance on the evaporation of binary droplets. *International Heat Transfer Conference Digital Library*, 1974.

[41] W. A. Sirignano. Fuel droplet vaporization and spray combustion theory. *Progress in Energy and Combustion Science*, 9(4):291–322, 1983.

[42] R. Kayser Jr and H. S. Bennett. Evaporation of a liquid droplet. *Journal of Research of the National Bureau of Standards. Section A, Physics and Chemistry*, 81(2-3):257, 1977.

[43] C. K. Law and H. Law. A d^2-law for multicomponent droplet vaporization and combustion. *AIAA journal*, 20(4):522–527, 1982.

[44] G. Godsave. Studies of the combustion of drops in a fuel spray—the burning of single drops of fuel. 4(1):818–830, 1953.

[45] F. Williams. *Combustion Theory*, volume 1. Addison-Wesley Publishing Company, Reading, 1965.

[46] D. R. Kassoy and F. A. Williams. Variable property effects on liquid droplet combustion. *AIAA Journal*, 6(10):1961–1965, 1968.

[47] C. K. Law. Quasi-steady droplet vaporization theory with property variations. *The Physics of Fluids*, 18(11):1426–1432, 1975.

[48] C. Chiang, M. Raju, and W. Sirignano. Numerical analysis of convecting, vaporizing fuel droplet with variable properties. *International journal of heat and mass transfer*, 35(5):1307–1324, 1992.

[49] B. Abramzon and W. Sirignano. Droplet vaporization model for spray combustion calculations. *International Journal of Heat and Mass Transfer*, 32(9):1605–1618, 1989.

[50] R. Clift, J. Grace, and M. Weber. *Bubbles, Drops and Particles.* Academic Press New York, 1978.

[51] N. Frössling. Uber die verdunstung fallender tropfen (the evaporation of falling drops). *Gerlands Beitrage zur Geophysik*, 52:107–216, 1938.

[52] G. Brenn, L. Deviprasath, F. Durst, and C. Fink. Evaporation of acoustically levitated multi-component liquid droplets. *International Journal of Heat and Mass Transfer*, 50(25-26):5073–5086, 2007.

[53] A. J. Marchese and F. L. Dryer. The effect of liquid mass transport on the combustion and extinction of bicomponent droplets of ethanol and water. *Combustion and Flame*, 105:104–122, 1996.

[54] G. Lupo and C. Duwig. A numerical study of ethanol–water droplet evaporation. *Journal of Engineering for Gas Turbines and Power*, 140(2):021401, 2018.

[55] X. Zhang, C. Shen, P. Cheng, and Q. Li. Response of subcritical evaporation of ethanol/water bi-component droplet to pressure oscillation. *Acta Astronautica*, 128:229–236, 2016.

[56] F. Yi and R. L. Axelbaum. Stability of spray combustion for water/alcohols mixtures in oxygen-enriched air. *Proceedings of the Combustion Institute*, 34(1): 1697–1704, 2013.

[57] S. F. L. Filho, G. C. Krieger Filho, J. A. van Oijen, A. Sadiki, and J. Janicka. A novel strategy to accurately represent the carrier gas properties of droplets evaporating in a combustion environment. *International Journal of Heat and Mass Transfer*, 137:1141–1153, 2019.

[58] B. E. Poling and J. P. Prausnitz, O'Connell. *The properties of gases and liquids*, volume 5. McGraw-Hill New York, 2001.

[59] S. S. Sazhin. Modelling of fuel droplet heating and evaporation: Recent results and unsolved problems. *Fuel*, 196:69–101, 2017.

[60] M. C. Heine and S. E. Pratsinis. Droplet and particle dynamics during flame spray synthesis of nanoparticles. *Industrial & engineering chemistry research*, 44 (16):6222–6232, 2005.

[61] R. Boichot and S. Krumdieck. Numerical modeling of the droplet vaporization for design and operation of liquid-pulsed CVD. *Chemical Vapor Deposition*, 21 (10-11-12):375–384, 2015.

[62] M. F. Stodt, C. Liu, S. Li, L. Mädler, U. Fritsching, and J. Kiefer. Phase-selective laser–induced breakdown spectroscopy in flame spray pyrolysis for iron oxide nanoparticle synthesis. *Proceedings of the Combustion Institute*, 38(1):1711–1718, 2021.

[63] P. Majerič and R. Rudolf. Advances in ultrasonic spray pyrolysis processing of noble metal nanoparticles. *Materials*, 13(16):3485, 2020.

[64] D. L. Gapale, S. A. Arote, and R. Y. Borse. Mathematical modeling of droplet formation, evaporation, and film growth to study crystallite size and film thickness of spray pyrolysis deposited TiO_2 thin films. *e-Journal of Surface Science and Nanotechnology*, 16:419–426, 2018.

[65] W. Widiyastuti, W.-N. Wang, I. W. Lenggoro, F. Iskandar, and K. Okuyama. Simulation and experimental study of spray pyrolysis of polydispersed droplets. *Journal of Materials Research*, 22(7):1888–1898, 2007.

[66] M. Stodt, J. D. Groeneveld, L. Mädler, J. Kiefer, and U. Fritsching. Microexplosions of multicomponent drops in spray flames. *Combustion and Flame*, 240: 112043, 2022.

[67] N. Jüngst, G. Smallwood, and S. Kaiser. Visualization and image analysis of droplet puffing and micro-explosion in spray-flame synthesis of iron oxide nanoparticles. *Experiments in Fluids*, 63(3):1–14, 2022.

[68] R. Fedorenko, D. Antonov, P. Strizhak, and S. Sazhin. Time evolution of composite fuel/water droplet radii before the start of puffing/micro-explosion. *International Journal of Heat and Mass Transfer*, 191:122838, 2022.

[69] S. W. Baek, J. H. Cho, et al. Microexplosion of aluminum slurry droplets. *International journal of heat and mass transfer*, 42(24):4475–4486, 1999.

[70] Y. Ren, J. Cai, and H. Pitsch. Theoretical single-droplet model for particle formation in flame spray pyrolysis. *Energy & Fuels*, 35(2):1750–1759, 2021.

[71] H. Li, C. D. Rosebrock, Y. Wu, T. Wriedt, and L. Mädler. Single droplet combustion of precursor/solvent solutions for nanoparticle production: Optical diagnostics on single isolated burning droplets with micro-explosions. *Proceedings of the Combustion Institute*, 37(1):1203–1211, 2019.

[72] P. Narasu, S. Boschmann, P. Pöschko, F. Zhao, and E. Gutheil. Modeling and simulation of single ethanol/water droplet evaporation in dry and humid air. *Combustion Science and Technology*, 192(7):1233–1252, 2020.

[73] C. K. Law. Recent advaces in droplet vaporization and combustion. *Progress in Energy and Combustion Science*, 8:171–201, 1982.

[74] G. Hubbard, V. Denny, and A. Mills. Droplet evaporation: Effects of transients and variable properties. *International Journal of Heat and Mass Transfer*, 18(9): 1003–1008, 1975.

[75] L. Ma, Y. Chou, X. Cui, and Z. Zheng. Research on double-component droplets evaporation properties. *Industrial Heating*, 43(1):13–16, 2014.

[76] P. Narasu, A. Keller, M. Kohns, H. Hasse, and E. Gutheil. Numerical study of the evaporation and thermal decomposition of a single iron (III) nitrate nonahydrate/ethanol droplet. *International Journal of Thermal Sciences*, 170: 107133, 2021.

[77] P. Narasu, A. Keller, M. Kohns, H. Hasse, and E. Gutheil. Numerical study of single iron (iii) nitrate nonahydrate/ethanol droplet evaporation in humid air. *Proceedings of the 5th World Congress on Momentum, Heat and Mass Transfer (MHMT'20)*, 2020.

[78] P. Narasu, A. Keller, M. Kohns, H. Hasse, and E. Gutheil. Numerical study of single iron (iii) nitrate nonahydrate/ethanol droplet evaporation in dry air. *21st Annual Conference on Liquid Atomization and Spray Systems, ILASS–Asia*, 2020.

[79] A. Gadalla and H. Yu. Thermal decomposition of fe(iii) nitrate and its aerosol. *Journal of Materials Research*, 5:1233–1236, 1990.

[80] J. Mu and D. Perlmutter. Thermal decomposition of metal nitrates and their hydrates. *Thermochimica Acta*, 56(3):253–260, 1982.

[81] P. Narasu and E. Gutheil. A new model for puffing and micro-explosion of single titanium(iv) isopropoxide/p-xylene precursor solution droplets. *International Journal of Heat and Mass Transfer, in press*, 2022.

[82] H. Grosshans, M. Griesing, T. Hellwig, W. Pauer, H.-U. Moritz, and E. Gutheil. A new model for the drying of mannitol-water droplets in hot air above the boiling temperature. *Powder Technology*, 297:259–265, 2016.

[83] S. Nešić and J. Vodnik. Kinetics of droplet evaporation. *Chemical Engineering Science*, 46(2):527–537, 1991.

[84] H. Renon and J. M. Prausnitz. Local compositions in thermodynamic excess functions for liquid mixtures. *AIChE Journal*, 14(1):135–144, 1968.

[85] S. Gopireddy and E. Gutheil. Numerical simulation of evaporation and drying of a bi-component droplet. *International Journal of Heat and Mass Transfer*, 66: 404–411, 2013.

[86] M. Manojkumar and B. Sivaprakash. VLE prediction of azeotropic systems using UNIQUAC and UNIFAC models and experimental validation using Othmer VLE Still. *Research Journal of Applied Sciences*, 13(3):216–224, 2018.

[87] J. Gmehling, P. Rasmussen, and A. Fredenslund. Vapor-liquid equilibriums by UNIFAC group contribution. Revision and Extension 2. *Industrial & Engineering Chemistry Process Design and Development*, 21(1):118–127, 1982.

[88] A. Fredenslund, R. L. Jones, and J. M. Prausnitz. Group-contribution estimation of activity coefficients in nonideal liquid mixtures. *AIChE Journal*, 21(6):1086–1099, 1975.

[89] P. B. Govindaraju and M. Ihme. Group contribution method for multicomponent evaporation with application to transportation fuels. *International Journal of Heat and Mass Transfer*, 102:833–845, 2016.

[90] L. Chen, Z. Liu, Y. Lin, and C. Zhang. Different spray droplet evaporation models for non-ideal multi-component fuels with experimental validation. *International Journal of Heat and Mass Transfer*, 94:292–300, 2016.

[91] M. Kleiber and R. Joh. Berechnungsmethoden für thermophysikalische stoffeigenschaften. In P. Stephan, D. Mewes, S. Kabelac, M. Kind, K. Schaber, and T. Wetzel, editors, *VDI-Wärmeatlas*, pages 1–45. Springer Reference Technik. Springer Vieweg, Berlin, Heidelberg, 2018.

[92] R. Wittig, J. Lohmann, and J. Gmehling. Vapor-liquid equilibria by UNIFAC group contribution. 6. Revision and Extension. *Industrial & Engineering Chemistry Research*, 42(1):183–188, 2003. doi: 10.1021/ie020506l.

[93] Dortmund Data Bank. `http://www.ddbst.com`, 2022.

[94] A. K. Coker. *Ludwig's applied process design for chemical and petrochemical plants.* gulf professional publishing, 2014.

[95] V. Majer and V. Svoboda. *Enthalpies of Vaporization of Organic Compounds: A Critical Review and Data Compilation.* Blackwell Scientific Publications, Oxford, 1985.

[96] M. Nanjaiah, P. Wollny, S. Apazeller, M. Gonchikzhapov, P. Narasu, E. Gutheil, H. Wiggers, C. Schulz, T. Kasper, A. Kempf, and I. Wlokas. Simulations of laminar methane flames doped with iron nitrate/1-butanol aerosol in a novel matrix burner. *Combustion and Flame, under preparation.*

[97] A. Keller, I. Wlokas, M. Kohns, and H. Hasse. Thermophysical properties of solutions of iron (iii) nitrate nonahydrate in mixtures of ethanol and water. *Journal of Chemical & Engineering Data*, 65(7):3519–3527, 2020.

[98] A. Keller, I. Wlokas, M. Kohns, and H. Hasse. Thermophysical properties of mixtures of Titanium (IV) Isopropoxide (TTIP) and p-xylene. *Journal of Chemical & Engineering Data*, 65(2):869–876, 2020. doi: https://doi.org/10.1016/j.ijmultiphaseflow.2022.104006.

[99] A. Shmakov, O. Korobeinichev, D. Knyazkov, A. Paletsky, I. Gerasimov, T. Bolshova, V. Kiselev, and N. Gritsan. Combustion chemistry of $Ti(OC_3H_7)_4$ in premixed flat burner-stabilized $H_2/O_2/Ar$ flame at 1 atm. *Proceedings of the Combustion Institute*, 34(1):1143–1149, 2013.

[100] P. Buerger, D. Nurkowski, J. Akroyd, and M. Kraft. A kinetic mechanism for the thermal decomposition of titanium tetraisopropoxide. *Proceedings of the Combustion Institute*, 36(1):1019–1027, 2017.

[101] R. Courant, K. Friedrichs, and H. Lewy. Uber die partiellen differenzengleichungen der mathematischen physik. *Mathematische Annalen*, 100:32–74, 1928.

[102] C. E. F. Vian, L. Rodrigues, and J. T. da Silva. Evolution in public policies designed to develop the sugar–energy industry in Brazil. In A. K. Chandel and M. H. L. Silveira, editors, *Advances in Sugarcrane Biorefinery*, chapter 14, pages 279–306. Elsevier, 2018.

[103] K. S. Hyun and S. L. Chang. A review on atomization and exhaust emissions of a biodiesel-fueled compression ignition engine. *Renewable and Sustainable Energy Reviews*, 8:1601–1620, 2016.

[104] R. C. Costa and J. R. Sodré. Hydrous ethanol vs. gasoline-ethanol blend: Engine performance and emissions. *Fuel*, 89(2):287–293, 2010.

[105] S. B. Saharin. *Vaporization and autoignition characteristics of ethanol and 1-propanol droplets: influence of water*. PhD thesis, Université de Bourgogne, Dijon, France, 2013.

[106] A. J. Marchese, F. L. Dryer, and V. Nayagam. Numerical modeling of isolated n-alkane droplet flames: initial comparisons with ground and space-based microgravity experiments. *Combustion and flame*, 116(3):432–459, 1999.

[107] S. Taneda. Experimental investigation of the wake behind a sphere at low Reynolds number. *Journal of the Physics Society of Japan*, 11:1104–1108, 1956.

[108] E. W. de Menezes, R. Cataluña, D. Samios, and R. da Silva. Addition of an azeotropic ETBE/ethanol mixture in eurosuper-type gasolines. *Fuel*, 85(17): 2567–2577, 2006.

[109] S. Apazeller, M. Gonchikzhapov, M. Nanjaiah, T. Kasper, I. Wlokas, H. Wiggers, and C. Schulz. A new dual matrix burner for one-dimensional investigation of aerosol flames. *Proceedings of the Combustion Institute*, 2022.

[110] Chemical Book, Chemical Search Engine. `https://www.chemicalbook.com/ChemicalProductProperty_EN_CB51099606.html`, 2022.

[111] Indiamart Intermesh Ltd. `https://5.imimg.com/data5/KT/AM/MY-1561863/iron-oxide-nanoparticles-500x500.jpg`, 2022.

[112] S. Wang and Y. Huang. Flame aerosol synthesis of wo3/ceo2 from aqueous solution: Two distinct pathways and structure design. *Chemical Engineering Science*, 152:436 – 442, 2016. ISSN 0009-2509. doi: https://doi.org/10.1016/j.ces.2016.06.045. URL `http://www.sciencedirect.com/science/article/pii/S0009250916303414`.

[113] C. Abram, M. Mezhericher, F. Beyrau, H. A. Stone, and Y. Ju. Flame synthesis of nanophosphors using sub-micron aerosols. *Proceedings of the Combustion Institute*, 37(1):1231 – 1239, 2019. ISSN 1540-7489. doi: https://doi.org/10.1016/j.proci.2018.06.040. URL `http://www.sciencedirect.com/science/article/pii/S1540748918302232`.

[114] P. Majerič, D. Jenko, B. Friedrich, and R. Rudolf. Formation mechanisms for gold nanoparticles in a redesigned ultrasonic spray pyrolysis. *Advanced Powder Technology*, 28(3):876 – 883, 2017. ISSN 0921-8831. doi: https://doi.org/10.1016/j.apt.2016.12.013. URL `http://www.sciencedirect.com/science/article/pii/S0921883116303855`.

[115] A. K. Gupta and M. Gupta. Synthesis and surface engineering of iron oxide nanoparticles for biomedical applications. *Biomaterials*, 26(18):3995–4021, 2005.

[116] M. Auffan, J. Rose, J.-Y. Bottero, G. V. Lowry, J.-P. Jolivet, and M. R. Wiesner. Towards a definition of inorganic nanoparticles from an environmental, health and safety perspective. *Nature Nanotechnology*, 4(10):634–641, 2009.

[117] M. H. Siddiqui, M. H. Al-Whaibi, A. M. Sakran, H. M. Ali, M. O. Basalah, M. Faisal, A. Alatar, and A. A. Al-Amri. Calcium-induced amelioration of boron toxicity in radish. *Journal of Plant Growth Regulation*, 32(1):61–71, 2013.

[118] I. Matsui. Nanoparticles for electronic device applications: a brief review. *Journal of Chemical Engineering of Japan*, 38(8):535–546, 2005.

[119] M. Javidi, M. Heydari, A. Karimi, M. Haghpanahi, M. Navidbakhsh, and A. Razmkon. Evaluation of the effects of injection velocity and different gel concentrations on nanoparticles in hyperthermia therapy. *Journal of Biomedical Physics & Engineering*, 4(4):151, 2014.

[120] M. Javidi, M. Heydari, M. M. Attar, M. Haghpanahi, A. Karimi, M. Navidbakhsh, and S. Amanpour. Cylindrical agar gel with fluid flow subjected to an alternating magnetic field during hyperthermia. *International Journal of Hyperthermia*, 31 (1):33–39, 2015.

[121] M. Heydari, M. Javidi, M. M. Attar, A. Karimi, M. Navidbakhsh, M. Haghpanahi, and S. Amanpour. Magnetic fluid hyperthermia in a cylindrical gel contains water flow. *Journal of Mechanics in Medicine and Biology*, 15(05):1550088, 2015.

[122] R. Bogusz, P. Magnuszewska, B. Florczak, A. Maranda, and K. Drożdżewska. Studies of the influence of nano iron (iii) oxide on selected properties of solid heterogeneous propellants based on htpb. *Central European Journal of Energetic Materials*, 13(4), 2016.

[123] P. Narasu and E. Gutheil. Modeling and parameterization of the evaporation and thermal decomposition of an iron (iii) nitrate nonahydrate/ethanol droplet for flame spray pyrolysis. *Fluids*, 7(5):146, 2022.

[124] P. Narasu and E. Gutheil. Modeling and simulation of the evaporation and thermal decomposition of an iron(iii) nitrate nonahydrate/ethanol droplet in hot convective air. *16th International Conference on Heat Transfer, Fluid Mechanics and Thermodynamics and Editorial Board of Applied Thermal Engineering (HEFAT)*, 2022.

[125] Volochem Inc. `https://cdn.shopify.com/s/files/1/0250/9033/products/VOL010060_CDimage.png?v=1425443874`, 2022.

[126] Santa Cruz Biotechnology Inc. https://www.scbt.com/de/p/p-xylene-106-42-3, 2022.

[127] W.-N. Wang, I. W. Lenggoro, Y. Terashi, T. O. Kim, and K. Okuyama. One-step synthesis of titanium oxide nanoparticles by spray pyrolysis of organic precursors. *Materials Science and Engineering: B*, 123(3):194–202, 2005.

[128] H. Teisala, M. Tuominen, M. Aromaa, J. Mäkelä, M. Stepien, J. Saarinen, M. Toivakka, and J. Kuusipalo. Development of superhydrophobic coating on paperboard surface using the liquid flame spray. *Surface and Coatings Technology*, 205(2):436–445, 2010.

[129] H. Dong, G. Tang, T. Ma, and X. Cao. One-step fabrication of inorganic/organic hybrid microspheres with tunable surface texture for controlled drug release application. *Journal of Materials Science: Materials in Medicine*, 27(1):1–8, 2016.

[130] M. Gonchikzhapov and T. Kasper. Decomposition reactions of $Fe(CO)_5$, $Fe(C_5H_5)_2$, and TTIP as precursors for the spray-flame synthesis of nanoparticles in partial spray evaporation at low temperatures. *Industrial & Engineering Chemistry Research*, 59(18):8551–8561, 2020.

[131] H. Li, C. Rosebrock, N. Riefler, T. Wriedt, and L. Mädler. Experimental investigation on microexplosion of single isolated burning droplets containing titanium tetraisopropoxide for nanoparticle production. *Proceedings of the Combustion Institute*, 36(1):1011–1018, 2017.

[132] All India Metal Corporation. `https://www.allindiametal.com/wp-content/uploads/2019/06/titanium-dioxide-powder-suppliers.jpg`, 2022.

[133] P. Narasu, M. Nanjaiah, I. Wlokas, and E. Gutheil. Numerical simulation and parameterization of the heating and evaporation of a titanium(iv) isopropoxide/p-xylene precursor/solvent droplet in hot convective air. *International Journal of Multiphase Flow*, 150:104006, 2022.

[134] Wikipedia contributors. Titanium isopropoxide - Wikipedia, the free encyclopedia. https://en.wikipedia.org/w/index.php?title=Titaniumn-isopropoxideoldid=1005040488, 2021.

[135] P. Narasu, M. Nanjaiah, I. Wlokas, and E. Gutheil. Numerical study of the interaction of a titanium (iv) isopropoxide/p-xylene precursor/solvent droplet with hot convective air. *15th Triennial International Conference on Liquid Atomization and Spray Systems (ICLASS)*, 2021.

[136] S.-C. Wong and A.-C. Lin. Microexplosion mechanisms of aluminum/carbon slurry droplets. *Combustion and flame*, 89(1):64–76, 1992.

[137] K. Tsao and C. Wang. Puffing and micro-explosion phenomena of water emulsion fuels. *SAE transactions*, pages 308–320, 1986.

[138] D. V. Antonov, G. V. Kuznetsov, P. A. Strizhak, O. Rybdylova, and S. S. Sazhin. Micro-explosion and autoignition of composite fuel/water droplets. *Combustion and Flame*, 210:479–489, 2019.

[139] Y. Zhang, R. Huang, S. Huang, P. Zhou, X. Rao, G. Zhang, and L. Qiu. Experimental study on puffing, auto-ignition and combustion characteristics of an n-pentanol-diesel droplet. *Energy*, 223:119994, 2021.

[140] P. Narasu and E. Gutheil. A new model to describe puffing and microexplosion of single titanium(iv) isopropoxide/p-xylene droplets in hot convective air. *31th Conference on Liquid Atomization and Spray Systems, ILASS–Europe*, 2022.

[141] L. Ma, X. Q. Qiu, J. Wang, Z. W. Zheng, Z. Y. Yi, and H. Q. Yang. Experimental research on single droplet evaporation factors. *Modern Chemical Industry*, 33(1): 103–06, 2013.

Abbreviations and symbols

Abbreviation	Meaning
AP-PMS	atmospheric pressure particle mass spectrometery
EHA	ethylhexanoic acid
EtOH	ethanol
FSP	flame spray pyrolysis
H_2O	water
IN	iron(III) nitrate
INN	iron(III) nitrate nonahydrate
LT-FSP	low temperature flame spray pyrolysis
NOx	nitrogen oxides
NRTL	non-random two-liquid
PDA	phase doppler anemometry
PS-LIBS	phase selective laser induced breakdown spectroscopy
TEM	transmission electron microscopy
TTIP	titanium(IV) isopropoxide
UNIFAC	universal quasichemical functional group activity coefficients
UNIQUAC	universal quasichemical activity coefficients
VLE	vapor liquid equilibrium

Symbol	Unit	Meaning
$\mathrm{B_M}$	[-]	Spalding mass transfer number
$\mathrm{B_T}$	[-]	Spalding heat transfer number
c_p	[J/(kg K)]	specific heat capacity
d	[m]	droplet diameter
D	[m^2/s]	diffusivity
E	[kJ/mol]	activation energy
$\mathrm{F_M}$	[-]	diffusion film correction factor
$\mathrm{F_T}$	[-]	thermal diffusion correction factor
G	[-]	number of different groups
h	[J/(m^{2}sK)]	heat transfer coefficient
H	[-]	number of components
k	[-]	number of structure groups
L	[J/kg]	latent heat of vaporization
Le	[-]	Lewis Number
m	[kg]	droplet mass
$\dot{m}$	[kg/s]	mass evaporation rate
Nu	[-]	Nusselt number
$\widetilde{\mathrm{Nu}}$	[-]	modified Nusselt number
p	[N/m^2]	pressure
Pr	[-]	Prandtl number
q_w	[-]	relative Van-der-Waals surface area
Q	[J]	heat transfer
Q_k	[-]	specific constant for group k
r	[m]	radial coordinate
r_d	[m]	droplet radius
r_w	[-]	relative Van-der-Waals volume
R	[J/(mol K)]	universal gas constant
Re	[-]	Reynolds number
RH	[%]	relative humidity
R_k	[-]	specific constant for group k
Sc	[-]	Schmidt number
Sh	[-]	Sherwood number
$\widetilde{\mathrm{Sh}}$	[-]	modified Sherwood number
t	[s]	time
T	[K]	temperature
$\overline{T}$	[K]	average temperature
u	[m/s]	velocity
X	[-]	mole fraction
Y	[-]	mass fraction
α	[-]	normalized mass
δ	[m]	liquid shell thickness
γ	[-]	activity coefficient

Symbol	Unit	Meaning
λ	[J/(m s K)]	thermal conductivity
$\mathcal{M}$	[-]	normalized mass
ν	[-]	number of structural groups
ϕ	[-]	exponent
ρ	[kg/m^3]	density
$\mathcal{T}$	[-]	normalized temperature
τ	[-]	normalized time

Subscript	Meaning
amb	ambience
atm	atmospheric
b	boiling point
d	droplet
evap	evaporation
f	film
g	gas
i	component
l	liquid
max	maximum
overlap	overlap
s	surface
sh	liquid shell
t	time
th	thermal decomposition
tot	total
v	vapor
∞	condition in the ambience
0	initial value

Superscript	Meaning
C	combinatorial
R	residual
+	transitional

Acknowledgements

The research work was carried out at Interdisciplinary Center for Scientific Computing (IWR), Heidelberg University, under the supervision of Prof. Dr. Eva Gutheil and this study is funded by Deutsche Forschungsgemeinschaft (DFG, German Research Foundation) through priority program SPP 1980 - Projektnummer 374463455.

First and foremost, I would to like to express my heartfelt respect and gratitude to my supervisor, Prof. Dr. Eva Gutheil, head of research group of Multiphase Flows and Combustion, Heidelberg University, for the continued and persistent support, motivation, and guidance throughout the course of my research work. I was offered the opportunity to pursue my doctoral studies in her group while I was working at Indian Institute of Technology (IIT), Madras as project associate after finishing my Master studies at the Ocean Engineering Department, IIT Madras. Although I did not have any prior domain knowledge in the field of work pursued in her group, she had utmost confidence and belief that I would be able to fulfill the objectives of the project in a very successful manner. Right from the moment I came to Heidelberg, she has always been present with constant support and always ensured that my path towards achieving the aim of successfully completing my doctoral education is as smooth as possible. Without her support, it would have been impossible to fulfill my research goals. At this moment, I would like to thank her for the relentless patience with which she corrected all my presentations, research papers, and this thesis. I learned the art of scientific writing from her and I am very much grateful for sharing your expertise with me. Even during the very difficult corona pandemic period, her care and kindness ensured that I was able to survive through the tough phase. Finally, I would like to thank Prof. Dr. Eva Gutheil for nominating me for the Dr. Sophie Bernthsen-Fonds Prize awarded by Die Fakultät für Chemie und Geowissenschaften der Ruprecht-Karls-Universität Heidelberg as recognition for the excellent performance during doctoral studies, which motivated me further to achieve greater heights in the field of research.

I am very thankful to Prof. Dr.-Ing. Udo Fritsching, for accepting to be the co-reviewer of the thesis. I wish to express my sincere thanks to panel members for accepting to be part of the evaluation process.

I express my sincere thanks to all my colleagues, M. Herrmann, Z. Ying, D. Kreitmayer, P. Pöschko, S. Boschmann, and R. Kugler for all the help extended to me during my precious time in the group of Prof. Dr. Eva Gutheil. I would like to convey my special thanks to M. Herrmann, D. Kreitmayer, and R. Kugler for translating the abstract in German. I sincerely thank E. Vogel for her timely help in all matters related to administration, especially with regard to my visa extension procedures, which ensured that I have a peaceful time in Heidelberg. I wish M. Trunk my special thanks for providing all the required technical support.

I owe my invaluable debt to all the staff of Heidelberg University for support, suggestions, and co-operation without which I could not have executed this project. I thank IWR and Heidelberg University for providing with the all the facilities.

I thank Prof. Dr.-Ing. Hans Hasse and his research group at TU Kaiserslautern for providing with the liquid thermophysical properties that was required for performing the numerical simulations with respect to INN/ethanol and TTIP/*p*-xylene droplets. I sincerely thank Dr.-Ing. Irenäus Wlokas and his research group at Universität Duisburg-Essen for providing with the gas phase properties and the initial conditions concerning the numerical study of butanol/water droplets. I am grateful to all the collaborators and co-authors of my research papers for providing with valuable expertise and thus, enhancing the quality of my research works. I would like to thank all the members of the DFG priority program SPP 1980 for their valuable input.

I thank my beloved family members, especially, my mother (K. Meenakshi) and my father (V. Narasu), for their constant support and endless love. I am forever grateful to them for their vital role as advisor, mentor, teacher, and constant motivator during the entire course of the thesis work. I would like to take this opportunity to convey special thanks to my wife (R. Anisha), who motivated and supported me throughout this journey.

Finally, I would like to express my sincere gratitude to my dearest friends for their constant help and support. The care that my friends provided me and making sure that they were always there for me during all the tough times was one of the significant reasons that I was able to survive in Germany. My friends became my family far away from my home.

Last but not least, the financial support of Deutsche Forschungsgemeinschaft (DFG, German Research Foundation) through priority program SPP 1980 - Projektnummer 374463455 and HGS- MathComp is gratefully acknowledged.

Above all, I thank almighty for giving me strength, courage and blessings to do this research.

Thank you all.

Eidesstattliche Versicherung gemäß § 8 der Promotionsordnung für die Gesamtfakultät für Mathematik, Ingenieur- und Naturwissenschaften der Universität Heidelberg / Sworn Affidavit according to § 8 of the doctoral degree regulations of the Combined Faculty of Mathematics, Engineering and Natural Sciences at Heidelberg University

1. Bei der eingereichten Dissertation zu dem Thema / The thesis I have submitted entitled

   Numerical Simulation of the Heating, Evaporation, Thermal Decomposition, Puffing, and
   ……
   Micro-Explosion of Single Alcohol/Water and Precursor/Solvent Droplets for Nanoparticle Synthesis in Spray Flames
   ……

   handelt es sich um meine eigenständig erbrachte Leistung / is my own work.

2. Ich habe nur die angegebenen Quellen und Hilfsmittel benutzt und mich keiner unzulässigen Hilfe Dritter bedient. Insbesondere habe ich wörtlich oder sinngemäß aus anderen Werken übernommene Inhalte als solche kenntlich gemacht. / I have only used the sources indicated and have not made unauthorised use of services of a third party. Where the work of others has been quoted or reproduced, the source is always given.

3. Die Arbeit oder Teile davon habe ich ~~wie folgt~~/bislang nicht(1) an einer Hochschule des In- oder Auslands als Bestandteil einer Prüfungs- oder Qualifikationsleistung vorgelegt. / I have not yet/have already(1) presented this thesis or parts thereof to a university as part of an examination or degree.

   Titel der Arbeit / Title of the thesis: ……………………………………………………………………………….

   Hochschule und Jahr / University and year: …………………..……………………………………………......

   Art der Prüfungs- oder Qualifikationsleistung / Type of examination or degree: ………………………….

4. Die Richtigkeit der vorstehenden Erklärungen bestätige ich. / I confirm that the declarations made above are correct.

5. Die Bedeutung der eidesstattlichen Versicherung und die strafrechtlichen Folgen einer unrichtigen oder unvollständigen eidesstattlichen Versicherung sind mir bekannt. / I am aware of the importance of a sworn affidavit and the criminal prosecution in case of a false or incomplete affidavit.

Ich versichere an Eides statt, dass ich nach bestem Wissen die reine Wahrheit erklärt und nichts verschwiegen habe. / I affirm that the above is the absolute truth to the best of my knowledge and that I have not concealed anything.

………………………………………..
Ort und Datum / Place and date

……………………………...………………………..
Unterschrift / Signature

---

(1) Nicht Zutreffendes streichen. Bei Bejahung sind anzugeben: der Titel der andernorts vorgelegten Arbeit, die Hochschule, das Jahr der Vorlage und die Art der Prüfungs- oder Qualifikationsleistung. / Please cross out what is not applicable. If applicable, please provide: the title of the thesis that was presented elsewhere, the name of the university, the year of presentation and the type of examination or degree.

The German text is legally binding.